



Freeze-casting of microchannels in magnetocaloric materials

Christiansen, Cathrine Deichmann

Publication date:
2019

Document Version
Publisher's PDF, also known as Version of record

[Link back to DTU Orbit](#)

Citation (APA):
Christiansen, C. D. (2019). *Freeze-casting of microchannels in magnetocaloric materials*. Technical University of Denmark.

General rights

Copyright and moral rights for the publications made accessible in the public portal are retained by the authors and/or other copyright owners and it is a condition of accessing publications that users recognise and abide by the legal requirements associated with these rights.

- Users may download and print one copy of any publication from the public portal for the purpose of private study or research.
- You may not further distribute the material or use it for any profit-making activity or commercial gain
- You may freely distribute the URL identifying the publication in the public portal

If you believe that this document breaches copyright please contact us providing details, and we will remove access to the work immediately and investigate your claim.

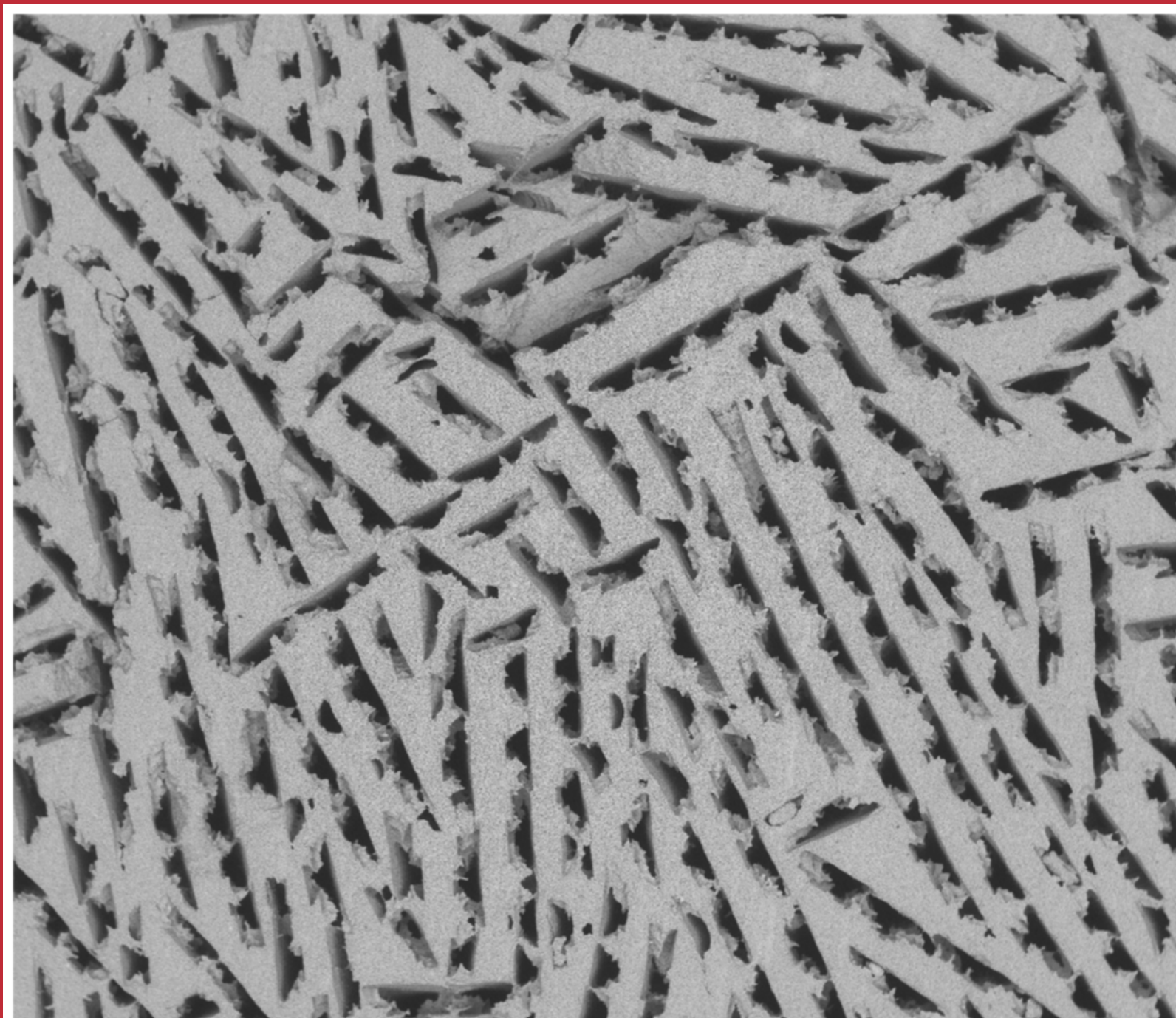


Cathrine D. Christiansen

Freeze-casting of microchannels in magnetocaloric materials

Cathrine D. Christiansen

Freeze-casting of microchannels in magnetocaloric materials



Technical University of Denmark

Department of Energy Conversion and Storage
Anker Engelunds Vej 1
2800 Kgs. Lyngby

www.energy.dtu.dk/



“Ignorance is the natural state of mind of the research scientist.”

– Neil DeGrasse Tyson, *Astrophysics for people in a hurry*

Preface

This thesis represents the work I did as a Ph.D. student at the Department of Energy Conversion and Storage, Technical University of Denmark (DTU), January 2017 – December 2019, and is submitted in partial fulfilment of the requirements for the degree of Ph.D.

The project was funded by The Independent Research Fund Denmark – Technologies and Productions Sciences, project no. 6111-00073B, with the majority of the work carried out at DTU supplemented with an external research stay of three months at the Department of Materials Science and Engineering, Clemson University, SC, United States, in collaboration with professor Rajendra K. Bordias research group.

The outcome of this project build on many years of experience with magnetic refrigeration at DTU and was sparked by a desire to implement and evaluate the fine micrometer sized structural features and anisotropic porosity of freeze-cast materials as a regenerator geometry in magnetic refrigeration. As such, this project is all about shaping materials by freezing for applications of cooling.

Cathrine D. Christiansen
Lyngby, December 2019

Acknowledgements

I am – do I dare say it – actually quite proud of my accomplishments in surviving three years of Ph.D. studies and of the overall outcome of this thesis. I could, however, absolutely not have managed this work without the help and support of a number of people:

My achievements in the lab builds on many years of experience and high-skilled competencies by the technical staff at DTU: Lene Knudsen, Pernille H. Nielsen, Kjeld B. Andersen and without a doubt Ebtisam Abdellahi. Without your willingness to share your knowledge and expertise throughout countless of discussions, I would probably still be somewhere in a forgotten corner of the process-lab trying to mix ceramic powder and water with a spoon.

Senior scientist Christian Bahl have proven himself an invaluable encyclopedia of theoretical knowledge and practical know-how; both regarding magnetic refrigeration and characterization, but in particular regarding tiny processing details of LCSM ceramics. In addition, being a part of the magnetocaloric cooling group at DTU has been an absolute joy! I have rarely met a group of such competent people with such a . . . unique sense of humour. In all honesty though, on dark days where frozen freeze-casts decided to not stay frozen but rather distribute themselves all over the place, there was always laughter to be heard and cheerful optimism somewhere in the corridors at Risø campus. Thank you for letting me be a part of your research family for a little while!

I want to acknowledge the contributions of senior researcher Peter Stanley Jørgensen who supplied parts of the software for analysis of SEM micrographs and who was a great part of our initial studies on 3D characterization of freeze-casts.

A part of this project led me across the Atlantic, to Clemson University, South Carolina, United States, where I joined professor Rajendra K. Bordias research group for three months. This gave me a unique opportunity to build on their experiences of freeze-casting and for that I am very grateful! Especially to Michelle Greenough for making Clemson a home for a little while and for giving me a friend for life. Clemson will always be so much more than endless days in lab; for me, it will forever be hiking under a burning sun, river rafting (without helmets) and chasing waterfalls in the Blue Ridge Mountains.

The finalization of this work have been carried out in collaboration with Jierong Liang, Ph.D. student at DTU. It was an amazing experience to see how these magnetocaloric freeze-cast structures suddenly fulfilled their purpose and I will be forever amazed and inspired by your persistence and hardworking spirit. And thank you for patiently explaining to me and dumbing down – even for the umpteenth time – the complexity of your research.

To my friends and family – all I can say is; I hope you still remember my face! I love you all, you keep me grounded, smiling and sane. Björn, I would have died of starvation if you hadn't fed me for three years. Thank you for partaking on this journey with me, for supporting me and putting up with me, without you it's a waste of time.

Ultimately, my deepest gratitude to my two supervisors, associate professor Kaspar K. Nielsen and professor Rasmus Bjørk. Words cannot begin to express how much I have enjoyed working with the two of you! I am grateful for the opportunity you gave me, amazed and inspired by your professional skills and scientific competencies and forever in awe of your trust and confidence in me. I am eternally grateful that you quickly understood that patting me on the head is by far the most efficient way to get me back on track and somehow you always managed to make me laugh and regain hope that there was actually a meaning to it all even when the furnaces had broken down for what felt like the 77th time that week. I will greatly miss our scientific discussions from which my brain would often spark with new ideas and inspiration, and I will forever carry with me the lessons of both science and work/life-balance that you have given me. Thank you for entrusting me with this project and thank you for letting me have a lot of fun – while getting paid – for three years!

Finally, even though this is only a Ph.D. thesis and as such merely a collection of three years of scientific work, it is nonetheless singlehandedly the biggest piece of work I will probably ever manage to produce in my life; I therefore want to dedicate it to my father, the most unselfish man I know who would slay Oliphants and cross oceans for his children.

“I don’t know if you ever catch up with your dreams. You sail up beside them, they change shape, like water, and dissolve. And as we all know, the Greek gods promised to punish those who dared to achieve their dreams. But dreams are an incredibly important motivating force. Dreams and visions give you the strength to go out and build that vision in reality.”

– Troels Kløvedal, Indonesia, 2006

Risø campus, Clemson campus and Blue Ridge Mountains.



Abstract

This thesis investigates the processing of magnetocaloric materials by freeze-casting with the overall scope of applications as regenerator geometries in magnetic refrigeration. Magnetic refrigeration utilizing the active magnetic regenerative (AMR) cycle offers an alternative to conventional refrigeration using chlorofluorocarbon gasses. The latter poses an environmental risk, while AMR technology is based on a porous magnetocaloric material through which an environmentally friendly fluid flows transferring heat. The magnetocaloric effect is the change in temperature of a ferromagnetic material upon varying an externally applied magnetic field, and is greatest in the vicinity of Curie temperature (T_C). T_C is defined as the transition temperature between the ferro- and paramagnetic states. The magnetocaloric material is thus invoked as both refrigerant and regenerator. A regenerator being a heat exchanger for intermittent storage of heat. The efficiency of the AMR cycle strongly depends on the geometry of the regenerator; an attractive structure could consist of microchannels while still maintaining a large surface area. Freeze-casting, or ice-templating, offers a processing route for structures meeting these specific criteria. In freeze-casting, directional solidification of a solvent, in which particulates of a material are suspended, is used to shape or template anisotropic pores on a micro scale in the given material. Under appropriate conditions, this processing route results in a structure with macroporosity in the form of parallel, well-defined pores, or microchannels, running throughout the structure with pore widths in the order of $\sim 1 - 100 \mu\text{m}$ and solid walls.

Dynamic control of the temperature during freezing is crucial for successful ice-templating. Thus, a freeze-casting device utilizing a thermoelectric element for high precision temperature control was designed and build as part of this work. The set-up is presented and evaluated in the thesis. Freezing front velocities of $6 - 21 \mu\text{m/s}$ with corresponding pore widths of $35 - 65 \mu\text{m}$ were achieved. Structural features of freeze-cast samples are quantified by a semi-automated image analysis of scanning electron micrographs in MATLAB®. Here, the procedure is described and evaluated.

Processing of magnetocaloric freeze-cast regenerators was achieved by freeze-casting of ceramic suspensions of $\text{La}_{0.66}\text{Ca}_{0.33-x}\text{Sr}_x\text{Mn}_{1.05}\text{O}_3$ (LCSM) powders in water. LCSM is a ceramic and was here chosen as a magnetocaloric model-material. LCSM freeze-cast regenerators were found to outperform the conventional regenerator geometry of packed particle beds, both regarding effectiveness and pressure drop. An optimal regenerator geometry exhibits a low pressure drop and high effectiveness.

The properties of the solvent during freeze-casting is investigated as gelation is evaluated as a processing lever for achieving altered freeze-cast morphologies. The addition of gelatin forms a polymer network which inhibits ice-crystal growth and thus alters the morphology of templated pores. Additionally, gelation provides a near-net shaping step of freeze-cast samples prior to freezing, which is applied for processing of functionally graded multi-material freeze-casts with varying T_C along the pore orientation. The latter has prospects for application as layered freeze-cast regenerators while gelation in itself provides a possibility of fine-tuning morphology and thus flow behaviour in freeze-cast regenerators.

Resumé

Denne afhandling undersøger frysestøbning af magnetokaloriske materialer til brug som regeneratorgeometrier i magnetisk køling teknologi. Magnetisk køling anvender den aktive magnetiske regenerative (AMR) cyklus og udgør et alternativ til konventionel køling som anvender chlorfluorcarbongasser. Sidstnævnte udgør en miljørisiko, mens AMR-teknologien er baseret på et fast, porøst magnetokalorisk materiale, hvorigennem en miljøvenlig væske strømmer og overfører varme. Den magnetokaloriske effekt er den ændring i temperatur som et ferromagnetisk materiale oplever i et varierende, eksternt magnetfelt. Effekten er stærkest ved faseovergangen mellem den ferro- og paramagnetiske tilstand, defineret som Curie temperaturen (T_C). Det magnetokaloriske materiale anvendes således som både kølemedie og generator. Sidstnævnte er en varmeveksler til periodisk lagring og afgivning af varme. Effektiviteten af AMR-cyklussen afhænger stærkt af regeneratorens geometri, hvor attraktiv struktur består af mikrokanaler, mens der dog stadig opretholdes et stort overfladeareal. Frysestøbning udgør en mulig fremstillingsprocedure for strukturer der opfylder disse specifikke kriterier. Ved frysestøbning anvendes retningsbestemt frysning af en væske, hvori partikler af et ønsket materiale er opslæmmet, til forme anisotrope porer i mikrostørrelsesordenen. Iskrystallerne fungerer da som skabelon for porerne. Under optimale betingelser resulterer frysestøbning i en struktur med makroporøsitet i form af parallelle, veldefinerede porer, eller mikrokanaler, der løber gennem strukturen. Kanalerne er i størrelsesordenen $\sim 1 - 100 \mu\text{m}$ og vægge er faste.

Dynamisk styring af temperaturen under frysning er afgørende for vellykket frysestøbning. Derfor blev en anordning til frysestøbning designet og bygget som en del af dette projekt. Frysestøberen anvender et termoelektrisk element til høj præcisionstemperaturstyring og opstillingen præsenteres og evalueres i denne afhandling. Frysefrontshastigheder på $6 - 21 \mu\text{m/s}$ med tilsvarende kanalstørrelser på $35 - 65 \mu\text{m}$ blev opnået. Struktur og morfologi af frysestøbte prøver evalueres ved hjælp af en semi-automatiseret billedanalyse af elektronmikroskopi billeder i MATLAB®. Proceduren beskrives og evalueres her.

Magnetokaloriske frysestøbte regeneratore blev fremstillet ved frysestøbning af opslæmninger af $\text{La}_{0.66}\text{Ca}_{0.33-x}\text{Sr}_x\text{Mn}_{1.05}\text{O}_3$ (LCSM) pulvere i vand. LCSM er et keramisk materiale og blev her valgt som et magnetokalorisk model-materiale. LCSM frysestøbte regeneratore viste sig at overgå den konventionelle regeneratorgeometri af pakkede kugler, både hvad angår effektivitet og tryktab. En optimal regeneratorgeometri udviser et lavt tryktab og høj effektivitet.

Den anvendte væskes egenskaber under frysestøbning er afgørende for strukturernes endelige morfologi og gelering undersøges derfor som et processeringshåndtag til at opnå ændrede frysestøbte morfologier. Tilsætningen af gelatine danner et polymernetværk, som modvirker iskrySTALLVÆKST og dermed ændrer morfologien af isformede porer. Derudover muliggør gelering et processeringstrin til formning af frysestøbte prøver før selve frysningen. Dette anvendes til fremstilling af frysestøbte prøver med graduerede materialeegenskaber og således med varierende T_C langs kanalretnigen. Sidstnævnte kan eventuelt anvendes som graduerede frysestøbte regeneratore, mens gelering i sig selv giver en mulighed for finjustering af morfologi og dermed strømningsadfærd i frysestøbte regeneratore.

List of publications

Cathrine D. Christiansen, Kaspar K. Nielsen, Rajendra K. Bordia, Rasmus Bjørk. The effect of gelation on statically and dynamically freeze-cast structures. *Journal of the American Ceramic Society* 2019;102:5796–5806. DOI: 10.1111/jace.16500. Referenced as Paper I.

Jierong Liang, Cathrine D. Christiansen, Kurt Engelbrecht, Kaspar K. Nielsen, Rasmus Bjørk, Christian R.H. Bahl. Heat transfer and flow resistance analysis of a novel freeze-cast regenerator. Submitted for peer-review in: *International Journal of Heat and Mass Transfer*. Referenced as Paper II.

Cathrine D. Christiansen, Kaspar K. Nielsen, Rasmus Bjørk. Novel freeze-casting device with high precision thermoelectric temperature control for dynamic freezing conditions. Submitted for peer-review in: *Review of Scientific Instruments*. Referenced as Paper III.

Cathrine D. Christiansen, Kaspar K. Nielsen, Rasmus Bjørk. Functionally graded multi-material freeze-cast structures with continuous microchannels. In print: *Journal of the European Ceramic Society*. Referenced as Paper IV

Jierong Liang, Cathrine D. Christiansen, Kurt Engelbrecht, Kaspar K. Nielsen, Rasmus Bjørk, Christian R.H. Bahl. Characterization of freeze-cast micro-channel monoliths as active and passive regenerators. Submitted for peer-review in: *Frontiers in Energy Research*. Referenced as Paper V

Cathrine D. Christiansen, Kaspar K. Nielsen, Rasmus Bjørk. Freeze-casting to create directional micro-channels in regenerators for magnetic refrigeration. In *Proceedings of TherMag VIII, 8th IIF-IIR International Conference on Caloric Cooling*, Darmstadt, Germany, 2018;96-101; DOI: 10.18462/iir.11072. Referenced as Paper VI

All papers are included in full in Part V of the thesis, however, some are largely included and integrated in the chapters of Part I-III. Chapters 4, 6 and 7 follow Papers III, I and IV, respectively, and these papers are thus completely included in the thesis. Here, the papers are moreover put into the context of the objectives of the present thesis and are discussed in relation to considerations of experimental procedures (and in some cases limitations) and follow-up experiments. Paper VI represents preliminary results on freeze-casting of magnetocaloric materials in a very simple freezing set-up, and some of the significant results are included throughout the thesis. Papers II and V represents results obtained in collaboration with another research project and as such, parts of the experimental work were carried out by others. The contributions of this work to Paper II and V are discussed and elaborated in Chapter 8 and the experimental conclusions of the papers are summarized and discussed accordingly.

Conference contributions

Cathrine D. Christiansen*, Kaspar K. Nielsen, Rajendra K. Bordia, Rasmus Bjørk. **Freeze-casting to create micro-channels in $\text{La}_{0.66}\text{Ca}_{0.26}\text{Sr}_{0.07}\text{Mn}_{1.05}\text{O}_3$** . Poster presentation at *International conference of Sintering 2017*, San Diego, CA, USA, 12-16 November 2017.

Cathrine D. Christiansen*, Kaspar K. Nielsen, Rasmus Bjørk. **Freeze-casting to create directional micro-channels in regenerators for magnetic refrigeration**. Oral presentation at *TherMag VIII, 8th IIF-IIR International Conference on Caloric Cooling*, Darmstadt, Germany, 16-20 September 2018.

Cathrine D. Christiansen*, Kaspar K. Nielsen, Rasmus Bjørk. **Freeze-casting as a processing route to fabricate active magnetic regenerators**. Oral presentation at *XVI ECerS Conference*, Turin, Italy, 16-20 June 2019.

Cathrine D. Christiansen*, Kaspar K. Nielsen, Rasmus Bjørk. **Freeze-casting of graded monolithic $\text{La}_{0.66}\text{Ca}_{0.33-x}\text{Sr}_x\text{Mn}_{1.05}\text{O}_3$ structures with micro-channels and varying Curie temperatures**. Oral presentation at *Delft Days on Magnetocalorics 2019*, Delft, Netherlands, 18-19 November 2019.

*Presenter

Contents

I	Introduction	1
1	Freeze-casting – shaping with ice	3
1.1	Terminology: freeze-casting & ice-templating	3
1.2	Basic principles	4
1.2.1	Morphologies & features	5
1.3	Freezing dynamics	8
1.3.1	Controlling kinetics	11
1.4	Thesis contributions to freeze-casting	12
2	Concepts of magnetic refrigeration	15
2.1	The magnetocaloric effect	15
2.1.1	Domains & magnetization	17
2.1.2	Magnetocaloric materials	18
2.2	The active magnetic regenerative cycle	20
2.2.1	Regenerator geometries	21
2.3	Freeze-casting of regenerator geometries	24
3	Materials & methods	25
3.1	$\text{La}_{0.66}\text{Ca}_{0.33-x}\text{Sr}_x\text{Mn}_{1.05}\text{O}_3$	25
3.1.1	Evaluation of properties	26
3.2	General freeze-casting procedure	27
3.2.1	Suspension preparation	27
3.2.2	Freeze-casting set-ups & procedures	28
3.2.3	Drying and densification	31
3.3	Quantification of freeze-cast geometries	34
3.3.1	Post-processing of freeze-casts	35
3.3.2	Image analysis of SEM micrographs	35
3.3.3	Hierarchical porosity	38
3.4	Summary	40
II	Novel Freeze-casting Device	43
4	The freeze-caster	45
4.1	Designing a freeze-casting device	45
4.2	Freeze-Casting Device	49
4.2.1	Vacuum sealing & thermal management	49

4.2.2	Moulds & temperature tracking	51
4.2.3	Implementation of temperature control	52
4.3	Freezing conditions	53
4.3.1	Implementation of temperature profiles	53
4.3.2	Directional freezing of water samples	53
4.4	Evaluation of freezing conditions and performance	54
4.4.1	Linear and exponential freezing profiles	56
4.4.2	Implementation of feedback mechanism	57
4.5	Summary	59
5	Dynamic freezing conditions	61
5.1	Modeling approaches for structural homogeneity	61
5.2	Linear and exponential freezing profiles	62
5.3	Dynamic freeze-casting of ceramics	64
5.3.1	General freezing procedure	64
5.3.2	Freezing conditions and capacity	65
5.3.3	Structural features and homogeneity	66
5.4	Considerations regarding reproducibility	69
5.5	Summary	73
III	Freeze-casting Regenerator Geometries	75
6	Gelation freeze-casting	77
6.1	Gelcasting and gelation freeze-casting	77
6.1.1	Properties of gelatin	78
6.1.2	Gelation of LCSM suspensions	80
6.2	Static & dynamic freezing conditions	83
6.3	Structural properties of macropores	84
6.3.1	Tortuosity of microchannels	86
6.3.2	Morphology of gelated structures	87
6.4	Low freezing rates & structural homogeneity	90
6.5	Summary	93
7	Functionally graded freeze-casts	95
7.1	Layered magnetocaloric regenerators	95
7.2	Freeze-casting of graded multi-material structures	96
7.2.1	Material properties and suspension preparation	97
7.2.2	Freeze-casting	101
7.3	Graded, multi-material freeze-casts	103
7.3.1	Structural continuity across interfaces	106

7.3.2	Structural geometry and additives	109
7.4	Summary	111
8	Freeze-cast regenerators	113
8.1	Processing of freeze-cast regenerators	113
8.1.1	Mechanical integrity during processing	115
8.1.2	Regenerator specifics	116
8.1.3	Mounting & housing	117
8.2	Performance of freeze-cast regenerators	118
8.2.1	Passive (& active) characterization	119
8.2.2	Mechanical integrity during operation	122
8.3	Summary	124
IV	Conclusions & Perspectives	125
9	Conclusion	127
9.1	Perspectives & future work	130
V	Papers	135
I	The effect of gelation on statically and dynamically freeze-cast structures	137
II	Heat transfer and flow resistance analysis of a novel freeze-cast regenerator	149
III	Novel freeze-casting device with high precision thermoelectric temperature control for dynamic freezing conditions	177
IV	Functionally graded multi-material freeze-cast structures with continuous microchannels	189
V	Characterization of freeze-cast micro-channel monoliths as active and passive regenerators	199
VI	Freeze-casting to create directional micro-channels in regenerators for magnetic refrigeration	223

Part I

Introduction

Freeze-casting – shaping with ice

The research field of freeze-casting is versatile and at the moment very dynamic with a doubling in published papers* just within the last three years alongside the evolvement of the present work. Trying to capture the versatility and diversity of the field within a single thesis is a cumbersome and almost impossible task as books could be written covering the vast amount of experimental results elucidating the complex phenomenology and broad range of applications of freeze-casting.† Freeze-casting is in this work used as a processing route for shaping of materials, specifically ceramics. This chapter thus briefly introduces the concept of freeze-casting, it covers the basic principles, structural features and applications, and summarizes some of the more significant experimental results which have laid the foundation of our current understanding of the dynamics and challenges of freeze-casting. A discussion of relevant freeze-casting studies follows throughout the thesis as results obtained in this work are continuously put into context and also summarized in the final Part IV. This chapter is concluded by briefly summarizing the contributions of the present work to the field of freeze-casting.

1.1 Terminology: freeze-casting & ice-templating

First things first, however. The term *freeze-casting* originally covers the process of near-net shaping by casting a high solid load suspension of particulates of a material in a mould and freezing it to retain the shape [2]. This processing route thus yields near-net shaped materials, of either high density or isotropic porosity (depending on post-processing), and was introduced more than half a decade ago in 1954 by Maxwell et al. [2] for fabrication of titanium carbide turbosupercharger blades. On the contrary, the term *ice-templating* covers the process where ice crystals are grown in a suspension of material particulates, using the crystals as sacrificial templates for pores retained in the final material, thus yielding high-porosity materials with anisotropic pores reflecting the anisotropic growth of ice crystals. Ice-templating, in this sense, was introduced 35 years ago by Tong et al. [3, 4] for polymers and 20 years ago for ceramics by Fukasawa et al. [5, 6]. Both found that a unique anisotropic porosity could be achieved in agar

*A search on Web of Science yields 1005 papers published from 1990–2020 fulfilling the topical search criteria: "freeze-casting" OR "ice-templating." 462 of these were published in the years 2017–2020, i.e. while this work was ongoing.

†A book on freeze-casting is actually a reality as of 2017 with Deville [1].

gels and alumina ceramics, respectively, using directionally grown ice crystals as templates.[‡]

Throughout the remainder of this thesis, all freezing procedures can be assumed implemented with the purpose of ice-templating, as it is the templated internal structure of freeze-casts which are interesting within the framework of this work as will be elaborated in Chapter 2. Here, the term *freeze-casting* thus solely refers to the procedure of directional freezing of ceramic suspensions using the ice crystals as templates, unless otherwise stated. Thereby following the terminology already established for Papers I–VI and the trend in freeze-casting literature. With the terminology in place, the basic principles of freeze-casting can be introduced.

1.2 Basic principles

Freeze-casting is based on the segregation of material in a suspension of material particulates due to the anisotropic growth of ice crystals upon directional freezing. A schematic of the stages of freeze-casting is shown in Figure 1.1. Directional freezing is achieved by bringing one side of the suspension into contact with a cooling source, later on referred to as the cold side, creating a thermal gradient across the suspension. When ice crystals grow in a suspension of particulates with an appropriate thermal gradient they will effectively push aside the particles causing them to segregate, resulting in a two-phase system of ice and material. Removing the ice by sublimation followed by densification results in a structure with anisotropic porosity in the form of directional macropores where the ice used to be. The macropores are templated by the ice crystals, and are as such the inverse imprint of the crystals in the green body. The dimensions of the macropores thus depend on the size of the ice crystals and are typically of the order $\sim 1 \mu\text{m}$ to $\sim 100 \mu\text{m}$ [9–11]. While water is the most common solvent, alternatives such as camphene [12, 13] or *tert*-butyl alcohol [14] have been used successfully, however, with different solidification temperatures and altered morphologies, as will be discussed a little later.

While Figure 1.1 specifically illustrates freeze-casting of a ceramic suspension – where ceramic particles are suspended in a solvent and the green body is densified by (partial) sintering – freeze-casting is not only applicable to ceramic materials. In principle, as long as a material can be suspended (homogenously) in a solvent, which solidifies such that the particle interaction with the solidification front results in the particles being ejected and segregated, a material can be templated by freeze-casting. Thus, even though freeze-casting of ceramics dominates the field, also materials of metals [15–18], polymers [19, 20] and composites between the three [21, 22] can be processed by freeze-casting.[§] In principle, the phenomena and applications of freeze-casting far exceeds that of materials processing [25]. However, for simplicity and to remain within the scope of this thesis, we will focus on freeze-casting of materials, specifically ceramics.

[‡]To make things even more complicated, Tong et al. [3, 4] referred to the procedure, although descriptively, as *directional freezing* while Fukasawa et al. [5, 6] referred to this procedure as *freeze-dry processing*. However, presently, the terms of *freeze-casting* and *ice-templating* dominates the literature.

[§]The principles of freeze-casting are even used within food science [23], and pharmaceutical sciences [24], however, for near-net shaping and isotropic porosities, and thus not templating of anisotropic pores.

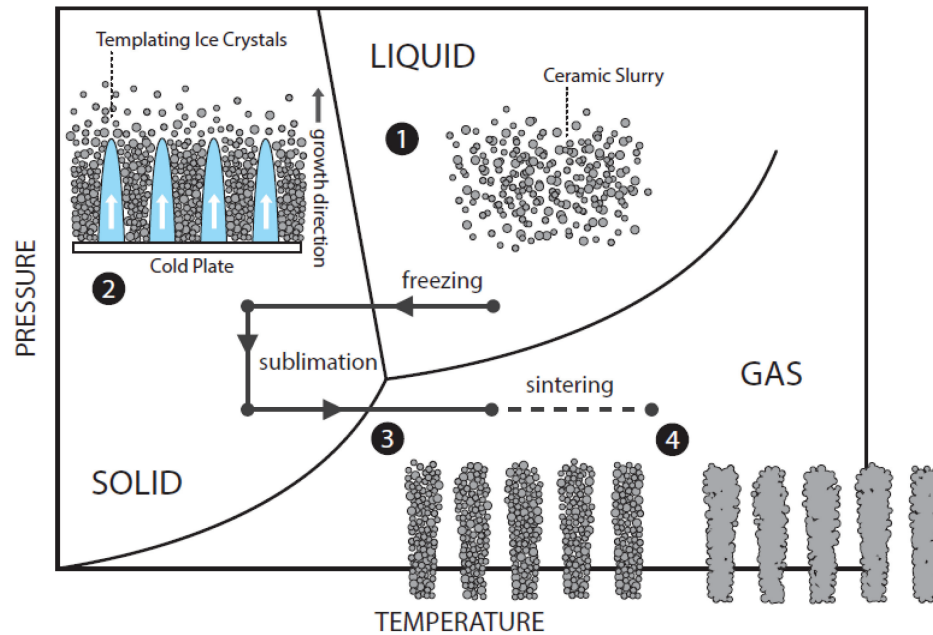


Figure 1.1: Freeze-casting, or ice-templating, is the segregation of suspended particles (a ceramic slurry in the case of ceramic freeze-casting, (1)) being ejected by the anisotropic solidification of the suspension solvent due to an applied thermal gradient (2). The solidified solvent phase is removed by sublimation (3) and the structure is densified (sintered in the case of ceramics (4)) now having retained pores where the solvent used to be. Figure originally from Deville [7] © 2008 WILEY-VCH Verlag GmbH & Co. KGaA, Weinheim and edited by Lichtner [8].

1.2.1 Morphologies & features

The structure of a typical, freeze-cast ceramic is visualized in Figure 1.2 showing cross sections imaged by scanning electron microscopy (SEM), Figure 1.2a–b), and a 3D reconstruction of freeze-cast LCSM ceramic based on tomography images obtained using an X-ray Microscope (ZEISS Xradia 520 Versa), Figure 1.2c). Visualized is a $\text{La}_{0.67}\text{Ca}_{0.27}\text{Sr}_{0.06}\text{MnO}_3$ (LCSM6) freeze-cast processed as a part of the work for the present thesis. The standard processing of freeze-cast samples throughout is described in Chapter 3, while the freezing conditions are described in Chapter 4–5. For now, however, we will merely consider Figure 1.2 as a standard freeze-cast structure frozen from an aqueous suspension of 30 vol% ceramic powder.

The most significant feature of a freeze-cast ceramic is obviously the templated pores, i.e. macropores, which are lamellar in shape, straight and running along the freezing direction, apparently throughout the structure. As such, freeze-cast structures exhibit a long range-ordering along the thermal gradient. However, when considering the perpendicular cross section, Figure 1.2a), it is seen that the pores are ordered in clusters or domains of various orientation. This phenomena is also referred to as macropore colonies [26] and is a typical feature of water-based

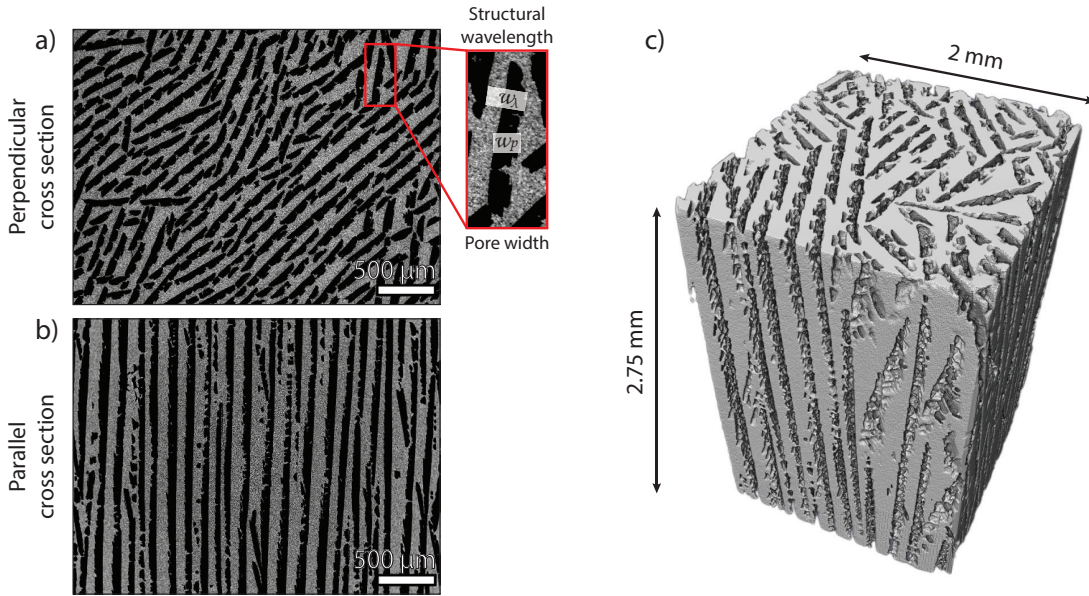


Figure 1.2: Visualization of typical freeze-cast structure. a–b) SEM micrographs of cross sections of a epoxy-infiltrated freeze-cast sample where grey areas are the ceramic walls and black areas are porosity in the form of aligned, lamellar channels. Micrographs are obtained at cross sections a) perpendicular and b) parallel to the freezing direction ~ 16 mm from the bottom of the sample. c) 3D reconstruction of freeze-cast LCSM ceramic based on interactive segmentation using Avizo software (Thermo Fischer Scientific) of tomography images obtained using an X-ray Microscope. Both SEM micrographs and tomography images were obtained from the same sample, frozen from a 30 vol% LCSM aqueous suspension. Figure revised from Paper II.

freeze-casts [8, 9, 26, 27]. The domains of various orientations of the lamellar pores reflect the orientation and domains already formed during nucleation [28] (as will be discussed later, see Figure 1.4), and thus, by affecting the nucleation, the morphology is altered. Successful 2D ordering of pores by aligning pore domains have been achieved by various mould-altering approaches; patterning of the freezing surface [29], introduction of a wedge between cooling source and suspension [30], illustrated in Figure 1.3E), or by using a mould with a cooling side as well, inducing bi-directional freezing [31].

The morphology of the macropores depend on the morphology of the crystallized solvent, and can as such be altered by changing the solvent, illustrated in Figure 1.3C–D). Water forms lamellar ice crystals and thus lamellar macropores [32], camphene yield highly dendritic macropores [12, 13] while *tert*-butyl alcohol yields hexagonal, or faceted, macropores [14]. Additionally, the solvent chemistry can be altered by additives, affecting the morphology of crystals and/or the interaction between the freezing front and the particles in the suspension, e.g. by changing the viscosity or pH of the suspension [29, 33]

Ceramic bridges connecting the walls have been found to form at high solid loads and/or

slow freezing [9, 34], as well as at increased viscosity of the suspension [33], as illustrated in Figure 1.3, where many ceramic bridges are seen vertically connecting the horizontally aligned lamellae walls. Lamellar bridging is interesting as it increases the mechanical strength of ceramic freeze-casts [26, 34, 35].

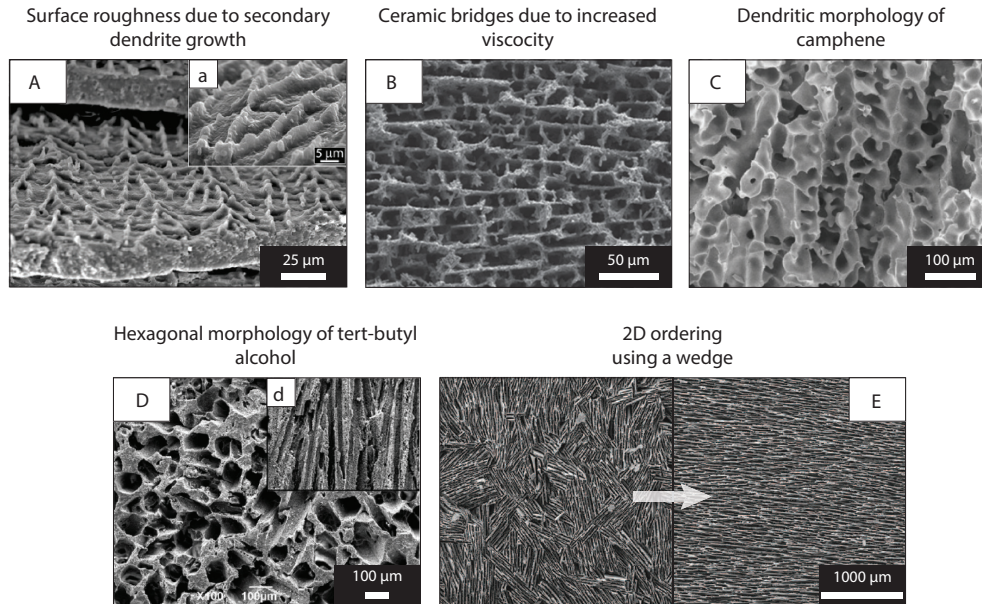


Figure 1.3: Morphology of freeze-cast ceramics. A) Surface roughness of alumina freeze-cast, typically only observed on one side of lamellae walls, due to secondary dendritic growth of ice crystals using water as solvent [9] © 2006 Acta Materialia Inc. Published by Elsevier Ltd. All rights reserved. B) Increased ceramic bridging in a TiO_2 freeze-cast connecting lamellae walls due to increased viscosity (addition of polyethylene glycol ($M_W \sim 2000$) for viscosity of 1.50 mPa s) of the suspension during freezing [33] © 2013 WILEY-VCH Verlag GmbH & Co. KGaA, Weinheim. Freezing direction is perpendicular to the plane. C) Dendritic morphology of freeze-cast hydroxyapatite macropores due to directional solidification of camphene at 20 °C [12] © 2007 The American Ceramic Society. Freezing direction is from bottom to top. D) Hexagonal morphology of freeze-cast alumina using 100% *tert*-butyl alcohol as solvent [14] © 2015 Elsevier Ltd. All rights reserved. Freezing direction is perpendicular to the plane, and bottom to top for (d). E) From left to right: elimination of domains and thus 2D ordering of lamellar macropores of hydroxyapatite freeze-cast due to the implementation of an insulating wedge between the cooling source and suspension inducing a second thermal gradient aligning the pores [30] © 2015, The Authors. Freezing direction is perpendicular to the plane.

The structure and morphology of freeze-casts are typically quantified by image analysis of optical or SEM micrographs of cross sections, similar to those in Figure 1.2a–b). In the perpendicular cross section, the pore size, typically width, w_p , and the structural wavelength, w_λ , are generally measured, both of which are indicated in the close-up of Figure 1.2a). The periodicity of the lamellar geometry is quantified by the structural wavelength which is determined as the

sum of the width of a pore and the width of the adjacent wall [9] and is convenient for comparing lamellar morphologies. Accordingly, the wall thickness is also measured. In some studies ellipses are fitted – typically, manually using image software – to pores, yielding the elliptic major and minor axis, i.e. pore length and width, and the corresponding pore/ellipsis area and circumference [36–38]. The ratio of pore area is often measured by appropriate segmentation of cross sectional images. Quantification and evaluation of structural features of freeze-casts in regards to this work is largely based on semi-automated image analysis of SEM micrographs and is presented in Chapter 3.

High permeability [39–41], low tortuosity [7, 13, 42–45], increased mechanical strength along the channel orientation [29, 44, 46–50] (when compared to similar materials but of isotropic porosity) are typical properties of freeze-cast ceramics. Additionally, the porosity is hierarchical [5, 6, 11, 51], with both porosity in the form of the templated pores but also remaining inter-particle porosity in the walls. For simplicity, we will refer to these as macro- and microporosity throughout the thesis. The ratio between microporosity and macroporosity can be altered by choosing a sintering temperature and time that more or less eliminates the first [5, 6, 8]. However, depending on the type of material as will be discussed further in Chapter 3.

The alignment of porosity ensures porous materials of e.g. enhanced mechanical strength and flow properties in the direction of the macropores, making these materials advantageous for e.g. biomedical applications [37, 46, 47, 51] – especially bone tissue scaffolds or dental implants [52] – or applications of mass flow transfer such as filters [44] and catalytic support structures for e.g. membranes or fuel cells [11, 41, 42].

1.3 Freezing dynamics

As mentioned, successful ice-templating is the directional solidification of the solvent of a particle suspension such that the particle interaction with the solidification front results in the particles being ejected and segregated. The latter requires a columnar or lamellar ice front, such that particles can be packed into the inter-lamellar or –columnar space, as illustrated on Figure 1.2(2). However, directional freezing may have one of two other outcomes, namely; evolution of a *planar* ice front parallel to the cooling source/suspension interface, growing along the thermal gradient and pushing the particles ahead *in front of it*; or the ice front growing into the inter-particle space, *engulfing* the particles in the solid phase, forming an isotropic frozen body of ice and particles. The outcome of directional freezing depends on the velocity of the advancing freezing front [53], and the concentration of particles in the liquid phase [53, 54], i.e. the solid load of the suspension. A critical ice front velocity, v_c , exists, above which material particles will be engulfed by the growing ice crystals instead of ejected by them, typically given as [9, 19, 51, 54]:

$$v_c = \frac{\Delta\sigma d}{3\eta R} \left(\frac{a_0}{d}\right)^z \quad (1.1)$$

where a spherical particle of diameter, R , interacts electrostatically with a liquid–solid interface separated by a liquid film of thickness d , in which solvent molecules are distanced a_0 apart. The viscosity, η , governs the fluid flow of solvent molecules from the liquid phase to the tip of the growing crystal (or the liquid film) and the drag force exerted on the particles when pushed ahead by the ice front. $\Delta\sigma$ is the free energy associated with the trapping of a particle in the solid phase:

$$\Delta\sigma = \sigma_{\text{ps}} - (\sigma_{\text{pl}} + \sigma_{\text{sl}}) \quad (1.2)$$

where σ_{ps} , σ_{pl} and σ_{sl} are the surface energies of the particle and solid phase, particle and liquid phase and solid phase and liquid phase, respectively. For entrapment of a particle to be thermodynamically favorable, the associated change in surface energy must be negative, i.e. $\Delta\sigma < 0$. The coefficient z in Equation (1.1) is a correction term that originates from the expression of the electrostatic force between a spherical particle and solid-liquid interface (not shown here; see reference [19] or [51]).

Although Equation (1.1) outlines some of the important parameters governing the entrapment or ejection of particles from a growing ice front, it describes a simplified, highly diluted system. It does thus not account for particle–particle interactions and forces such as gravity and buoyancy acting on the particle; although, the latter two are often neglected altogether when generally considering freeze-casting of ceramic particles as these are typically very small [15]. Additionally, the parameters in the equation itself are not trivial, e.g. how does one determine the film thickness d and account for odd shapes of particles with surface roughness? The point being, that for a new system of material, solvent and additives, the dynamics of freezing and corresponding structural features should initially, at least to some degree, be mapped.

Finally, Waschkie et al. [53] showed experimentally that the transition velocity between a planar ice front and lamellar ice front drops with increased particle concentration, while the critical velocity for particle entrapment drops with increased particle size due to increased drag force on the particles. Although the critical velocity too depends on the solid load [34], making things a little more complicated, these two parameters are easily adjustable for a new material system to ensure sufficient solidification velocities during ice-templating. As we shall see throughout Parts II and III of this thesis, too slow or too fast solidification velocities were never a non-manageable issue in this work.

Having outlined the conditions for successful ejection and segregation of particles, Figure 1.4 illustrates the morphology of the ice crystals and segregated particle phase, revealing the evolution of the lamellar ice front in a suspension, as the progress it is literally frozen in time when evaluating the morphology from bottom to top. Deville et al. [28] investigated the morphology of a directionally frozen aqueous alumina suspension using *in situ* X-ray tomography identifying three morphological phases of the solidification process. When a suspension of particles is brought into contact with a cooling source, a thermal gradient arises perpendicular to the interface between the cooling source and the suspension. Eventually, when the temperature of the suspension at the cooling source is at the solidification temperature of the suspension –

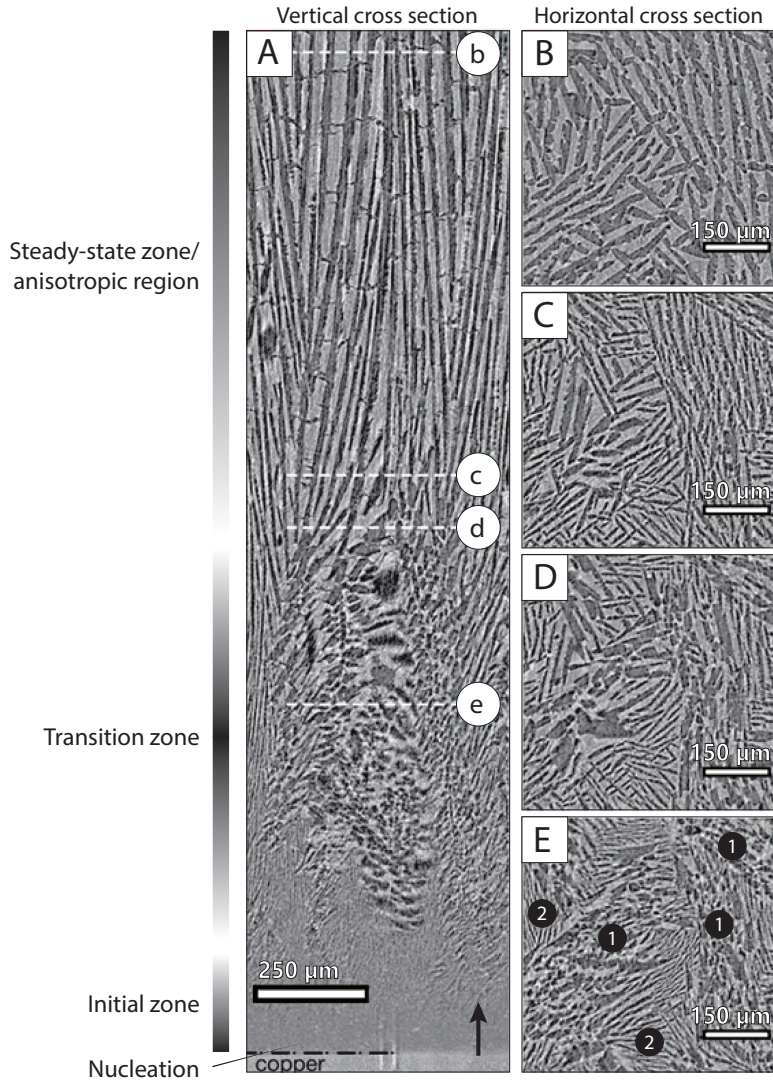


Figure 1.4: Tomography reconstructed cross sections of a directionally frozen aqueous alumina suspension with the vertical cross section being parallel to the freezing direction, while the dashed white lines indicates the position of the horizontal slices. The morphology can be categorized in three zones; initial, transition and steady-state depending on the orientation of lamellar ice crystals, with (1) indicating random oriented crystals and (2) indicating crystals that are aligned with the temperature gradient. As the solidification front evolves, crystals aligned along the thermal gradient are favored and are thus the only ones remaining in the steady-state zone. Figure edited from Deville et al. [28] © 2009 The American Ceramic Society.

or often below due to supercooling – ice crystals will, primarily, nucleate at the interface. Ice crystals has a hexagonal structure and are as such in themselves anisotropic and crystalizes to a lamellar morphology [32]. Initially the overall orientation of the crystals are random, with a short range ordering of orientation, which will later result in the domains discussed earlier. Figure 1.4E) illustrates how some crystals are oriented along the thermal gradient, region 2, while some are not, region 1. Moving away from the bottom (up through horizontal cross sections E, D and C), the growth of the already aligned crystals are favored, while the non-aligned crystals are either eliminated or evolved into aligned crystals in the steady-state zone. The suspension in Figure 1.4 was frozen with a linear temperature profile, meaning that the temperature of the cooling source was decreased at -5 K/min. Implementation of parabolic temperature profiles was later found to decrease the extent of the transition zone [55].

The presence of an initial zone, transition zone and steady-state zone was evident for all freeze-casts prepared throughout this work. For applications and evaluation of structural homogeneity of freeze-casts evaluated in this thesis, the bottom part of the samples were thus always discarded.

In the steady-state zone, the structural wavelength is inversely proportional to the velocity of the solidification, or freezing, front [9, 53]:

$$w_\lambda \propto v_f^{-n} \quad (1.3)$$

with n typically being in the order of ~ 1 [8, 9, 33, 53]. Thus, the faster the freezing front moves, the finer the final microstructure will be, with approximately constant freezing front velocities yielding nearly homogeneous macropore sizes throughout the freeze-cast structures [10, 53]. Constant freezing front velocities are achieved by dynamic freezing conditions, i.e. a dynamically decreasing temperature of the cooling source. For a constant temperature of the cooling source, however, the growing solid part of the suspension will act as an increasing thermal resistance, slowing down the freezing front velocity. Constant temperature of the cooling source therefore leads to graded structures of varying pore sizes [45, 56].

1.3.1 Controlling kinetics

Being the most crucial step affecting the final dimension, homogeneity and morphology of pores, not much is required to freeze a suspension. With a cooling source of a temperature below the solidification temperature of the suspension (solvent), a thermal gradient can be applied across by bring one side of the suspension into contact with the cooling source, and directional freezing will occur. However, as just demonstrated, successful freeze-casting with segregation of particles constitutes a little more than "just freezing." Controlling the thermal gradient across the suspension amounts to controlling the kinetics, i.e. the freezing front velocity, and freezing direction in the suspension and thus the resulting structural features and dimensions. The thermal gradient depends on the temperature of the cooling source, and high precision temperature control of the cooling source coupled with either visual monitoring or high spatial

resolution temperature monitoring of the freezing sample is therefore crucial in the engineering of materials by freeze-casting. Different approaches to freeze-casting set-ups are presented and discussed in Chapter 4, along with the design and evaluation of a novel set-up design, which was build as a part of the present work.

For most freeze-casting set-ups, some degree of temperature control is thus an essential but also easily integrated component. Thus, many approaches have been made to model the solidification behaviour of a freezing suspension in order to control the freezing kinetics directly by the temperature of the cooling source. Various dynamic temperature profiles of the cooling source during freeze-casting have been tested, where both linear [9–11, 45], exponential [57–59] and parabolic [55] freezing functions were found to significantly increase the homogeneity of structural features and dimensions of macropores throughout the freeze-casts. Implementation of such freezing functions will be discussed further in Chapter 4 and 5.

1.4 Thesis contributions to freeze-casting

With the desired application of freeze-cast structures of magnetocaloric materials for regenerators in magnetic refrigeration, and thus not so much on the fundamental phenomena and concepts governing the process of ice-templating, the contributions of this thesis to the field of freeze-casting are summarized here:

Mapping/screening of structural features and freezing conditions when ice-templating magnetocaloric (specifically LCSM) materials – the reason for which will be outlined and elaborated further in Chapter 2.

A semi-automated image analysis of SEM micrographs to evaluate structural features such as pore and wall thickness, pore area ratio/macroporosity, specific surface area and tortuosity is presented in Chapter 3.

Simple freeze-caster design, presented and evaluated in Chapter 4, using a thermoelectric unit for implementation of dynamic freezing conditions. The varying intrinsic thermodynamical properties of water in liquid and solid form is used to identify the freezing conditions by spatially obtained temperature profiles. The analysis is kept simple and straightforward, and can easily be implemented across set-ups and materials.

The investigation of the correlation between dynamic freezing conditions and homogeneity of pores is continued throughout Chapters 5–8. In addition, given the desired application, all freeze-cast structures in this thesis are characterized with respect to sample height, i.e. structural parameters are evaluated throughout the sample.

Gelation in combination with freeze-casting and its effect on the morphology is investigated in Chapter 6. Gelation offers an additional near-net-shaping step which is then used in Chapter 7, along with other solvent altering steps, to investigate the fabrication of graded, multi-material freeze-cast structures.

Application of magnetocaloric freeze-cast structures as both passive and active regenerators. The performance of magnetocaloric freeze-cast regenerators are evaluated in Chapter 8.

Concepts of magnetic refrigeration

In this chapter, the concepts of magnetic refrigeration and the magnetocaloric effect are introduced. Magnetic refrigeration offers an alternative to conventional gas-compression refrigeration [60], however, as is elaborated in this chapter, the efficiency of magnetic refrigeration strongly depend on the geometry of the porous magnetocaloric material invoked as both regenerator and refrigerant. Benchmark regenerator geometries are presented as freeze-casting is introduced as a possible shaping route of microchannel regenerator geometries.

2.1 The magnetocaloric effect

The magnetocaloric effect is an intrinsic property of all magnetic materials, that when subjected to a changing external magnetic field, experiences a change in temperature. The phenomenon was first predicted more than a century and a half ago [61] by William Thomson (now recognized as Lord Kelvin) in 1860 [62], but not observed experimentally until more than 50 years later [63] by Weiss and Piccard [64], who measured a temperature change of a little less than 1 K in magnetized Ni (1.5 T).

Under adiabatic conditions – i.e. conditions where no heat is exchanged with the surroundings – the magnetocaloric effect thus manifests itself as a temperature change, as illustrated in Figure 2.1. Meanwhile, it manifests itself as an increase in total entropy of the material under isothermal conditions – i.e. conditions where the temperature remains constant.

When an external magnetic field, H , is applied to a magnetic material, the spin of unpaired electrons in the material tend to align themselves with the magnetic field, resulting in magnetic ordering, i.e. lowering of the magnetic entropy, of the material, as illustrated in Figure 2.2. The total entropy, S_{total} , of a magnetic material is given as the sum of its magnetic entropy of magnetization, lattice entropy related to vibrations of the crystal lattice and electronic entropy, S_m , S_l and S_e , respectively. While all of them depend on the temperature of the material, only the magnetic entropy depends on the applied field [63]:

$$S_{\text{total}}(H, T) = S_m(H, T) + S_l(T) + S_e(T) \quad (2.1)$$

For an adiabatic process, the total entropy is conserved, and hence, the lattice entropy and/or the electronic entropy is consequently increased when the magnetic entropy decreases due to

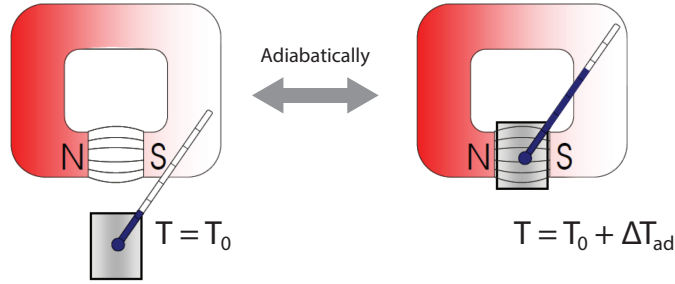


Figure 2.1: Adiabatic temperature change in a magnetic materials due to the application of an external magnetic field. This phenomena is referred to as the magnetocaloric effect. The effect is completely reversible. Figure edited from Petersen et al. [65].

ordering of the spins. Increasing the lattice entropy increases the vibration of the lattice and thus the thermal energy of the material. Increased thermal energy is equivalent to an increase in temperature of the material, referred to as ΔT_{ad} in Figure 2.1. The process can be completely reversed by removing the applied magnetic field, where an increase in magnetic entropy is compensated by a decrease in vibrational energy of the lattice and thus lowering of temperature.

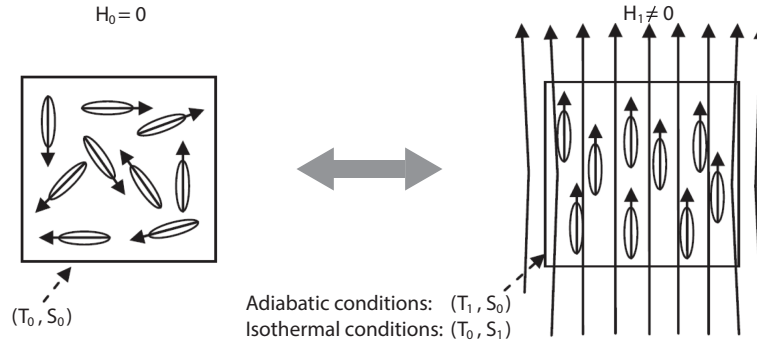


Figure 2.2: Schematic of the magnetocaloric effect, which is due to the alignment of unpaired spins in a magnetic material due an applied external magnetic field. Figure edited from Romero Gómez et al. [63]. © 2012 Elsevier Ltd. All rights reserved..

The adiabatic temperature change associated with the magnetocaloric effect is related to temperature as follows [65]:

$$\Delta T_{\text{ad}} = -\mu_0 \int_{H_0}^{H_1} \frac{T}{C_H} \left(\frac{\partial M}{\partial T} \right)_H dH \quad (2.2)$$

where μ_0 is the permeability of free space, while C_H is the total heat capacity and M the specific magnetization of the material, respectively. Although, it should be noted, that the integral in Equation (2.2) is far from trivial as T is a function of H , while C_H is a function of both T and H . It thus have to be evaluated as a line integral as described in detail by Smith et al. [60].

For isothermal conditions, however, the temperature is constant, and the magnetocaloric effect materializes as a decrease in total entropy by a decrease in the magnetic entropy resulting in heat being exchanged between the material and the surroundings. The isothermal entropy change associated with the magnetocaloric effect is related to the rate of change of the magnetization with temperature as follows [65]:

$$\Delta S_m = -\mu_0 \int_{H_0}^{H_1} \left(\frac{\partial M}{\partial T} \right)_H dH \quad (2.3)$$

2.1.1 Domains & magnetization

For ferromagnetic materials, unpaired spins interact and align in smaller sections of the material resulting in domains of magnetic moments of random orientations, as illustrated in Figure 2.3a). However, while the spins within a domain are parallel, spins of neighbouring domains are not

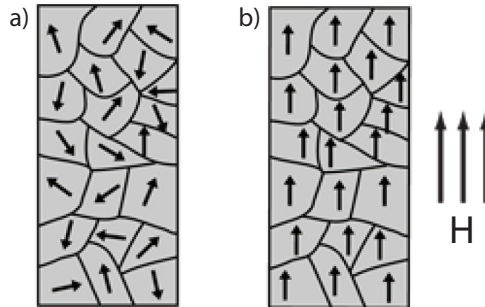


Figure 2.3: Magnetic domains in ferromagnetic materials. a) Unpaired spins interact and align in ferromagnetic materials in domains of specific magnetic moments, overall in random orientations more or less cancelling out the total magnetization of the material. b) Application of an external magnetic field align all domains and a maximum saturation magnetization is reached. Figure edited from Nave [66].

and the overall net magnetization of the material might be very small or completely cancelled out. If an external magnetic field is applied, the spins of the domains will tend to align, as illustrated in Figure 2.3b) and an increased magnetization of the material is observed until a complete alignment of magnetic moments occur resulting in the highest possible magnetization, also referred to as the magnetic saturation.

The magnetization also varies with temperature as given in Equations (2.2) and (2.3), with the magnetic saturation being greatest at 0 K [63]. Increasing the temperature of the material is equivalent to increasing the thermal, or vibrational, energy. The vibrational energy eventually overcomes the electronic exchange forces aligning spins and thus randomizing the directions of spins in the material, i.e. the material transitions from a ferromagnetic to a paramagnetic state. For ideal ferromagnetic materials, the temperature at which the magnetization has completely vanished at zero applied field is called the Curie temperature, T_C , and the change

in magnetization with temperature, i.e the term $\left|\frac{dM}{dT}\right|$, is largest exactly at T_C . Due to the domains in ferromagnetic materials, the magnetization has typically not completely disappeared at T_C , as illustrated in Figure 2.4a), with the magnetization curve flattening out slowly at T_C . By extension, both the adiabatic temperature change and the isothermal entropy change will be greatest around T_C , Figure 2.4b–c), i.e. the magnetocaloric effect is greatest at T_C .

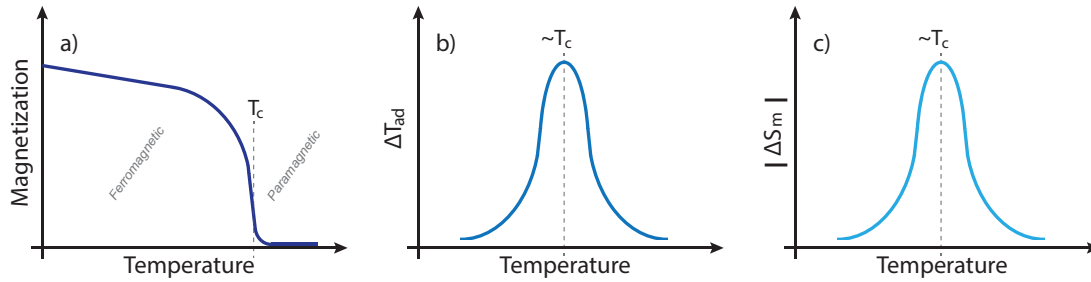


Figure 2.4: The Curie temperature is defined as the transition temperature between the ferromagnetic and the paramagnetic phase of a magnetic material, and is a) the temperature at which the magnetization of the material completely vanishes. b) The adiabatic temperature change, ΔT_{ad} , and c) the isothermal entropy change, ΔS_m , related to the magnetocaloric effect is greatest around the Curie temperature. The peak height of both ΔT_{ad} and $|\Delta S_m|$ depend on the field strength of the applied magnetic field. Figure adapted from Petersen et al. [65].

2.1.2 Magnetocaloric materials

The magnetocaloric effect materializes in all magnetic materials subjected to a changing magnetic field. Magnetocaloric materials can thus be used for cooling or heating purposes. However, as the magnetocaloric effect is greatest in the vicinity of the Curie temperature, the choice of magnetocaloric materials for application purposes depends on operating temperatures. However, as the present thesis does not investigate the performance related to individual magnetocaloric materials, only a brief introduction of materials follow here, with the perspective that future application of freeze-casting of magnetocaloric structures should consider a broader range of materials.*

For household refrigeration appliances, the operational temperature range is approximately $5 - 25\text{ }^\circ\text{C}^\dagger$, and the magnetocaloric material should thus be chosen with a corresponding T_C . This greatly limits the choice of material.

Magnetocaloric materials are divided into second order and first order materials, depending on the order of the phase transition between the ferromagnetic and paramagnetic state [60]. The transition depicted in Figure 2.4a) is thus a second order phase transition material, as

*For an extensive overview of materials for magnetic refrigeration, the reader is referred to Smith et al. [60], Kitanovski et al. [67] or Lyubina [68].

[†]E.g. temperature span a refrigerator at N 55° 47' 8.927", E 12° 31' 9.62" will have to sustain during a fairly decent summers day.

the magnetization continuously decreases to zero as the temperature increases. A discontinuity would here be seen for first order materials; the magnetization would be decreasing continuously and then suddenly disappear [69]. Without dwelling too much on the physical definition and distinctions of the two, as the phenomena behind far exceeds the scope of this work, it should be mentioned that there are advantages and drawbacks of both. Due to the discontinuity in magnetization at the phase transition, first order materials typically exhibit a large magnetocaloric effect, but within an even more narrow temperature range than the second order materials [68, 69]. E.g. Bjørk et al. [70] found that the full width half max (FWHM) temperature range of the ΔT_{ad} peak of the second order material Gd was ~ 40 K while it was only ~ 15 K[‡] for the investigated first order materials belonging to the $\text{LaFe}_{13-x-y}\text{Co}_x\text{Si}_y$ -series. Besides the more narrow temperature range of the magnetocaloric effect, hysteresis often result in thermal losses and thus decreases the performance of first order materials in magnetic refrigeration [60, 71, 72].

Gd was in 1935 found to have a second order phase transition from a ferro- to a paramagnetic state at T_C near-room temperature by Urbain et al. [73] and was as such the first ferromagnetic material with a near-room temperature transition to be discovered [60, 67]. With a T_C of 295 K, an adiabatic temperature change of 3.3 K and an isothermal entropy change of 3.1 J/(kg K) in a field change of 1 T [70], this is the only element which in itself is magnetocaloric with a near-room temperature T_C , and with extensive application and characterization throughout the literature of magnetic refrigeration it can be considered a benchmark material. However, it is rather expensive [60] and thus commercially unattractive.

Of promising magnetocaloric materials with near-room temperature T_C can be mentioned: $\text{La}(\text{Fe},\text{Si},\text{Mn})_{13}\text{H}_z$ [74–77], $\text{MnFeP}_{1-x}\text{As}_x$ [71, 78], $\text{La}(\text{FeCoSi})_{13}$ [70, 79, 80], $\text{La}_{0.67}\text{Ca}_{0.33-x}\text{Sr}_x\text{MnO}_3$ (LCSM) [81, 82]. All of them, except the latter, showing first order phase transitions and thus a significant magnetocaloric effect. Meanwhile, the latter is the only ceramic; being composed of solely non-metallic elements [83]. Thus, general procedures of ceramic processing can be used in the shaping of LCSM as we shall see in the coming chapters.

However, the adiabatic temperature change for even some of the best performing magnetocaloric materials with T_C around room temperature is still only in the order of a few K in magnetic fields achievable by permanent magnets ($< 2\text{T}$)[§] [60]. These temperature changes are far from sufficient for practical refrigeration applications and thus a regenerative cycle is introduced in magnetic refrigeration, referred to as the active magnetic regenerative (AMR) cycle.

[‡]Note that both temperature ranges are roughly estimated from plots of ΔT_{ad} from Figure 6 in Bjørk et al. [70].

[§]Considering commercialization and power consumption of magnetic refrigeration devices, permanent magnets are preferred over superconducting magnets [84, 85].

2.2 The active magnetic regenerative cycle

Magnetic refrigeration is similar to traditional gas-compression refrigeration as known from conventional household refrigerators. However, instead of using a gas, magnetic refrigeration utilizes a magnetocaloric material in combination with a heat transfer fluid; referred to as the solid and liquid refrigerant, respectively. The heat transfer fluid is typically water with anti-corrosion agents if necessary [69]. Additionally, the magnetocaloric material acts as a thermal regenerator, i.e. a heat exchanger for intermittent storage of heat, for simply moving heat from a cold side – e.g. a refrigerator – to the hot side – e.g. surroundings – during reciprocated cycles, thus facilitating a build up of a temperature span greater than ΔT_{ad} of the magnetocaloric effect. The AMR cycle was originally presented by Barclay [86] in 1983.

The AMR cycle is illustrated in Figure 2.5 and proceeds in four steps. 1) The porous regenerator of magnetocaloric material is adiabatically magnetized, increasing the temperature of the regenerator and thus of the fluid inside the regenerator matrix. 2) Fluid is pushed from the cold reservoir to the hot, transferring heat, Q_H , from the regenerator to the hot reservoir. The regenerator thus regains its initial temperature gradient. 3) Consequently, demagnetization of the regenerator decreases its temperature further, and 4) fluid is pushed from the hot to the cold reservoir, from which the regenerator absorbs heat, Q_C , and again regains its initial temperature gradient. The cycle is repeated for continuous removal of a cooling load.

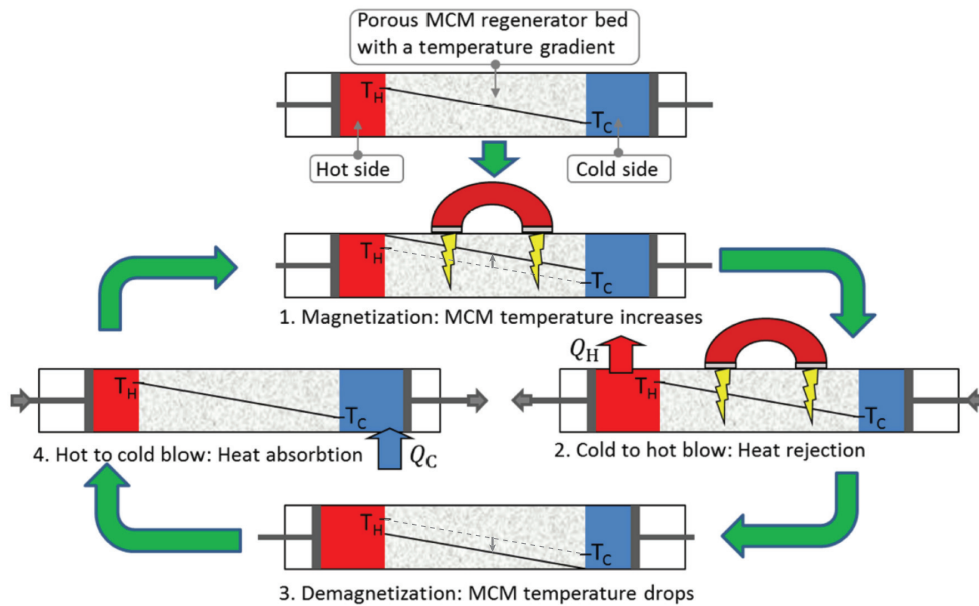


Figure 2.5: The active magnetic regenerative cycle. Figure from Eriksen et al. [87].

Utilizing the AMR cycle in a magnetic refrigerator prototype, achieved a regeneration of about a factor of 6.5 in Gd; i.e. reaching a temperature span of 29 K under no cooling load in an applied field of 1.47 T [88](under the same conditions, ΔT_{ad} of Gd is about 4 K).

Acting as both refrigerant and regenerator, the efficiency of a magnetic refrigeration device strongly depend on both intrinsic and geometrical properties of the magnetocaloric material. For application as regenerator in an AMR cycle, a few additional property requirements – besides the near-room temperature T_C – can be added for the magnetocaloric material itself:

- i) it must have a low specific heat and a high transverse thermal conductivity;
- ii) it must be porous with a large surface area available for heat transfer;
- iii) exhibit good mechanical properties and high mechanical integrity while maintaining a porous shape;
- iv) be resistant to corrosion and thus not react with the liquid refrigerant or oxidize in air;
- v) and last, regarding manufacturing, the overall manufacturing costs should be low, both regarding rarity and price of elements of the material, but also regarding processing and shaping routes.

Regarding item ii), shaping of the magnetocaloric material is an essential step in optimizing the performance of the AMR cycle and thus of a magnetic refrigeration device. This is thus exactly where the present thesis strives to contribute to the field of magnetic refrigeration by presenting an alternative regenerator geometry by a low-cost, environmentally friendly processing route. For context, a brief overview of current state of the art regenerator geometries are given in the following section.

2.2.1 Regenerator geometries

A regenerator geometry is porous with optimum porosities of 0.35–0.65 depending on the geometry [89]. Figure 2.6 depicts the parallel plate and packed bed regenerators. These consist of stacked magnetocaloric plates with a slight spacing in between and magnetocaloric particles, respectively. The particles are either irregular or spherical, packed together in a housing and typically bonded by a few wt% epoxy.

Regenerator geometries are typically evaluated by their heat transfer effectiveness; pressure drop; and cost of production. The latter will not be considered further here, however, the first two significantly affects the performance of a magnetocaloric refrigeration device. When evaluating the performance of such a device, they are typically quantified by the temperature span between the hot and cold side, their cooling power, \dot{Q} , and their coefficient of performance, COP, i.e. the ratio between the cooling power, and the operational power consumed by the device, \dot{W} [60]:

$$\text{COP} = \frac{\dot{Q}}{\dot{W}} \quad (2.4)$$

The cooling power is defined as the amount of heat transferred from the cold side to the hot side – or vice versa for e.g. a heat pump – per unit of time. The cooling power is directly related to the regenerators heat transfer effectiveness. The effectiveness of a regenerator is defined as

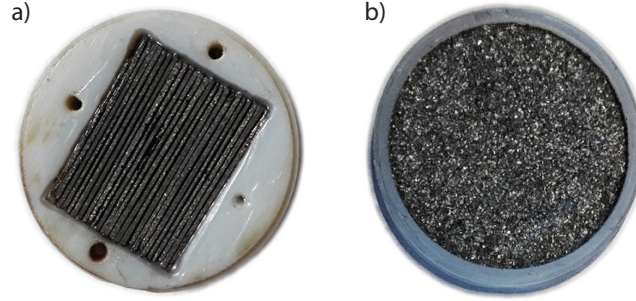


Figure 2.6: Regenerator geometries. Pictured is a) a parallel plate regenerator and b) an irregular particle packed bed regenerator. The flow direction is perpendicular to the page and the circular housing of each regenerator is ~ 30 mm. Note that both regenerators are actual tested samples and are thus worn. The circular holes in the parallel plate regenerator are for mounting and are thus not flow channels.

the ratio between the amount of heat transferred and the heat available [90]. The first refers to the energy actually transferred between the liquid and solid during step 2) or 4) of the AMR cycle. The latter term refers to heat available for transfer due to the temperature difference between the liquid and the solid, i.e. the difference between the thermal gradient represented by the solid and dashed line in step 1) and 3) of the AMR cycle illustrated in Figure 2.5.

Meanwhile, the operational power consumed by the device depends, among others, on the power required to pump fluid through the regenerator. The flow resistance – equivalent of the pressure drop across the regenerator – depends on the geometry. I.e. low tortuosity geometries, like the parallel plates, exhibit a low flow resistance, while high tortuosity geometries, like the packed bed, exhibit a very high flow resistance. Besides increasing the pump power and thus lowering the COP, highly tortuous geometries with large pressure drops moreover experiences unwanted heating in the system due to viscous dissipation in the regenerator [91].

Evaluated by effectiveness and pressure drop, the three benchmark geometries of parallel plates, packed screen beds and packed (spherical) particle beds are all illustrated in Figure 2.7.

Here, the parallel plate geometry is quantified by the width of plates, W_p , plate thickness, H_{p1} , and channel thickness, H_{p2} . Accordingly, the packed screen bed geometry is quantified by the thickness of the wires, D_{sc} , distance between neighbouring wires along the flow direction, $1/M_{sc}$, and the displacement of stacked screens, $2D_{sc}$ (with the latter two not directly depicted in Figure 2.7). The packed bed geometry for cylindrical spheres is quantified by the diameter of spheres, D_{sp} . Additionally, all geometries are quantified by their porosity.

From Figure 2.7, we see that the parallel plate regenerators ideally exhibit a very high heat transfer effectiveness while maintaining a low pressure drop. However, the parallel plate regenerators have inherent issues with the tolerances of the stacking of plates during manufacturing. While the ideal construction of a parallel plate regenerator would lead to high effectiveness,

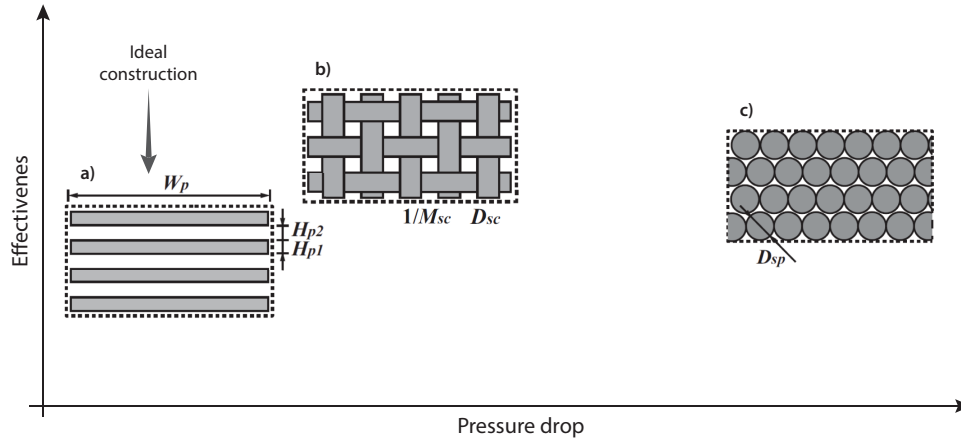


Figure 2.7: Schematic of the a) parallel-plate, b) packed screen bed, and c) packed particle bed geometries relative to one another regarding effectiveness and performance. Flow direction is defined perpendicular to the plane. Note that the effectiveness of an ideally constructed parallel-plate regenerator is high, but in reality a lot lower [92, 93]. Plot is based on results evaluated for: parallel plates; [89–93] packed screens; [89, 90, 94] and packed beds. [89, 90, 95] Insert a), b) and c) adapted from Lei et al. [89].

slight variations in both H_{p1} and H_{p2} were found to induce a significant decrease in performance [92, 93]. Meanwhile, the heat transfer effectiveness of packed beds of both spherical and irregular particles is high, however, at the cost of a large pressure drop. Packed screen beds seem like an apparent promising compromise, but with complex and costly processing routes for fabricating very thin wires or fibers of magnetocaloric materials [89, 94].

A geometry not shown in Figure 2.7 is the microchannel geometry. Regenerators of microchannel geometries are typically manufactured by extrusion [96] or (wire) machining [97] yielding straight, low tortuosity channels; or by selective laser melting [79] for relative complex channel shapes. Ideally, their effectiveness is relatively high [89] and should be placed close to the effectiveness of the ideal parallel plate geometry in Figure 2.7, with the additional benefit of a much larger surface area. However, as with the parallel plates, for the low tortuosity channels slight variations in spacing of the channels have been found to significantly decrease the heat transfer performance of this geometry [89, 98]. Additionally, the performance gain in COP, estimated in accordance with Lei et al. [89] and normalized to the performance of an operational magnetic regenerator prototype [99], is evaluated for regenerators of packed spheres and parallel plate regenerators of various channel sizes in Figure 2.8 It appears that channel widths in the order of $100 \mu\text{m}$ is desired for microchannel geometries [89], however, for which no shaping route thus far have proved sufficient. Similar to the plate regenerators, fabrication of homogenous microchannel geometries thus poses a major challenge in reaching the desired dimensions and homogeneity of an optimum regenerator geometry.

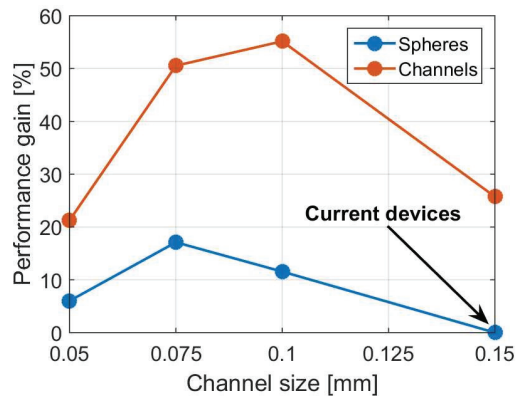


Figure 2.8: Gain in performance (COP) based on modelling results in Lei et al. [89], normalized to the performance of an operational magnetic regenerator prototype [99] indicated as *current device*. The microchannel geometry is seen to, ideally, outperform the packed bed of spherical particles, with an optimum channel size of 0.1 mm. Figure from Bjørk [100].

2.3 Freeze-casting of regenerator geometries

Freeze-casting presents an alternative shaping route for fabrication of exactly microchannel structures. With both tunable macropore, or microchannel, widths and porosities, low tortuosity and high mechanical strength, and versatility regarding material systems, freeze-casting of magnetocaloric materials presents a hitherto unexplored potential for a tunable regenerator geometry.

The overall scope of this project is thus implementation and evaluation of the fine micrometer-sized structural features and anisotropic porosity of freeze-cast materials as a regenerator geometry for magnetic refrigeration.

With the purpose of freeze-casting regenerator geometries of magnetocaloric materials, a freeze-casting device was designed and built at DTU, as will be presented in Chapter 4. As discussed in Chapter 1, a new material system for freeze-casting requires appropriate mapping of conditions for successful ice-templating. Choosing LCSM as a magnetocaloric model-material, Chapter 5–7 thus investigates various structural features of magnetocaloric freeze-cast LCSM ceramics – although, with the scope of the latter two chapters expanding beyond regenerator applications. Meanwhile, Chapter 8 summarizes the performance of actual freeze-cast regenerator geometries. We will thus return to Figure 2.7 in Chapter 8 and then place the freeze-cast regenerator geometry in relation to those geometries just presented.

Materials & methods

This chapter introduces general experimental procedures regarding both characterization of ceramic powders and magnetocaloric materials, freeze-casting, freeze-casting set-ups as well as post-processing and characterization of freeze-cast geometries. As such, experimental work in this thesis follows that described in this chapter unless otherwise specified.

Specifically, the preparation of suspensions for freeze-casting is outlined, while the three different freeze-casting set-ups used in this work are presented and evaluated. The structural characterization of freeze-cast samples throughout this thesis is primarily based on image analysis of SEM micrographs. The concept of this procedure have been published in Paper I and section 3.3 of this chapter is thus partly based on section 2.3 in Paper I.

3.1 $\text{La}_{0.66}\text{Ca}_{0.33-x}\text{Sr}_x\text{Mn}_{1.05}\text{O}_3$

The $\text{La}_{0.66}\text{Ca}_{0.33-x}\text{Sr}_x\text{Mn}_{1.05}\text{O}_3$ -series (LCSM) is a magnetocaloric ceramic, making it subjective to conventional ceramic processing routes. Although its magnetocaloric effect is limited as it is a second order material, with $\Delta T_{\text{ad}} \sim 1$ K (1T) [82] – which is e.g. one third of Gd [70] – temperature spans of 9.3 K for a two-material parallel plate regenerator have been achieved in an AMR prototype [82] partly owing to LCSMs ease of shaping. Additionally, the processing and characterisation of LCSM at DTU builds on 15 years of experience with this material [81, 82, 96, 101–104] and as such LCSM was chosen as a magnetocaloric model-material for implementation of freeze-casting for processing of regenerator geometries.

LCSM belongs to the family of mixed valence manganites [105] with a perovskite structure ABX_3 as illustrated in Figure 3.1. For LCSM the larger La^{3+} cation occupy the A-site, while the smaller Mn^{3+} occupy the B-site. Additionally, some of the trivalent La^{3+} ions are substituted by divalent Sr^{2+} and Ca^{2+} , thereof the name *mixed valence*. To maintain charge neutrality, trivalent Mn^{3+} are shifted towards tetravalent Mn^{4+} . While the substitution solely with Ca ($\text{La}_{1-y}\text{Ca}_y\text{MnO}_3$) show Curie temperatures in the range 225 – 260 K [107], the substitution with both Ca and Sr in LCSM, with $x \in [0; 0.33]$, show Curie temperatures in the range of 267 – 369 K [81], making it attractive as a regenerator material for room-temperature applications.

All LCSM powders used throughout this work were purchased from CerPoTech, Norway. Accordingly, the scope of this work has not been to synthesize and characterize LCSM. Characterization of powders have thus been with the aim of optimizing suspension properties and to asses quality. The synthesis of LCSM powders of various Sr/Ca doping ratios and the effect on

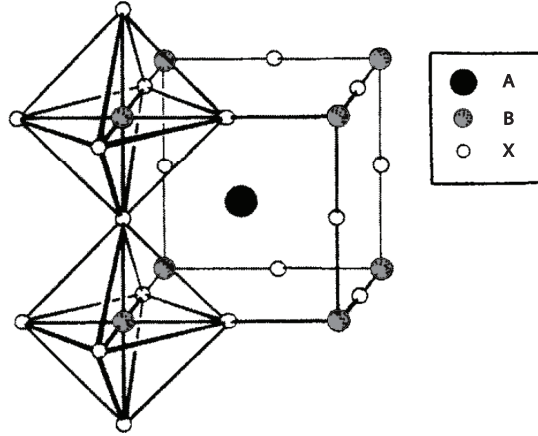
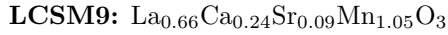


Figure 3.1: Perovskite structure, ABX_3 , where A and B are cations of different size, with $A > B$, and X is an anion. Figure edited from Bhalla et al. [106] © Springer-Verlag Berlin Heidelberg 2000.

magnetocaloric properties is described in detail by Dinesen [104]. In this work, three different LCSM compositions were used:



3.1.1 Evaluation of properties

Properties related to general processing of powders, suspensions or freeze-cast samples are discussed in this chapter, while properties significant for discussion of specific experimental procedures and/or results are given and evaluated throughout the thesis when relevant. General measurement procedures are described here.

Magnetocaloric entropy change and Curie temperature was evaluated by magnetization measurements obtained using a vibrating sample magnetometer (VSM, 7407, Lake Shore Cryotronics), where the magnetization of a sample in a homogeneous magnetic field is measured by vibrating the sample, thereby inducing a current in a pickup coil where the current then is proportional to the magnetization of the sample. Measuring the magnetization as a function of temperature at a range of applied magnetic fields fulfills Equation (2.3), page 17, for evaluation of the isothermal entropy change, ΔS_m . The magnetization was measured up to a maximum field of $\mu_0 H_{ext} = 1.6$ T from 250 K to 340 K with temperature steps of 2 K for determination of the Curie temperature and indirect measurements of the isothermal entropy change. The Curie temperature was then estimated as the peak temperature of $|\Delta S_m|$ (see Figure 2.4, page 18). The purity of purchased LCSM powders were evaluated by their Curie temperatures (see Section 3.1.1), as a slight alteration

in doping ratio would lead to a significant change in T_C . The purity of powders were confirmed by comparison with Curie temperatures given by [81, 108].

Density of powders were measured by gas pycnometry, i.e. measurements of gas displacement, using an AccuPyc II 1340 (Micromeritics) with He. Densities of powders were used to estimate porosity of processed samples, as described in Section 3.3.3.

Surface charge as a function of pH was measured using a Zeta potentiometer coupled with a pH probe, Zeta Potential Analyzer (Colloidal Dynamics), and determined by titration of an aqueous suspension of 0.9 w/w% powder/MiliQ water with 0.1 M NaOH and 0.1 M HCl. Measurements of zeta potential was carried out to estimate the surface charge of particles in suspension in order to optimize dispersion, as will be discussed in Section 3.2.1.

Particle size distribution (PSD) was determined by laser diffraction using a LS 13 320 Laser Diffraction Particle Size Analyser (Beckman Coulter). PSD was evaluated from diluted samples from prepared suspensions and measurements were carried out continuously for all suspensions used for freeze-casting to ensure sufficient homogenization and elimination of possible agglomerates.

3.2 General freeze-casting procedure

The processing steps of freeze-casting is essentially outlined in Figure 1.1 on page 5; 1) suspension preparation; 2) directional freezing; 3) sublimation/drying; 4) densification. The procedures described throughout this section are the general procedures used for processing of freeze-cast LCSM ceramics. Specific experimental procedures are described and discussed throughout the thesis when relevant.

3.2.1 Suspension preparation

Ceramic suspensions for freeze-casting were prepared from 14–40 vol% powders of LCSM, calcined at 1000 °C for 2 hours, in MiliQ water, with the addition of 2.5 wt%, solid to ceramic ratio, of DURAMAX™ D-3005 (Rohm and Haas, Dow Chemical) as dispersing agent and 1.5–2.0 wt%, solid to ceramic ratio, of DURAMAX™ B-1022 (Rohm and Haas, Dow Chemical) as binder. The role of the dispersant and binder is to ensure proper dispersion of particles in the suspension – i.e. eliminating formation of agglomerates and hinder sedimentation – and to bind the particles together in the green body, respectively. A dispersant is thus typically a polymeric or ionic species which adsorbs onto the particle surface effectively dispersing particles by making them either electrostatically repel one another; by steric hinderance of agglomeration; or by electrosteric interactions combining the first two. The binder is typically a polymeric species forming a continuous polymer matrix, binding the particles together when the solvent has been removed. The binder thus provides green strength, e.g. for applications in freeze-casting, this

ensures that the templated pores are maintained when the solvent is removed by sublimation and until the sample is densified by sintering.

Additives were chosen based on their low viscosities. High viscosity suspensions for freeze-casting yield increased secondary dendrite formation resulting in increased surface roughness in the form of ceramic struts/dendrites and ceramic bridges [33], as illustrated on Figure 1.1B) on page 5. However, with the aim of templating low tortuosity macropores and being able to fine-tune the pore size, low viscosity commercial dispersant and binder were chosen. DURAMAX™ D-3005 is the ammonium salt of a polyelectrolyte with a viscosity of <100 mPa s [109], while DURAMAX™ B-1022 is an acrylic polymer emulsion with a viscosity of 400 mPa s [110].* The ratio of dispersant was based on approximate observations of sedimentation rate; suspensions for freeze-casting must prove stable throughout the duration of full solidification, i.e. about an hour for samples prepared in this work.

Measurements of the surface charge found the isoelectric point of all LCSM powders to be in the proximity of ~ 8.6 – 8.8 and revealed that the zeta potential reaches a plateau of constant surface charge at the lower pH range, indicating that a stable suspension due to electrostatic dispersion is achieved at $\text{pH} < 7$. All suspensions were thus adjusted from a $\text{pH} \sim 8.5$ to $\text{pH} \sim 6$ by dropwise addition of nitric acid.

In order to achieve a sufficient dispersion and homogenization of powders, the suspensions consisting of powders, MiliQ water, dispersant and nitric acid were mixed in a PE flask with a few alumina mixing balls ($\text{Ø}10\text{mm}$) using a low energy ball mill for at least 48 hours or until all agglomerates had been eliminated and a consistent particle size distribution was established. The binder was added and mixed for an additional 1–24 hours at 15 rpm without any mixing media. Suspensions were sieved (~ 30 μm mesh), and de-aired under low vacuum for a few minutes immediately before casting.

3.2.2 Freeze-casting set-ups & procedures

As outlined in Chapter 1 the freezing conditions are crucial for achieving successful freeze-casting and for control of the final microstructure, and as such, many freeze-casting set-ups or devices exist. Throughout this work, three different set-ups for freeze-casting have been used for directional freezing of LCSM suspensions:

Set-up A) *Copper rod directly immersed in liquid N_2* was used for directional freezing of samples with no other temperature control than that of liquid nitrogen, i.e. 77 K. A cylindrical acrylic custom-designed, see-through mould, with an inner diameter of 16.5 mm, an outer diameter of 36 mm and with a detachable copper bottom was placed on top of the vertically positioned, half immersed copper rod ($\text{Ø}20\text{mm}$, L315mm). The mould was equipped with thermocouples (K-type, gauge 36, Omega) positioned along the height of the mould 6 mm apart in inserts drilled radially inward in the mould leaving 0.75 mm mould wall between the thermocouples and the suspension for temperature tracking of the

*For comparison, the approximate viscosity of water is 1 mPa s at *rt* while that of honey is ~ 10000 mPa s.

freezing front. Although the mould design proved efficient for tracking of the solidification progression in the suspension by evaluating the temperature, the freezing front could not be tracked visually, as seen on Figure 3.2, and the conditions of freezing could not be kept constant.

Set-up B) *Copper rod with fins for high freezing rates* was used for directionally freezing of samples at static and dynamic temperature profiles. The set-up is described in detail by Lichtner et al. [8, 26], who also originally designed and developed the set-up. The set-up consisted of a large copper rod ($\text{\O}76$ mm) immersed in a bath of liquid nitrogen. A large interface between copper and liquid nitrogen achieved by fins cut into the copper rod provided increased temperature control as well as a faster freezing of samples and allowed for manual control of the freezing rate, by controlling the amount of liquid nitrogen in the bath, see Figure 3.3 and Figure 4.2 on page 46. The temperature of the copper rod was monitored by the application of a K-type thermocouple. Cylindrical acrylic moulds of inner and outer diameter of 18 mm and 45 mm, respectively, were directly mounted on the top of the copper rod using vacuum grease while the top of the moulds were left open to ambient conditions. The large thermal mass of the copper rod and the thick walls of the acrylic mould with high thermal resistance ensured continuous freezing conditions and minimal heat exchange with the surroundings.

Set-up C) *Novel freeze-casting device with thermoelectric temperature control for dynamic freezing rates* is described in detail in Chapter 4. The set-up utilized a thermoelectric element for high precision temperature control for implementation of dynamic freezing conditions. The procedure for freezing samples using this set-up is described in detail in Section 5.3 on page 64.

The set-ups are here ordered chronologically, i.e. initially the simplistic **Set-up A** was built at DTU to explore the various processing levers of freeze-casting, even for such a simplistic set-up. An initial mould design of see-through acrylic glass and a scalebar incised directly into the mould was tested in combination with various LCSM powders in suspensions with various dispersant and binder systems. The results hereof are reported in Paper VI. These experiments revealed the significance of temperature control, as the pores were found to triple in size throughout a sample length of only a few centimeters. Additionally, due to the colour of LCSM, the freezing front could not be tracked visually, as seen in Figure 3.2. However, the temperature tracking of the freezing front proved efficient and was thus implemented in a modified version in **Set-up C** as will be discussed further in Chapter 4.

In collaboration with professor Rajendra K. Bordias research group at the Department of Material Science and Engineering, Clemson University, SC, their high speed freeze-caster [8, 26] was used for processing of dynamically frozen samples using constant cooling rates of -10 K/min and compared with static freezing conditions. **Set-up B** is shown in Figure 3.3. A schematic of the set-up is moreover found in Figure 4.2 on page 46. The results of these

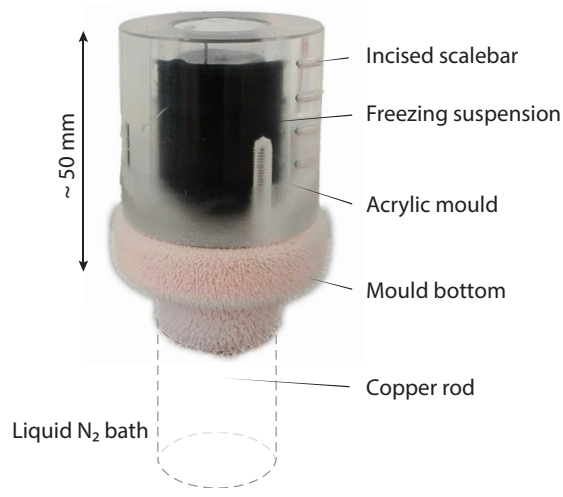


Figure 3.2: See-through custom-designed moulds were used with freeze-casting **Set-up A** in order to visually track the progression of freezing in the suspension. However, due to the color of LCSM this was not feasible.

freezing conditions, as well as the effect of gelation, are reported in Paper I and discussed in Chapter 6.

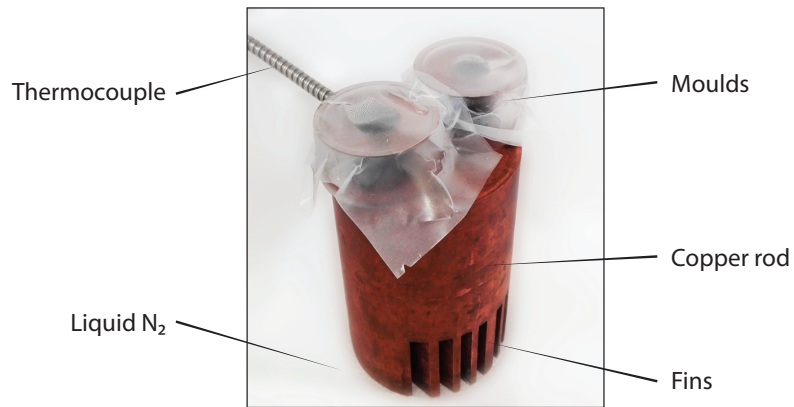


Figure 3.3: Freeze-casting **Set-up B** developed and described in detail by Lichtner et al. [8, 26], where a copper rod with fins immersed in a bath of liquid N₂ provides a cooling source for freeze-casting. Two acrylic moulds containing LCSM suspensions are mounted on top of the copper rod.

Set-up C was designed and built as part of the scope of the present Ph.D. work. It was the goal to have a functioning, easily operational freeze-caster unit with high temperature precision and a large degree of control of freezing conditions, implemented at the Department of Energy Conversion and Storage, DTU, at the finalization of this project. The device is constructed from the same base units as other pieces of equipment at the department [111] for high inter-

changeability, ease of troubleshooting and the possibility of upgrading single components for optimization of performance and processing requirements. The design of the set-up was based upon experiences from working with **Set-up A** and **Set-up B**, and was used for freezing of the majority of freeze-cast structures presented throughout this thesis.

3.2.3 Drying and densification

All freeze-cast samples prepared throughout this work were frozen using water as solvent. This eliminates concerns and considerations of toxicity and volatility as water is neither. Following the freeze-casting procedure itself as outlined in the previous section, ice was sublimated from the frozen samples using commercial freeze driers, either a FreeZone 2.5 (0.200 mBar, 223 K, Labconco) or Christ Alpha 1-2 LD plus (0.200 mBar, 218 K, Buch & Holm), for at least 24 hours. Preferably, frozen samples should be removed from moulds before sublimation of ice in order to expose a large surface area. However, as de-moulding required the use of compression tools to push the frozen sample out of the cylindrical mould, this would most often result in sample deformation of unknown extent and samples were therefore dried in the moulds with the bottom part of the mould removed. After sublimation of ice, samples were easily de-moulded with no apparent deformation.

Green LCSM freeze-cast samples were densified by sintering. Sintering is a heat treatment of ceramic particles, packed in a green body, resulting in coalescence and bonding of adjacent particles which results in a rigid ceramic structure. Sintering removes the inter-particle pores, microporosity, of the green sample, often causing some degree of shrinkage for the final ceramic. With the purpose of freeze-casting regenerator geometries for heat transfer and storage, ideally, dense walls was desired, as the anisotropic macropores was imagined to be facilitating mass transfer of a heat transfer fluid, while micropores would represent dead volume, i.e. not being either flow channels or magnetocaloric material. Additionally, the thermal conductivity of ceramics depend on the bulk density, where an increase in density, often as a result of elevated sintering temperatures, yield a corresponding increase in thermal conductivity [112]. Almost complete removal of microporosity, only retaining the macroporosity, have been accomplished for freeze-cast ceramics [5, 8, 16, 113], however, the success of doing so depends on the sintering behaviour of the chosen ceramic.

Sintering behaviour of LCSM was investigated by dilatometry performed using a single push-rod dilatometer (DIL 402, NETZSCH) with a 2 hour hold at 550 °C for burnout of additives and a hold at 1100–1250 °C for densification under normal atmosphere (flow rate of 20 mL/min). Shrinkage curves were analyzed using *Proteus Thermal Analysis* software (NETZSCH) for evaluation of onset temperatures and relative length change.

Pellets for dilatometry were prepared by slip-casting, given that the microporosity of slip-cast pellets to a larger degree resembles that of freeze-casts compared to e.g. pressed pellets. For slip-casting, custom-made cylindrical polytetrafluoroethylene (PTFE) moulds with inner

diameter of 6 mm were placed on an alabaster plaster medium. Standard suspensions of LCSM prepared as described in Section 3.2.1, were poured into the moulds and left to dry for at least 48 hours. Pellets for dilatometry were used in the green state.

LCSM ceramics are typically sintered at temperatures of 1150–1500 °C [81, 82, 96, 101–104]. However, as also observed by Pryds et al. [96], LCSM severely deforms at elevated temperatures. LCSM freeze-casts were frozen in cylindrical moulds, and the green samples were thus also perfectly cylindrical after drying. However, when sintering at temperatures >1200 °C, while placing samples upright in the furnace, deformation was clearly evident as the samples would open up in the top, resembling a blooming flower. Meanwhile, no deformation was seen for sintering temperatures <1150 °C. A deformed and a perfectly cylindrical sintered freeze-cast LCSM samples are shown in Figure 3.4. The deformation behaviour of freeze-cast LCSM samples could be elucidated further by optical dilatometry analysis. Nonetheless, realizing that



Figure 3.4: Deformed and cylindrical freeze-cast LCSM samples, sintered at 1300 °C and 1100 °C, respectively.

freeze-cast samples could not be sintered at temperatures above 1150 °C the sintering behaviour with respect to hold times were thus investigated, with the desire of increasing the density of walls while still avoiding severe deformation. Dilatometry measurements showing the sintering behaviour and corresponding heating profiles of LCSM6 slip-cast pellets are given in Figure 3.5. While the onset temperature is consistently 1100 °C the shrinkage of samples strongly depended on sintering time and temperature.

The relative length change, $\frac{dL}{L_0}$, is the shrinkage of pellets during sintering, dL , normalized to the initial sample length, L_0 . The total shrinkage of all samples are listed in Table 3.1. Assuming isotropic shrinkage and negligible mass loss, the sintered density can be calculated from the relative length change and the density of the green pellets, ρ_{SC} , [114]:

$$\rho_{\text{sin}} = \frac{\rho_{SC}}{\left(1 + \frac{dL}{L_0}\right)^3} \quad (3.1)$$

The green body density of slip-cast LCSM6 pellets was measured to $\rho_{SC} = 2.6 \text{ g/cm}^3$. Assuming that the ideal sintering would result in a ceramic with the same density as the LCSM powder itself, $\rho_{\text{dense}} = 6.10 \text{ g/cm}^3$ (see Table 3.2), the relative density of sintered samples can be evaluated. Relative densities are also listed in Table 3.1. As expected, the relative density

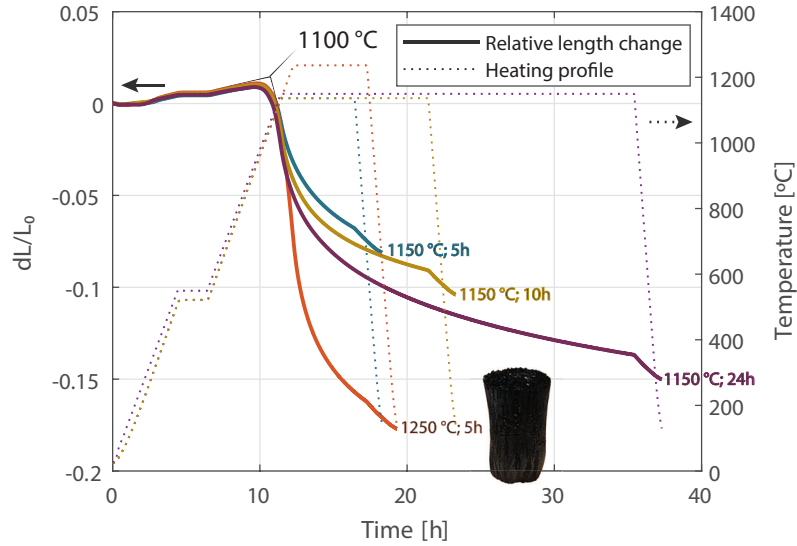


Figure 3.5: Shrinkage of slip-cast LCSM6 pellets during sintering at various heating profiles, where sintering temperature and hold time is indicated by each curve. The onset temperature is evaluated using *Proteus Thermal Analysis* software and is estimated at 1100 °C. The freeze-cast LCSM sample in the bottom of the plot is deformed due to elevated sintering temperature.

is greatest for the slip-cast LCSM sample sintered at 1250 °C reaching a relative density of 77% with a hold time of 5 hours. Meanwhile, even with a hold time of 24 hours, the relative density of samples sintered at 1150 °C only reached 69%. This is of course an important consideration when freeze-casting regenerator geometries, as will be discussed further in Chapter 8, however, for evaluation of suspension properties and freezing conditions and the resulting effect on morphology of the macropores, partial sintering is assumed sufficient. Therefore, a standard sintering temperature of 1100 – 1150 °C with a hold of 3 hours was chosen for all LCSM freeze-casts. Inevitably, this leaves a large degree of microporosity in the structure; we

Table 3.1: Summarization of dilatometry analysis of slip-cast LCSM6 pellets for evaluation of sintering behaviour of LCSM.

Temperature [°C]	Hold time [h]	Relative length change, dL/L_0	Sintered density ρ_{sin} , [mg/cm ³]	Relative density $\rho_{\text{sin}}/\rho_{\text{dense}}$
1150	5	-0.08	3.4	0.55
1150	10	-0.10	3.6	0.59
1150	24	-0.15	4.2	0.69
1250	5	-0.18	4.7	0.77

will return to the hierarchical nature of the porosity of freeze-cast LCSM in Section 3.3.3.

Thermogravimetric analysis of the chosen dispersant and binder – as provided by the manufacturer [109, 110] – showed that decomposition of the former is initiated at ~ 100 °C and continues steadily until ~ 550 °C, while the latter starts decomposing at ~ 250 °C until ~ 400 °C. A standard heating profile for sintering of LCSM freeze-casts is thus illustrated in Figure 3.6, considering both the burnout of dispersant and binder, onset temperature of sintering of LCSM ceramics and deformation at elevated temperatures.

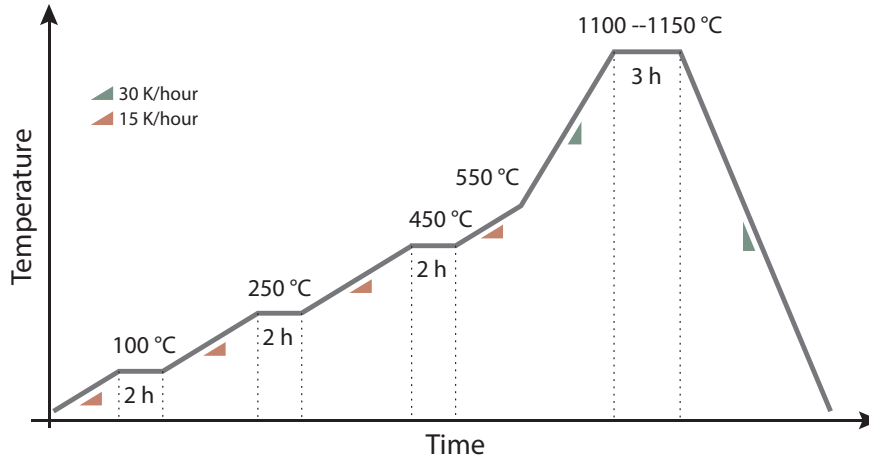


Figure 3.6: Standard heating profile for sintering of freeze-cast LCSM ceramic.

3.3 Quantification of freeze-cast geometries

As briefly discussed in Chapter 1, various approaches have been taken to characterise and quantify morphology of freeze-cast microstructures. Generally, the structures are characterized from a 2D approach, where pore and wall sizes are measured in optical images or SEM micrographs of perpendicular cross-sections. Additionally, for lamellar morphologies the periodicity is typically quantified by the structural wavelength. Anisotropy of pores is usually evaluated by simple visual comparison between perpendicular and parallel cross-sections. Low tortuosity of macropores is often claimed as a characteristic for freeze-cast structures [7, 41–44], but is rarely calculated and evaluated with respect to freezing conditions. Miller et al. [13] calculated tortuosities, however, only for static freezing conditions and only at one sample height. Porosity is typically measured by Archimedes measurements or simply by evaluating mass and dimensions of samples.

With this work, it was the desire to implement a semi-automatic and consistent procedure for characterizing freeze-cast structures and as such eliminate e.g. manual measurements of features in images. To maintain an automatic, fast and reproducible workflow for analysis of a large quantity of SEM micrographs for morphological characterisation of freeze-cast structures,

MATLAB® (The MathWorks, Inc.) has been used. Implementation of software developed by Jørgensen et al. [115–118] for 2D measurements of tortuosity, automatic detection and evaluation of macropore and wall sizes, measurements of macroporosity and specific surface area, has thus provided a consistent quantification and evaluation of the microstructure and homogeneity of macropores in freeze-cast LCSM throughout this thesis.

3.3.1 Post-processing of freeze-casts

Ceramic samples were prepared for mechanical handling and structural analysis by infiltration with epoxy (EpoFix, resin and hardener, Struers). Epoxy infiltrated samples were cut in half parallel to the freezing direction and one half was then sliced perpendicular to the freezing direction in thicknesses of 2–4 mm. These were then polished and coated with a ~ 12 nm thick carbon layer.

Scanning electron microscopy (SEM) was used to obtain micrographs of the perpendicular and parallel cross sections of freeze-cast LCSM using a TM3000 (15 kV, Hitachi High-Technologies).

The microstructure of samples was thus generally investigated as a function of sample height, that is, the vertical distance — parallel to the freezing direction — from the bottom of the sample and to the specific point of interest. The processing of LCSM samples for SEM analysis is schematized in Figure 3.7.

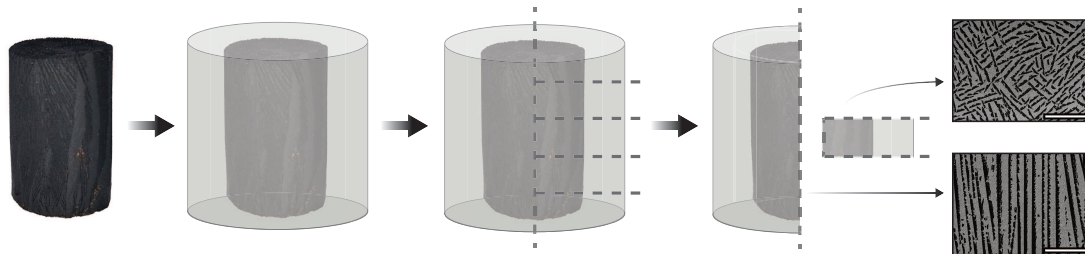


Figure 3.7: Mounting of freeze-cast sample in epoxy allowed for imaging with SEM at very precise sample positions.

3.3.2 Image analysis of SEM micrographs

Given that processed LCSM freeze-casts for SEM analysis consisted of a single phase of an electronically conducting material (LCSM) and a single phase of pores (epoxy), SEM micrographs showed a great contrast for easy binarization using the `imbinarize` function provided with the Image Processing Toolbox™ [119] in MATLAB®, as shown in Figure 3.8a). Additionally, individual features smaller than $\sim 5 \mu\text{m}$ in diameter, such as small pores or grains, were removed. As such, only the larger features such as macropores and macroporosity were evaluated by this

method. The analysis then depends on whether parallel or perpendicular cross-sections, with

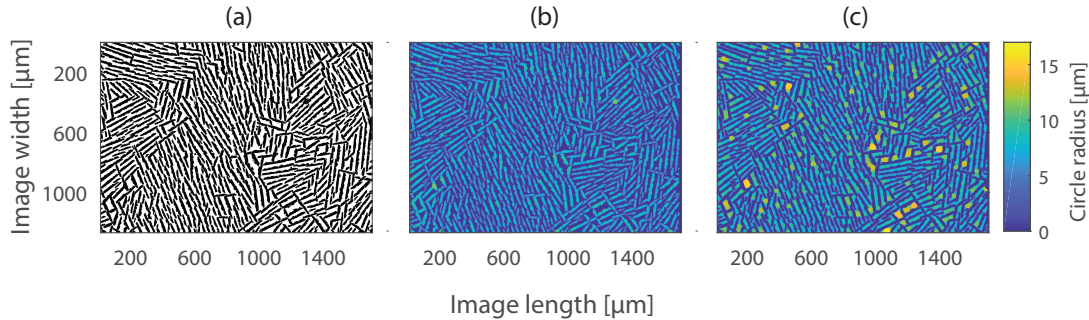


Figure 3.8: Processing of SEM images obtained from cross-sections perpendicular to the freezing direction in order to estimate channel and wall sizes. a) Binarized SEM image, where white indicates ceramic walls and black is voids or pores. Circles are fitted to either the b) pores or c) walls, with the fitted circle radius indicated by the colorbar. Figure revised from Paper I.

respect to the freezing direction, were investigated:

For SEM micrographs of cross-sections perpendicular to the freezing direction, the size of the macropores or walls were estimated by a continuous particle size distribution method. This is done by fitting circles of increasing size in every point in all pores (or walls) in a binarized image, determining the largest circle that can be fitted within all points in the pores (or walls), yielding a direct measure of the size of the pore (or wall) [116]. The radius of these fitted circles are shown for the pores and the walls in Figures 3.8b) and 3.8c), respectively. As can be seen from the images, the above procedure results in a distribution of fitted circles throughout the SEM image, as shown in Figure 3.9. The average pore or wall diameter can then be calculated from this distribution, by averaging the distributions of fitted circles weighed by area at each perpendicular cross-section. Generally three SEM micrographs, each containing $\gg 100$ pores were evaluated at each sample position. Additionally, macroporosities were estimated from the binarized images as the ratio between the two phases and the specific surface area was measured as the interface distance between the two [115, 118]. This of course means that both porosity and surface area determined from image analysis are limited by the resolution of micrographs and the threshold of the binarization, and are thus characteristics of the macropores and thus not comprehensive for a complete quantification of the full microstructure. However, as the scope of this project is evaluation and optimization of the ice-templated macropores for use as flow channels for fluids, these measurements are initially assumed adequate for describing the morphological features. Moreover, as the analysis is semi-automated, a large quantity of micrographs could be analyzed allowing time for e.g. a greater spatial resolution along the sample lengths.[†] SEM images used for estimating the pore and wall sizes, macroporosities and specific surface area have been obtained at magnifications of $\times 50 - \times 500$. The analysis of these parameters were found to be independent of magnification in this range. Structural parameters

[†]2000+ SEM micrographs have been obtained and analyzed throughout the course of this Ph.D. project.

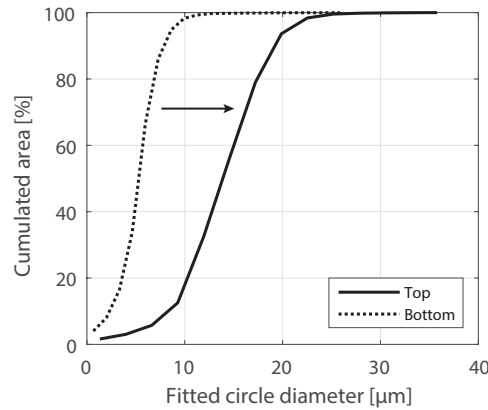


Figure 3.9: Size distribution of circles fitted to pores of cross-sectional SEM micrographs. Only distributions at cross-sections at the top (sample height of 8 mm) and bottom (sample height of 2 mm) of a statically frozen freeze-cast are shown here (see Chapter 6). The arrow indicate the change in pore size going from the bottom to the top of the sample. Figure revised and edited from Paper I © 2019 *The American Ceramic Society*.

measured by image analysis are throughout the thesis given as a mean of three micrographs \pm one standard deviation, unless otherwise specified.

For SEM images of cross-sections parallel to the freezing direction, the quality of the structure in terms of allowing a fluid to pass through pores can be estimated. This is done by calculating the tortuosity, τ , of the channels. Tortuosity is a measure of the curviness of pores, in this case, evaluating the ratio between the direct distance across a cross-section of a SEM micrograph, L_{SEM} , and the distance across the same cross-section through a pore, L_{pore} :

$$\tau = \frac{L_{pore}}{L_{SEM}} \quad (3.2)$$

A factor of $\tau = 1$ corresponds to a direct flow path, while the greater the tortuosity the greater the curviness or skewness of the pores. Tortuosity was calculated using the TauFactor application [43] in MATLAB®. The software calculates the tortuosity in 2D from SEM cross-sectional images instead of the more intricate and time consuming procedure of doing a 3D X-ray tomography analysis of entire samples [116–118], although the latter obviously gives a more extensive description of the morphology. However, calculating tortuosity from 2D cross-sections requires considerations about the magnification of analyzed SEM micrographs. A too large magnification results in very few pores per image, while a too small magnification results in what appears to be closed pores due to the tilt and random orientation of domains as discussed in Chapter 1.

Images obtained at different sample heights at a magnification of $\times 500$ met the aforementioned criteria while still representing and maintaining general pore structure characteristics in form of wall morphology, skewness of pores and width of pores and walls. Thus, tortuosity

was calculated parallel to the freezing direction across cross-sectional areas of $331 \times 248 \mu\text{m}$ for all samples in this thesis. It should be noted, that the tortuosities calculated here are thus not directly comparable to those obtained in other studies, but are, nonetheless, a strong tool for internal comparisons of structures within this work.[‡]

3.3.3 Hierarchical porosity

The image analysis only quantifies the macroporosity of samples, however, as discussed in Chapter 1 the porosity of freeze-cast ceramics is typically hierarchical. The macro- and microporosity of a freeze-cast LCSM6 sample are shown in Figure 3.10. Besides the hierarchical

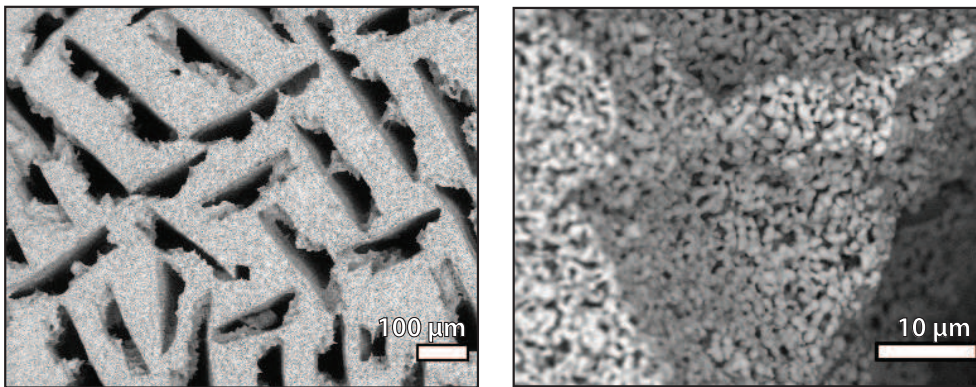


Figure 3.10: SEM micrographs showing the hierarchical porosity of a freeze-cast sample. Macroporosity in the form of ice-templated pores and microporosity in the form of inter-particle porosity between the particles in the walls. The sample is frozen using a constant cooling rate of -1.5 K/min from a suspension of 25 vol% solid load and sintered at $1100 \text{ }^\circ\text{C}$ for 3 hours.

porosity, which we will return to shortly, another significant feature of freeze-cast samples frozen using water as solvent is evident from the images; namely, the ceramic dendrites, or struts, on the ceramic walls extending perpendicular into the pores. The origin of these secondary features have been attributed to the growth of secondary ice crystal dendrites on one side of the lamellar ice crystals [28, 32], and they greatly alters the surface roughness of the macropores.

The total porosity throughout this thesis was generally determined by the mass and dimension of full samples. As samples were mostly perfect cylindrical, this proved as a simple, non-destructive approach, where the total porosity, P , was determined from the mass, m , and volume, V , of samples in accordance with [33, 44]:

$$P = 1 - \rho_{\text{ratio}} \quad (3.3)$$

[‡]SEM micrographs evaluated for calculation of tortuosities – and structural features in general – in published Papers I and IV are all freely available at the DTU Data repository with the exact purpose of direct comparisons with other studies utilizing other analysis procedures and calculations. DOIs of data repositories can be found in Part V.

where ρ_{ratio} is the ratio between the sample density, ρ , and the density of fully dense LCSM, ρ_{LCSM} :

$$\rho_{\text{ratio}} = \frac{\rho}{\rho_{\text{LCSM}}} = \frac{mV^{-1}}{\rho_{\text{LCSM}}} \quad (3.4)$$

Assuming that the density of fully dense LCSM can be estimated as the density of powders, the density of all LCSMs are given in Table 3.2.

Table 3.2: Densities, ρ_{LCSM} , for all LCSMs measured by gas pycnometry.

	LCSM6	LCSM7	LCSM9
Density [g/cm ³]	6.10	6.04	6.08

The porosity of freeze-cast LCSM can also be determined from Archimedes measurements or intrusion porosimetry, however, using the method outlined by Equation (3.3) and (3.4) does not require any processing of samples and they could then be infiltrated directly with epoxy and processed for SEM analysis.

In order to evaluate the validity of both the porosities estimated from Equation (3.3) and (3.4) and the macroporosity and pore size estimated from image analysis, as described in Section 3.3.2, these were compared to measurements of pore size distributions and porosity by mercury intrusion porosimetry.

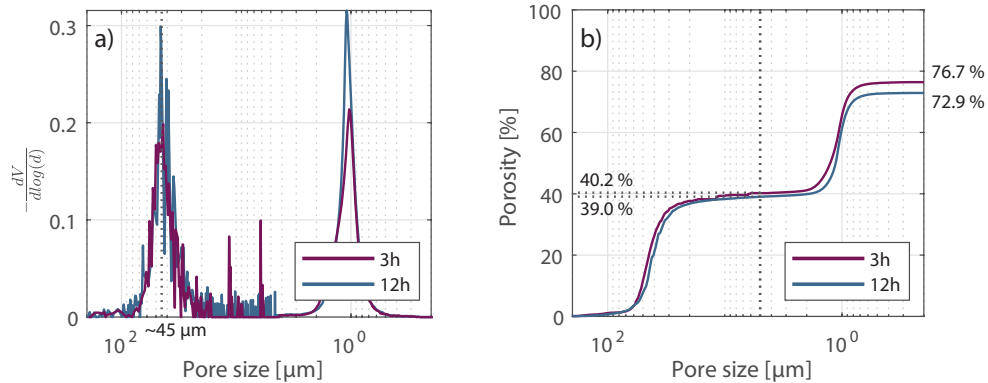


Figure 3.11: Porosimetry measurements by mercury intrusion of freeze-cast LCSM samples, both frozen at a constant freezing rate of -1.5 K/min, from a suspension of 25 vol% LCSM6, and sintered at 1100 °C for 3 and 12 hours, respectively. a) Both samples show a bimodal distribution of pore sizes, i.e. a peak in the range of $30 - 50$ μm and a peak in the range $0.5 - 1$ μm . b) A slight variation in total porosity and porosity distribution is evident, although it appears that the effect of increasing the sintering time is almost negligible. Note that the scattered peaks at pore sizes around 5 μm represents an instrumental error.

The pore size of the macropores estimated from porosimetry measurements by the approximate center of the first peak in Figure 3.11a) is for both samples is $\sim 45 \mu\text{m}$, while the corresponding pore sizes measured from image analysis are $47.3 \pm 1.1 \mu\text{m}$ and $46.7 \pm 0.9 \mu\text{m}$, for a sintering time of 3 and 12 hours, respectively. Additionally, the total porosity/macroporosity evaluated from image analysis is $72.9/37.8 \pm 0.5\%$ and $72.9/38.0 \pm 0.6\%$. Thus, there is a good agreement between measurements of the pore size using image analysis and intrusion porosimetry, while measurements of porosity using image analysis and Equation (3.3) and (3.4) results in a slight overestimation. Regarding sintering behaviour, the porosimetry measurements show a very reduced effect of sintering at extended time intervals regarding elimination of microporosity, as the porosity distribution in Figure 3.11b) appear to be more or less the same.

3.4 Summary

In this thesis the perovskite LCSM is chosen as a magnetocaloric model-material. Although its magnetocaloric effect is relatively small – e.g. T_{ad} of LCSM is one third of that of Gd – it is attractive due to ease of shaping and its Curie temperature which is tunable around room temperature, i.e. 267 – 369 K, making this material ideal for room temperature applications.

Successful dispersion of LCSM powders in MiliQ water was achieved with the addition of 2.5 wt% a low-viscosity commercial dispersant, DURAMAX™ D-3005, while 1.5 – 2.0 wt% DURAMAX™ B-1022 was added as binder.

Freeze-casting of LCSM suspensions are in this work carried out using one of three set-ups with varying complexity and correspondingly varying user-control: a set-up consisting of a copper rod directly immersed in liquid N_2 with no temperature control other than that of the refrigerant (**Set-up A**); a set-up consisting of a copper rod with fins for high, constant freezing rates (**Set-up B**); and a set-up with a thermoelectric element for high precision temperature control (**Set-up C**). The latter was build as part of this Ph.D. work and the majority of freeze-cast structures presented throughout this thesis was thus prepared with this set-up.

In order to achieve rigid freeze-cast LCSM structures, they must be sintered. The onset temperature of LCSM is $\sim 1100 \text{ }^\circ\text{C}$, and while dilatometry measurements show an effect on relative density of slip-cast pellets, i.e. with an increase in density of samples with increased sintering time, the same effect was not seen with mercury intrusion porosimetry in actual freeze-cast LCSM samples. Here, the effect of increasing the sintering time was found to be negligible. Based on thermal analysis of powders and additives a standard heating profile was chosen, outlined in Figure 3.6, with sintering at 1100 – 1150 $^\circ\text{C}$ for 3 hours. Although, as intrusion porosimetry and SEM micrographs reveal, this heating profile does not eliminate inter-particle microporosity.

Image analysis, semi-automated in MATLAB®, is used throughout this thesis to quantify structural parameters such as pore and wall size, macroporosity, specific surface area and tortuosity. Although, due to the resolution of SEM micrographs, these parameters thus primarily describe the features of the macropores and thus not the entirety of the microstructure of

freeze-cast LCSM ceramic. A good agreement between pore sizes evaluated by image analysis and intrusion porosimetry is shown, while the porosity estimated from image analysis appears to be slightly overestimated. Structural parameters measured by image analysis are throughout the thesis given as a mean of three micrographs \pm one standard deviation, unless otherwise specified.

Part II

Novel Freeze-casting Device

The freeze-caster

In this chapter, the design and performance of a custom-build freeze-caster is presented and evaluated. For every research group working with ice-templating, a unique, experimental set-up for freeze-casting exists; including the freeze-caster built at DTU in connection with the present Ph.D. thesis.

The freeze-casting device presented here utilizes thermoelectric temperature control for implementation of dynamic freezing conditions in combination with a novel interchangeable mould design using temperature measurements for tracking of the freezing front. The set-up was previously briefly presented in Chapter 3, and is throughout the thesis referenced as either *the freeze-caster* or *Set-up C*. All freeze-cast ceramics presented in this work are frozen using this device unless otherwise specified.

This chapter is partially based on Paper III.

4.1 Designing a freeze-casting device

In all its simplicity, all that is required for a functioning freeze-caster is a cooling source, i.e. a thermal reservoir with a temperature below that of the suspension solidification temperature. A container that keeps the suspension such that only one side is brought into thermal contact with the cooling source is then mounted on the reservoir. In this way, a thermal gradient is created throughout the suspension, which is also isolated from the ambient.

The **cooling source** most often consist of a liquid refrigerant brought into thermal contact with a coldfinger or a plate of a material with large thermal conductivity [5, 11, 30, 37, 41, 57, 59, 120]. In the most common freeze-casting set-up, a copper rod is immersed directly into a container of ethanol or liquid nitrogen. This was the case for one of the first experimental freeze-casting set-ups for ice-templating of alumina ceramic particles, illustrated in Figure 4.1. Using this simple set-up, Fukasawa et al. [5] were able to achieve alumina ceramics with the characteristic hierarchical porosity of directional macropores and micropores in the walls, and showed how the distribution of total porosity between the two depends on sintering temperatures, while the total porosity depends on the solid load of the initial suspension. Our initial freeze-casting set-up, **Set-up A** as described in Chapter 3, page 28, greatly resembled the one by Fukasawa et al. [5], although using a thin copper rod immersed directly in liquid nitrogen. Such a set-up poses no other immediate control of temperature than that of the refrigerant.

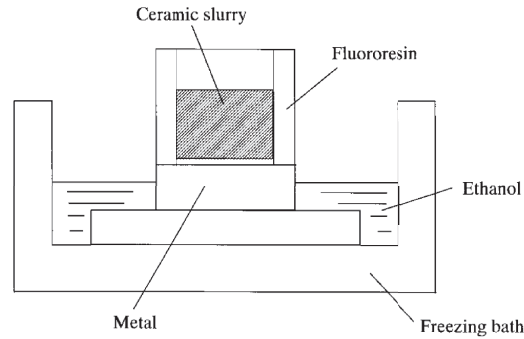


Figure 4.1: Simple freeze-casting set-up, where the **cooling source** consists of a liquid refrigerant in the form of ethanol ($-50\text{ }^{\circ}\text{C}$). The resin mould with a metal bottom containing an alumina suspension is placed on a metal plate in the freezing bath. Figure from Fukasawa et al. [5] © *The American Ceramic Society*.

A larger degree of **temperature control** of the non-immersed end of the rod can then be achieved by either the level of refrigerant in the container [11] or by a heating sleeve installed at the top of the rod typically equipped with a thermocouple and PID control [11, 30, 37, 41, 57, 59]. In such a set-up, one side of a suspension contained in a mould can be brought into contact with the copper rod. This type of set-up is thus referred to as a **one-sided set-up**. Figure 4.2 illustrates the two one-sided freeze-casting set-ups used by Lichtner et al. [8, 11, 26]. One set-up with a heat-sleeve and PID-control (low-speed freeze-caster) and one with a copper

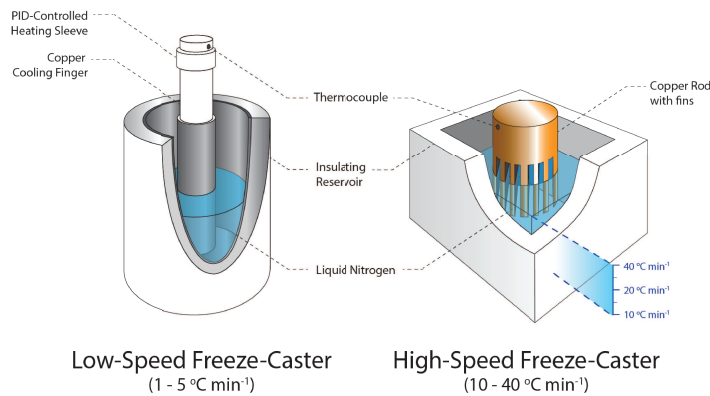


Figure 4.2: Schematic of low-speed and high-speed freeze-caster, where a PID-controlled heating sleeve provides low freezing rates for the first, while a large thermal mass and fin in the copper rod provides large freezing rates for the latter. Figure from Lichtner [8].

rod with fins (high-speed freeze-caster). The latter set-up is identical to the one described in Chapter 3, page 29, as **Set-up B**. The large thermal mass and increased contact surface area between the copper rod and refrigerant due to the fins, allows for fast cooling rates of -10 to -40 K/min.

With the implementation of an additional cooling source of greater temperature at the opposite side of the freezing suspension, in a so-called **double-sided set-up** [9, 10, 53], almost full thermal control across the sample and thus of the thermal gradient is achieved, however, with difficulties arising from the expansion of the freezing suspension. The double-sided freeze-casting set-up used by Waschkie et al. [10, 53] is illustrated in Figure 4.3. With the implementation of fine-tuned dynamic temperature profiles of both the bottom and top coldfinger, almost homogeneous lamellar spacings were achieved [10] throughout freeze-cast alumina ceramics, with freezing front velocities ranging from $5 \mu\text{m/s}$ – $30 \mu\text{m/s}$ [53]. Implementation of dynamic freezing profiles to achieve structural homogeneity will be discussed further in Chapter 5.

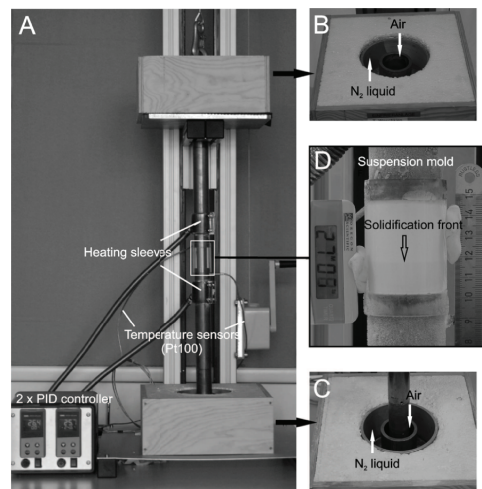


Figure 4.3: Double-sided freeze-casting set-up where PID-controlled heating-sleeves provides temperature control of both top and bottom coldfinger. Insert (D) show the visual tracking of the solidification, i.e. freezing, front by use of a see-through acrylic mould equipped with a ruler and a timer. Figure from Waschkie et al. [53] © 2011 Acta Materialia Inc. Published by Elsevier Ltd. All rights reserved.

Additionally, a multi-sided set-up can be achieved for mould designs with one or more sides of a thermally conducting material perpendicular to the cooling source or by introducing a wedge of thermal insulating material between the suspension and the cooling source resulting in **bidirectional freezing** [30, 31, 121]. Bidirectional freezing imposes a second thermal gradient on the freezing suspension, perpendicular to that due to the cooling source, and thus additional ordering of the channel orientations in the plane perpendicular to the freezing direction, as

illustrated in Figure 1.3 on page 7. Furthermore, the ordering of the structural and material gradients in the final freeze-cast can be altered by e.g. rotational freezing for fabrication of tubes [40], freezing in magnetic– [37, 121, 122] and electrostatic [121] fields and tape-freeze casting [123].

Designing a freeze-casting device is all about controlling the freezing conditions, common for all freeze-casting set-ups is therefore the need for a cooling source with temperature control. While the liquid refrigerant for the aforementioned set-ups is typically in the form of volatile liquid nitrogen or ethanol, a thermoelectric element where the applied voltage determine the temperature represents an alternative cooling source [13, 20], as illustrated in Figure 4.4.

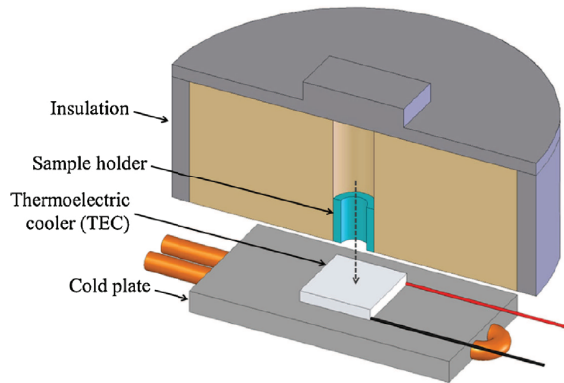


Figure 4.4: Freeze-casting set-up where the cooling source consists of a thermoelectric unit of which the temperature can be adjusted by adjusting the applied voltage. Figure from Miller et al. [13] © 2015 Elsevier Ltd. Published by Elsevier Ltd. All rights reserved.

Furthermore, a possibility of tracking the freezing front is desired. Tracking of the freezing front can be done visually by using a see-through mould made from e.g. acrylic glass and equipped with a scalebar [10, 11], as seen on Figure 4.3d). However, this requires a clear visual distinction between the solid phase and the liquid phase, which is not always the case [124], as demonstrated in Figure 3.2 on page 30. Temperature measurements of the freezing suspension, either by attaching thermocouples [22, 59] or by use of thermal infrared imaging [8], poses an alternative tracking method granted that the exact solidification temperature of the suspension is known. The solidification temperature of the suspension moreover defines the desired working range of the freeze-casting set-up. In this work, the freeze-casting device is optimized for aqueous suspensions as water is easily accessible and exerts a low vapour pressure at STP, thus, no precautions against solvent evaporation is necessary in the experimental set-up. With a solidification temperature of 273.15 K for pure water, the desired operational temperature span of the freeze-caster must therefore be in a range around this temperature.

Controlling the thermal gradient across the suspension amounts to controlling the kinetics,

i.e. the freezing front velocity, and freezing direction in the suspension and thus the resulting structural features and dimensions. The thermal gradient depends on the temperature of the cooling source, and high precision temperature control of the cooling source coupled with high spatial resolution temperature monitoring is therefore crucial in the engineering of materials by freeze-casting. The freeze-casting device presented here, was thus designed for implementation of temperature profiles for freezing control as well as measures regarding mould design for monitoring of freezing conditions.

4.2 Freeze-Casting Device

The freeze-casting device is shown in Figure 4.5. The central part of the freeze-caster is contained within the vacuum chamber (A) where the thermoelectric unit (Peltier element) for temperature control is found. The thermoelectric unit is powered by a power supply (Aim-TTi CPX 400SP)(D). A Pfeiffer turbo pump (Hicube 80 ECO)(F) is running during operation, keeping the pressure inside the vacuum chamber at 10^{-4} mbar to avoid condensation and to ensure proper performance, while a Julabo temperature bath (CF 40)(G) is connected to a heat sink on which the Peltier element is mounted. A PC (C) is connected, running control software and logging temperature measurements from the Keithley (2700 DMM, with scanner card 7700)(E).

Inside the vacuum chamber (A) is a Cu coldfinger (K) mounted on a Peltier element (Quick-Cool QC-127-2.0-15.0 accepting up to 15.5 V and 15 A)(J). The gap between coldfinger and vacuum chamber is sealed using a Teflon flange (L) and heat is transported away from the Peltier element by a heatsink (Custom Thermoelectrics WBA-3.0-0.85-CU-01)(I) connected to the Julabo. Tubes for cooling fluids and electronics are attached through port holes (H). The term *electronics* cover power supply for the Peltier element and Pt-100 elements (M) attached at both the top of the Peltier element and the top of the coldfinger, just inside the vacuum chamber, for precise monitoring and control of temperature.

4.2.1 Vacuum sealing & thermal management

The sealing of the vacuum chamber is carried out with conventional O-ring seals. The critical point of the chamber is the top sealed with a custom Teflon vacuum flange; see Figure 4.5)(F). Here, a radial seal is implemented with tolerances that allow for the Cu and Teflon parts to shrink as the temperature is decreased. As seen in Table 4.1, the Teflon flange has a much larger coefficient of thermal expansion than Cu, however, as both the O-ring and the Teflon flange are made of materials with very low thermal conductivity, the resulting contraction of the Teflon flange is comparable to or smaller than that of the Cu rod. As a result, the vacuum holds sufficiently throughout the entire specified temperature range of the device.

The heat exchanger at the bottom of the Peltier element is positioned on a steel-plate (for modest thermal conductivity) that in turn is positioned on four legs made of plastic screws

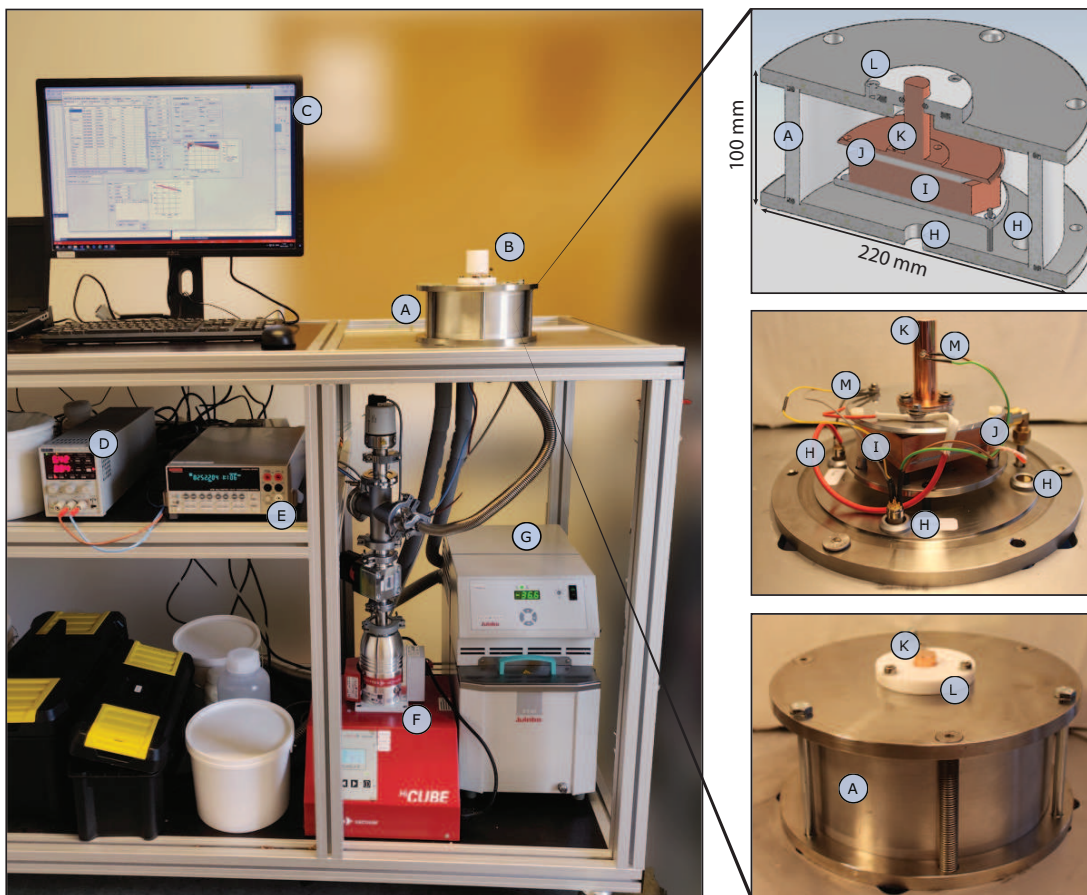


Figure 4.5: Full freeze-casting set-up. A: Vacuum chamber. B: Teflon mould mounted on coldfinger. C: PC running control and data logging software. D: Power supply. E: Keithley. F: Turbo pump. G: Julabo CF40 chiller, H: Port holes for tubing and electronics, I: Heat exchanger, J: Peltier element, K: Coldfinger, L: Teflon vacuum flange, M: Pt-100 elements. Figure revised from Paper III.

ensuring a large thermal resistance from the heat exchanger to the frame of the vacuum chamber. On top of the Peltier element a thin Al-disk is mounted, with the Cu coldfinger mounted on top. The Al-disk is clamped with plastic screws to the bottom steel plate. Choosing aluminum for the plate on top of the Peltier element is a balance between having a large thermal conductivity and a minimal thermal mass. Furthermore, Al is easier to machine than Cu. The cold-finger is made of Cu as the largest possible thermal conductivity is desired. The cooling power of the device is spent both on increasing the temperature gradient across these internal parts and to absorb the latent heat of fusion from the freezing front. Hence, the finger has been made as thin and short as possible given various room requirements in order to ensure as small a thermal mass as possible. This ensures i) a quick response of the system when the temperature is set to be changed and ii) the ability to reach the lower temperature limit set by the combined

Peltier-element and chiller in combination at the top of the Cu-finger as the combined thermal mass of the Al- and Cu-components is low relative to the latent heat of fusion at the freezing front.

4.2.2 Moulds & temperature tracking

The mould design for the freeze-caster is interchangeable for high flexibility and various freezing conditions. For now, a simple, cylindrical design was chosen. The mould walls are made of Teflon with a detachable copper bottom for optimal thermal conductivity between sample and coldfinger. Teflon mould and Cu bottom are assembled using vacuum grease for easy and quick disassembly. The mould is shown in Figure 4.6.

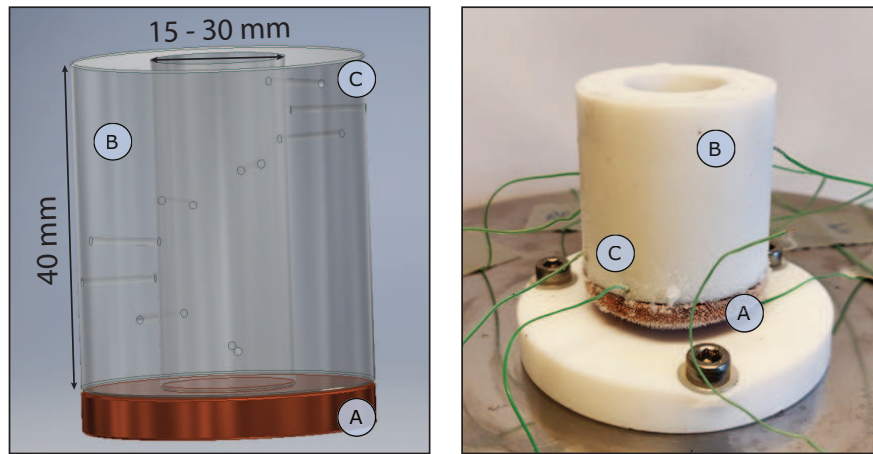


Figure 4.6: Cylindrical mould design for freeze-caster. A: Detachable Cu bottom. B: Cylindrical Teflon mould. C: Thermocouple inserts in helical pattern, 4 mm apart. Figure revised from Paper III.

Teflon has a very low coefficient of friction easing the demoulding of samples. Moreover, the thermal conductivity, k , of Teflon is also very low, see Table 4.1, thermally isolating the freezing sample from the surroundings while not cooling down faster than the sample. This prevents bidirectional freezing, i.e. where the mould walls act as a cooling source as well as the mould bottom.

The thermal contraction of Teflon is larger than that of Cu, which causes an issue with a composite mould of both materials. However, assembling the mould parts using vacuum grease allows the two materials to contract independently without tension. Moreover, the mould is kept open at the top in order to allow room for the water expanding as it transitions into ice.

The mould is equipped with a detachable copper bottom with the primary function of ensuring high thermal conductivity between the freezing sample and the coldfinger of the freeze-casting device. A thermocouple insert ($\text{Ø}1 \text{ mm} \times 4.5 \text{ mm}$ depth) for temperature monitoring and a circular 3.5 mm indentation matching the diameter of the coldfinger are drilled into the bottom of the Cu mould-part for easy mounting and demounting of the mould.

Table 4.1: Thermal properties of Teflon, copper and ice: coefficient of linear thermal expansion, α , thermal conductivity, k , and thermal diffusivity, λ .

	α [10^{-6}K^{-1}]	k [$\text{Wm}^{-1}\text{K}^{-1}$]	λ [$10^{-6}\text{m}^2\text{s}^{-1}$]
Teflon	112 - 125	0.250	0.124
Copper	17	401	111
Ice	51	2.2	1.13

As previously mentioned, the freezing front velocity – and thus the cooling rate of the coldfinger – is paramount for the resulting internal dimensions of the freeze-cast structure and temperature control and monitoring is thus vital in order to evaluate the processing of a freeze-cast structure. Thermocouple inserts ($\text{\O}1$ mm) are drilled into the Teflon mould along its height. Inserts are 9.25 mm deep leaving 0.75 mm of Teflon wall between the freezing suspension and the thermocouple, inevitably resulting in a thermal lag with regards to tracking the freezing front position. However, as the lag is assumed to be consistent for all thermocouple positions, this will in principle not affect the evaluation of the freezing front velocity, but only provide an offset to the freezing front position with respect to time. The thermocouple inserts are placed in a helical pattern along the length of the mould, as shown on Figure 4.6(C), with a 4 mm spatial resolution along the freezing direction. This pattern ensures that the thermal loss due to changes in mould wall thickness is distributed radially across the sample to avoid a significant distortion of the freezing front surface. Thermocouples type K are mounted in the inserts with thermal paste to ensure proper thermal conduction.

4.2.3 Implementation of temperature control

The control software is custom made in C# and facilitates a PID (proportional-integral-derivative) controller with a feedback loop for controlling the temperature of the coldfinger. The coldfinger is equipped with a Pt-100 element just inside the vacuum chamber as close to the freezing sample as possible; see Figure 4.5(M). The temperature at this position is continuously fed to the software and adjusted according to the PID settings to fit a given set-temperature. The set-temperature can be constant or defined to be a function of time, e.g. a linear function or an exponential function, as has been suggested for obtaining a constant freezing front velocity [59].

4.3 Freezing conditions

In order to evaluate the performance and demonstrate the capabilities and limitations of the freeze-caster, samples of water were frozen using various dynamic temperature profiles. In Chapter 5 similar conditions will be implemented and evaluated for ceramic suspensions of LCSM.

4.3.1 Implementation of temperature profiles

An exponential cooling function was chosen based on work by Stolze et al. [58, 59] and Flauder et al. [57], as described below, while constant freezing rates were chosen in the range of -1 to -20 K/min, resulting in linear temperature profiles. Under equivalent conditions, these freezing rates should yield freeze-cast ceramics with approximate constant channel dimensions in the order of $1 - 100 \mu\text{m}$ [9, 11, 45], and is thus a desirable operational range for the freeze-caster.

Stolze et al. [58, 59] derives and verifies an exponential cooling function, Equation (4.1), for maintaining a constant freezing front velocity, during directional solidification of a ceramic suspension:

$$f(t) = T_0 + \frac{H_f}{c_s} \left(1 - \exp\left(\frac{v_f^2}{\lambda_s} t\right) \right) \quad (4.1)$$

Here subscript s and f denote the solid and fluid, respectively. T_0 is the solidification temperature of the suspension, H_f is the heat of fusion, c_s is the specific heat capacity and λ_s is the thermal diffusivity, where the latter is related to the thermal conductivity, k_s , as follows: $\lambda_s = k_s / (\rho_s c_s)$.

For exponential freezing of water samples, coefficients for the exponential cooling function $f(t) = A + Be^{Ct}$ were chosen such that it fulfills Equation (4.1) with the physical properties of water at 273 K listed in Table 4.2 and $v_f = 5, 10, 15, 20 \mu\text{m/s}$, assuming that Equation (4.1) also holds true for water alone.

Table 4.2: Physical properties of water at 273 K; heat of fusion, specific heat capacity, density and thermal conductivity, respectively.

H_f	c	ρ	k
333.55 kJ kg ⁻¹	2.108 kJ (kg K) ⁻¹	920 kg m ⁻³	$2.2 \cdot 10^{-3}$ kW (m K) ⁻¹

4.3.2 Directional freezing of water samples

Samples of water were frozen using both exponential and linear freezing profiles. In order to avoid significant supercooling of water, tap water containing natural minerals was used.

The water and mould was pre-cooled in an ice-bath. The mould was then mounted directly onto the coldfinger. The mould was equipped with thermocouples while ensuring sufficient thermal contact by applying thermal paste at the contact interface between the copper bottom

and coldfinger as well as in the thermocouple inserts. Mould and sample were encapsulated in insulating foam and a styrofoam box which kept the ambient temperature below 280 K at all times. The temperature was kept constant at 275 K for 5–10 minutes before applying an either linear or exponential freezing profile. Temperature measurements were obtained until the sample was frozen solid. Three samples were frozen for each applied temperature profile in order to realize a statistically significant data set.

4.4 Evaluation of freezing conditions and performance

All temperature curves for samples frozen at various freezing rates showed a few reoccurring characteristics. The measured temperature profiles for all thermocouple positions for a sample of water frozen at -2 K/min are shown in Figure 4.7a). Small fluctuations are filtered away by a median filter in MATLAB® and temperature measurements of the thermocouple furthest away from the coldfinger was evaluated as in Figure 4.7b).

For all samples of water a super cooling followed by rapid nucleation resulted in a sudden release of latent heat, observed as a spike in temperature measurements with a temporal delay up along the sample. The spike is indicated by the arrow in Figure 4.7a). This phenomenon was also observed for suspensions of ceramic powders, as discussed in Chapter 5, however, to a much smaller degree, as the powder particulates introduces an extensive number of nucleation sites compared to the water and super cooling is thus significantly less dominating.

For pure water at 1 atm the freezing point is 273.15 K, however, for tap water and especially for water-based ceramic suspensions with both particulates and organic additives, freezing point depression will result in a lower freezing temperature. Thus, 273.15 K cannot be used as a temperature indicator for the position of the freezing front as the actual freezing point will be lower. However, when looking at the temperature profiles at various thermocouple position during freezing in Figure 4.7, a significant bump in the temperature curve for the thermocouple at 25.5 mm is evident at $T_{\text{trans}} = 271.45$ K with the equivalent time $t_{\text{trans}} = 2074.4$ s indicating an increase in the cooling rate. As the thermal conductivity of ice is four times greater than that of water, an increase in cooling rate at a given position is exactly what is expected to occur as the liquid water transitions into ice, and this bump thus indicates the transition temperature, i.e. the freezing temperature for the water sample – or the freezing temperature of the ceramic suspension in the coming chapters. Therefore, the time at which the freezing front reaches a given thermocouple position can be estimated and thereby the average freezing front velocity between two thermocouple positions can be calculated. Generally, the bump related to the transition temperature can be identified for all thermocouple positions. For practical reasons, the transition temperature is found from the temperature curve for the thermocouple furthest away from the coldfinger when freezing kinetics are evaluated for frozen samples in Section 4.4.1.

In Figure 4.7b), the second bump at time t_{solid} , evident at all thermocouple positions at the same time, indicates an increase in the cooling rate of the sample when it has completely

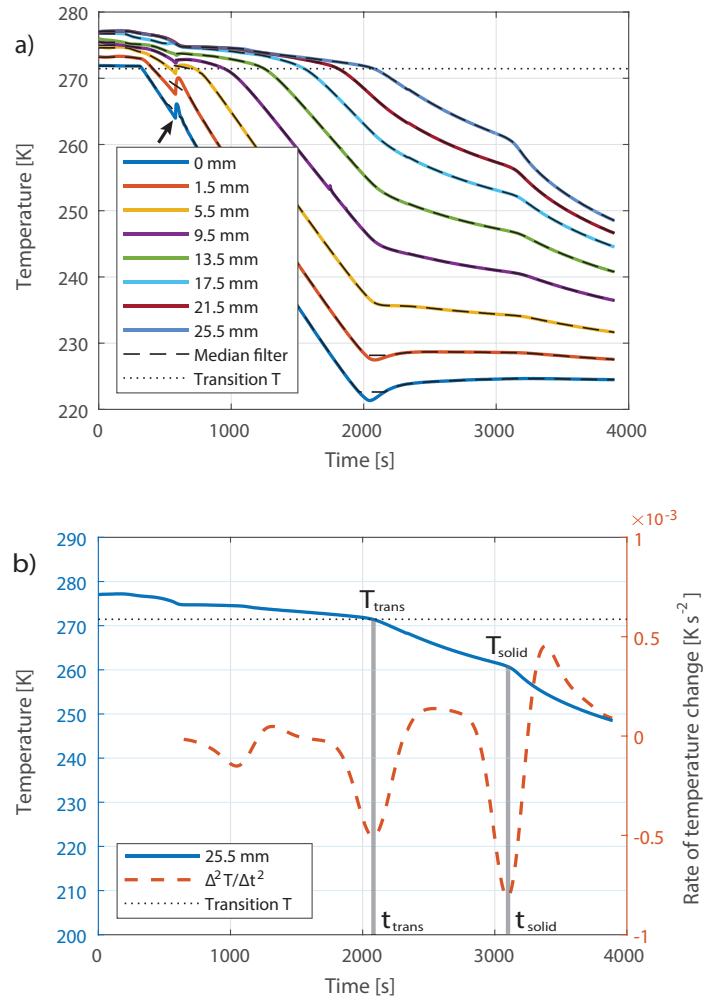


Figure 4.7: Temperature measurements at all thermocouple positions as a function of time obtained for a water sample frozen at -2 K/min. a) All temperature measurement are filtered using a median filter in MATLAB[®]. The black arrow indicates the onset of freezing with a spike in temperature due to release of latent heat upon sudden nucleation in a super cooled sample. b) The orange curve shows $\frac{\Delta^2 T}{\Delta t^2}$ for the thermocouple positioned at 25.5 mm. From peak analysis the change in cooling rate for estimating the freezing temperature, T_{trans} , and thus the freezing front position at t_{trans} as well as the total freezing time, t_{solid} , of the sample is evaluated. Figure revised from Paper III.

transitioned into ice and no more latent heat is released in the system. t_{solid} is thus the total freezing time.

In the case of samples frozen at -2 K/min, the time, t_{trans} , at which the thermocouple at the top of the mould reaches T_{trans} coincides with the coldfinger reaching the minimum temperature of the freeze-caster. 25.5 mm sample height is thus close to the capacity of the freeze-caster for samples of water frozen at this temperature profile, as the temperature of the coldfinger beyond t_{trans} no longer follows the preset temperature profile. This is illustrated in Figure 4.8, where the absolute value of the offset temperature is seen to significantly increase beyond 2000 s. The minimum temperature of ~ 220 K of the current freeze-casting device can be decreased by replacing the Julabo chiller with a chiller of lower minimum temperature thereby increasing the achievable sample height for aqueous samples.

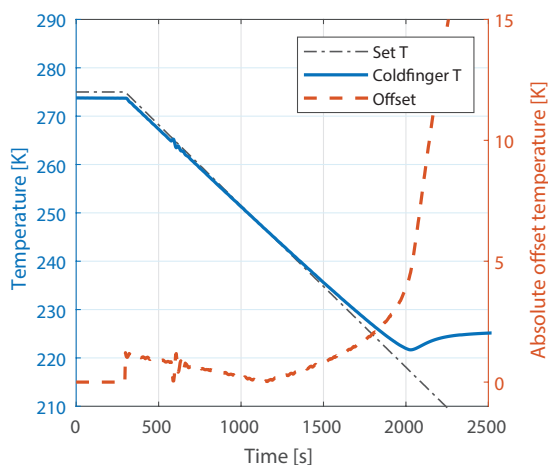


Figure 4.8: Coldfinger and preset temperature as a function of time for a water sample frozen at a constant freezing rate of -2 K/min. Eventually, the coldfinger reaches the minimum temperature of the freeze-caster in its current configuration, and the absolute offset temperature, i.e. the temperature difference between the two, significantly increases. Figure revised from Paper III.

Furthermore, the current maximum temperature of the freeze-casting device is defined by the maximum operational temperature of the Peltier element of 440 K, making it also suitable for freeze-casting of suspensions with alternative solvents such as camphene [13] or *tert*-butyl alcohol [14], with solidification temperatures of 325 K and 298 K, respectively. Both are well within the operational temperature span of the freeze-casting set-up presented here.

4.4.1 Linear and exponential freezing profiles

By evaluating measured temperature curves as described in the previous section, the capacity of the freeze-caster can be evaluated for various dynamic freezing profiles. Estimated freezing front velocities and maximum heights for water samples are given in Figure 4.9 for both linear

freezing profiles (a–b) and exponential freezing profiles (c–d).

As the bottom part of the suspensions typically underwent super cooling followed by sudden nucleation, as previously discussed and indicated by the arrow on Figure 4.7a), large deviations of freezing front velocities were found for velocities estimated close to the copper bottom. Only freezing front velocities from a distance of 7.5 mm from the copper bottom are thus plotted on Figure 4.9a,c).

As previously discussed, t_{solid} indicates the time at which the sample is completely frozen. For greater freezing rates this occurs after the coldfinger has reached the minimum temperature of the set-up. The maximum height in Figure 4.9b,d) is thus estimated as the height of the frozen part of a freezing sample at the time where the offset between the temperature of the coldfinger and the preset temperature profile exceeds 3 K, and is thus the maximum sample length that can be achieved at a given temperature profile.

For the purpose of freeze-casting where a constant freezing front velocity throughout a specific sample length is desired, here 25 mm, only linear freezing profiles with cooling rates of -1 K/min and -2 K/min or exponential freezing profiles with estimated velocities of 5 $\mu\text{m/s}$ and 10 $\mu\text{m/s}$ met these criteria. Regarding the latter, samples of *estimated* freezing front velocities of 5 and 10 $\mu\text{m/s}$ almost matched the measured *actual* freezing front velocities, validating Equation (4.1). Additionally, applying exponential temperature profiles versus linear temperature profiles appear to have a slight influence on the consistency of the freezing front velocity throughout the samples, however, a larger sample batch is required to fully confirm this assumption.

From Figure 4.9 it appears that the maximum freezing front velocity maintainable over the length of a 25 mm sample is ~ 15 $\mu\text{m/s}$ for the current freeze-caster configuration. As less latent heat will have to be removed during freezing from a ceramic suspension as a given volume fraction is substituted with ceramic powder, it is expected that the maximum freezing front velocity would be slightly greater for a ceramic suspension. We will return to this assumption in Chapter 5, where a similar evaluation of the performance of the freeze-caster is presented for ceramic suspensions.

The capacity of the current freeze-caster set-up could be improved by replacing the chiller, allowing for greater freezing front velocities and larger samples. The set-up presented here is prepared for liquid nitrogen as a cooling fluid if larger cooling rates capacities are needed in the future.

4.4.2 Implementation of feedback mechanism

The current freeze-caster configuration allows for implementation of various dynamic temperature functions for the temperature of the coldfinger during freeze-casting. These can be derived from modeling, experimental data or empirical knowledge. A possible future upgrade of the freeze-casting device presented here is to implement a direct feedback loop while freezing. Monitoring the freezing front with an appropriate temporal and spatial resolution while continuously

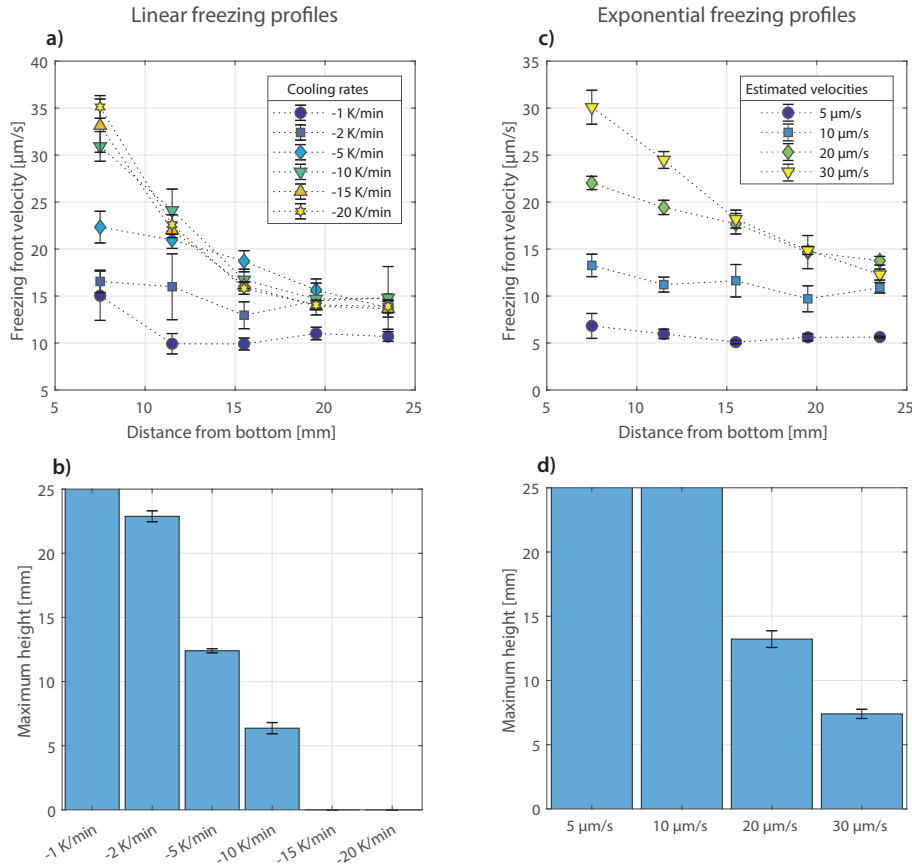


Figure 4.9: Evaluated freezing front velocities and estimated maximum height based on $|T_{offset}| < 3$ K for samples frozen using linear (a–b) or exponential (c–d) temperature profiles. Note that an indicated maximum sample height of 25 mm in (b,d) is merely the maximum measurable height. Actual maximum sample heights are assumed greater. Figure revised from Paper III.

adjusting the set temperature could enhance the accuracy of reaching the desired temperature profile.

4.5 Summary

A freeze-casting device utilizing a thermoelectric element for high precision temperature control for implementation of dynamic freezing conditions was presented. The design of the device was based partly on practical experience with two other freeze-casting set-ups and partly based on a realization from studying set-ups described in literature. Namely, that precise and dynamic temperature control with high spatial resolution tracking of the freezing front is essential. The performance of the device was evaluated by directional freezing of water samples using both linear and exponential freezing profiles.

The freezing front was successfully tracked by measuring the temperature gradient along the sample height using thermocouples directly mounted in the freeze-casting mould. Using the varying intrinsic thermodynamical properties of water in liquid and solid form the freezing front was easily identified, allowing for a straightforward estimation of the freezing front velocity. A similar analysis of measured temperature profiles for ceramic suspensions is used throughout the thesis for evaluation of freezing conditions. The maximum freezing front velocity maintainable over the length of a 25 mm water sample was $\sim 15 \mu\text{m/s}$ for the current freeze-caster configuration.

The current operational temperature range of the freeze-caster is $\sim 220 - 440 \text{ K}$. The performance and capacity of the freeze-casting device can be enhanced by implementation of i) a direct feedback loop for immediate adjustment of the freezing profile, and ii) liquid nitrogen as cooling fluid.

Dynamic freezing conditions

The freeze-caster presented in Chapter 4 allows for implementation of dynamic freezing conditions, and so, this chapter discusses the effect of dynamic freezing conditions during freeze-casting of LCSM ceramics. Specifically, dynamic conditions in the form linear temperature profiles and exponential temperature profiles of the cooling source – similar to those discussed in Chapter 4 – are investigated. Additionally, the general freezing procedure for freeze-casting of ceramic LCSM suspensions using the freeze-casting device described in Chapter 4 is presented and considerations regarding reproducibility of freeze-cast ceramics are briefly discussed.

5.1 Modeling approaches for structural homogeneity

With the final goal of freeze-casting structures suitable as regenerator, homogeneity of microchannel dimensions throughout the sample length is crucial. As discussed in Chapter 1, regarding freezing conditions, the final pore size in freeze-cast ceramics directly depends on the freezing front velocity. Presumably, achieving a constant pore size – or width of microchannels – in a freeze-cast sample is thus equivalent of achieving a constant freezing front velocity throughout the suspension during the entire freezing process.

Based on this assumption, modeling of the thermodynamic phenomena which control the progression of the freezing front during freeze-casting of a particulate suspension, have been used to propose temperature conditions, and more specifically, temperature functions of the cooling source in order to achieve constant freezing front velocities.

A common approach, amongst others pursued by Wegst et al. [51] and Waschkes et al. [10], considers the latent heat which is continuously released from the slab of water transitioning into ice at the freezing front, i.e. at the phase boundary between solid and liquid, and the increasing thermal resistance of the growing solid part of the sample when transporting the latent heat to the cooling source. As the heat of fusion of water is much greater than the specific heat capacity of ice (see Table 4.2 page 53), the continuous removal of latent heat far dominates that of continuously decreasing the temperature of the solid phase. The position of the freezing front can thus be solved as a quasi-static approximation to the Stefan problem of a moving phase boundary during solidification [10, 51, 125]. Keeping the freezing front velocity constant yields a linear proportionality between the temperature of the cooling source and time*, suggesting that a linearly decreasing temperature of the cooling source, i.e. a constant

*For a detailed derivation of this solution, the reader is referred to Wegst et al. [51]

freezing rate, yields a constant freezing front velocity [10, 51]. By combining linear temperature profiles of the cooling sources with a double-sided set-up, as previously mentioned in Chapter 4 (see Figure 4.3 on page 47), keeping the second cooling source at 0 °C throughout the freezing procedure, Waschkie et al. [10] achieved constant freezing front velocities resulting in almost constant lamellae spacing, only increasing by 6 – 8 %/cm over a sample length of 3 cm.[†] Many freeze-casting studies follow the approach of Wegst et al. [51] and Waschkie et al. [10] and implements linear temperature profiles, but as Scotti and Dunand [56] summarizes, an increase in lamellae spacing, or pore width, throughout the sample length is generally observed for freeze-casts frozen using linear temperature profiles.

Bareggi et al. [55] includes convection and conduction effects in the suspension and from the surroundings in solving the moving boundary phase problem and assumes parabolic temperature profiles of the cooling source. Although, Bareggi et al. [55] finds that the implementation of parabolic cooling functions greatly increases the steady-state zone, i.e. the zone in which ice-crystals are aligned and grow along the thermal gradient (see Figure 1.4 on page 10), they do not report structural features as a function of sample height for various parabolic temperature profiles. They do, however, state the observation that an increasing freezing rate appears to decrease the extent of increasing pore size throughout the freeze-cast ceramics.

In continuation, Flauder et al. [57] proposes a general solution to the moving boundary phase problem, yielding an exponential temperature profile of the cooling source for upholding a constant freezing front velocity. The temperature function is subsequently derived by Stolze et al. [59] and is introduced in Chapter 4 as Equation (4.1) on page 53. This solution assumes a constant freezing front velocity; and a one-directional heat transfer only across the frozen part of the sample; as the temperature of the liquid part of the sample is assumed to be very close to the transition temperature [57]. Flauder et al. find constant pore sizes throughout a sample length of 20 mm for a pre-set freezing front velocity of 20 $\mu\text{m/s}$ in freeze-cast β -tricalcium phosphate.

Thus, in this chapter, the structural homogeneity of LCSM freeze-casts frozen using linear cooling functions are compared to freeze-casts frozen using the exponential cooling function suggested by Flauder et al. [57, 59], as given in Equation (4.1).

5.2 Linear and exponential freezing profiles

Equation (4.1) describes the temperature as a function of time of the cooling source for achieving a constant freezing front velocity, v_f , in an aqueous ceramic suspension with heat capacity, c_p and thermal diffusivity, λ_s , of the frozen suspension. The heat capacity and thermal diffusivity of the suspension depends on the thermal properties and mass fraction of constituents, in this

[†]The increase per sample length summarized here, are estimated from Figures 10 and 11 in Waschkie et al. [10].

case simplified to ice and LCSM.[‡] Thermal properties of LCSM and water is listed in Table 5.1.

Table 5.1: Physical properties of water and LCSM at 273 K; mass fraction in suspensions, heat of fusion, specific heat capacity, density and thermal conductivity, respectively.

	Mass fraction, x	H_f kJ kg ⁻¹	c kJ (kg K) ⁻¹	ρ kg m ⁻³	k 10 ⁻³ kW (m K) ⁻¹
Ice	0.31	333.55	2.108	920	2.2
LCSM	0.69	–	0.525 ^a	6095.9 ^b	2 ^c

^aDinesen et al. [81] ^bDetermined by gas pycnometry, see section 3.1.1 ^cTurcaud et al. [126]

When evaluating the thermal diffusivity, $\lambda_s = k_s/(\rho_s c_s)$, of the frozen LCSM/ice sample in Equation (4.1), the rule of mixtures [13] was applied and it is simply calculated as the sum of the properties weighed by the mass fraction, x , of the components in the sample according to Flauder et al. [57] and Stolze et al. [59]. That is:

$$\rho_s c_s = (\rho_{\text{ice}} x_{\text{ice}} + \rho_{\text{LCSM}} x_{\text{LCSM}})(c_{\text{ice}} x_{\text{ice}} + c_{\text{LCSM}} x_{\text{LCSM}}) \quad (5.1)$$

Similar, assuming that the ice and LCSM particles in the frozen sample are completely separated into well-aligned lamellae parallel to the thermal gradient, the thermal conductivity of the frozen sample was also calculated according to the rule of mixtures as:

$$k_s = k_{\text{ice}} x_{\text{ice}} + k_{\text{LCSM}} x_{\text{LCSM}} \quad (5.2)$$

However, as discussed by Flauder et al. [57] and Waschies et al. [10], this is probably an overestimation of the actual thermal conductivity, as the LCSM is in the form of a packed bed of particulates, all surrounded by both a thin film of polymer additives (binders and dispersants) and ice. Thus, the LCSM phase is far from pure and uniform. A proper estimation of the thermal conductivity taking into account the geometry and composition of the packed particles and ice structure, or a measurement of the thermal conductivity of the frozen suspension in order to implement an exponential temperature function of the cooling side truly in accordance with Equation (4.1) as derived by Stolze et al. [59], is thus an obvious continuation of this work. Although, given that the thermal conductivity of LCSM and water are actually very similar, the effect of the error is expected to be small.

Nonetheless, assuming that the thermal conductivity of the frozen suspension can be estimated as in Equation (5.2) for an exponential cooling function:

$$f(t) = A + B e^{Ct} \quad (5.3)$$

coefficients A , B and C fulfilling Equation (4.1) and (5.3) for pre-set freezing front velocities are given in Table 5.2.

[‡]A more thorough account would additionally include the thermal properties weighed by mass fractions of ionic and polymer species from suspension additives such as dispersant and binder systems.

Table 5.2: Calculated coefficients for Equation (5.3) in fulfilment of Equation (4.1), for pre-set, constant freezing front velocities for LCSM aqueous suspensions.

Pre-set freezing front velocities	A	B	C
$\mu\text{m/s}$	K	K	10^{-4} s^{-1}
5	374.68	-101.53	0.553
10	374.68	-101.53	2.211
15	374.68	-101.53	4.976

Exponential cooling functions are compared with linear cooling functions of constant freezing rates, all shown in Figure 5.1. The constant freezing rates of -0.5 K/min , -1.5 K/min and -2.5 K/min were chosen based on the capacity of the freeze-caster as discussed in Chapter 4.

As is seen from Figure 5.1, the exponential cooling functions show an approximate linear behaviour – for a lower thermal conductivity of the frozen suspension a more significant exponential decrease in freezing rate would be evident.

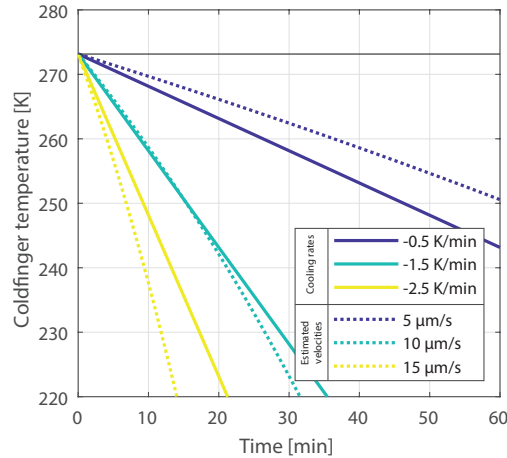


Figure 5.1: Linear and exponential temperature profiles, where the latter is defined by Equation (5.3) and Table 5.2.

5.3 Dynamic freeze-casting of ceramics

5.3.1 General freezing procedure

The general procedure for freezing of ceramic suspensions using the freeze-caster described in Chapter 4 follows below. All ceramic freeze-cast samples presented in this thesis follows the freezing procedure described here unless otherwise specified. The general preparation of

ceramic suspensions and the following processing of frozen and sintered samples are described in Chapter 3.

The ceramic suspension and mould was pre-cooled in an cooling bath of water and ice. Thus, both mould and suspension had a core temperature of approximately 0 °C before mounting thereby ensuring similar initial conditions of all freezing experiments. If moulds had been pre-cooled in e.g. a freezer at temperatures below the freezing point of water, the mould walls would effectively provide a second cooling source imposing a second thermal gradient on the suspensions resulting in bi-directional freezing conditions, as previously described in section 4.1. Upon pre-cooling, the mould was mounted directly onto the coldfinger and equipped with thermocouples. Sufficient thermal contact was ensured by applying thermal paste at the contact interface between the copper bottom and coldfinger as well as in the thermocouple inserts. Meanwhile, bubbles were removed from the ceramic suspension either using sonication or by vacuum and the de-aired ceramic suspension was then transferred to the mould. Mould and sample were encapsulated in insulating foam and a styrofoam box equipped with cooling elements which kept the ambient temperature below 280 K at all times. The temperature was kept constant at 275 K for 5–10 minutes before applying an either linear or exponential freezing profile. Temperature measurements were obtained until the sample was frozen solid.

5.3.2 Freezing conditions and capacity

The freezing front velocities and maximum height of freeze-cast ceramic samples are evaluated as described in Chapter 4, section 4.4, similar to that of water samples. In summary, freezing front velocities are averaged over 4 mm calculated from the time it takes the freezing front to move between two thermocouple positions. The freezing front is identified by the change in cooling rate at the thermocouple position due to the difference in thermal conductivity of liquid and solid water. Additionally, the capacity of the freeze-caster is moreover evaluated by the maximum sample height, which is the height of the frozen sample at the time the freeze-caster no longer can uphold the set temperature profile. The maximum heights are summarized in Table 5.3. Figure 5.2 show the freezing front velocities as a function of sample positions measured from the bottom. Each plotted data-set – or freezing condition – represents one sample measurement. The average transition temperature, as defined in Chapter 4, section 4.4, was found to be 271.3 ± 0.7 K for LCSM suspensions.

The measured freezing front velocities appear to be more or less consistent for samples frozen by exponential cooling functions, Figure 5.2c). However, so does the measured freezing front velocities for samples frozen using constant cooling rates, Figure 5.2a). Keeping in mind, that only one sample is frozen per freezing condition, additional samples will have to be frozen under the same conditions in order to determine whether or not a significant difference in freezing front velocities can be measured using the current tracking of the freezing front with thermocouples.

As discussed in Chapter 4, the maximum freezing front velocity maintainable over the length of a 25 mm water sample is $\sim 15 \mu\text{m/s}$. For ceramic samples, it appears that a more or less

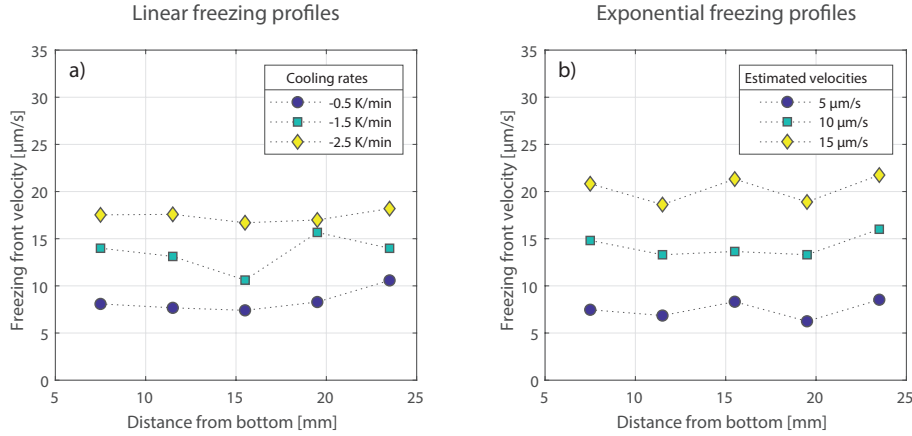


Figure 5.2: Evaluated freezing front velocities for ceramic samples frozen using a) linear or b) exponential temperature profiles from suspensions with a solid load of 30 vol%.

consistent freezing front velocity of $\sim 20 \mu\text{m/s}$ is maintainable over the length of a 25 mm sample, for both samples frozen using linear and exponential cooling functions, as in Figure 5.2a) and b), respectively. As mentioned, this is assumed to be due to the decrease in latent heat which have to be removed from the freezing sample as $\sim 69 \text{ wt\%}$ of the sample is now ceramic. As the freezing front velocity is increased slightly, so is the capacity of the freeze-caster, in the sense that more sample will be frozen before the device reaches its minimum temperature of 220 K and thereafter no longer can uphold consistent freezing conditions.

5.3.3 Structural features and homogeneity

Structural features of densified, freeze-cast LCSM ceramics such as pore size, wall size, macroporosity and specific surface area are given as a function of sample height in Figure 5.3. All parameters for a given freezing condition are averaged by image analysis of three SEM micrographs per sample position.

Even though freezing front velocities in Figure 5.2a) and b), appear to be more or less consistent, for all samples, the pore size – and wall size and thus also the structural wavelength, the latter being the sum of the first two – increase throughout the sample lengths, as evident from Figure 5.3. The percentage increase in pore size per sample length is summarized in Table 5.3. For samples frozen at both linear and exponential cooling rates, the same trend of increasing pore sizes throughout the samples are observed, however, when evaluating the percentage increase of pore size in Table 5.3, the effect appear to be less significant for the samples frozen using exponential cooling profiles. This indicates that the implementation of increasing freezing rates in the form of exponential cooling functions at least to some degree counteracts the increase in pore size.

Additionally, the percentage increase in pore sizes per sample length as reported in Table 5.3

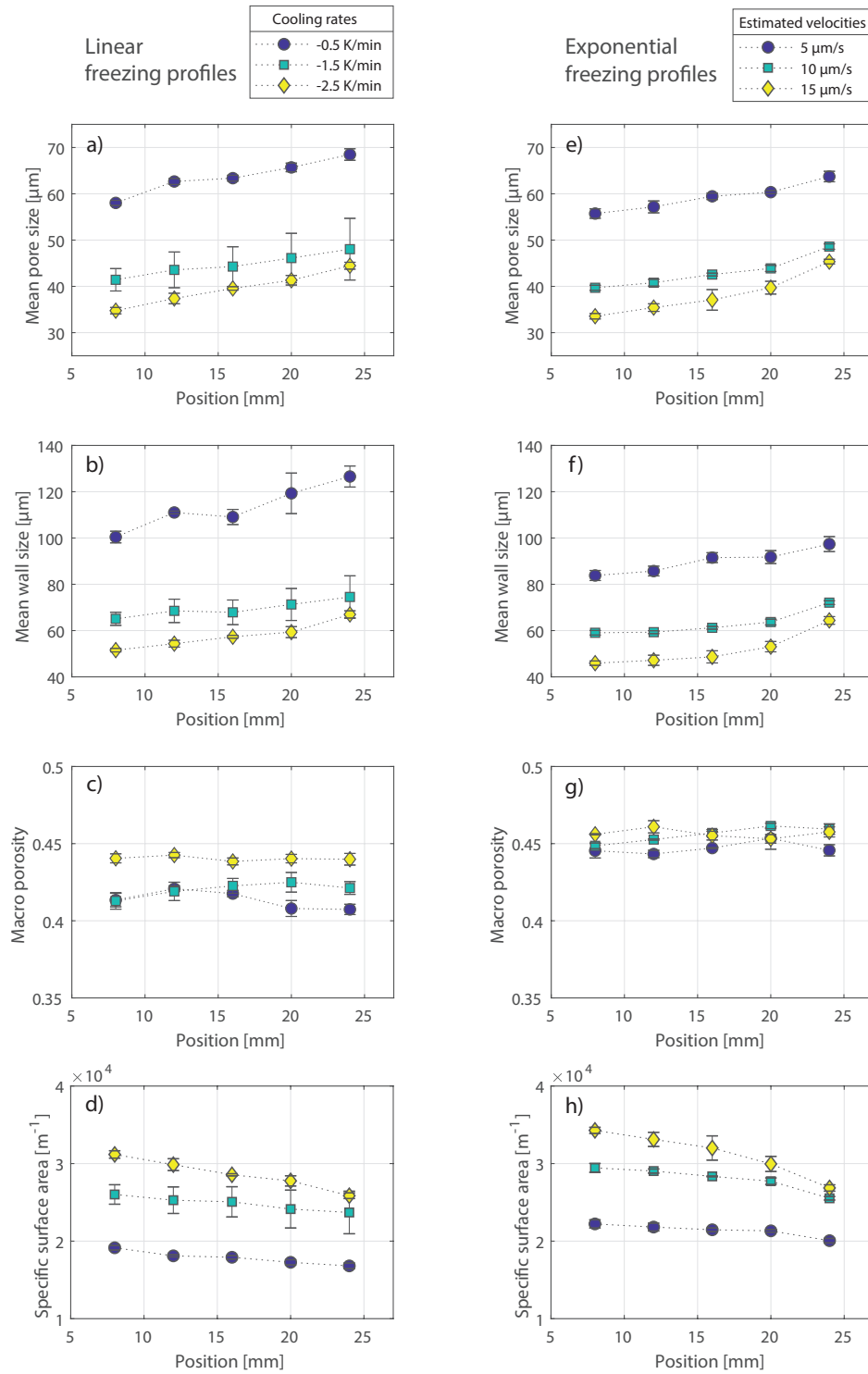


Figure 5.3: Structural features – from top to bottom; pore size; wall size; macroporosity; and specific surface area – of LCSM freeze-casts frozen using linear freezing profiles (a–d) and exponential freezing profiles (e–h) from suspension of 30 vol% solid load.

are comparable in magnitude to those referenced earlier in this chapter by Waschkies et al. [10] for structures frozen using a double-sided set-up.

From Figure 5.3 it appears that the porosity of freeze-cast samples is independent on the evaluated freezing conditions. This is in accordance with studies showing that for freeze-cast structures, the total porosity only depends on the solid load of the suspension and sintering temperature during densification [5, 8, 11, 48]. More specifically, the porosity in the green body is the voids remaining after the solvent has been sublimated, and thus directly depend on the volume ratio between solid and solvent. Upon sintering, inter-particle porosity – i.e. microporosity in the walls – is removed to a given degree depending on the temperature during densification [5, 8, 113], as discussed in Chapter 3.

Additionally, the tortuosity also appears unaffected by the changing freezing conditions. Tortuosity for freeze-cast ceramics have been found to depend on the suspension solvent [13] – changing tortuosity due to altered suspension properties will be discussed further in Chapter 6 and 7.

Table 5.3: Summary of dynamically frozen ceramic samples. Freezing conditions of either constant cooling rates or estimated freezing front velocities – i.e. linear or exponential freezing profiles, respectively – measured freezing front velocity, averaged pore size and pore increase per sample length, average porosity and calculated average tortuosity. All averaged values are given with their respective standard deviations and are averaged over the a sample length up until the evaluated maximum sample height.

Freezing conditions		v_f $\mu\text{m/s}$	H_{max} mm	Pore size μm	Increase %/cm	Porosity %	τ –
–0.5	K/min	7.9 ± 0.4	25.5+	62.4 ± 3.2	11.1	42.1 ± 0.6	1.75 ± 0.14
–1.5		13.3 ± 2.1	24.4	43.8 ± 1.9	9.5	42.0 ± 0.4	1.75 ± 0.31
–2.5		17.2 ± 0.4	20.1	38.3 ± 2.8	15.8	44.1 ± 0.2	1.62 ± 0.40
5	$\mu\text{m/s}$	7.2 ± 0.9	25.5+	58.2 ± 2.1	6.9	44.7 ± 0.4	1.69 ± 0.07
10		13.8 ± 0.7	23.2	41.7 ± 1.9	8.8	45.4 ± 0.7	2.07 ± 0.66
15		20.3 ± 1.4	15.4	35.4 ± 1.8	13.3	45.6 ± 0.4	1.68 ± 0.34

Averaged pore sizes as a function of freezing front velocity for samples frozen using various linear freezing profiles or exponential freezing profiles are given in Figure 5.4 with corresponding cooling rates or *estimated* freezing front velocities in the legend. As is evident from the figure, the mean pore size strongly depends on the freezing front velocity, decreasing in size with an increase in freezing rate, achieving channel widths in the range $\sim 35 - 65 \mu\text{m}$. Pore size and freezing rate appear to be inversely proportional. Given that the wall size is proportional to the pore size throughout the sample length, and given that the structural wavelength is the sum of the two, the structure of freeze-cast LCSM ceramics described in this chapter thus follow the inverse proportionality between structural wavelength and freezing front velocity described by

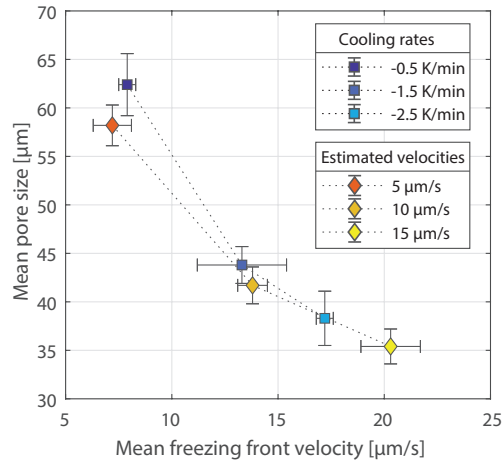


Figure 5.4: Mean pore size as a function of mean freezing front velocity. Figure partly revised from Paper III.

Equation (1.3) and discussed in Chapter 1.

As the effect of implementing exponential freezing profiles compared to linear freezing profiles is insignificant – at least under the conditions described in this chapter – the latter is generally used throughout the remainder of this thesis. The structural differences of freeze-cast ceramics frozen using linear freezing profiles and static conditions, i.e. a constant temperature of the cooling source, is investigated and discussed further in Chapter 6. For now, one final general consideration regarding the conditions of freeze-casting LCSM ceramics have to be addressed.

5.4 Considerations regarding reproducibility

Reproducibility of freeze-cast ceramics – and within material science in general – is crucial for the application as functional materials. With low reproducibility a larger scale production of materials with the same e.g. structural features is not guaranteed, which is an absolute no-go for industrial production but also problematic for lab-scale testing. E.g. in this work, a range of processing conditions and freezing conditions are investigated as levers for achieving and fine-tuning specific structural features of freeze-cast specimens; features that then again are assumed to influence the flow properties in the freeze-cast microchannels. As of writing this thesis, to the best of my knowledge, only one study has done a thorough statistical analysis of reproducibility of freeze-cast zirconia ceramics. Naleway et al. [38] fabricated a total of 24 samples from suspensions of three different solid loads; i.e. a total of eight samples of each composition. Using a one-way ANOVA test they found a statistically significant variability for all samples by evaluating structural features – quantified by manually fitting ellipses in SEM

micrographs yielding pore width, length, aspect ratio and area – and mechanical properties – mechanical strength and modulus by compression testing along the freezing direction. Thus, even samples from the same suspension composition were found to significantly vary from one another.

However, as discussed in Chapter 3 both suspension preparation and post-processing of samples involve many steps that may vary greatly from lab to lab, e.g. in the case of the manual fitting of ellipses to SEM micrographs, this may even vary from individual to individual.[§] Additionally, as summarized in Chapter 4, the varying design features of freeze-casting set-ups are many-fold. Further assessment of reproducibility of freeze-cast ceramics is thus greatly needed.

Assuming that reproducibility depends on consistent suspension preparation, freezing conditions and post-processing of freeze-cast specimens, in this work, the individual steps of each procedure was initially decreased as much as possible. E.g. for a standard suspension recipe, as few additives as possible was added, while a careful pre-cooling of moulds and suspensions as well as consistent ambient conditions was always ensured during the freezing step. In this work, where freeze-casting is used as a way of producing flow channels in a magnetocaloric medium, good reproducibility is thus evaluated by the consistency and homogeneity of structural features of the channels across presumable identical samples. To make a preliminary evaluation the reproducibility of LCSM freeze-cast ceramics prepared using the freeze-caster, two presumably identical suspensions were prepared and processed under presumably identical conditions over two days, yielding a total of five freeze-cast samples. It must be emphasized, that results and conclusions presented in this chapter are only preliminary, as five samples are too few to do a proper statistical analysis evaluating whether the samples are significantly different or not. However, it is still deemed enough to indicate and possibly identify and clarify the most critical processing steps in achieving multiple freeze-cast of consistent structural features. The preparation of suspensions follow the general procedure for preparation of LCSM aqueous suspensions used throughout this work:

Two suspensions, **I** and **II**, was prepared from 30 vol% LCSM powder in MiliQ water with the addition of 2.5 wt% DURAMAX™ D-3005 dispersant and dropwise 1M nitric acid until a neutral pH had been reached in order to achieve a stable suspension. The suspensions were prepared in parallel, but of varying total amounts. Both suspensions were homogenized for 48 hours on the same low energy ball mill with only a few alumina mixing balls (Ø10mm). The pH was adjusted to 7.34 and 7.35, respectively, by additional dropwise addition of 1M nitric acid and 2 wt% binder, DURAMAX™ B-1022, was added to both suspensions followed by additional 24 hours of homogenization on the same low energy ball mill. After a total of 72 hours of ball milling, the median particle size was measured for both suspensions, yielding $d_{50}^I = 1.2\mu\text{m}$ and $d_{50}^{II} = 0.8\mu\text{m}$.

Samples were frozen following the general procedure described in section 5.3.1 on two consec-

[§]From personal experience, for a single individual, this even varies with the amount of caffeine in the bloodstream.

utive days. On *Day 1*, three samples – A, B and C – were frozen; the first two from suspension **I** and the latter from suspension **II**. Remaining suspensions were left on the low energy ball mill overnight without any mixing balls in the suspensions. Additional two samples – D and E, suspension **I** and **II**, respectively – were frozen the following day, *Day 2*. All samples were dried and sintered simultaneously as described in section 3.2.3, page 31.

SEM micrographs of cross sections perpendicular to the freezing direction of all samples, A–E, are shown in Figure 5.5. Even without quantification of the morphology, a significant visual difference is present in the structural features of the channels, as the structures frozen from suspension **II** appear to have many more dendrites, struts and ceramic bridges than the samples from suspension **I**. Meanwhile, no obvious visual difference is evident between samples frozen on *Day 1* compared to those frozen on *Day 2*.

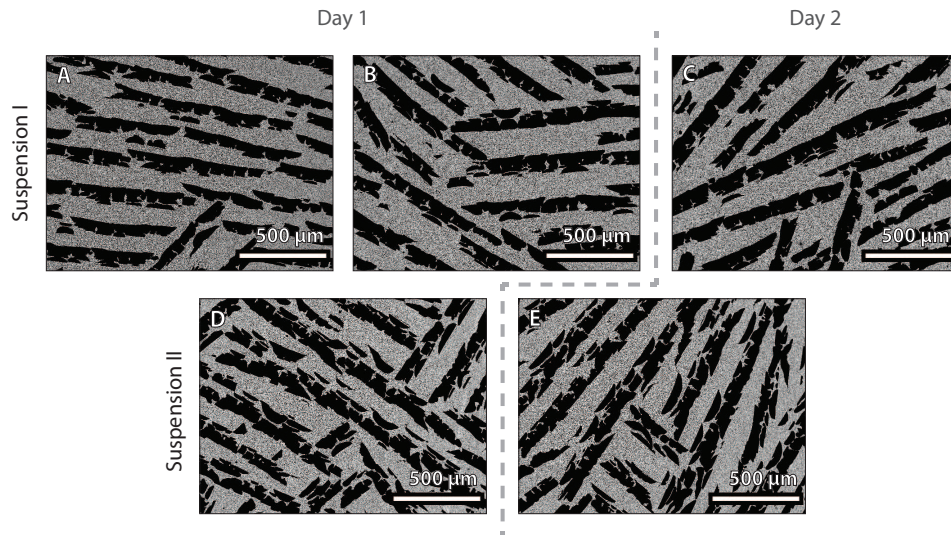


Figure 5.5: SEM micrographs of freeze-cast samples frozen from two presumably identical suspensions, **I** and **II**, all frozen at a similar freezing conditions with a constant cooling rate of -1 K/min, on two consecutive days, *Day 1* and *Day 2*. Micrographs were obtained at cross sections perpendicular to the freezing front at a sample height of 12 mm.

Evaluation of the freezing conditions, as described in section 4.4, and structural features by image analysis of SEM micrographs, as described in section 3.3, yield a similar conclusion; namely that the pore and wall size is apparently different between the two suspensions, when considering one standard deviation, as summarized in Table 5.4.

Meanwhile, no apparent difference is seen for freezing conditions given that the measured freezing front velocity, v_f , and transition temperature, T_{trans} , appear to be independent of both suspension number and casting day. Additionally, so is the case for porosity and tortuosity, τ .

Increase in dendrites and ceramic bridges have generally been observed for freeze-cast ceramics prepared from high ceramic loads [29] or altered suspension properties due to changes

Table 5.4: Summarization of evaluated freezing conditions and measured structural features of freeze-cast samples frozen from two apparently identical suspensions, **I** and **II**, over two consecutive days, *Day 1* and *Day 2*. All samples are frozen using constant cooling rates of -1 K/min. Freezing conditions are evaluated as described in section 4.4, while structural parameters are averaged over the full sample length (omitting the bottom 4 mm) from image analysis of SEM micrographs, as described in section 3.3. The listed *Porosity* is thus the macro- or channel porosity. The tortuosity, τ , was calculated from SEM micrographs obtained at a single cross section of 12 mm from the sample bottom. All averaged values are given with one standard deviation.

	Freezing conditions			Structural features					
	V_f $\mu\text{m/s}$	H_{max} mm	T_{trans} K	Pore size μm	Increase %/cm	Wall size μm	Porosity %	τ —	
I	Day 1	11.6 ± 1.3	$25.5 +$	271.0	61.6 ± 4.5	15.4	109.3 ± 4.7	39.0 ± 0.8	1.72 ± 0.57
	Day 1	11.7 ± 2.9	$25.5 +$	271.0	63.0 ± 2.8	9.2	116.5 ± 6.5	38.3 ± 0.6	1.95 ± 0.31
	Day 2	11.7 ± 1.4	$25.5 +$	270.9	65.3 ± 3.0	10.0	113.1 ± 5.8	39.1 ± 0.1	1.96 ± 0.42
II	Day 1	10 ± 1.4	$25.5 +$	271.4	50.4 ± 1.4	5.3	81.5 ± 1.4	43.4 ± 0.3	2.12 ± 0.62
	Day 2	11.3 ± 1.3	$25.5 +$	270.9	52.0 ± 0.7	2.7	84.5 ± 1.4	43.3 ± 0.7	1.95 ± 0.46

in viscosity or pH [29, 33]. The latter was presumably consistent for both suspension **I** and **II**, however, the viscosity was not measured. Nonetheless, both viscosity and pH depends on the suspension compositions. In this case, it is thus assumed, that inconsistency in the preparation of the suspensions have led to evident differences in the pore and wall sizes of the freeze-cast ceramics.

For a future thorough evaluation of the reproducibility of freeze-cast ceramics, evaluating the critical steps of possible inconsistency during the entire processing route is suggested. Thus, significant differences in e.g. suspension properties or freezing conditions can possibly be correlated to significant differences in structural features of the freeze-cast ceramic. E.g. in this case, a valuable addition to the characterization of the suspension properties would have been a measurement of rheological properties, e.g. the suspension viscosity, or perhaps the zeta potential of particles in the suspension. Although, the latter would require a dilution of the suspensions, introducing an additional probable step of inconsistency regarding reproducibility. Additionally, a much greater sample population is required to perform a proper statistical analysis.

Based on the results presented in this section, all freeze-cast samples presented throughout this thesis was prepared in batches, such that each experimental hypothesis was evaluated from the same batch of freeze-casts. E.g. all freeze-cast structures compared in section 5.3 of this chapter were prepared from the same LCSM suspension and post-processed simultaneously. Likewise is the case for structures presented throughout the remainder of the thesis unless otherwise clearly specified. Conclusions drawn in this work regarding correlations between processing and final structural features of freeze-cast LCSM are thus expected to hold.

5.5 Summary

Dynamic freezing conditions in the form of linear and exponential temperature profiles of the cooling source, with the purpose of upholding constant freezing front velocities, were investigated for freeze-cast LCSM ceramic using the freeze-caster presented in Chapter 4. However, no significant influence of exponential freezing functions compared to linear freezing functions were observed, as the freezing front velocities as well as structural features appeared more or less consistent for both procedures.

Regarding the capacity of the freeze-caster, a more or less constant freezing front velocity of $\sim 20 \mu\text{m/s}$ – for both linear and exponential temperature profiles – was maintained over the length of a 25 mm sample. This is 30 % faster than the maximum freezing front velocity of pure water samples. Although, an increase in pore size of 6.9 – 15.8 %/cm was still observed, however, in the best case these results are comparable to literature results from a double sided freeze-casting set-up [10].

Implementing linear freezing profiles and exponential freezing profiles with freezing front velocities 6 – 21 $\mu\text{m/s}$ resulted in LCSM ceramics with lamellar microchannels with pore widths of $\sim 35 - 65 \mu\text{m}$. The structure of freeze-cast LCSM ceramics described in this chapter was

found to follow the inverse proportionality between structural wavelength and freezing front velocity described by Equation (1.3) in accordance with freeze-casting literature. Meanwhile, porosity and tortuosity were found to be independent on freezing conditions.

As no apparent difference was evident between using linear and exponential temperature profiles of the cooling source during freeze-casting within the experimental framework of this work, linear temperature profiles are thus used throughout the thesis as a lever to, primarily, control pore size.

Moreover, reproducibility of LCSM freeze-cast ceramics was considered, finding that inconsistency in the preparation of the suspensions presumably led to evident differences in the pore and wall sizes of the freeze-cast samples. To confirm this assumption, however, a more thorough study is needed. Nonetheless, all freeze-casts presented throughout this thesis was prepared in batches, such that each experimental hypothesis was evaluated from the same batch of freeze-casts, thus assuring validity of conclusions.

Part III

Freeze-casting Regenerator Geometries

Gelation freeze-casting

The morphology of the ice-templated pores very strongly depends on the freezing conditions, as discussed in Chapter 5. Thus, controlling the freezing front velocity is equivalent to controlling the structural dimensions. Another possible way of controlling the morphology of the pores of a freeze-cast structure is to alter the chemical composition of the solvent and thus the physical properties of the solvent during freezing. One way of doing so is by gelation of samples prior to freezing, achieved by introducing a gelling agent, such as gelatin, into the suspension.

In this chapter, the implementation of dynamic freezing profiles together with gelation is investigated and compared to static freezing conditions. The combined influence of these processing conditions on the resulting morphology of ice-templated pores is evaluated. Besides altering the morphology, the formed gel network offers an increased viscosity or gel strength for stabilizing the suspension and provides an additional step of net-shaping if desired. In Chapter 7, a practical application of net-shaping of gelated samples is investigated.

6.1 Gelcasting and gelation freeze-casting

Gelation has previously been used in ceramic processing for gelcasting [127] as a near-net-shaping technique for achieving complex-shaped materials, as shown in Figure 6.1. Combining

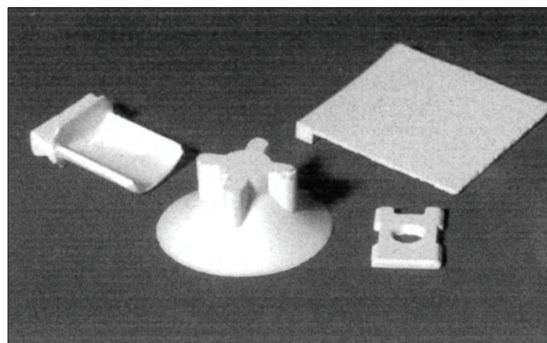


Figure 6.1: Complex-shaped alumina ceramics obtained by gelcasting. Figure from Gilissen et al. [127] © 2000 Elsevier Science Ltd. All rights reserved.

gelation and freeze-casting using gelatin was introduced by Nakata et al. [128] and Fukushima et al. [129, 130] (same research group), who showed that initial gelation of samples completely

alters the morphology of the ice-templated pores while achieving complex shapes throughout the entire ceramic body.

The principles of gelation freeze-casting is illustrated in Figure 6.2. In gelation freeze-

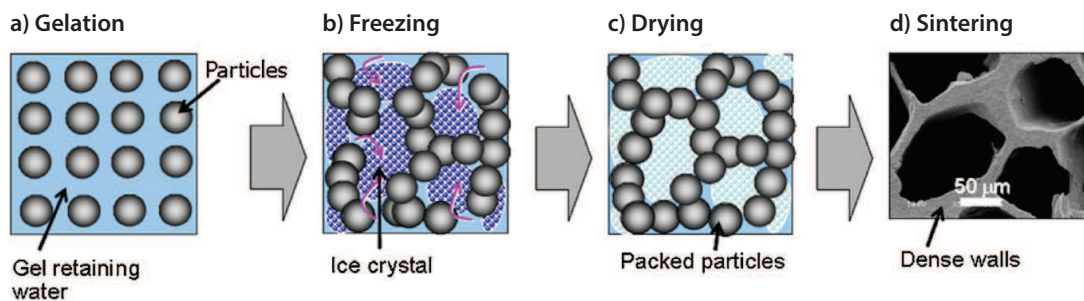


Figure 6.2: Principle of gelation-freeze-casting. a) Ceramic particles are fixed in a water-based gel. b) Upon freezing, water is released from the gel-network for ice crystal formation and particles are pushed aside and packed together. c) During drying, the gelatin supports the green body. d) The gelatin is burned out during sintering and the walls are densified. Figure edited from Fukushima et al. [131] © 2014 WILEY-VCH Verlag GmbH & Co. KGaA, Weinheim.

casting, ceramic particles are fixed in a water-based gel, a hydrogel. Upon freezing, water is released from the gel-network for ice crystal formation, indicated by the purple arrows in Figure 6.2b), and particles are pushed aside and packed together. The ice is removed by sublimation and the dried gel acts as a binder to support the green sample. As with standard ceramic suspension additives, the gelatin is burned out during sintering and the walls are densified, resulting in a ceramic structure with macropores where the ice used to be.

The gelled freeze-cast structures have primarily been used for processing of insulating materials [129], membranes [132] and biomedical purposes [18], all utilizing the hierarchical nature of freeze-cast structures. However, until now gelled freeze-cast structures have been processed using primarily static freezing conditions [18, 129, 130, 132]. For static freezing conditions the cold side is kept at a constant temperature below the freezing temperature of the solvent throughout the freeze-casting process. Static freezing conditions lead to a changing freezing front velocity during casting, as discussed in previous chapters, resulting in structures with varying macropore sizes throughout the length of the structure [9–11].

6.1.1 Properties of gelatin

Gelatin is derived from partial hydrolysis of collagen [133–135]; a naturally occurring family of proteins in e.g. mammals such as humans, cattle and pork and gelatin is therefore typically industrially manufactured from the skin, bones and tissue of the latter two. Gelatin is thus a biopolymer. Because of its non-toxicity, gelatin has a range of applications mainly within food sciences as a texturizing agent and in the pharmaceutical industry as an agent in drug delivery systems [134, 135].

Commercially available gelatin differ in molecular weight and abilities in gel formation depending on conditions of hydrolysatation and origin of collagen [133, 134, 136], and thus varies from company to company. In this work, granular gelatin, type A from porcine, from both *Ward's Science* and *Sigma-Aldrich* have been used, in accordance with the experimental work having been carried out in two different laboratories.

An important property of gelatin is its ability to form a gel. As gelatin molecules denaturate in water upon heating they form a colloidal solution. Upon cooling, intermolecular forces will give rise to the formation of a cross-linked polymer network throughout the solution resulting in loss of fluidity; i.e. a rigid gel. The gelling power or gel strength is characterized by its Bloom value. The Bloom value is the force required to depress the surface of a gel by 4 mm using a 0.5 inch plunger, for a gel containing 6.67% gelatin having hardened for 17 hours at 10 °C [135]. The Bloom value for the granulated gelatin from *Sigma-Aldrich* is listed as ~175 g Bloom for concentrations of 6.67 % in de-ionized water. Additionally, *Sigma-Aldrich* states that "when heated at 100 °C in the presence of air, it (gelatin ed.) swells becomes soft and disintegrates." [137]. To investigate the thermal properties of gelatin, a thermal gravimetric analysis was performed, using a vertical thermobalance (STA 409CD, Netzsch), heating to 1000 °C at 1 K/min under normal atmosphere with a flow rate of 25 mL/min. A baseline run has been subtracted.

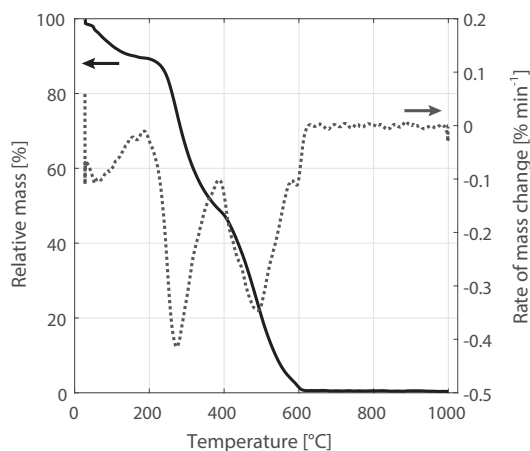


Figure 6.3: Thermal gravimetric analysis of the burnout of gelatin at a heating rate of 1 K/min.

From the shape of the curve of the relative mass of gelatin in Figure 6.3, it is evident that the burnout of gelatin occurs in three steps. Presumably, water is evaporated from the gelatin below 100 °C during the first step, followed by two steps of decomposition and gasification, leaving a residual mass of 0.3 % indicating an almost complete and satisfactory burnout.

The curve of the rate of mass change, i.e. the first derivative of the relative mass with respect to time, shows two significant peaks at 279 °C and 484 °C. At these temperatures, the burnout rate of gelatin is thus greatest. Isothermal dwell times of 2 hours at temperatures of

250 °C and 450 °C was therefore maintained in the sintering program of gelated freeze-casts*.

Furthermore, preliminary sintering of gelated freeze-cast samples showed a significant deformation of the shape, with samples collapsing and bulging out, as illustrated on Figure 6.4. This effect was more pronounced with an increase in gelatin content. Presumably, either wa-

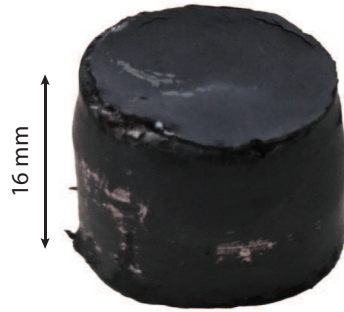


Figure 6.4: Preliminary gelated sample sintered at 1150 °C for 3 hours with a heating rate of 60 K/hour and a single isothermal step at 450 °C of 4 hours for burnout of gelatin. The sample is deformed and bulges out in the middle.

ter released from the gelatin upon heating or the melted gelatin itself, dissolves the ceramic particles enough to make the sample slightly collapse and deform. By decreasing the burnout rate of gelatin by lowering the heating rate during sintering to only 15 K/min and adding an additional isothermal step of 2 hours at 50 °C, for a slower evaporation of water, the overall green body shape could be maintained.

6.1.2 Gelation of LCSM suspensions

For gelation of LCSM suspensions for freeze-casting, following experimental considerations were taken into account:

- i) gelation of gelatin requires it to be denatured, i.e. unfolded by heating. However, excessive heating will cause gelatin to decompose and solvent to evaporate;
- ii) for a homogenous gel-network to form, LCSM ceramic particles must be properly dispersed in an aqueous suspension prior to gelation. LCSM is magnetic and magnetic stirring will thus not be successful;
- iii) upon freeze-casting, gel strength must be such that the growing ice crystals are able to deform and extract water from the gel-network such that anisotropic and aligned ice-crystals are formed. Additionally, the strength of the gel-network must be such that the gel exhibits no flow and thus can retain the gelated shape.

*As illustrated in Figure 3.6, page 34, similar dwell times for structures from DURAMAX™-based suspensions were already established.

To address the last item first; a qualitative assessment of gel strength was performed simply by observing the rigidity and fluidity over time of aqueous gelatin gels and gelated suspensions.

Figure 6.5 illustrate two water-based gelatin gels of 1 wt% and 2 wt% gelatin after hardening at 2 °C for 20 hours, Figure 6.5a) and b), respectively. The gel of only 1 wt% gelatin collapsed while the gel of 2 wt% gelatin maintained its shape for at least 30 minutes.

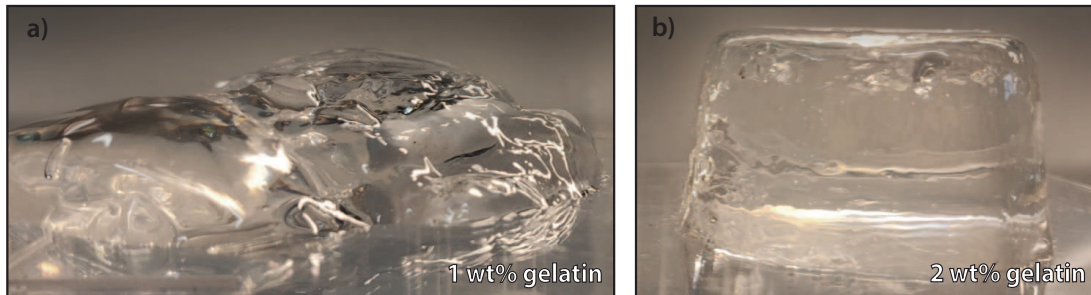


Figure 6.5: Aqueous gelatin gels of varying gelatin content. After hardening for 20 hours, the gel containing only 1 wt % gelatin collapsed, while the gel containing 2 wt% gelatin maintained its shape for at least 30 minutes.

Likewise, the rigidity and fluidity of gelated LCSM suspensions were observed for various concentrations of gelatin. Gelation tests of gelatin from *Sigma-Aldrich* are shown in Figure 6.6 for concentrations of 1 – 2 wt% gelatin. The cotton swab is seen to completely sink into the gelated suspension of only 1 wt% gelatin, while it lays nicely on top of the 2 wt% gelatin gelated suspension. However, during preliminary freezing trials of high concentration gelatin gelated suspensions, the gel was found to rupture upon freeze-casting, causing severe defects in the final structure. The lowest possible gelatin content was therefore desired. The gelated suspension with 1.5 wt% gelatin is slightly moist, as seen on the tip of the cotton swab, but still retains its shape. 1.5 wt% gelatin, relative to water content, was therefore chosen as an optimum concentration for suspensions prepared with gelatin from *Sigma-Aldrich*. Similar tests were performed for gelatin from *Ward's Science* with an optimum gelatin concentration of 0.45 wt%, relative to water content.

To ensure samples with no agglomerates, item ii), a suspension of 20 vol% LCSM in MiliQ water was dispersed with the addition of 2.5 wt% DURAMAX™ dispersant and homogenized for at least 24 hours on a low energy ball mill until measurements of the particle size distribution proved consistent. Item i), the denaturation of gelatin, was addressed according to the laboratory in which the samples were prepared. I.e. gelation freeze-casting was carried out both at Clemson University, Department of Materials Science and Engineering as well as at the Technical University of Denmark, Department of Energy Conversion and Storage. In the first case, granular gelatin was dissolved in a small amount of water, stirred and kept at 45 °C in a sealed beaker to avoid evaporation for 30 minutes and then manually mixed into the pre-heated suspensions (gelated freeze-cast specimens in Section 6.2). Consistent temperature between suspension and dissolved gel was found to be crucial in order to avoid formation of gelatin

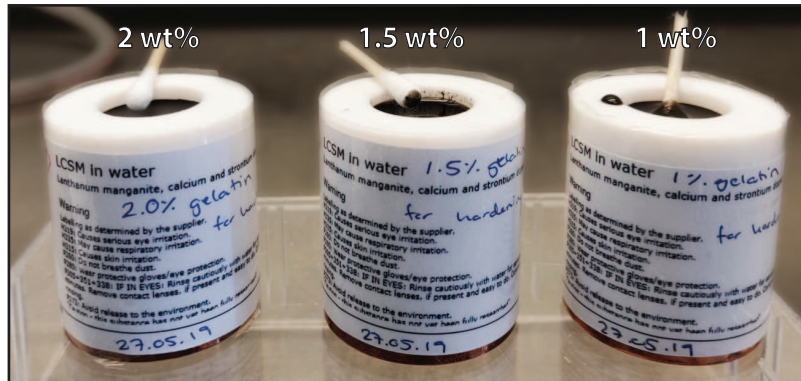


Figure 6.6: Qualitative assessment of gelatine content in LCSM suspensions after 17 hours of hardening at 2 °C. The cotton swap sinks into the still fluid 1 wt% gelatin gel while it lays on top of the 2 wt % gelatin gel.

lumps in the final gelated sample. Alternatively, in the latter case, the LCSM suspensions were heated in a water bath at 45 °C, the granular gelatin was then dissolved directly in the suspension by stirring for 30 minutes with a mechanical stirrer equipped with a propeller (gelated freeze-cast specimens in Section 6.4 and Chapter 7). The latter set-up is shown in Figure 6.7 and ensured a more consistent heating and mixing and thus homogenous gel-formation.

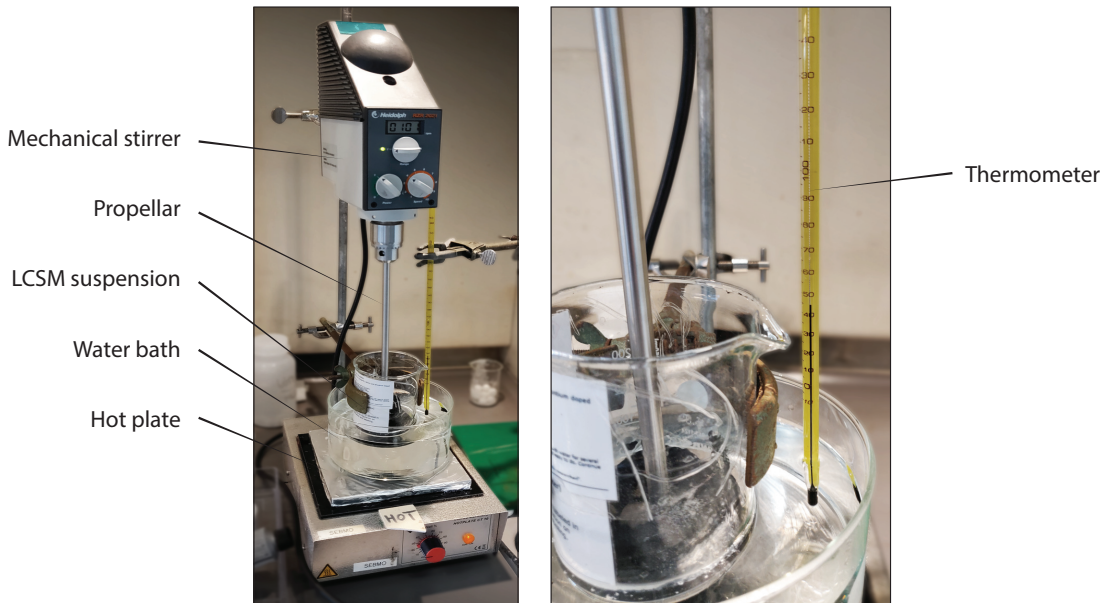


Figure 6.7: Set-up for dissolving gelatin directly in a heated LCSM suspension, keeping a consistent temperature of 45 °C while stirring using a mechanical stirrer equipped with a propeller.

The solutions were poured into pre-heated moulds and then immediately de-aired in a

vacuum-chamber for 5 minutes. Samples were left to harden at 2 °C for ~17 hours.

6.2 Static & dynamic freezing conditions

For comparison, both gelled and non-gelated samples were frozen directionally at static and dynamic temperature profiles, as illustrated in Figure 6.8, using freeze-casting **Set-up B**, previously described on page 29.

Dynamic freeze-casting of samples was achieved by manually adjusting the level of liquid nitrogen resulting in a freezing rate of -10 K/min. Moulds with either gelled samples or empty moulds into which de-aired suspension was poured, was placed on the copper rod still at *rt*. The temperature was decreased continuously from ambient and the freezing rate was kept constant during the entire freezing procedure until samples were frozen solid.

Static freeze-casting of samples was achieved by placing the copper rod in a cooling bath of liquid nitrogen and acetone, reaching a steady temperature of 177 K. Moulds containing de-aired suspension or a gelled sample were transferred directly to the pre-cooled copper rod. Due to the large thermal mass of the copper rod, the temperature of the rod did not change significantly during freezing of samples and was thus assumed to be constant resulting in a static freezing.

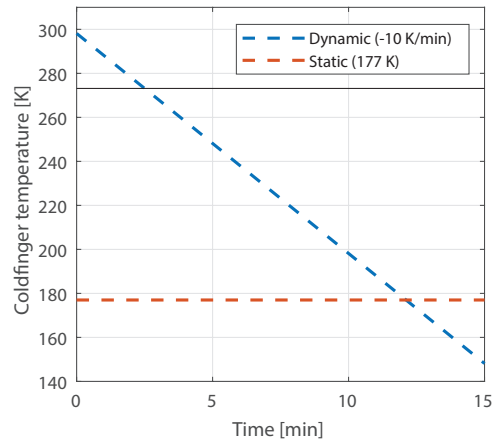


Figure 6.8: Dynamic and static freezing profiles, where the temperature of the copper rod is either decreased by -10 K/min from *rt* or kept constant at 177 K, respectively.

Dynamic and static freezing conditions both resulted in anisotropic macroporosity in the form of macropores running along the freezing direction. As evident on Figure 6.9, the cross-section of each pore is ellipsoidal, giving an overall lamellar morphology, and the pores are

ordered in domains of various orientations. The porosity is hierarchical with macroporosity in the form of templated macropores and microporosity in the ceramic walls.

Introducing an initial gelation of the solvent by adding gelatin and leaving it to harden causes the medium in which the ice grows to change, thereby changing the final morphology of the ice crystals and thus the resulting pores [18, 129, 131, 132]. While the macroporosity of the gelated structures are still lamellar and the perpendicular pore shape is overall ellipsoidal, the general morphology of gelated samples was found to be significantly different.

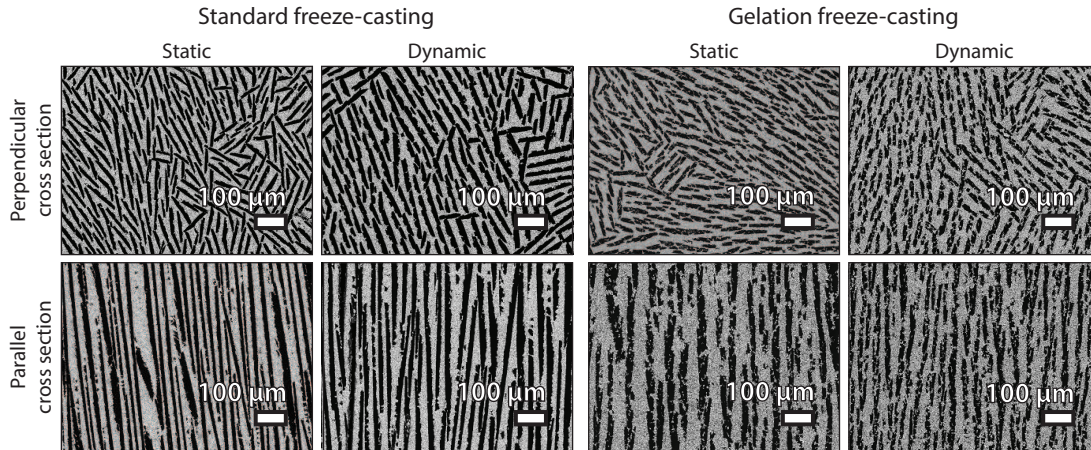


Figure 6.9: SEM micrographs of cross-sections perpendicular and parallel to the freezing direction at sample heights of 6 mm and 6 ± 2 mm, respectively. Grey areas are ceramic walls while black areas are porosity in the form of lamellar, ellipsoidal pores. The total porosity of non-gelated freeze-cast samples are $\sim 65\%$ while the gelated samples have a total porosity of $\sim 70\%$. Samples were sintered at 1150°C . Figure revised from Paper I © 2019 The American Ceramic Society.

6.3 Structural properties of macropores

Analyzing the SEM micrographs of cross-sections perpendicular to the freezing direction of freeze-cast structures by image analysis as described in Section 3.3.2 yields average pore and wall sizes. The average pore and wall size, as a function of distance from the coldfinger, for both statically and dynamically frozen samples, as well as for non-gelated and gelated samples, are shown in Figure 6.10. As can be seen from Figure 6.10a) freeze-cast structures frozen using a static freezing profile of 177 K have inhomogeneous microstructure, where both pore size and wall size increase along the sample height, indicating a conical shape of pores.

When the temperature of the cold finger is static the suspension will initially freeze very fast. As the freezing front moves further away from the cold finger, the temperature gradient at the freezing front decreases due to increased thermal resistance of the growing frozen part of the sample, which reduces the freezing kinetics, i.e. the freezing front velocity, giving the ice

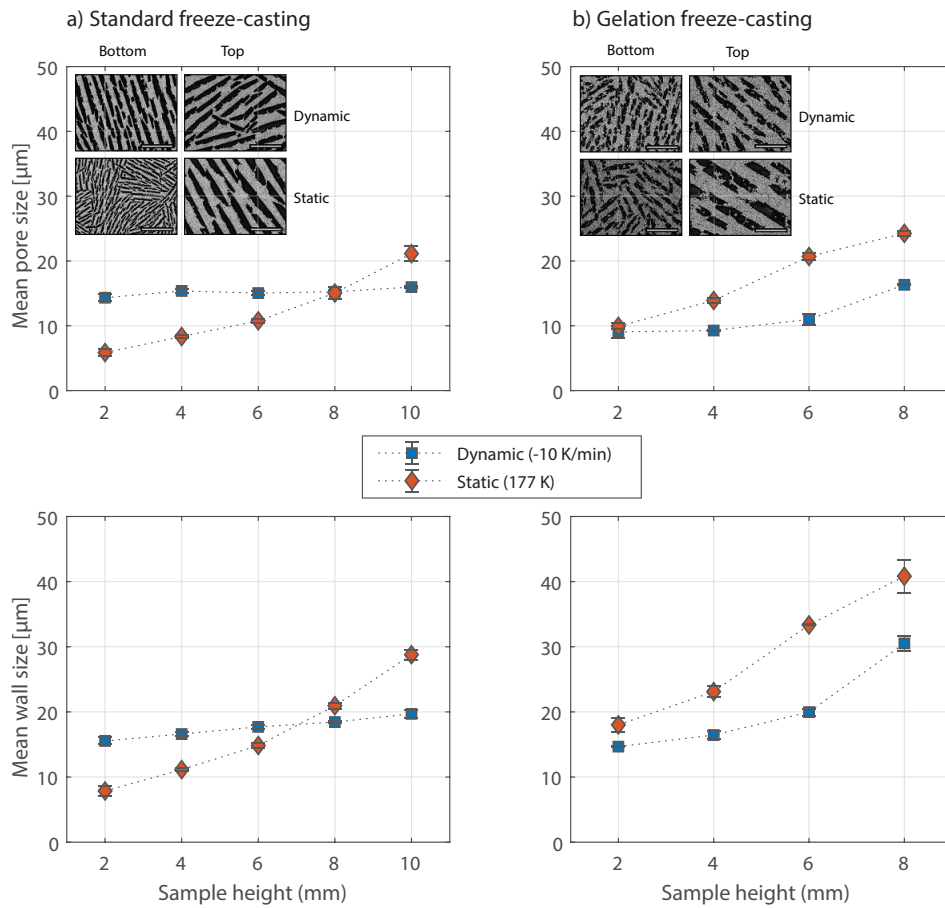


Figure 6.10: Channel and wall size as a function of distance from the coldfinger (sample height) of freeze-cast structures frozen under static (\diamond) and dynamic freezing (\square) profiles a) without and b) with gelatin. SEM insets are of cross-sections perpendicular to the freezing direction at a sample height of 2 mm (bottom) and 8 mm (top), where the scale bar indicates 100 μm . Figure revised from Paper I © 2019 The American Ceramic Society.

crystals more time to grow perpendicular to the freezing direction. Larger ice crystals result in larger pore and wall sizes. However, while the pore sizes of the statically frozen structures were found to increase by a factor of five from bottom to the top, the dynamically frozen structures maintained a pore size of $\sim 15 \mu\text{m}$ all the way through for the non-gelated samples. By implementing a dynamic temperature profile with a constant cooling rate of -10 K/min the increasing thermal resistance from the frozen part of the sample is compensated, resulting in steady freezing kinetics and thus in homogenous pore and wall sizes throughout samples, as also discussed in Chapter 5. In Figure 6.10, however, we clearly see the effect of dynamic conditions compared to static conditions. Moreover, for smaller cooling rates of -0.5 K/min to -2.5 K/min an increase in pore size was still evident throughout samples (see Figure 5.3 on page 67), while this is not the case for samples frozen at constant cooling rates of -10 K/min .

Regarding gelated samples, however, here the dynamic freezing conditions did not result in a homogenous structure. We will return to the discussion of the overall morphology of gelated samples in Section 6.3.2.

6.3.1 Tortuosity of microchannels

A similar conclusion, as for the size variation of pore widths, can be reached when evaluating the tortuosity of templated pores, or microchannels, frozen without initial gelation, as seen in Figure 6.11a).

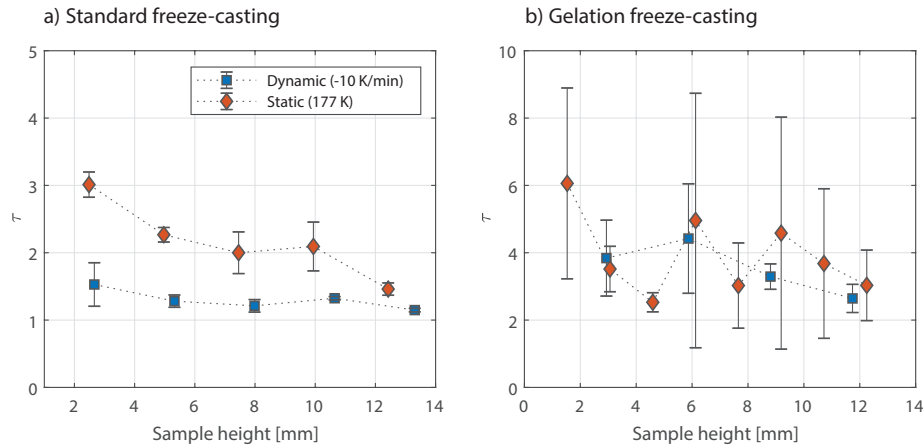


Figure 6.11: Calculated tortuosities, τ , as a function of distance from the cold finger (sample height) of freeze-cast structures frozen statically and dynamically. Tortuosity is calculated from cross-sections of $331 \mu\text{m} \times 248 \mu\text{m}$ parallel to the freezing direction. Three cross-sections have been evaluated at each sample height. Results of both non-gelated (a) and gelated samples (b) are shown. Figure revised from Paper I © 2019 The American Ceramic Society.

Tortuosity can be directly correlated to the nature of ice crystal growth. In the steady-state region (see Figure 1.4 on page 10), the larger and more aligned the ice crystals are, the

larger and straighter will the resulting pores be, leading to smaller tortuosities. The calculated tortuosities of microchannels in freeze-cast structures frozen statically are shown in Figure 6.11. As can be seen from the figure, samples frozen without an initial gelation step, Figure 6.11a), have a decreasing tortuosity along the sample height, while tortuosity is more or less constant for the dynamically frozen structures

From calculations of tortuosity and measurements of pore sizes we can thus conclude that implementing dynamic freezing profiles increases the morphological homogeneity of non-gelated freeze-cast structures, making them almost completely homogenous with respect to pore size and tortuosity.

While calculated tortuosities of non-gelated samples reflect freezing conditions, tortuosity for the gelated structures, however, is seen to have significantly larger error bars and no clear trend is evident of the calculated tortuosities with respect to sample height. This is due to the morphological change in freeze-cast samples due to initial gelation.

6.3.2 Morphology of gelated structures

As is evident from Figure 6.9, the pores of gelated freeze-cast structures – similar to those without gelation – are lamellar and the cross-sections are ellipsoidal, however, less elongated. Aspect ratios of the cross section of the pores were determined by manually fitting ellipses to pores in ImageJ[†] and then calculating the ratio between the minor and major axis. For the relevant samples approximately 100 pores at a sample height of 6 mm was fitted with ellipses to determine the average aspect ratios, which are listed in Table 6.1. The aspect ratio for pores in

Table 6.1: Aspect ratios and pore-porosity of dynamically and statically frozen freeze-cast structures.

	Freezing conditions	Aspect ratio	Macroporosity [%]
Standard	Dynamic (−10 K/min)	7.3±3.6	49±1
	Static (177 K)	6.6±2.8	47±2
Gelation	Dynamic (−10 K/min)	3.9±1.4	41±1
	Static (177 K)	3.3±1.5	43±2

the gelated samples are significantly smaller than those from non-gelated samples frozen under the same conditions. The pores of the gelated samples thus become less ellipsoidal, converging towards a more cylindrical shape, as also observed by Fukushima et al. [138]. The change in morphology is likely due to the increased resistance/viscosity the growing ice crystals meet due to the gel network making it harder for the crystals to push aside suspended particles and making it more difficult for water molecules to diffuse to the tip of the growing ice crystals. A consequence of the resistance from the gel network can be seen in the higher magnification micrographs in Figure 6.12a), where the walls seem slightly less dense in the gelated freeze-cast

[†]Open-source image software: imagej.nih.gov/ij/

structure.

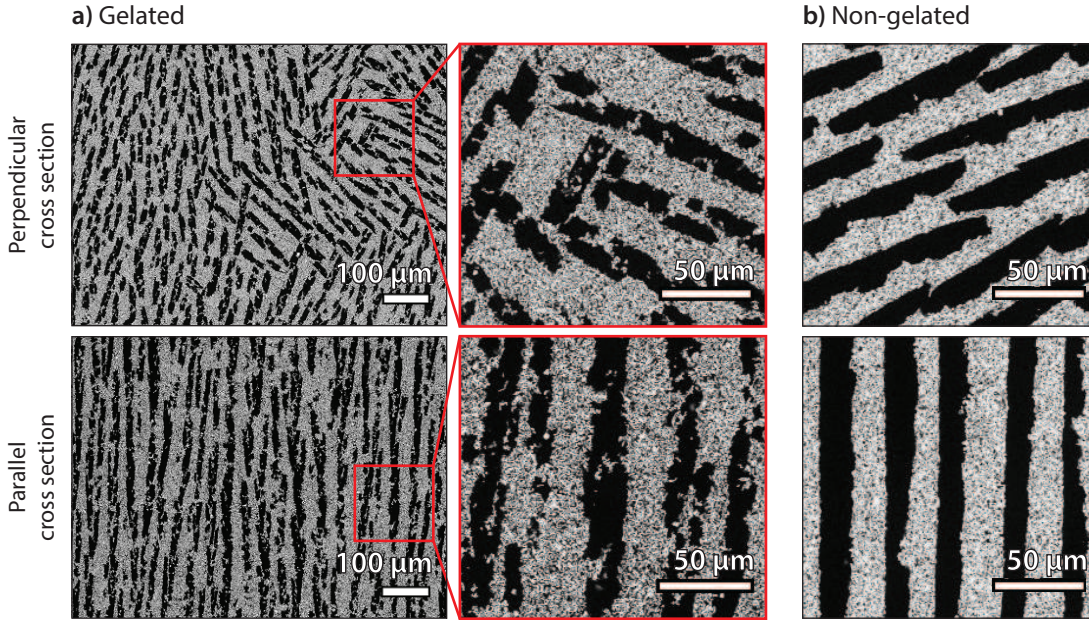


Figure 6.12: SEM images of cross-sections perpendicular and parallel to the freezing directions of a) a gelated and b) a non-gelated sample, both frozen dynamically at -10 K/min. Perpendicular and parallel cross-sections are at sample heights of 6 mm and 6 ± 2 mm, respectively. Higher magnification micrographs show the rougher nature of the wall surface of gelated structures in the form of dendrites and ceramic bridges connecting the walls of the pores. In addition, the walls of the gelated sample appear less dense than those of the non-gelated sample. Figure revised from Paper I © 2019 The American Ceramic Society.

Porosimetry measurements of pore sizes of gelated and non-gelated samples both frozen at dynamic freezing conditions, shown in Figure 6.13 reveals a significant difference in distribution of porosity between pore porosity and porosity in the structure walls.[‡] Choosing an arbitrary threshold of $5 \mu\text{m}$ – as this is also the limit for minimum size of pores detected by image analysis as described in section 3.3.2 and here indicated in Figure 6.13b) by a dotted line – the distribution of total porosity into pore and wall porosity can be determined. This analysis reveals that 20 % of the total porosity is contained as microporosity within the walls for non-gelated samples, while 30 % of the total porosity is found within the walls for gelated samples. During freeze-casting the formation of ice crystals pushes the suspended particles together causing these to segregate into what will become the walls of the structures upon drying and sintering. Based on the distribution of porosity, it is assumed that the gel network inhibits this segregation to some extent during the casting process, resulting in a less dense packing of

[‡]Note, that the coloring of curves in Figure 6.13 differs from previous plots in this chapter, as the samples were frozen using **Set-up C**, maintaining the same suspension composition and properties, but frozen under slower freezing rates of only -1.5 K/min.

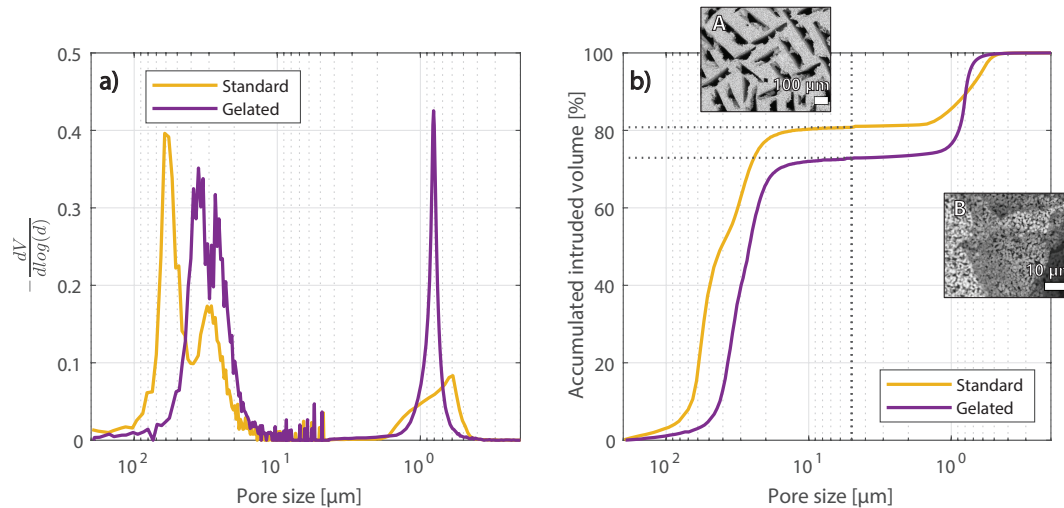


Figure 6.13: Porosimetry measurements by mercury intrusion of a standard and gelated sample, both frozen at a constant freezing rate of -1.5 K/min. a) Both samples show a bimodal distribution of pore sizes, i.e. a peak in the range of $30 - 50 \mu\text{m}$ and a peak in the range $0.5 - 1 \mu\text{m}$. b) 80 % and 70 % of the total porosity is due to the ice-templated pores for the standard and gelated sample, respectively, when pore porosity is defined as that from pores greater than $5 \mu\text{m}$. SEM insert **A** illustrates pore porosity, while SEM insert **B** illustrates wall porosity. SEM images are obtained from a non-gelated sample and are here merely illustrative.

particles in the walls of the gelated samples and an increased porosity in the walls.

While the implementation of a dynamic freezing profile – compared to static freezing – were found to significantly change the dimensions of the pores along the sample height for non-gelated structures, resulting in more homogenous pore sizes and tortuosities, as evident from Figures 6.10 and 6.11, this was not the case for gelated structures. Both statically and dynamically frozen gelated structures are inhomogeneous in pore size as can be seen in Figure 6.10b), where an increasing pore and wall size along the sample height is observed. It is especially remarkable that the pore sizes for the gelated samples are not homogenous throughout the sample, as is clear from Figure 6.10b), even though the dynamic freezing profile is used. This could be due to the altered structure of the gelated freeze-cast sample, which is more unstructured than the corresponding standard freeze-cast sample. The significant difference in internal structure, or morphology, is clearly seen in Figure 6.11 showing the tortuosity of the respective samples. The larger tortuosity of the gelated samples reveal a somewhat more chaotic morphology which is thought to further decrease the thermal conductivity of the frozen part of the sample. Hence, throughout the length of the sample the freezing conditions change due to an increasing thermal resistance, not only because of liquid water transitioning into ice, but also because of a more chaotic morphology, resulting in larger pores at the top of the sample. However, the effect is

small as the pores are seen only to increase in size in the latter part of the sample.

The resulting pores in the freeze-cast gelled structures are, despite the change in morphology and homogeneity, in the same size range as the standard freeze-cast ones. Meanwhile, the calculated tortuosities of structures frozen with an initial gelation step, Figure 6.11b), are generally larger than non-gelated structures and not directly correlated with sample height or pore size, but rather, scattered around $\tau \approx 4$ inconsistently. The variability in the pore size and calculated tortuosity is partly due to the presence of dendrites and ceramic bridges across pores. As can be seen on the horizontal cross-sections in Figure 6.12a), ceramic bridges connect pore walls across the pores, while dendrites results in an obviously higher surface roughness than non-gelated structures when comparing parallel cross-sections in Figure 6.12a) and 6.12b). Bridges and dendrites increase the overall curviness of pores. For gelated freeze-cast samples, the finer scale contributions of dendrites and bridges to the calculated tortuosity overshadow that of the size and skewness of the pores.

Gelation thus provides an obstacle in fine-tuning and specific engineering of structures if one has a specific pore size in mind and a need for homogeneous, low tortuosity pores. It does, however, provide a way of altering the morphology of pores in freeze-cast structures, making the pores less ellipsoidal, more tortuous and more connected. While not obviously ideal as regenerator geometries, these types of microstructures could have other advantages and applications. Specifically, it has been shown that the bridges between pore pores have a significant effect on the mechanical properties of freeze-cast materials [26, 35]. Additionally, gelation provides a possibility of near-net-shaping, which we will return to and exploit in Chapter 7.

6.4 Low freezing rates & structural homogeneity

In this chapter, the gelated freeze-cast thus far described, was frozen under static and dynamic conditions, i.e. a constant temperature of 177 K or a constant freezing rate of -10 K/min, respectively, using **Set-up B**, described on page 29. However, as discussed in Chapter 4, the freeze-caster, i.e. **Set-up C**, has a maximum freezing rate of only -2 K/min for a desired sample length of minimum 25 mm. Similar gelation freeze-casting experiments as just described in this chapter was thus carried out using the freeze-caster. It should be noted, that samples frozen using the freeze-caster was only sintered at 1100 °C while those frozen using **Set-up B** was sintered at 1150 °C.

Although samples cannot be directly compared due to the different experimental circumstances of both freezing conditions and post-processing, the trend of the structural differences between gelated and non-gelated samples frozen under dynamic conditions using the freeze-caster, are in accordance with those from samples frozen under dynamic conditions using **Set-up B**. I.e. the variation in pore size throughout samples from bottom to top, is considerably greater for the gelated sample, than for the non-gelated sample, while the same trend applies for wall size, as shown in Figure 6.14a–b).

As discussed previously in this chapter, the increase in mean pore size from bottom to top

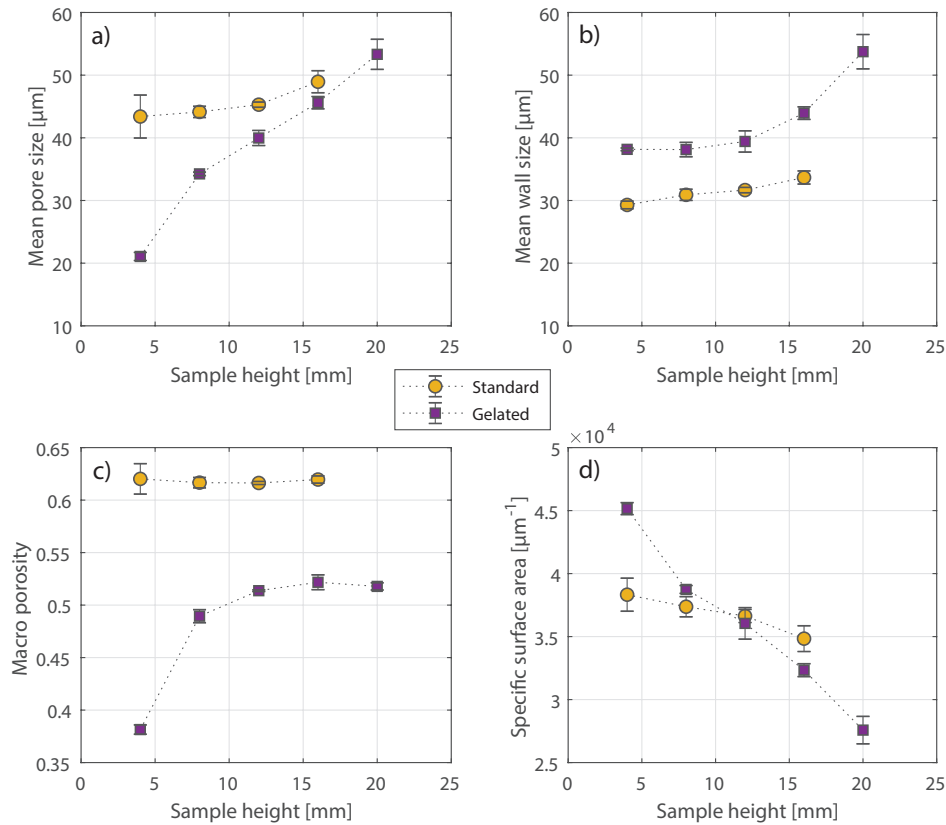


Figure 6.14: Structural properties of standard and gelled samples frozen at a constant freezing rate of -1.5 K/min. a) mean pore size, b) mean wall size, c) macro porosity, i.e. pore porosity, and c) specific surface area. All parameters are evaluated from two samples, one gelled and one non-gelled (standard). Parameters are evaluated from image analysis of SEM micrographs and are averaged from three images at each sample height.

of gelled samples is still significant despite the dynamic freezing conditions of constant cooling rates. Fukushima et al. [130] claims that the addition of anti-freeze proteins along with fast freezing during gelation freeze-casting – i.e. in the given study static cold side temperatures of -20 to -40 $^{\circ}\text{C}$ – will inhibit nucleation, meaning that less ice crystals will form resulting in a more uniform pore size distribution throughout the sample body. A discussion of the effect of anti-freeze proteins is beyond the scope of this work, as Fukushima et al. [129–132, 138] appear to thus far being the only research group investigating the combination of gelation and anti-freeze proteins. However, as such, using anti-freeze-proteins in combination with gelation is thus an obvious continuation of this work, as it could provide the missing step for processing of freeze-cast regenerator geometries in achieving homogeneous pore sizes and gelled morphologies.

Fukushima et al. claims, that the increased freezing rate too inhibits nucleation [130], thus

resulting in increased homogeneity of pores throughout freeze-cast structures. The latter is actually the case when comparing the pore size variation with length of non-gelated samples frozen at a cooling rate of -10 K/min, Figure 6.10a), with non-gelated samples frozen at cooling rates of -10 K/min, Figure 6.14a), where the variation with sample length is about 10 % for the former and negligible for the latter. Although, the exact mechanism of which a uniform pore size is maintained throughout samples is a little unclear in reference [130]. Alternatively, or additionally, the increase in pore size variation throughout the length of non-gelated samples with a decrease in cooling rate, could simply be because ambient conditions are more dominating for slower freezing rates than faster freezing rates.

Regarding the freezing conditions and capacity of the freeze-caster, neither the freezing front velocity nor the maximum sample height appear to depend significantly on whether samples were gelated or not, when considering Figure 6.15, although a larger data set is required. Additionally, T_{trans} was determined at 271.3 K and 270.9 K for the gelated and standard sample, respectively, again indicating similar freezing conditions.

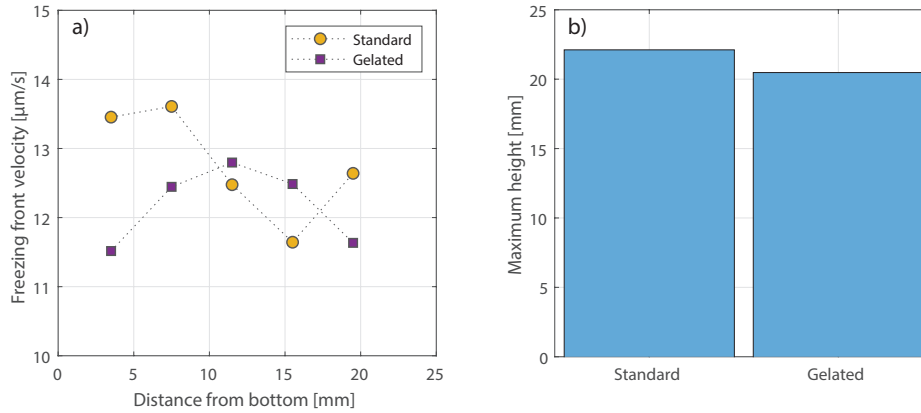


Figure 6.15: Freezing conditions for gelated and standard samples frozen at a constant freezing rate of -1.5 K/min using the freeze-caster. a) Freezing front velocity and b) estimated maximum height.

Tortuosity was only evaluated at one sample height in the center of samples, and is therefore not included in Figure 6.14. The tortuosity was averaged from three SEM micrographs obtained at a sample height of 15 mm and was calculated as 1.79 ± 0.42 and 2.02 ± 0.28 for non-gelated and gelated samples, respectively. The tortuosity of a gelated sample frozen at a freezing rate of -1.5 K/min is significantly lower than those calculated for a sample frozen at a freezing rate of -10 K/min in Figure 6.11. Two varying parameters might cause this difference: i) The pores are larger for the sample frozen at lower rate and thus, the tortuosity will be smaller, as previously concluded. ii) The gel strength was not quantified and differs presumably between the two experimental series, being stronger for samples frozen at -10 K/min, resulting in a larger degree of dendrites and ceramic bridges which increases the tortuosity.

Regarding processing of functional materials using gelation freeze-casting, it is worth noticing the sharp increase in macroporosity in the bottom of the gelled sample after which the macro porosity more or less evens out around 52 %, as seen in Figure 6.14. This could indicate a degree of sedimentation due to insufficient dispersion of ceramic particles in the initial suspension or faulty gelation conditions[§]. Precaution of possible sedimentation was taken for additional gelled samples, as discussed in Chapter 7.

6.5 Summary

Freeze-casting of LCSM suspensions, with and without gelation prior to freezing, at both dynamic freezing conditions and static freezing conditions were investigated. Static conditions of 177 K and dynamic conditions of constant cooling rates of -10 K/min and -1.5 K/min depending on freeze-casting set-up were applied. Gelation of suspensions prior to freezing forms a cross-linked polymer network throughout the suspensions and the gelatin content was chosen such that samples just lost fluidity. Implementing an initial gelation step prior to freezing inhibits ice crystal growth during the freezing process which was found to significantly change the morphology, making the cross-sections of pores in gelled samples less ellipsoidal, while introducing more dendrites and ceramic bridges. Additionally, the inhibited ice crystal growth due to gelation resulted in a shift in the macro-/microporosity ratio, as ceramic walls in the case of gelled samples contained a larger degree of microporosity than the non-gelled samples.

In the case of gelled samples, both statically and dynamically frozen structures showed an increase in pore size throughout the sample lengths. For non-gelled samples, static freezing conditions resulted in a significant variation in pore size throughout samples. However, for dynamic conditions a fast cooling rate of -10 K/min was found to result in more or less consistent pore sizes throughout freeze-cast samples, while slower cooling rates of -1.5 K/min still showed a slight increase in pore size throughout the sample, in accordance with results from Chapter 5. The former cooling rate resulted in pore sizes of ~ 15 μm while the latter resulted in pore size of ~ 45 μm with a corresponding freezing front velocity of ~ 13 $\mu\text{m/s}$ for the latter.

The calculated tortuosity of non-gelled samples followed the trend of the pore sizes. For statically frozen samples, tortuosity decreased from $\tau = 3$ at the end close to the coldfinger to $\tau = 1.5$ at the top. For dynamically frozen samples at cooling rates of -10 K/min, the tortuosity was constant at $\tau \approx 1.3$ throughout the sample. For gelled samples the calculated tortuosities at various sample heights showed significant variation around $\tau \approx 4$. This is attributed to the

[§]In the case of the samples reported on in this section, frozen at a constant freezing rate of -1.5 K/min, I much later found, that the fridge used to cool samples during the gelation step, had a tendency to malfunction overnight. The thermostat would switch off resulting in inconsistent temperatures. With someone restarting it in the morning, I remained oblivious to this malfunction. However, it must be emphasized, that it is only a vague assumption, and there was definitely no malfunctioning fridge in the case for gelled samples in Chapter 7, as I was literally guarding these during gelation.

increased presence of dendrites and ceramic bridges infiltrating the pore space and dominating the flow path through the structures.

Although the homogeneity of the morphology of gelated freeze-cast LCSM structures are not consistent throughout the full sample lengths, gelation freeze-casting presents a tunability of tortuosity and a near-net-shaping step which might be of interest regarding processing of freeze-cast regenerator geometries. The latter will be addressed further in Chapter 7.

Functionally graded freeze-casts

In this chapter, graded, multi-material freeze-cast structures of $\text{La}_{0.66}\text{Ca}_{0.24}\text{Sr}_{0.09}\text{Mn}_{1.05}\text{O}_3$ (LCSM9) and $\text{La}_{0.67}\text{Ca}_{0.27}\text{Sr}_{0.06}\text{Mn}_{1.05}\text{O}_3$ (LCSM6) are presented. They are engineered by optimizing the suspension viscosities with the addition of polyvinylpyrrolidone (PVP) of various concentrations and average molecular weights and by gelation-freezing and net-shaping using gelatin. This chapter is largely based on Paper IV.

Freeze-casting of functionally graded or layered structures with two or more phases of material separated by a distinct interface perpendicular to the macropore orientation between the two phases has – to my current knowledge – not yet been achieved. It would, however, be extremely useful in applications such as e.g. membrane- and filter-applications, flow catalysis or magnetic refrigeration, as the material properties can thus be varied along the microchannels throughout the freeze-cast structure. For the latter application, graded, multi-material freeze-cast magnetocaloric regenerators could increase the efficiency of the regenerative cycle.

7.1 Layered magnetocaloric regenerators

In order to optimize achievable operational temperature spans and cooling powers of porous regenerators of magnetocaloric material, a chemically graded, or layered, structure along the direction of the channels is desired [67, 82, 139]. The magnetocaloric effect peaks around the Curie temperature of the magnetic material. For LCSMs this peak is rather narrow, meaning that the temperature span at which the material can operate, i.e. has a significant magnetocaloric effect, is small [81]. For practical applications this significantly limits the use of LCSM as a solid refrigerant. During operation of the AMR cycle, a thermal gradient arises along the flow direction of the regenerator, as illustrated on Figure 2.5 page 20. When considering a single-material regenerator, only a small section will thus operate under its optimum temperature of $\sim T_C$ and the overall magnetocaloric effect will be limited. Spatially grading the regenerator, however, such that the T_C of each section more or less follows the thermal gradient will presumably increase the overall magnetocaloric effect and thus the performance of the regenerator.

Generally, it has been shown, that for regenerators, joining multiple similar materials with slightly varying chemical properties and thus varying T_C , enhances the temperature range over which the AMR device operates [82, 140]. Specifically, Bahl et al. [82] found, that a graded plate regenerator geometry of LCSMs ($x = 0.045$ and 0.0375), manufactured by side-by-side

tape-casting [102], increased the operational temperature span 7.5 times compared to that of the individual materials.

Experimental as well as model studies show that fine-tuning of layers with regards to thickness and Curie temperature is crucial for reaching actual larger operational temperature spans upon layering [75, 139, 140]. For LCSM, highly accurate fine-tuning of the Curie temperature by adjustment of the Sr:Ca ratio has already been established [81]. Thus, regarding processing of graded, multi-material freeze-cast structures, a sharp, planar and distinct material interface is therefore desired.

7.2 Freeze-casting of graded multi-material structures

In freeze-casting, the macropores are directly shaped from the ice crystals and are in the ceramic green body the direct imprint of these. The continuity and low tortuosity of pores are due to the intrinsic properties of water during ice crystal formation under an applied thermal gradient. Layering of two separately frozen freeze-casts would therefore lead to a discontinuity in the pores across the interface between the two materials causing undesired distortion of the otherwise homogeneous pores.

In order to achieve a structural continuity across the interface between two materials in freeze-casting, the freezing step should also be continuous across the material interface ensuring continuous ice crystals. In order to do so, the materials must be layered in the wet stage, i.e. as liquid suspensions prior to freezing. However, upon being poured on top of each other with no further measures, the two suspensions will inevitably mix due to advection, convection and diffusion. An approach to inhibit this mixing and achieve a proper layering of liquid suspensions could be to alter the flow properties of the suspensions. Here, two approaches for doing so are investigated:

1. Inhibiting flow/miscibility by increasing viscosity using polymeric/steric additives
2. Elimination of flow/miscibility by gelation

PVP has previously been studied for its effects on rheological properties of ceramic suspensions, where viscoelasticity and viscosity were found to depend on the average molecular weight and suspension concentration of PVP [141, 142]. Here, various PVP concentrations are thus added to ceramic suspensions for freeze-casting to increase viscosity and thus inhibit flow and miscibility of suspensions in order to achieve a wet layering of these.

As discussed in Chapter 6, gelation freeze-casting has successfully resulted in freeze-cast ceramics of well-defined parallel channels, however, with a slightly altered morphology [45, 131, 138] (see Figure 6.9 on page 84). Gelation freeze-casting provide an additional processing step in the gelation of suspensions, where net-shaping of the gelled suspension is possible if desired. If gelation is carried out such that the suspension loses fluidity, gelled suspensions can in principle be processed and stacked perpendicular to the freezing direction, resulting in a composite gelled sample of layered suspensions of different materials.

Graded freeze-cast ceramics were prepared from layered aqueous suspensions of LCSM powders. Samples were prepared from the same stock suspensions, with various concentrations of PVP or gelatin in order to change suspension properties and freezing conditions to achieve a distinct layering of the final freeze-cast structures.

7.2.1 Material properties and suspension preparation

As the preparation of the suspensions for graded freeze-casting for some specific step varies significantly from the standard procedure described in Section 3.2.1, it is here described in detail:

Two stock ceramic suspensions were prepared from 20 vol% powders in MiliQ water: one suspension was prepared solely from LCSM9, while the other was prepared from LCSM6 and $\text{Ce}_{0.9}\text{Gd}_{0.1}\text{O}_2$ (CGO, CerPoTech) in weight ratio 9:1, in the following referred to as suspensions/samples LCSM9 and LCSM6/CGO, respectively. As LCSM6 and LCSM9 are very similar chemically, a CGO marker was added to the LCSM6 phase in order to distinguish the two phases chemically by energy-dispersive X-ray spectroscopy, as successfully done for graded tape-cast plates [102]. Material and suspension properties are summarized in Table 7.1.

Table 7.1: Summarization of properties of LCSM6/CGO and LCSM9, where density was measured on powders that had been calcined at 1000 °C for 2 hours, the median particle size, d_{50} , is of suspensions after ball milling while onset temperature, T_{onset} , and Curie temperature, T_C , is measured on green and sintered pellets, respectively.

	Density [g/cm ³]	d_{50} [μm]	T_{onset} [°C]	T_C [K]
LCSM6/CGO	6.92 / 6.10	0.41	1015	288 / –
LCSM9	6.08	0.49	930	300

To establish a sufficient dispersion of particles 2.5 wt%, solid to ceramic ratio, of dispersant (DURAMAX™ D-3005) and dropwise addition of nitric acid to adjust the pH of suspensions from ~8 to ~6.5 was added. Suspensions were homogenized by ball milling in PE flasks using small zirconia balls ($\text{Ø}3\text{-}4$ mm) as grinding media.

From Figure 7.1a), it is evident, that the particle size affects the structural properties and dimensions of the templated pores. Thus, to ensure even freezing kinetics and ice crystal growth through both layers of a sample, and thus homogeneous pore sizes, suspensions were ball milled until homogeneous and comparable in particle size distributions as shown on Figure 7.1b). Thus, LCSM6/CGO was ball milled at 25 rpm for ~72 hours while LCSM9 was ball milled at 45 rpm for ~72 hours. From the stock suspensions, suspensions of increased viscosity, suspensions for gelation, and samples for measurements of material characteristics were prepared.

Pellets for dilatometry and magnetization measurements were prepared by slip-casting, as described in Chapter 3, from stock suspensions with the addition of 2 wt% binder (DURAMAX™ B-1022). Pellets for dilatometry were used in the green state while pellets for magnetization

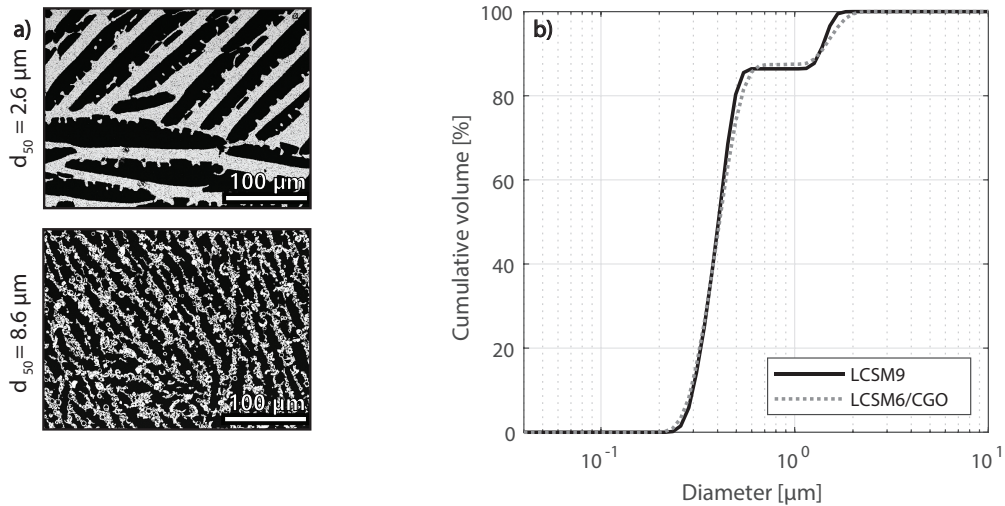


Figure 7.1: a) Morphological effect of different particle size for structures frozen under similar freezing conditions. SEM micrographs were obtained at cross sections perpendicular to the freezing direction at a sample height of 18 mm. Freeze-cast structures are frozen from LCSM suspensions of similar solid load but different median particle sizes, d_{50} . Micrographs revised from Paper VI. b) Particle size distribution of suspensions after ball milling reaching median particle sizes of $d_{50} = 0.49 \mu\text{m}$ and $d_{50} = 0.41$ for LCSM9 and LCSM6/CGO suspensions, respectively. Plot revised from Paper IV © 2019 Elsevier Ltd. All rights reserved.

measurements were sintered using the same heating program as used for sintering of the freeze-cast samples. A slight mismatch in onset temperatures were observed from the shrinkage curves of both LCSM9 and LCSM6/CGO pellets shown in Figure 7.2a). This mismatch resulted in a large degree of strain in the interface between materials of sintered samples, when sintered as described in section 3.2.3 at 1100 °C, causing samples to easily fracture upon handling compared to one-material freeze-casts. As samples were infiltrated in epoxy for characterization, strain build-up in the material interface did not pose any practical challenges in characterizing the interface shape and structural parameters of samples and were therefore, in the case of DURAMAX™ and PVP samples, not addressed further. However, gelled samples showed a severe tendency to develop crack formations upon sintering, possibly because of a sharper interface and therefore a smaller interface area – as will be discussed in the coming sections – and a more cautious sintering temperature of 1000 °C, with a dwell time of 3 hours, and a heating rate of 30 K/hour was chosen for gelled samples. No apparent strain build-up was found for gelled samples. For possible processing of actual layered regenerators with freeze-cast geometry, one would have to consider strain build-up in the sintered structures to avoid the transition of the geometry into that similar to beds of packed particles. As gelled samples were successfully sintered at 1000 °C, a similar densification temperature at an extended time

interval or a proper matching of onset temperatures of the two material phases is proposed for future work.

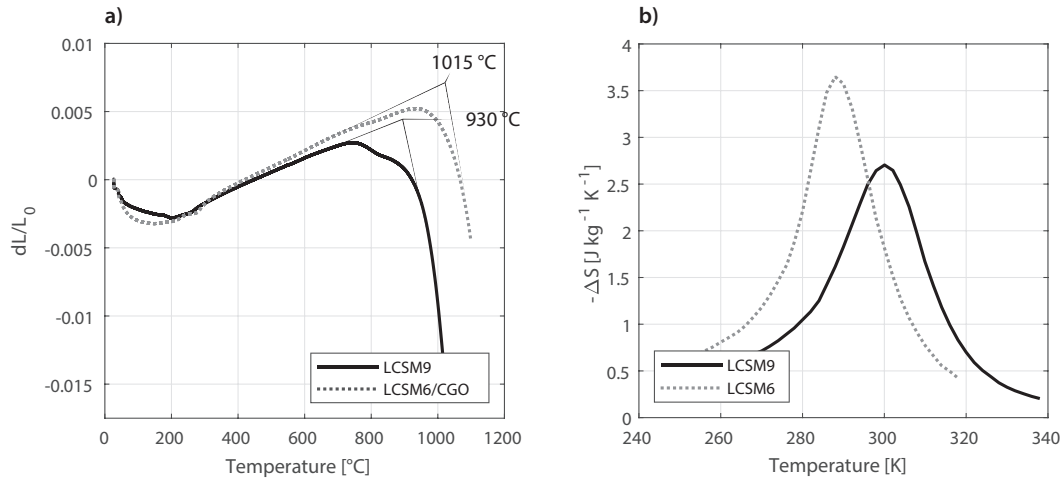


Figure 7.2: Thermal and magnetic properties of LCSM6 and LCSM9. a) Dilatometry measurements showing the shrinkage of slip-cast LCSM9 and LCSM6/CGO pellets during densification. Onset temperatures have been evaluated by analyzing shrinkage curves using *Proteus Thermal Analysis* software (NETZSCH) and are indicated in the plot. b) Isothermal entropy change for slip-cast, sintered pellets of LCSM6 and LCSM9 at an applied field of 1.6 T, where the peak temperature indicate the approximate Curie temperature. Figure revised from Paper IV © 2019 Elsevier Ltd. All rights reserved.

Indirect measurements of the isothermal entropy change, where the peak indicates the approximate Curie temperature, is shown in Figure 7.2b), confirming the range in magnetocaloric properties of the two materials. Peak values and Curie temperatures are in good accordance with Dinesen et al. [81], confirming the purity of the two materials.

Viscosity

Viscous suspensions were prepared from stock suspensions of LCSM6/CGO and LCSM9, respectively, by adding 5 or 10 wt%, solid to ceramic ratio, PVP K30 ($M_w \sim 40,000$, Sigma-Aldrich) or 5 wt%, solid to ceramic ratio, PVP K90 ($M_w \sim 360,000$, Fluka Chemika). For comparison, suspensions with the addition of 2 wt%, solid to ceramic ratio, of a low viscosity commercial binder (DURAMAX™ B-1022) were likewise prepared from both stock suspensions of LCSM6/CGO and LCSM9.

Suspensions were mixed on a low-energy ball mill at 10 rpm for ~ 24 hours, after which viscosity curves of the eight suspensions were obtained using a rheometer (HAAKE Rheostress 600, Thermo Electron Corporation) equipped with a plate spindle (Platte P60 Ti L, Thermo Electron Corporation) with pre-shearing and reversing increase in shear rate from 0.1 to 50 s^{-1} at $21 \text{ }^\circ\text{C}$. The plate spindle was equipped with a solvent trap to minimize evaporation during

measurements. Viscosity curves are shown in Figure 7.3, where it is evident that an increase in PVP load increases the viscosity.

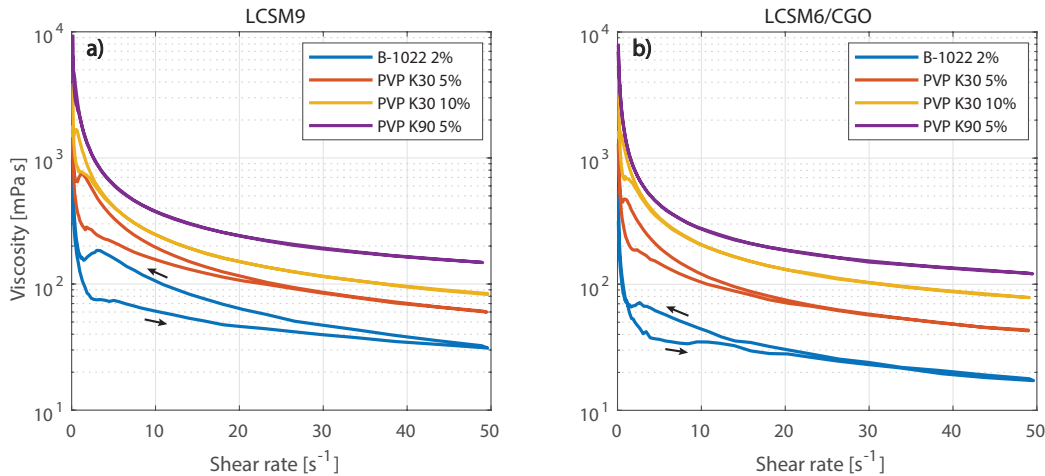


Figure 7.3: Viscosity curves of a) LCSM9 and b) LCSM6/CGO suspensions with 2.5% DURAMAX™ B-1022 binder, 5 or 10 wt% PVP K30 or 5 wt% PVP K90. The addition of the long polymers of PVP K30 and K90 significantly increases the viscosity of the suspensions. Arrows indicate the direction of measurements, and are only given for the bottom curve, but the trend is the same for all suspensions. Figure revised from Paper IV © 2019 Elsevier Ltd. All rights reserved.

Concentrations of PVP were chosen such that a sufficient range of viscosities was achieved. Increasing the PVP wt% further was found to increase the viscosity further. However, increased concentrations of PVP in the suspensions led to sticky and unmanageable suspensions that proved difficult to de-air and pour into moulds due to too large viscosity. Sintered freeze-cast ceramics would also often show severe crack formation. Thus, a maximum of 10 wt% PVP is used in the present work.

Viscous and standard suspensions were de-aired in vacuum and pre-cooled along with the Teflon moulds in an ice bath for at least 30 minutes prior to freeze-casting.

Gelation

Gelation of LCSM suspensions follows the procedures and considerations discussed in the previous chapter, section 6.1.2. Gelated samples were prepared from the stock suspensions of LCSM9 and LCSM6/CGO with the addition of 1.5 wt%, solid to ceramic ratio, of gelatin from *Sigma-Aldrich*. Samples were gelated directly in the freeze-casting moulds. To ease the de-moulding of samples, the mould was equipped with a piece of foil folded into a cylinder in which the suspension was gelated, as depicted in Figure 7.4. The gelated samples could then easily be removed from the moulds in the foil, avoiding deformation and rupture of the gel. Gelated suspensions were then sliced into 1-2 cm cylindrical specimens. The bottom ~5 mm

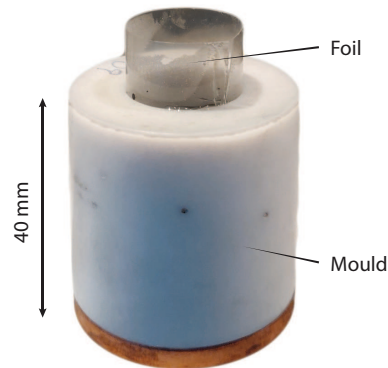


Figure 7.4: Teflon mould with foil to ease de-moulding of gelled samples and transfer of gelled composite samples back into the freeze-casting mould.

was discarded, as Figure 6.14 on page 91 showed a significant lower macroporosity in the bottom part of gelled freeze-casts than throughout the rest of the structure. The gel slices were stacked such that each final sample were composed of a slice of LCSM6/CGO in the bottom and a slice of LCSM9 in the top. The composite samples were then carefully transferred back to a mould by wrapping them in foil and sliding them back into the freeze-casting moulds. Stacked samples were left to settle at 2 °C for 1 hour before freeze-casting.

7.2.2 Freeze-casting

Layered samples were frozen using the freeze-caster with constant cooling rates of -1.5 K/min from an equilibrated temperature of 275 K. A linear temperature profile was chosen to ensure more or less homogeneous pore sizes throughout the samples [9–11, 45], as discussed in Chapter 5. However, in order to achieve a distinct material interface, preparation of samples and freeze-casting procedure were varied depending on altered suspension or freezing conditions as follows:

Stepwise freezing was achieved by the initial freezing of one suspension, followed by freezing of the other suspension. Pre-cooled LCSM6/CGO suspension with B-1022 binder was poured into a mould open to ambient conditions of ~ 5 °C. Sample and mould were equilibrated at a coldfinger temperature of 275 K for 300 seconds before being frozen using a constant cooling rate of -1.5 K/min. The suspension was frozen solid and the mould and frozen suspension were subsequently equilibrated at 270 K by adjusting the coldfinger temperature. Pre-cooled LCSM9 suspension was poured on top of the frozen suspension and frozen by immediately decreasing the temperature of the coldfinger from 270 K by -1.5 K/min until the top suspension was also completely frozen.

Continuous freezing follows the initial procedure of *stepwise freezing*, however, instead of letting the bottom suspension freeze solid, the LCSM9 suspension was added to the

mould just before the freezing front, i.e. the solid/liquid interface, reached the top of the suspension. The freezing front position was evaluated by measuring the temperature along the height of the mould and the position of the freezing front was estimated at the position of 0 °C. A constant cooling rate of -1.5 K/min of the coldfinger was maintained during the entire freezing process until the sample was frozen solid.

Increased viscosity allowed a direct layering of the liquid suspensions. Composite samples were prepared from suspensions of LCSM6/CGO and LCSM9 of the same binder content, respectively. 3 mL of LCSM6/CGO suspension was poured into a mould. Carefully, another 3 mL of LCSM9 suspension was layered on top using a syringe equipped with a 1.2 x 40 mm blunt filling needle. The tip of the needle was positioned such that it barely broke the surface of the first suspension at the approximate center of the mould and the other suspension was very slowly transferred to the mould in order to maintain a layering of suspensions. Mould and layered suspension were left open to ambient conditions of ~ 5 °C and equilibrated at a coldfinger temperature of 275 K for 300 seconds before applying constant temperature change rate of -1.5 K/min until the sample was frozen solid.

Gelation freezing was achieved by freezing the already gelated and stacked samples. Pre-cooled gelated samples in Teflon moulds were mounted directly on the coldfinger of the freeze-caster, left open to ambient conditions of ~ 5 °C, equilibrated at a coldfinger temperature of 275 K for 600 seconds and frozen using a constant temperature change rate of -1.5 K/min until the sample was frozen solid.

Structural & chemical characterization

Following the procedure of Bulatova et al. [102], CGO was added to the LCSM6 phase as a marker to facilitate tracking of that specific phase. The LCSM9—LCSM6/CGO interface was evaluated at cross sections parallel to the freezing direction by SEM micrographs and energy-dispersive X-ray spectroscopy (EDS, Bruker). EDS spectra for elemental analysis were collected at interfaces over 512x384 pixels (pixel size of 3.2x3.2 μm , i.e. a total sample area of 1638x1229 μm), with a 128 μs dwell time per pixel and a total collection time of 600-1800 seconds. Accumulated EDS spectra either over a selection, as illustrated by yellow boxes in Figure 7.5, or over all pixels in a sample area were analyzed using *Quantax Esprit 2.1* software (Bruker Microanalysis Software, Bruker), where deconvolution of peaks was achieved by series fit and quantified by standardless P/B-ZAF method.

The LCSM9—LCSM6/CGO interface was detected by evaluation of Ce-content at a given sample position. Cerium has a distinct L_{α} emission peak at 4.84 keV, as seen in the EDS spectra in Figure 7.5, where accumulated EDS spectra of the selection above and below the interface is shown on the right. The Ce-peak is only clearly visible for the selection below the interface, i.e. the LCSM6/CGO phase. The element analysis was carried out for signals from lanthanum, calcium, strontium, manganese and cerium, thus, the overall analysis yielded the *relative Ce-content* of a given sample at a given position.

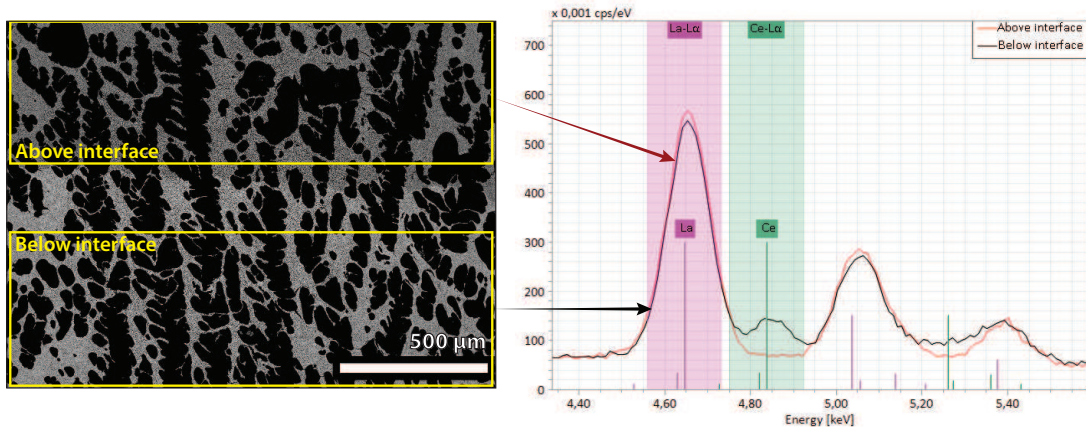


Figure 7.5: Accumulated EDS spectra obtained above and below the LCSM9 and LCSM6/CGO interface, respectively, of a gelated freeze-cast sample. The analyzed region of the sample is indicated by the yellow boxes. The Cerium L_{α} -peak at 4.84 keV is only clearly distinguishable in the accumulated spectra of the selection below the interface. Figure revised from Paper IV © 2019 Elsevier Ltd. All rights reserved.

Accumulated, deconvoluted EDS spectra and identified background for all analysis points can be found as supporting data for Paper IV.

7.3 Graded, multi-material freeze-casts

Freeze-casting of LCSM suspensions with the implementation of stepwise, continuous, highly viscous and gelation freezing all resulted in a distinct layering of suspensions. This yielded a clearly visible and sharp interface between the two layers in both the green and sintered samples, as seen on Figure 7.6, where the white CGO made the LCSM6/CGO phase grey and thereby visually identifiable.

Freeze-casting of a homogeneous suspension of particles generally results in structures with directional porosity in the form of macropores along the freezing direction, which was also the case for samples in this study, as evident from Figure 7.7. However, what is remarkable, is that all procedures except for stepwise freezing, led to continuous pores across the interface. The interfaces in Figure 7.7 are enhanced by adjusting the grayscale threshold of SEM images and correlating these with Ce-mapping in EDS analytical software. For ease of visualization in compressed and printed images a semi-transparent dashed line indicating the interface has been added as an eye-guide.

The relative Ce-content above and below the interfaces given in Figure 7.7 are evaluated as described in Figure 7.5. However, standardless EDS analysis is not sufficient for an exact quantification of the elemental composition. For comparison, EDS elemental analysis of a freeze-cast sample of only LCSM6 still yields a relative atomic Ce-content of 0.32 %. Although, as

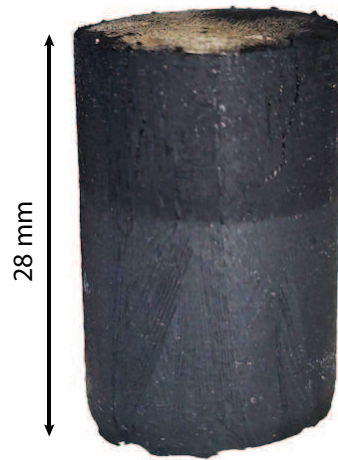


Figure 7.6: Freeze-cast green sample frozen from LCSM6/CGO (grey bottom layer) and LCSM9 (black top layer) suspensions with 5 wt% PVP K30. Figure revised from Paper IV © 2019 Elsevier Ltd. All rights reserved.

the qualitative elemental composition of samples are known, the measured relative Ce-contents can still be evaluated between samples and are in this work thus used as a both visual and chemical marker of the LCSM6 phase.

The pore geometry in freeze-cast ceramics is directly shaped from the growing ice crystals during the freezing phase. Ideally, the material interface should be in the steady-state zone of the freeze-cast samples (see Figure 1.4 on page 10). However, when freezing samples stepwise, the initial suspension frozen in the first step act as a cold side for the second suspension and a new nucleation zone occurs at the interface. This results in a second initial- and transition zone and thus discontinuous pores as is evident from the significant size difference of pores above and below the dashed line in Figure 7.7a). To avoid a second nucleation zone, the second suspension was added before the freezing front had reached the top of the suspension, i.e. while the top of the first suspension was still liquid, and samples were then frozen continuously, eliminating the second transition zone as seen on Figure 7.7b) and ensuring continuous pores.

Generally, freezing conditions were chosen such that they could be kept consistent and reproducible, however, the continuous freezing conditions are much more difficult to reproduce as they rely on exact determination of the freezing front position. Given that the spatial resolution of thermocouples is 4 mm in the current configuration of the freeze-caster, there will always be an uncertainty in immediate determination of freezing-front position and thus inconsistent freezing conditions. Additionally, the freezing front position is estimated at the thermocouple where the temperature is 0 °C, however, freezing point depression due to organic additives and ceramic particulates will lower the actual freezing point of the suspension and thereby increase the uncertainty of the freezing front position. By extension, it should be mentioned, that

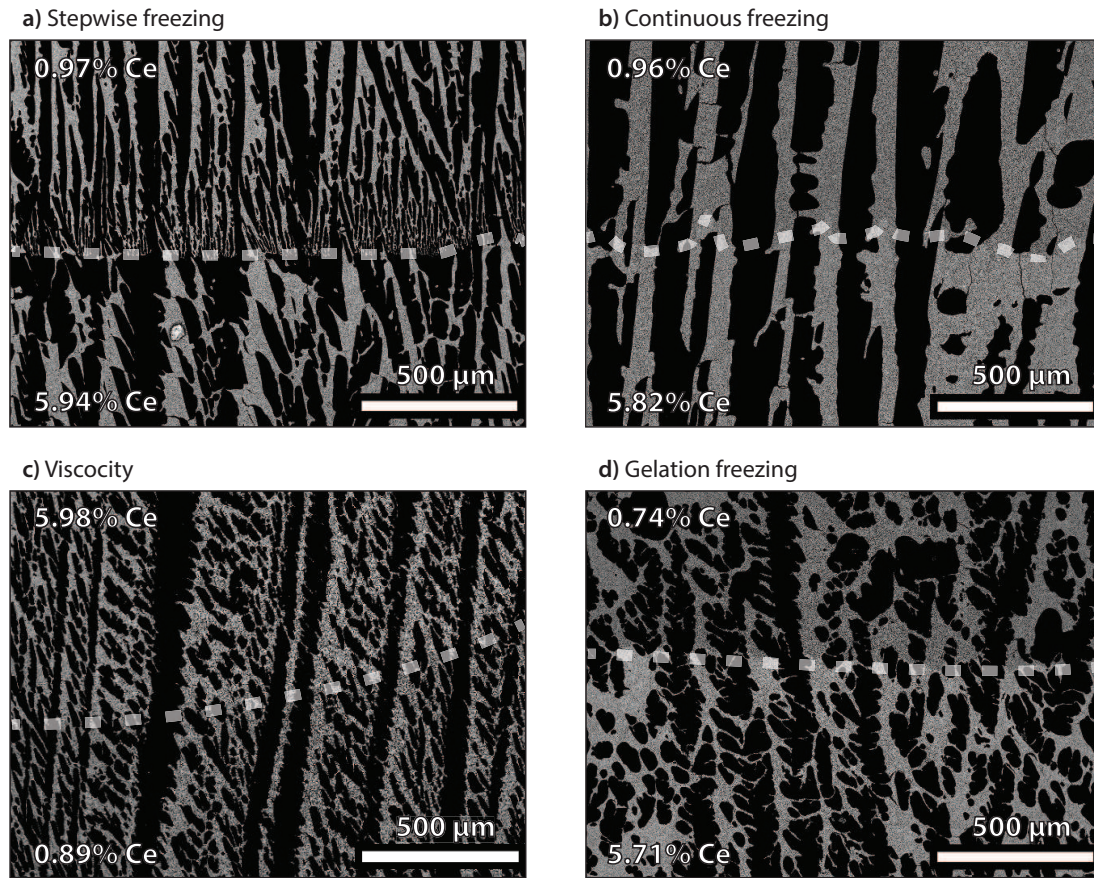


Figure 7.7: SEM micrographs showing the interface between the LCSM9 and LCSM9/CGO layer of freeze-cast samples, where a) is frozen stepwise, b) is frozen continuously, c) is frozen of a suspension with 10% PVP K30 for increased viscosity, and e) is gelated prior to being frozen. The measured relative atomic content of Cerium for the two layers are indicated in the left corners and the dashed lines are eye-guides to emphasise the interface between the two layers. Images are obtained at cross sections parallel to the freezing direction at the approximate center of the samples. Note that (a–b) and (d) are frozen with LCSM6/CGO layer at the bottom, while (c) is frozen with the LCSM6/CGO layer at the top. Figure revised from Paper IV © 2019 Elsevier Ltd. All rights reserved.

continuously frozen samples for which the position of the freezing front was underestimated, resulted in discontinuous pores across the interface similar to those of stepwise freezing, as the conditions for these samples more closely resembled the latter procedure. However, as the interface does appear sharp and more or less planar with continuous pores across, continuous freezing of suspensions is a feasible processing route for achieving distinct layers in a freeze-cast structure for freeze-casting set-ups with precise and immediate monitoring of the freezing front. An obvious approach for immediate tracking of the freezing front is visually. As the freezing front has been found to be a well-defined, slightly concave planer interface perpendicular to

the freezing direction [55], visual tracking has been successful in previous freeze-casting studies with the application of an acrylic glass mould equipped with a scale bar [10, 11]. However, as already discussed, due to the color of LCSM, the freezing front could not be tracked visually.

7.3.1 Structural continuity across interfaces

As the freezing conditions for continuously frozen samples could not be kept consistent and stepwise frozen samples showed a clear discontinuity in pores across the LCSM9—LCSM6/CGO interface, a structural analysis was only carried out for freeze-cast samples frozen from viscous or gelled suspensions. Both of these displayed continuous pores across a distinct interface as is clear from Figure 7.7c–d).

Various viscosities of suspensions were tested in order to clarify the effect of viscosity on the sharpness and possibly the shape of the LCSM9—LCSM6/CGO interface. With the addition of long polymer chains in the form of PVP, the intermolecular forces and entanglement between polymer chains resist flow and thus miscibility of suspensions. The effect increases with increased concentration and length of polymers, e.g. the PVP K90 consists of on average longer chains than PVP K30 and thus results in greater viscosity at similar concentrations. In Figure 7.7c) the interface of a freeze-cast frozen from highly viscous suspensions with 10 wt% PVP K30 is shown. The interface is rather concave in shape. This shape is in accordance with the sample preparation procedure where the LCSM6/CGO suspension is added at the center, pushing the other suspension radially aside, which will inevitably create a concave interface provided that the two suspensions do not mix.

The sharpness and position of LCSM9—LCSM6/CGO interfaces are evaluated by analyzing the relative Ce-content as a function of sample height in the center of the samples as in Figure 7.8 where the sample position is normalized at the interface. An increase in relative Ce-content thus indicates a transition from one layer to the other, where the steeper the curve the sharper the interface. The miscibility of viscous solutions appear to generally be very low and all interfaces are sharp with a steep increase in relative Ce-content. All samples follow this trend, except for the sample frozen from suspensions with the commercial B-1022 binder and thus low viscosity. Here, a significant peak in relative Ce-content is found below the interface, followed by a drop in Ce-content immediately before a steep increase indicating the interface beyond which the relative Ce-content is more or less constant. This is due to the miscibility of the two suspensions, where, presumably, a drop of the LCSM6/CGO suspension has sunk into the LCSM9 phase and mixed. Additionally, the interface of the samples frozen from suspensions with only 5 wt% PVP K30 and thus the second lowest viscosity appears less sharp than for samples frozen from suspension of higher viscosity as the increase in relative Ce-content stretches over 4 mm, indicating a more blurred interface. Although a sharp interface is not achieved, these results hint that a graded interface could possibly be achieved by application of suspensions of fine-tuned viscosities somewhere between that of the B-1022 suspensions and that of the 5 wt% PVP K30 suspensions. Alternatively, a graded interface could be achieved by

layering of three or more highly viscous suspensions with one or more mixed LCSM6/LCSM9 phase(s) between the two pure ones.

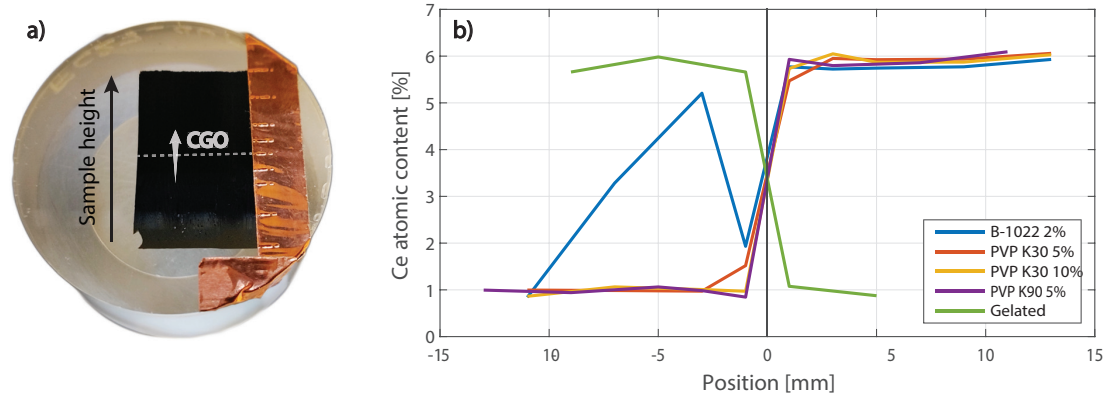


Figure 7.8: CGO as a marker indicating the LCSM6 phase. a) Cross section of graded, freeze-cast sample, mounted in epoxy. The sample height, CGO gradient and approximate interface is indicated by a black arrow, a white arrow and a dashed line, respectively. The dented copper tape acts as a scalebar to indicate sample position along the sample height during SEM imaging. b) Relative atomic Ce-content as a function of sample height for samples with varying viscosity or an initial gelation-step prior to freezing, evaluated using EDS elemental analysis. The greater the viscosity, the sharper the interface. Note that samples with B-1022 binder and PVP polymers are frozen with the LCSM6/CGO layer at the top, while the gelated sample is frozen with the LCSM6/CGO layer at the bottom. b)-part of figure revised from Paper IV © 2019 Elsevier Ltd. All rights reserved.

The freezing kinetics and thus resulting pore size and shape strongly depend on suspension properties such as particle size, viscosity and powder load [9, 33]. Extra care was therefore taken to ensure equivalent particle loads, viscosities and particle sizes of both the LCSM9 and LCSM6/CGO suspension, as described in section 7.2.1, which ensured structural continuity across the interface. Figure 7.9a-c) show structural properties of samples frozen from viscous and gelated suspensions. Structural features of freeze-cast samples were characterized by image analysis of SEM images, as described in section 3.3. Continuity of all structural properties is maintained across the interface, however, with a slightly increasing mean pore size for all samples in Figure 7.9a). Although, it is not unambiguous that the increase in mean pore size is due to changes in suspension properties. As discussed in Chapter 5 and 6, linear temperature profiles does not completely compensate the increasing thermal resistance in the growing frozen part of the sample during freezing and as such, an increase in pore size is seen throughout the sample lengths. A vague tendency of decreasing freezing front velocities throughout samples are seen in Figure 7.9d), however, the data is too scattered to draw any definitive conclusions. Although, the freezing front velocity for all samples is $\sim 13 \mu\text{m/s}$ independent on gelatin or polymer content.

For gelated samples the interface between the two layers of LCSM9 and LCSM6/CGO di-

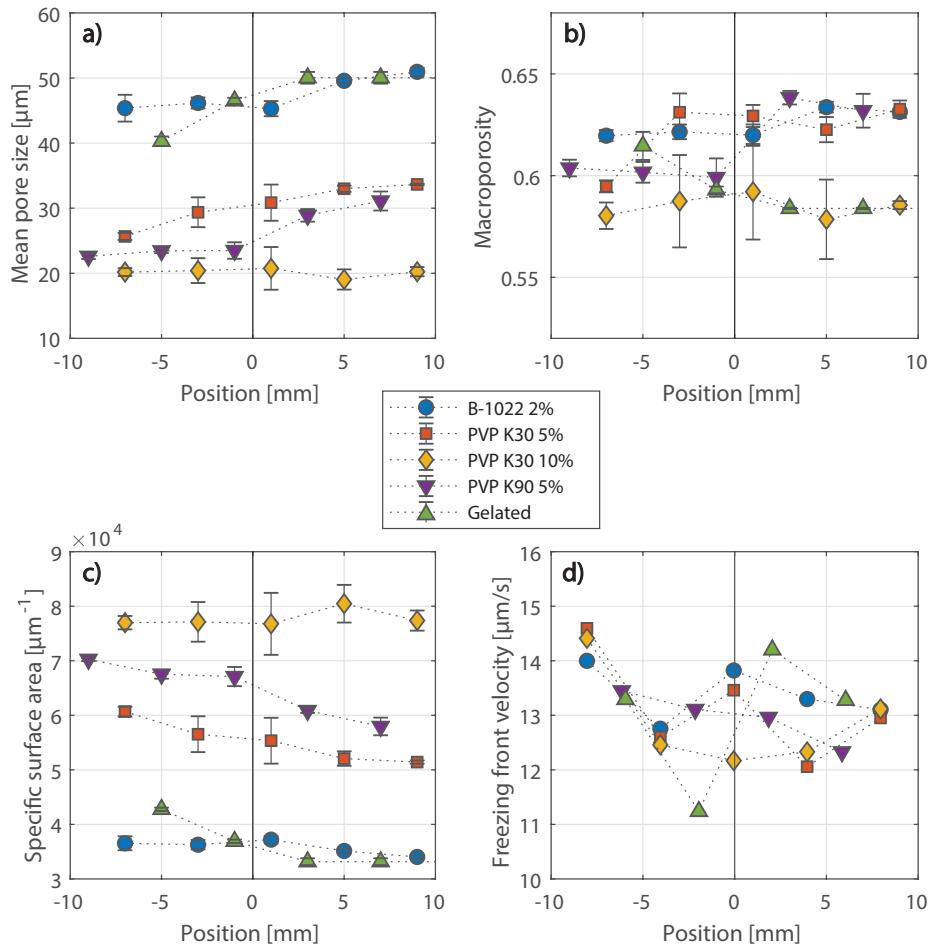


Figure 7.9: Structural characterization of freeze-cast samples across the LCSM6/CGO—LCSM9 interface, where a) mean pore size, b) macroporosity and c) specific surface area are all evaluated from image analysis of SEM micrographs. In d) estimated freezing front velocities are given, all samples are frozen using the same freezing rate of the coldfinger of -1.5 K/min. Figure revised from Paper IV © 2019 Elsevier Ltd. All rights reserved.

rectly reflects the shape of the cut-out specimens of gelled suspensions. Gelation of suspensions prior to freezing thereby ensures a sharp and planar material interface, as seen on Figure 7.7d). With a homogeneous and proper gelation, the shape or possible tilt of the interface can be fine-tuned along with the layer thickness and geometry. However, introducing a gelation-step also introduces additional possibilities of structural failure, as shown in Figure 7.10. Figure 7.10a) illustrates delamination which can occur if the stacking of gelled suspensions are sloppy. Samples that were not stacked carefully prior to freezing were found to delaminate and fracture along the interface.

Another critical failure in gelled freeze-cast structures is due to circular voids in the fired structure due to bubbles in the suspension, as can be seen on Figure 7.10b). As the suspension is heated and stirred using a propeller immediately before gelation, it is possible that air will be stirred into the solution forming bubbles. The freeze-cast in Figure 7.10b) was left to gelate without being de-aired in vacuum, and thus, circular cavities were found in the fired ceramic. As in gelcasting [127], de-airing the suspension immediately after it had been transferred to the mould proved efficient for eliminating bubbles and thus cavities.

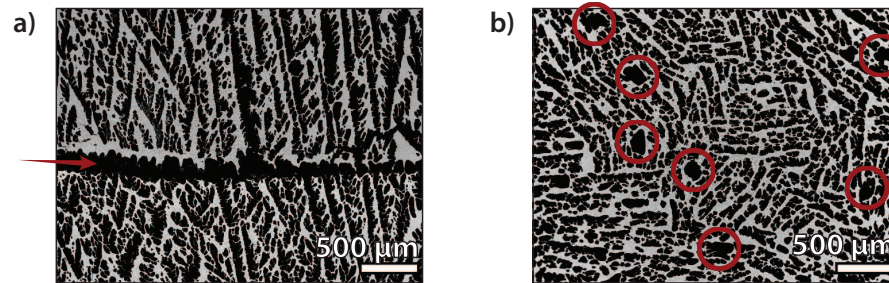


Figure 7.10: Examples of failed gelled samples with a) delamination along the interface due to faulty stacking of gelled specimens and b) circular cavities in the structure due to bubbles in the suspension that was trapped during gelation. Figure revised from Paper IV © 2019 Elsevier Ltd. All rights reserved.

7.3.2 Structural geometry and additives

Changing the suspension composition and properties significantly changed the resulting pore morphology as revealed in Figure 7.9a–c) where changes of the pore, or channel, morphology due to the addition of either PVP or gelation freezing is evident from the changing structural parameters. This is also clear by simple visual inspection of SEM micrographs of cross sections perpendicular and parallel to the freezing direction, as shown in Figure 7.11.

While the measured macroporosity is more or less the same for all samples independent of additives, Figure 7.9b), this is not the case for pore sizes, Figure 7.9a). Freeze-casts prepared from highly viscous suspensions generally exhibited smaller pore sizes than samples frozen from low viscosity or gelled suspensions. During freezing, the long, entangled polymer chains

presumably inhibit the fluidity of the highly viscous suspensions, thereby limiting the diffusion of water molecules to the growing ice crystals. The inhibited diffusion of water molecules results in smaller ice crystals and thereby smaller pores in the fired freeze-cast. This effect is significant when comparing the pore sizes in Figure 7.11a) and b). Accordingly, the inverse phenomena is seen for the specific surface area, Figure 7.9c), which is larger with increased viscosity and thus smaller pore sizes. The addition of PVP and pre-gelation does not seem to significantly affect the measured freezing front velocities plotted in Figure 7.9d). Ice crystal growth along the thermal gradient during freeze-casting is thus not significantly affected by PVP or gelatin, meanwhile, the radial growth of ice crystals is suppressed due to limited diffusion of water.

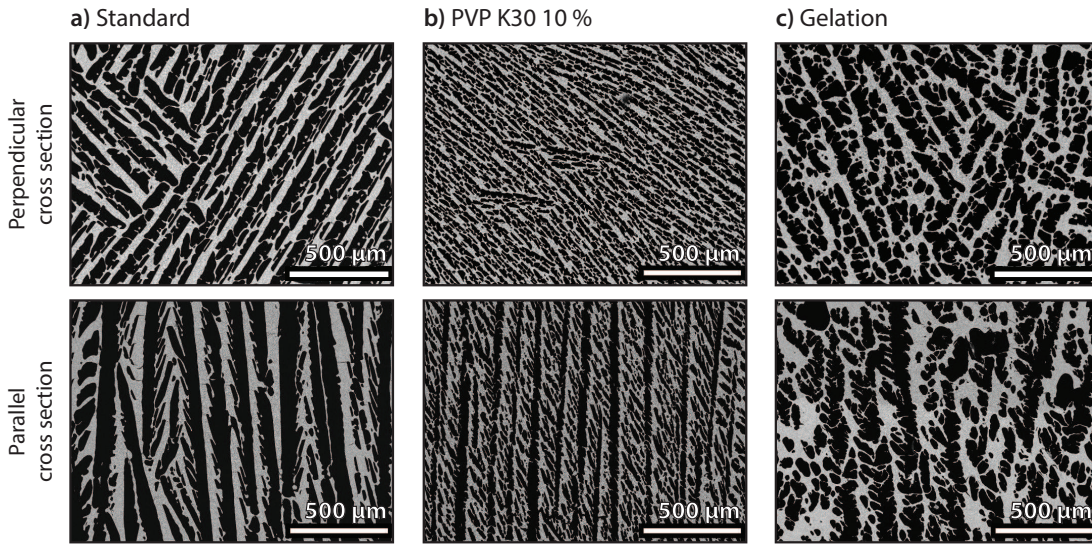


Figure 7.11: SEM micrographs of freeze-cast cross sections of a) a standard sample with DURAMAX™ binder, b) a sample with 10 wt% PVP K30 for increased viscosity and c) a gelated sample. Micrographs are obtained at sample heights of 8 mm of samples frozen at constant freezing rates of -1.5 K/min. The ceramic solid load for all suspensions were ~ 20 vol%.

A thorough discussion of the effect of gelation on morphology can be found in Chapter 6. Additionally, the effect on the pore morphology due to addition of polymers resulting in an increased viscosity [33] and pre-gelation using gelatine [45, 131, 138]. Additionally, all samples frozen with various concentrations of PVP or pre-gelation, was found to be easily infiltrated with epoxy, indicating high interconnectivity of pores; a very crucial property of freeze-cast with the prospects of being a medium for fluid flow. To fully quantify the interconnectivity of pores, 3D characterization of tomography data is required.

7.4 Summary

Functionally graded freeze-casts of LCSM6 and LCSM9 with continuous microchannels and structural integrity were engineered by implementation of stepwise, continuous, highly viscous and gelation freezing. All procedures were based on a criteria of inhibiting or altogether eliminate flow/miscibility in the suspensions in order to layer these wet in wet to ensure continuous ice crystal growth during freeze-casting. All procedures resulted in a distinct layering of suspensions, yielding a clearly visible and sharp interface between the two material layers in both the green and sintered samples. The latter three procedures resulted in continuous pores across the interface.

The two chemically very similar phases of LCSM6 and LCSM9 were successfully distinguished from one another by the addition of 10 wt% CGO to the LCSM6 phase, making it possible to track this phase using EDS analysis in order to evaluate the relative atomic Ce-content and using this as a marker.

Keeping the solid load and particle size distribution of all suspensions consistent, while ensuring an approximate constant freezing front velocity of $\sim 13 \mu\text{m/s}$ by implementing a constant temperature change rate of -1.5 K/min during freeze-casting, a structural continuity was maintained across the LCSM9—LCSM6/CGO interface. While the interface was concave in shape for frozen viscous suspensions, the interface of gelated samples directly reflected the shape of the cut-out specimens of gelated suspensions, thus ensuring a sharp and planar material interface. The overall pore morphology was found to reflect the changes in suspension properties. While the macroporosity of freeze-casts was found to be independent of changes in additives and gelation, the overall pore size of freeze-casts was found to decrease with an increase in PVP concentration and thus the viscosity. Both gelation and addition of PVP changed the pore morphology of freeze-cast specimens.

Although the procedures described here requires additional optimization of e.g. sintering, freeze-casting of both layered viscous suspensions and gelated suspensions represent attractive processing routes for magnetocaloric freeze-cast regenerator geometries of graded Curie temperatures.

Freeze-cast regenerators

The initial curiosity which sparked the realization of the present work, was a desire to implement and evaluate the fine micrometer sized structural features and anisotropic porosity of freeze-cast materials as a regenerator geometry in magnetic refrigeration. However, to do so, the whole processing route of freeze-casting of magnetocaloric materials had to be investigated. This chapter summarizes and discusses some of the processing levers of freeze-casting which are relevant for fabricating freeze-cast regenerator geometries. The processing and fabrication of four freeze-cast regenerators are presented and some of the most notable results regarding the heat transfer and cooling performance are summarized.

Thus, this chapter is partly based on results presented in Paper II and Paper V.

8.1 Processing of freeze-cast regenerators

Throughout the previous chapters of this thesis, many levers for adjusting the morphology and structural features of freeze-casts have been presented. Generally, structural homogeneity throughout the freeze-cast is crucial for regenerator applications as the flow conditions must be more or less independent on flow direction. Therefore, freeze-cast samples characterized throughout this work have been analyzed as a function of height, and optimized for large degree of homogeneity throughout the sample lengths. Figure 8.1 summarizes the three most significant levers for adjusting the structural features significant for regenerator applications of LCSM freeze-casts, as the effect of pore and wall size, macroporosity and specific surface area are evaluated as a function of freezing rate, solid load and sintering time. All structural features are evaluated by image analysis as described in section 3.3.

We see that pore and wall sizes are controlled by the freezing rate, with the width of the latter also depending slightly on sintering time as the inter-particle microporosity decreases, as discussed in section 3.2.3. Macroporosity is controlled by solid load, while the specific surface area typically increases with decreasing pore and wall size, i.e. with increasing freezing rate.

An additional row to Figure 8.1, is of course understanding the mechanical integrity of LCSM freeze-casts with the variables given. Porter et al. [33] found that smaller pore areas increase mechanical strength, while Lin et al. [48] and Seuba et al. [44] both found that increased solid load resulting in decreased porosity yields an increase in mechanical strength of freeze-cast structures. However, Deville et al. [49] concluded – based on a meta-analysis of the mechanical properties of freeze-cast ceramics – that the relationship between pore size, porosity

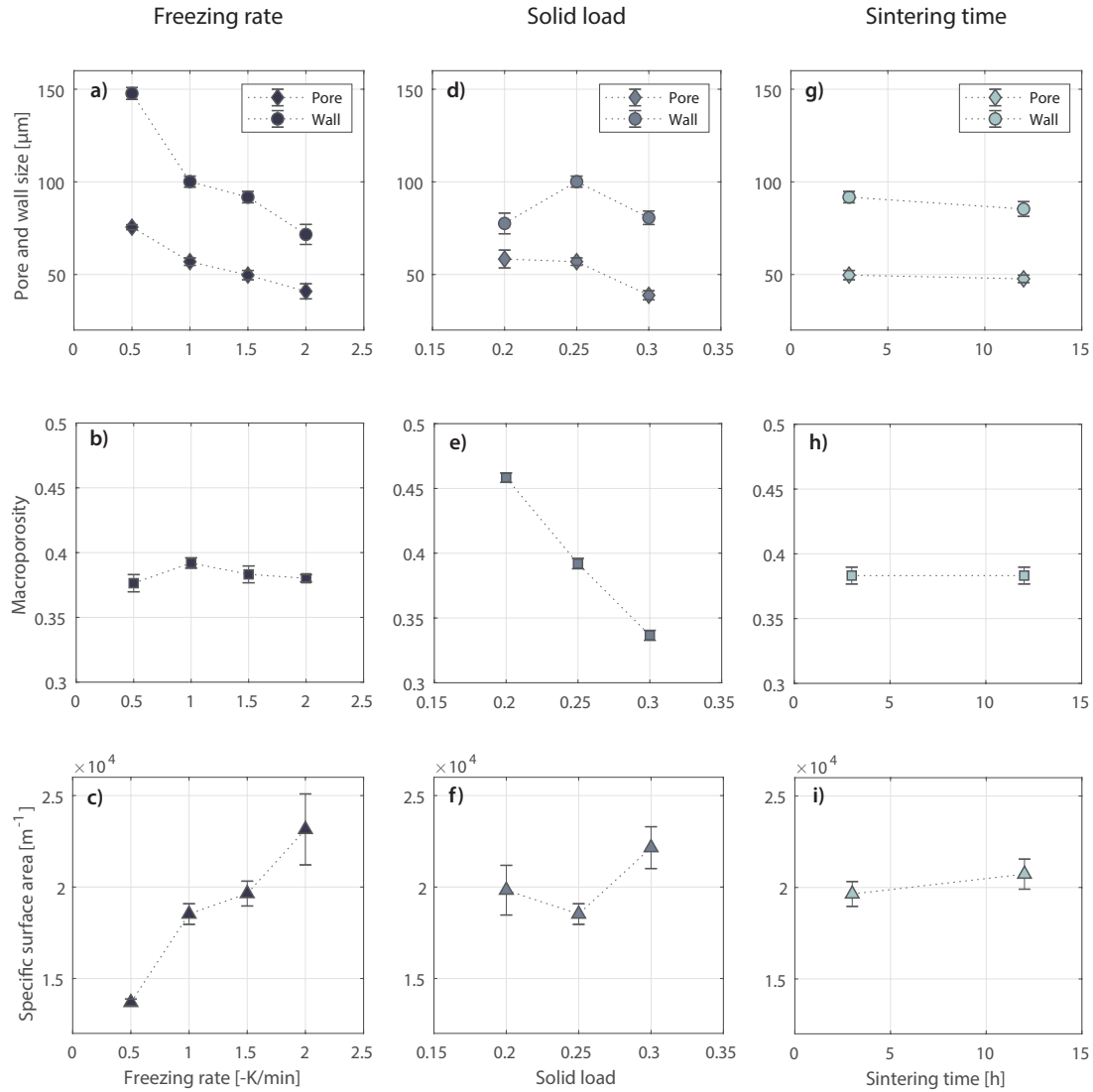


Figure 8.1: Levers for controlling structural features of LCSM freeze-casts. The effect on pore and wall size, macroporosity and specific surface area as a function of freezing rate (a–c), solid load (d–f) and sintering time (g–h). For each column, only one parameter is varied, while the rest is maintained constant accordingly: freezing rate of -1.5 K/min, solid load of 25 vol% and sintering time of 3 hours.

and mechanical strength for water-based freeze-cast ceramics is not exactly as straightforward. They found that for high porosity studies, larger pores increase the mechanical strength. Meanwhile, for low porosity studies, they found the inverse correlation, i.e. smaller pores increase mechanical strength. As the performance of microchannel-geometries is expected to increase with increasing porosity (>0.5) for channel widths in the order of $10\text{--}100\ \mu\text{m}$ [89], this might be very relevant to investigate for LCSM freeze-casts.

8.1.1 Mechanical integrity during processing

Generally, the mechanical strength of freeze-cast ceramics is much greater along the axis parallel to the pore orientation than perpendicular to the pore orientation [47, 48]. In fact, LCSM freeze-cast samples were found to deform and the lamellar pores collapse if handled such that too much pressure was applied perpendicular to the pore orientation just by handling them by hand. This posed a challenge regarding processing of freeze-cast ceramics for regenerators. As the bottom and top part of freeze-cast ceramics needed to be removed for mounting in a cylindrical housing, samples had to be mounted in a holder for cutting them using a cut-off saw equipped with a diamond blade (Accutom-5, Struers). The mechanical durability of freeze-cast samples for structural characterization was increased by infiltrating these with epoxy. However, this would require a careful subsequent burnout of epoxy for freeze-cast ceramics for regenerators. Instead, the radial surface of freeze-casts were coated with a thin layer of suspension using a small paint brush. A raw and a coated green body freeze-cast sample are shown in Figure 8.2. From the

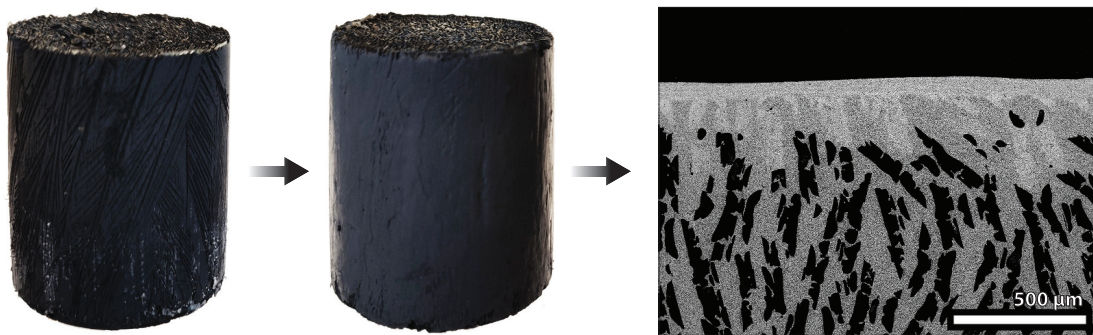


Figure 8.2: Coating of sample to increase mechanical strength around the edge.

figure, open macropores can be seen on the radial surface of the raw sample. A $50\text{--}70\ \mu\text{m}$ layer closed all the open macropores, increasing the mechanical durability around the edge and – following sintering – made it possible to mount the freeze-cast samples for regenerators in a holder without damaging them. As can be seen on the SEM micrograph in Figure 8.2, the coating layer did not penetrate further into the freeze-cast than a few hundred micrometers.

8.1.2 Regenerator specifics

Freeze-cast regenerators were processed over two experimental series. Regenerator #4, *series I*, and regenerators #1–3, *series II*, as indicated in Figure 8.3 and Table 8.1. All freeze-cast structures for regenerators – a total of eight as each regenerator was composed of two pieces, see section 8.1.3 – were prepared as described in Chapter 3 and 5 from aqueous suspensions of 30 vol% LCSM and using a mould with an inner diameter of 30 mm. However, as discussed in section 5.4, reproducibility of freeze-casts across various ceramic suspensions within the framework of this work cannot be assumed. Thus, regenerators are also distinguished according to their "batch" or experimental series. Looking at Figure 8.3 we see that this is a very relevant distinction, as there is an evident visual difference between the structural features of *series I* and *series II*, with more ceramic dendrites and bridges in samples from the latter. Additionally, considering Figure 8.1a), and the inverse proportionality between freezing rate and pore/wall size demonstrated there, the pore size of regenerator #4 is expected to be somewhere between that of regenerator #1 and #2 given that the freezing rate is in between. However, as summarized in Table 8.1, regenerator #4 shows the largest pore width of all the fabricated regenerators.

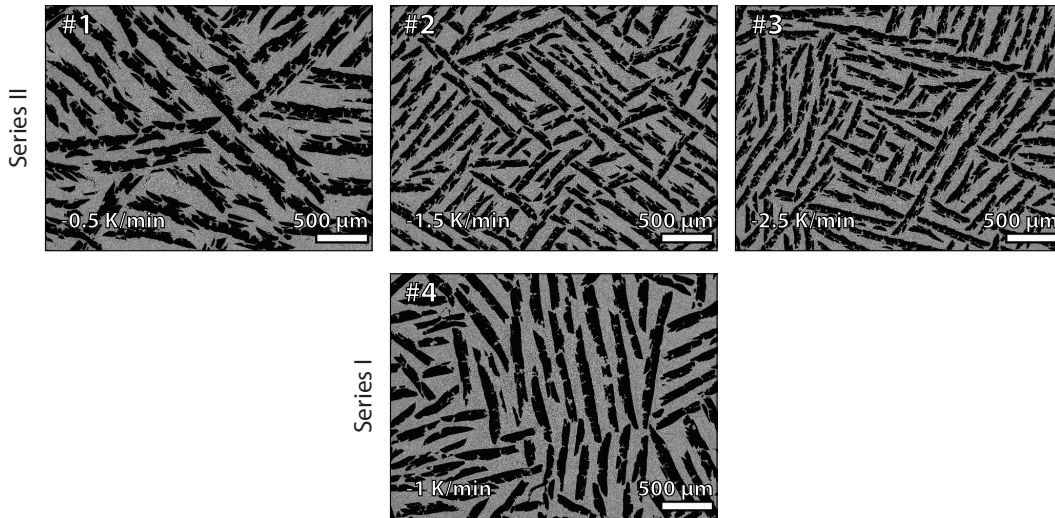


Figure 8.3: Regenerator cross sections. Sample height 15 mm – i.e. middle of regenerator piece.

Regenerators were produced over two experimental series, as *series I* was initially fabricated to establish procedures for mounting, testing and preliminary evaluation of mechanical integrity and performance, while *series II* was fabricated to evaluate the performance of freeze-cast regenerators with varying structural features, specifically pore width and specific surface area.

The hydraulic diameter, D_h , is defined as four times the ratio between the cross sectional pore area and the perimeter of the pore [90]. For freeze-cast structures it can thus be calculated

Table 8.1: Geometrical parameters of the freeze-cast regenerators #1–4 from two sample series. Structural characteristics are from image analysis of scanning electron micrographs. The corresponding measurements for each regenerator are based on the analysis of 15 images evenly distributed along the axial direction and are given as an average. A single freeze-cast regenerator matrix is composed of two combined monolithic pieces of freeze-cast samples frozen at identical conditions and thus with homogenous structural characteristics.

Parameters	Series II			Series I
	#1	#2	#3	#4
Pore width (μm)	66.3 \pm 4.6	49.6 \pm 4.6	43.1 \pm 5.1	71.6 \pm 6.4
Porosity (%)	73	72	73	72
Macroporosity (%)	41.5 \pm 0.6	42.0 \pm 0.6	44.1 \pm 0.5	42.0 \pm 0.8
Hydraulic diameter (μm)	94.9 \pm 7.8	75.0 \pm 6.9	66.3 \pm 8.3	104 \pm 7.6
Specific surface area ($\times 10^4 \text{ m}^{-1}$)	1.75 \pm 0.11	2.24 \pm 0.16	2.66 \pm 0.27	1.61 \pm 0.08
Tortuosity	1.75 \pm 0.14	1.75 \pm 0.31	1.62 \pm 0.40	1.61 \pm 0.3
Mass (g)	29.85	29.33	30.04	27.33

from the macroporosity, ϵ_m , and specific surface area, α , [143]:

$$D_h = \frac{4\epsilon_m}{\alpha} \quad (8.1)$$

LCSM freeze-casts for fabrication of regenerators were sintered for 12 hours with the hope of reducing inter-particle microporosity in the walls. However, as discussed in section 3.2.3, and illustrated in Figure 3.11 on page 39, the effect of increasing the sintering time from 3 hours to 12 hours only has a limited effect in reducing the ratio of macroporosity to total porosity, $\frac{\epsilon_m}{\epsilon}$, from 0.52 to 0.54. Thus, there was still a large degree of microporosity retained in the walls of the freeze-cast structures from which regenerators were fabricated.

8.1.3 Mounting & housing

A single freeze-cast regenerator matrix is composed of two combined monolithic pieces of freeze-cast ceramic frozen at identical conditions and thus with presumably homogenous structural characteristics. Two pieces were used to ensure a sufficient length and thermal mass of the regenerator for the AMR system used. Each piece of 15 mm was cut from a full freeze-cast sample with a length of approximately 29 mm. Due to the nature of freeze-cast ceramics, the bottom part of the sample does not contain aligned channels [28, 55] (the initial- and steady-state zone of Figure 1.4 on page 10) and thus the bottom 8 mm and remaining top of the samples were discarded. The matrix was mounted in a resin housing ($\text{\O}30 \times 40$ mm) using silicone glue, sealing possible gaps between the housing and the solid matrix and thus avoiding fluid flowing around the freeze-cast matrix. A mounted freeze-cast regenerator is shown in Figure 8.4.

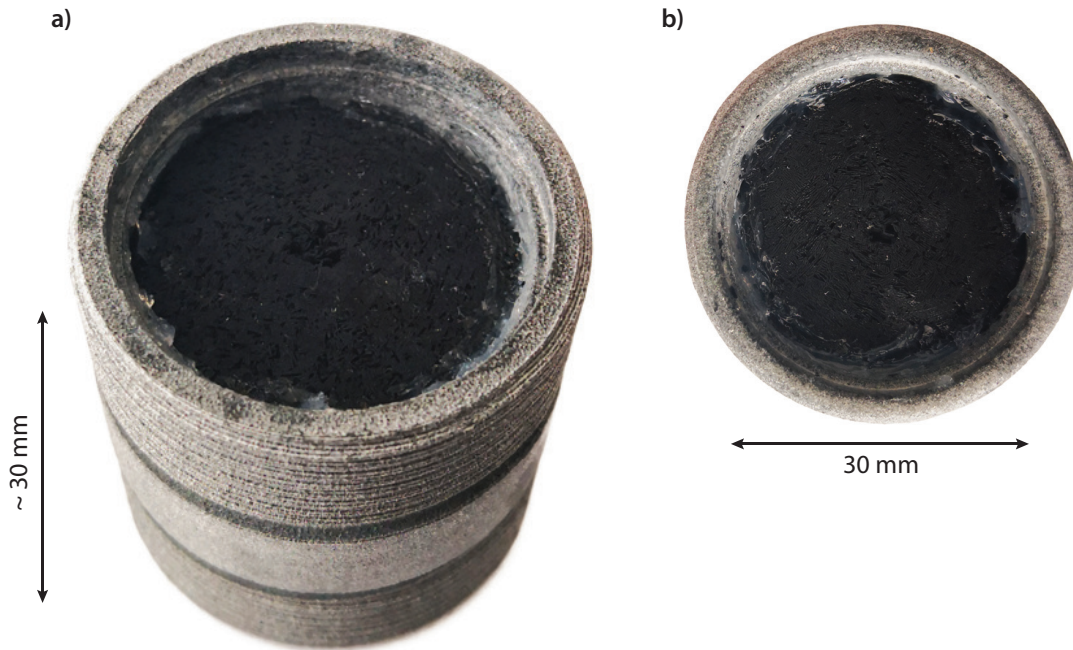


Figure 8.4: Freeze-cast regenerator composed of two combined pieces of freeze-cast LCSM ceramic. Picture credit: Jierong Liang.

8.2 Performance of freeze-cast regenerators

The performance of freeze-cast regenerators were tested by Jierong Liang, Ph.D. student at DTU, and this section is thus merely a summary of the most significant results regarding the performance of freeze-cast microchannel structures as active and passive regenerators. For a full account of experimental procedures and results, the reader is referred to Paper II and Paper V.

The AMR cycle is described in Chapter 2. Simulating operating conditions of this, the performance of fabricated freeze-cast regenerators were evaluated in a passive and an active rig, i.e. oscillating fluid flows without and with magnetization/demagnetization of the regenerator, respectively. Both testing rigs are custom-built at DTU.

Passive rig: In passive testing, the regenerator serves as a thermal storage heat exchanger, where the regenerator is mounted with a cold reservoir at one end, i.e. the cold end, and a hot reservoir at the other end, i.e. the hot end. The heat transfer between the regenerator and liquid is then evaluated over a period of two fluid flows or blows: 1) hot-to-cold blow: fluid from the hot reservoir is pushed through the regenerator, while heating up the regenerator on its way; 2) cold-to-hot blow: the flow is reversed, now pushing fluid from the cold reservoir towards the hot reservoir, making the regenerator

release its heat to the fluid. During testing, the frequency of the oscillating flow can be varied, and temperature profiles of both the hot and cold end are obtained as well as measurements of the pressure for evaluation of the pressure drop across the regenerator during operation. The passive test rig was developed and described in detail by Lei et al. [90, 95]. A schematic of the passive test rig can be found in Paper II.

Active rig: The principle of operation of the active rig is similar to that of the passive rig, although, with additional magnetization and demagnetization steps: 1) magnetization: a magnetic field is applied across the magnetocaloric regenerator, by moving the regenerator into the field of a cylindrical Halbach magnet (maximum field strength of 1.1 T [144]), and the magnetocaloric material heats up due to the magnetocaloric effect; 2) cold-to-hot blow: fluid is pushed through the regenerator from the cold reservoir towards the hot reservoir and the regenerator releases its excess heat to the fluid; 3) demagnetization: the applied magnetic field is removed by removing the regenerator from the Halbach magnet and the temperature of the magnetocaloric material drops; 4) hot-to-cold blow: the fluid flow is reversed, being pushed from the hot reservoir to the cold, heating up the regenerator while it absorbs heat from the fluid. During testing, the performance is evaluated by the achievable temperature span across the regenerator by evaluating the temperature profiles at both the hot end and the cold end. Additionally, for a fixed temperature span, a cooling load can be applied using a small heater at the cold end. The active rig was developed and described in detail by Bahl et al. [145]. A schematic of the active test rig can be found in Paper V.

8.2.1 Passive (& active) characterization

In the passive rig, the regenerator performance can be evaluated by its heat transfer coefficient – quantified by Nusselt number, Nu , and Reynolds number, Re – effectiveness and pressure drop. Figure 8.5 show the correlation between Nu and Re for freeze-cast regenerator #4. Nu describes the convective heat transfer at the boundary of a fluid flow, and is defined as follows [125]:

$$Nu = \frac{h D_h}{k_f} \quad (8.2)$$

where h is the heat transfer coefficient – i.e. the heat flow across an area driven by a temperature difference – and k_f is the thermal conductivity of the fluid.

Re describes the behaviour of fluid flow, with low Re indicating laminar flow and larger Re indicating turbulent flow, and is defined as follows [125]:

$$Re = \frac{\rho_f \frac{v_f}{\epsilon_m} D_h}{\mu_f} \quad (8.3)$$

where ρ_f , v_f and μ_f are the fluid density, velocity and dynamic viscosity, respectively.

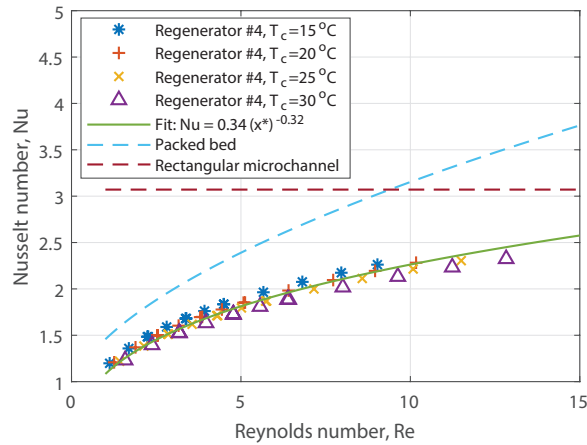


Figure 8.5: Correlation between Nusselt number and Reynolds number for freeze-cast regenerator #4, for various cold end temperatures, T_C . The plot of the packed bed is from Engelbrecht [146], while that of the rectangular microchannel geometry (aspect ratio of 3.0) is from Incropera and DeWitt [147]. Figure revised from Paper II.

From Equation (8.2) and (8.3) we thus see that correlating Nu with Re yields the behaviour of the heat transfer coefficient with changing fluid velocity. Additionally, as geometrical/dimensional features of the regenerator – D_h and ϵ_m – are contained within the expressions of Nu and Re , this allow us to directly compare the heat transfer coefficient of freeze-cast regenerator #4 with that of the packed bed [146] and microchannel [147] geometries, as indicated by dashed lines in Figure 8.5. From the figure it is seen that the trend of the behavior of Nu with Re for regenerator #4 is similar to that of the packed sphere bed [146], with the latter eventually outperforming regenerator #4. Meanwhile, both are different from the constant relationship between Nu and Re for rectangular microchannels which resembles that of parallel plate geometries [90, 148], the latter with $Nu \sim 7.54$ [147]. In principle, this behavior means that during operation, we can increase the heat transfer performance of the freeze-cast regenerator by increasing the fluid flow velocity, up to a certain point, while this is not the case for the parallel-plate regenerators [98, 148]. In a household refrigeration application it is desirable to be able to adjust the cooling power dynamically. E.g. a refrigerator requires a larger cooling power as groceries of ambient temperature are stored, while less cooling power is required as the groceries have been cooled. This adjustment is possible with packed spheres and freeze-cast regenerators, but not so much for e.g. parallel plates.

From Figure 8.5 it appears that Nu , and thus the heat transfer coefficient, of the packed bed outperforms that of the freeze-cast regenerator, however, h is given per area and thus, in order to evaluate the overall heat transfer performance of the full regenerator structure, the overall interface area between the solid and fluid must be taken into account as well. This is done in Figure 8.7, which we will return to a little further on in this section.

The effectiveness of regenerator #4 compared to that of various packed bed geometries is evaluated as a function of utilization in Figure 8.6. The effectiveness of a regenerator is defined

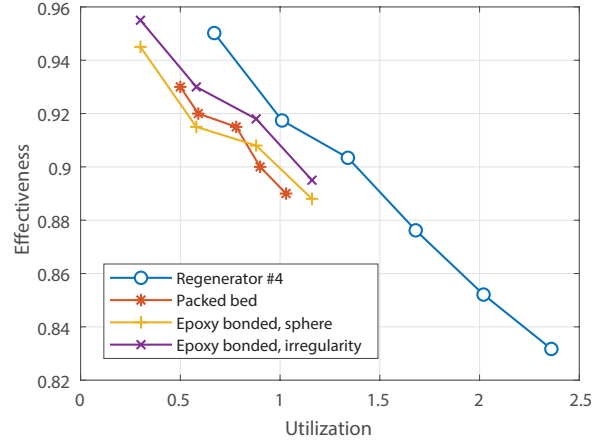


Figure 8.6: Effectiveness as a function of utilization for regenerator #4. Figure revised from Paper II.

as the ratio between the amount of heat transferred between the liquid and the solid during a blow cycle and the heat available for transfer due to the temperature difference between the liquid and the solid [90]. Accordingly, utilization indicates the operating conditions being the ratio between the thermal capacity of the fluid flowing through the regenerator during a blow cycle and the thermal capacity of the regenerator. As is evident from Figure 8.6, the effectiveness of the freeze-cast regenerator is greater than that of the various packed bed geometries.

Figure 8.7 show the correlation between the heat transfer performance quantified as UA – which is the heat transfer coefficient times the regenerator surface area – and the pressure drop. The pressure drop is the difference in pressure across the regenerator, and as discussed in Chapter 2, a high pressure drop requires greater pump power and increases the viscous dissipation [91], i.e. the internal friction in the fluid where kinetic energy of the fluid is lost as it is converted into heat, heating up the fluid instead. The latter being one of the major loss mechanisms in AMRs [67, 90].

The evaluated heat transfer performance of freeze-cast regenerators are found to exceed that of the packed bed regenerator, as seen on Figure 8.7a). Evaluating the heat transfer performance of freeze-cast regenerators compared to geometrical features of the freeze-casts, regenerators with a smaller pore width, and thus a larger surface area, were found to have higher heat transfer effectiveness, as seen on Figure 8.7b). Additionally, regenerators with smaller pore widths also showed an overall higher cooling performance when evaluating the specific cooling capacity and temperature span between regenerators #1 and #3. Although, the temperature spans and cooling capacities of LCSM freeze-cast regenerators achieved in the active testing rig are small, this can primarily be attributed to the low adiabatic temperature

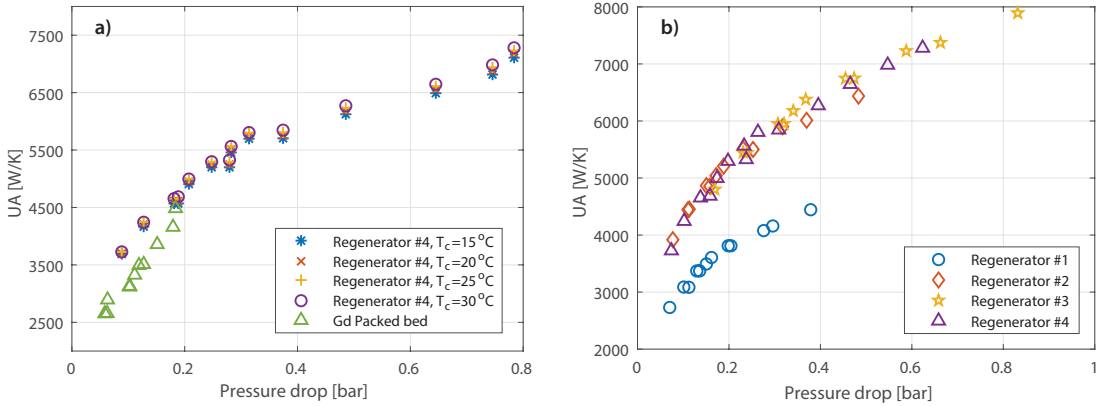


Figure 8.7: Heat transfer performance with pressure drop for a) regenerator #4 at various cold end temperatures, T_c , compared to a Gd packed bed regenerator, and for b) freeze-cast regenerators of varying channel size. Figure a) revised from Paper II. Figure b) revised from Paper V.

change in LCSM compared to other state-of-the-art magnetocaloric materials [71, 75–78]. As the heat transfer effectiveness in the passive testing showed very promising results, freeze-cast materials are suggested as future regenerator geometries – not just for AMRs, but as passive heat exchange geometries as well.

Returning to Figure 2.7, introduced in Chapter 2, we can now place the freeze-cast regenerator geometry relative to the previously introduced geometries as shown in Figure 8.8, with the freeze-cast regenerator geometry demonstrating a large effectiveness but also a high pressure drop.

8.2.2 Mechanical integrity during operation

A magnetocaloric regenerator for application in a device running continuous AMR cycles, undergoes a great mechanical stress during operation. I.e. a fluid flow is constantly being pushed through the interior channels while the material is simultaneously being introduced into and pulled out of an external magnetic field. If the regenerator start to degenerate and fracture under operation, this might lead to blocked channels and a resulting significant decrease in performance, or even worse, the regenerator simply crumpling away.

The four regenerators evaluated in Paper II and Paper V were all tested in a passive device running hundreds of hours with oscillating fluid flow. Initially, for all LCSM freeze-cast regenerators a fine ceramic powder was found in the fluid, however, this was only the case for the first few experiments, after a short while, no more powder came out with the fluid during operation. Additionally, no change in performance was observed when comparing initial and final performance parameters, i.e. same operating conditions, but with hundreds of operational hours in between. This indicates a satisfactory operational and mechanical integrity of LCSM freeze-cast ceramics.

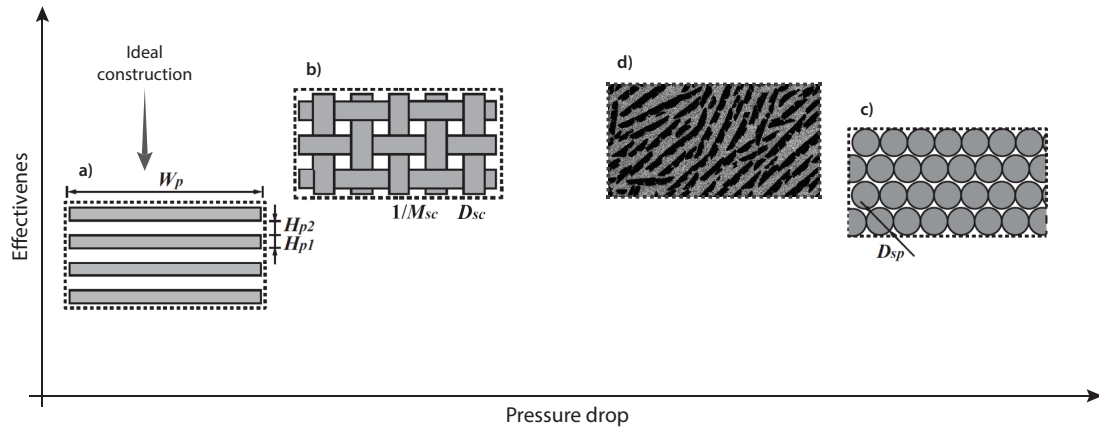


Figure 8.8: Revision of Figure 2.7, placing the a) parallel-plate, b) packed screen bed, and c) packed particle bed geometries relative to one another regarding effectiveness and performance, here including the d) freeze-cast regenerator geometry. Flow direction is defined perpendicular to the plane. Note that the effectiveness of an ideally constructed parallel-plate regenerator is high, but in reality a lot lower [92, 93]. Plot is based on results evaluated for: parallel plates; [89–93, 98] packed screens; [89, 90, 94] packed beds; [89, 90, 95] as well as Paper II and V. Insert a), b) and c) adapted from Lei et al. [89].

Moreover, the tested regenerators showed no degeneration in either performance nor physical appearance following testing in both the passive and active rig, except one. Regenerator #1, with the second largest average pore width and greatest amount of ceramic dendrites and bridges developed severe cracks when subjected to a periodic magnetic force. Although, increased ceramic bridging of freeze-casts has been shown to lead to increased compression strength [26, 35, 47], the opposite appears to be the case here. However, the mechanical stress in the case of the regenerators is not applied as a load across the entire structure, but rather applied directly by the fluid to the channels and thus also the smaller features of the ceramic dendrites and bridges. Presumably, with more ceramic dendrites and bridges, more of the ceramic material is contained within these thin structures and less in the solid walls. With thinner ceramic structures, the probability of finding a defect leading to fracture upon application of mechanical stress is greater [44], causing degeneration of the entire structure. However, this is merely a hypothesis, but it emphasizes the need to expand our understanding of the relationship between structural features and hydrostatic mechanical stress within the channels and not just the load capacity of the full freeze-casts. Understanding the degeneration of regenerator #1 requires a de-mounting of the ceramic from the housing and investigation of the structural features either in 3D by X-ray tomography or by 2D image analysis as described in section 3.3. Additionally, a 3D analysis of a representative volume section of a freeze-cast regenerator could facilitate identification of pore interconnectivity and dead volume, i.e. either closed pores or dead end pores identifying in inactive parts in the freeze-cast regenerator.

8.3 Summary

Magnetocaloric LCSM freeze-cast regenerators were processed and evaluated by both passive and active testing. The effect of processing levers such as freezing rate, solid load and sintering time were mapped out for LCSM freeze-casts, revealing that the former controls pore/wall size and specific surface area; the second controls the macroporosity; while the latter influences pore/wall size and specific surface area, although insignificantly compared to the effect of altering the freezing rate. Regarding processing of freeze-cast regenerator geometries, the most significant correlations showed that a solid load of 20 – 35 vol% yielded macroporosities in the range of 34 – 46 %, while freezing rates from -0.5 to -2 K/min yielded pore sizes in the range 75 – 40 μm . For processing of freeze-cast regenerators, only the freezing rates were varied here.

In order to increase mechanical integrity of freeze-cast LCSM for processing, the outer radial surface was coated with a thin layer of excess LCSM suspension. This proved as an efficient way of ensuring durability during machining. A freeze-cast regenerator matrix thus consisted of two freeze-cast parts of 15 mm each mounted in a cylindrical housing. Freeze-cast regenerators were tested in both a passive and an active testing rig. The behaviour of the heat transfer coefficient with fluid flow, i.e. the correlation between Nusselt number and Reynolds number, of the freeze-cast regenerator resembles that of the packed particle bed geometry, however, with the latter outperforming the former. Freeze-cast regenerators resembling the packed particle bed geometry and not e.g. the rectangular microchannel geometry is probably due to the complexity of the flow channels. I.e. the surface roughness and ceramic dendrites/bridges extending into the pore space disrupts the flow, making the flow more complex, similar to that in the packed beds.

When considering the significantly larger specific surface area of the freeze-cast regenerator, the heat transfer performance of the freeze-cast regenerator outperforms that of the packed bed regenerator for all evaluated pore sizes. By extension, for relative comparison between freeze-cast regenerators of varying pore size, the smaller the pore width, and thus the greater the specific surface area of freeze-cast regenerators, the larger the heat transfer performance.

Freeze-cast regenerators exhibited a high effectiveness, exceeding that of the packed particle bed geometry, however, at the cost of a fairly large pressure drop, although still smaller than the packed bed geometry. Overall, within the framework of the results summarized here, the freeze-cast geometry thus poses as an attractive alternative to conventional regenerator geometries with a high degree of tunability and satisfactory operational and mechanical integrity.

Part IV

Conclusions & Perspectives

Conclusion

With the scope of implementing and evaluate the fine micrometer sized structural features and anisotropic porosity of freeze-cast materials as a regenerator geometry for magnetic refrigeration, the work presented in this thesis have been focused on three main aspects:

1. Development of a freeze-casting set-up and systematic characterization procedure for quantification of structural features of freeze-cast materials.
2. Processing, characterization and performance of magnetocaloric freeze-cast regenerators.
3. Investigation of processing levers for morphological alteration(s) of freeze-cast structures with focus on characteristics relevant for regenerators, i.e. flow properties and magnetocaloric properties.

A freeze-casting set-up with thermoelectric temperature control

A freeze-casting device utilizing a thermoelectric element for high precision temperature control for implementation of dynamic freezing conditions, build as a part of this Ph.D. work, was presented. The design of the device was based partly on practical experience with two other freeze-casting set-up, both using liquid N₂ as refrigerant with varying degree of operational complexity and correspondingly temperature control. And partly based on a realization from studying set-ups described in literature, namely, that precise and dynamic temperature control with high spatial resolution tracking of the freezing front are essential features for control and assessment of freezing conditions and thus morphology and consistency of freeze-cast materials.

An inter-changeable mould-design was developed for processing of samples of various sizes and for assessment of freezing conditions by tracking of the freezing front. The freezing front was successfully tracked by measuring the temperature gradient along the sample height using thermocouples directly mounted in the freeze-casting mould. Using the varying intrinsic thermodynamical properties of water in liquid and solid form the freezing front was easily identified, allowing for a straightforward analysis for estimation of the freezing front velocity. The tracking of the freezing front was contained within the mould-design. Meanwhile, the analysis of obtained temperature profiles in principle were independent on mould geometry and freeze-casting set-up, as long as temperature profiles were obtained spatially perpendicular to the progressing freezing front during casting. This procedure is thus easily applicable to other freeze-casting set-up.

Dynamic freezing conditions in the form of linear and exponential temperature profiles of the cooling source, with the purpose of upholding constant freezing front velocities, were investigated. However, within the experimental conditions outlined in Chapter 5, no significant influence of exponential freezing functions compared to linear freezing functions were observed, as the freezing front velocities as well as structural features appeared more or less consistent for both procedures. Of course with the conclusion that the faster the freezing rate, the finer the microstructure of freeze-cast LCSM, following the inverse proportionality between structural wavelength and freezing front velocity which is well-described in many freeze-casting studies. Additionally, the processing lever of freezing rate/freezing front velocity was successfully adjusted for controlled processing of regenerator geometries of varying pore size.

Implementation of linear freezing profiles and exponential freezing profiles with freezing front velocities of 6 – 21 $\mu\text{m/s}$, the latter being the current maximum capacity of the freeze-caster, resulted in LCSM ceramics with lamellar microchannels with pore widths of $\sim 35 - 65 \mu\text{m}$. Although, in spite of more or less consistent freezing front velocities, an increase in pore size of 6.9 – 15.8 %/cm throughout freeze-cast LCSM samples was still observed. With no apparent difference, only linear freezing profiles were used for freezing of freeze-cast LCSM regenerator samples.

In order to correlate the freezing conditions during freeze-casting with structural features in freeze-cast LCSM samples, a consistent and systematic procedure for characterization and quantification of geometrical properties by semi-automated image analysis of SEM micrographs was implemented in MATLAB[®]. This procedure quantified structural parameters such as pore and wall size, macroporosity, specific surface area and tortuosity. Although, due to the resolution of SEM micrographs and the threshold of binarization, these parameters thus primarily described the features of the macropores and thus not the entirety of the microstructure of freeze-cast LCSM ceramic. A good agreement between pore sizes evaluated by image analysis and intrusion porosimetry was shown, while the porosity estimated from image analysis appeared to be slightly overestimated. The procedure presented here is directly applicable to other freeze-cast materials.

Monolithic freeze-cast regenerators with continuous microchannels

Magnetocaloric freeze-cast regenerators were successfully processed from LCSM freeze-cast ceramics. Here, the perovskite LCSM was chosen as a magnetocaloric model-material. Although, it was argued that the magnetocaloric effect of LCSM is relatively small, it is attractive as a magnetocaloric model-material partly due to ease and experience of shaping and partly due to its near-room, tunable Curie temperature.

The effect of processing levers such as freezing rate, solid load and sintering time were mapped out for LCSM freeze-casts, revealing that the former controls pore/wall size and specific surface area; the second controls the macroporosity; while the latter influences pore/wall size and specific surface area, although insignificantly compared to the effect of altering the freezing rate. Regarding processing of freeze-cast regenerator geometries, the most significant

correlations showed that a solid load of 20 – 35 vol% yielded macroporosities in the range of 34 – 46 %, while freezing rates from -0.5 to -2 K/min yielded pore sizes in the range 75 – 40 μm . As only the effect of changing freezing rates were investigated here, tuning of porosity is thus an obvious continuation of this work.

Freeze-cast regenerators were tested in both a passive and an active testing rig, although with emphasis on the results from the first, as ΔT_{ad} is small for LCSM. The behaviour of the heat transfer coefficient with fluid flow, i.e. the correlation between Nusselt number and Reynolds number, of the freeze-cast regenerator resembled that of the packed particle bed geometry, presumably due to similar flow behaviour. Freeze-cast regenerators exhibited a high effectiveness, exceeding that of the packed particle bed geometry, however, at the cost of a fairly large pressure drop. Although, the pressure drop of the freeze-cast regenerator was still found to be smaller than the packed particle bed geometry. Overall, within the framework of the results summarized in this work, the freeze-cast geometry thus poses as an attractive alternative to conventional regenerator geometries with a high degree of tunability and satisfactory operational and mechanical integrity.

Gelated and graded freeze-casts morphologies

With the construction of a functional freeze-caster at DTU, additional processing levers for altering the freeze-cast morphology with regards to flow properties and magnetocaloric fine-tuning were investigated. Although the effect of these processing steps were not directly correlated to regenerator performance, the final structures poses as future possible alterations of the freeze-cast regenerator geometry.

Gelation of suspensions prior to freezing forms a cross-linked polymer network throughout the suspensions. Choosing the gelatin content such that samples just loses fluidity moreover adds a step of near-net shaping prior to freezing if so desired. Implementing an initial gelation step prior to freezing inhibited ice crystal growth during the freezing process. This was found to significantly change the morphology of the freeze-cast microstructure, making the cross-sections of pores in gelated samples less ellipsoidal, while introducing more dendrites and ceramic bridges. This effect was clearly seen in the difference between tortuosities of gelated and non-gelated samples. While the tortuosity of the former was constant at $\tau \approx 1.3$ throughout the sample under dynamic freezing conditions, calculated tortuosities at various sample heights of gelated samples showed significant variation around $\tau \approx 4$. This was attributed to the increased presence of dendrites and ceramic bridges infiltrating the pore space and dominating the flow path through the structures. Although non-gelated freeze-casts were found to be homogeneous throughout the sample length when considering pore/wall size and tortuosity, gelated samples frozen under the same dynamic freezing conditions did not display the same homogeneity. Nonetheless, gelation freeze-casting presents a tunability of tortuosity and a near-net-shaping step which might be of interest regarding processing of freeze-cast regenerator geometries. The latter was here specifically applied for processing of graded freeze-cast for a spatially varying material composition and thus varying Curie temperature.

Functionally graded freeze-casts of LCSM6 and LCSM9 with continuous microchannels and structural integrity were engineered by implementation of stepwise, continuous, highly viscous and gelation freezing. All procedures were based on a criteria of inhibiting or altogether eliminate flow/miscibility in the suspensions in order to layer these wet in wet to ensure continuous ice crystal growth during freeze-casting. Keeping the solid load and particle size distribution of all suspensions consistent, while ensuring an approximate constant freezing front velocity of $\sim 13 \mu\text{m/s}$ by implementing a constant temperature change rate of -1.5 K/min during freeze-casting, a structural continuity was maintained across the LCSM9—LCSM6/CGO interface. Moreover, it ensured continuous pores across the material interface for all procedures except the stepwise frozen samples. While the interface was concave in shape for frozen viscous suspensions, the interface of gelated samples directly reflected the shape of the cut-out specimens of gelated suspensions, thus ensuring a sharp and planar material interface. The overall pore morphology was found to reflect the changes in suspension properties. While the macroporosity of freeze-casts was found to be independent of changes in additives and gelation, the remaining structural features were significantly affected by change in viscosity/gelation, although maintaining the unique anisotropic porosity of freeze-cast materials. Freeze-casting of both layered viscous suspensions and gelated suspensions thus represent attractive processing routes for magnetocaloric freeze-cast regenerator geometries of graded Curie temperatures, or alternative applications where a material gradient is desired along a flow path such as e.g. filters or flow reactors.

9.1 Perspectives & future work

No Ph.D. project have ever been completed with checkmarks at all tasks on the to-do list, and so is the case for the present project.* As such, numerous scientific questions and ideas have thus originated from this work, some have already been addressed throughout the thesis, while a few are summarized here:

Freeze-casting of first-order magnetocaloric materials

In this work, LCSM was chosen as a magnetocaloric model-material, however, as argued, the magnetocaloric effect is rather small for this material, and as such, freeze-casting of a first-order material of much greater magnetocaloric effect (see Section 2.1.2 on page 18) is desirable. Three issues arise when considering freeze-casting for shaping of these magnetocaloric materials: i) iron corrodes in water; ii) particle size is large; iii) they are often difficult to sinter and are very brittle due to the first-order transition. Item i) is easily addressed by simply substituting water as solvent with e.g. camphene or *tert*-butyl alcohol. As discussed in Chapter 4, the freeze-caster is already optimized for the temperature requirements of these solvents, however, volatility of

*I would even dare say that the to-do list have grown exponentially with every passing day the past three years.

both would have to be considered. Item ii) is a little more difficult to deal with. As discussed in Chapter 1 and demonstrated in Figure 7.1 on page 98, the critical velocity of the freezing front for effective segregation of particles strongly depend on particle size. However, with the experiences of gelation freeze-casting obtained in this work, fixing the particles in a gel might prove as a possible way of ice-templating larger particle suspensions. For freeze-cast samples in this work, the ice-templated ceramic green bodies were sintered to achieve a rigid structure. Given item iii) this proves more difficult for first-order magnetocaloric materials. Regenerators of packed beds of particles of a first-order material are typically bonded together to increase mechanical integrity by epoxy [76, 77, 95]. Accordingly, hybrid freeze-cast materials of ceramic particles in a polymer matrix have been processed, resulting in a composite structure of increase mechanical strength, without sintering [22]. Applying the same procedure for freeze-casting of first-order magnetocaloric materials could hypothetically yield a magnetocaloric structure benefitting from the anisotropic porosity of freeze-casts and mechanical strength of a polymer matrix.

Further assessment of performance of freeze-cast regenerators

As discussed in Chapter 3, a large degree of inter-particle porosity in the ceramic walls of freeze-cast LCSM remained even after sintering. Efforts were made to remove this microporosity, although, unsuccessful. However, in the passive testing of regenerator performance, primarily the geometrical properties are evaluated. As such, a freeze-cast ceramic of a material for which the inter-particle porosity is easily removed, such as alumina [5, 6], could be tested instead to remove the unknown factors and uncertainties of the microporosity from evaluation of regenerator performance.

Besides gelation and material grading as presented in Chapter 6 and 7 of this work, many more processing levers for fine-tuning of morphological features of freeze-cast structures have been elucidated in various freeze-casting studies. As such, tunability of porosity, change of solvent properties for e.g. hexagonal pores or dendritic pores [12–14], 2D ordering by altered mould designs [29–31] and many order approaches could prove desirable for processing of freeze-cast regenerators. In combination with morphological changes to the freeze-cast structure, a full 3D characterization for comparison and correlation with performance results are necessary. 3D characterization by X-ray tomography could reveal the degree of interconnectivity between pores along with an assessment of the flow paths in 3D by calculation of permeability and tortuosity. Additionally, the degree of dead ends with changing morphology of ice-templated pores is interesting to evaluate, as dead ends represent volume that does no work during the AMR cycle.

Reproducibility of freeze-cast materials

Reproducibility of freeze-cast ceramics were briefly considered in Chapter 5. Here, it appeared that inconsistency in the preparation of the suspensions presumably led to evident differences

in the pore and wall sizes of the freeze-cast samples. First and foremost, a much greater sample population than five is required to perform a proper statistical analysis. Secondly, based on the considerations and experiences of this work, a thorough evaluation of the reproducibility of freeze-cast ceramics is suggested to include an evaluation of each critical step of possible inconsistency during the entire processing route. Naleway et al. [38] evaluated the variability of structural features of final freeze-casts, however, in order to understand what actually cause the variability in structural features of freeze-cast samples that were supposed to be identical, processing of powders, suspension preparation and freezing conditions should too be quantified for each sample. Thus, significant differences in e.g. suspension properties or freezing conditions can possibly be correlated to significant differences in structural features of the freeze-cast ceramic. Additionally, quantification of both structural features of freeze-casts and processing steps should too be consistent and systematic. Understanding the factors regarding reproducibility of freeze-casting is crucial for larger scale applications.

“However the hope is that if we do understand the ice crystal we shall ultimately understand the glacier.”

– Richard Feynman, *The Character of Physical Law*

Part V

Papers

The effect of gelation on statically and dynamically freeze-cast structures

Cathrine D. Christiansen, Kaspar K. Nielsen, Rajendra K. Bordia, Rasmus Bjørk

Published in: *Journal of the American Ceramic Society* 2019; 102; 5796—5806. DOI: 10.1111/jace.16500

Related publication(s): Supporting data – The effect of gelation on statically and dynamically freeze-cast structures. DOI: 10.11583/DTU.7813523

Experimental work carried out at Department of Materials Science and Engineering, Clemson University, under supervision of professor and chair Rajendra K. Bordia during my external research stay of three months in the second semester of the Ph.D. period. Post processing and data analysis carried at Department of Energy Conversion and Storage, Technical University of Denmark. I am the first-author of the paper.

ORIGINAL ARTICLE

The effect of gelation on statically and dynamically freeze-cast structures

Cathrine D. Christiansen¹  | Kaspar K. Nielsen¹  | Rajendra K. Bordia²  |
Rasmus Bjørk¹ 

¹Department of Energy Conversion and Storage, Technical University of Denmark, Roskilde, Denmark

²Department of Materials Science and Engineering, Clemson University, Clemson, South Carolina

Correspondence

Cathrine D. Christiansen, Department of Energy Conversion and Storage, Technical University of Denmark, Frederiksborgvej 399, DK-4000 Roskilde, Denmark.
Emails: cdech@dtu.dk, cathdechr@gmail.com

Funding information

Teknologi og Produktion, Det Frie Forskningsråd, Grant/Award Number: 6111-00073B

Abstract

Freeze-casting is a technique used to produce structures with anisotropic porosity in the form of well-defined microchannels throughout a sample. Here, this technique is used on the magnetocaloric ceramic $\text{La}_{0.66}\text{Ca}_{0.26}\text{Sr}_{0.07}\text{Mn}_{1.05}\text{O}_3$. We show that a dynamic freezing profile, where the temperature is decreased continuously at -10 K/min , results in homogeneous, lamellar channels with widths of $\sim 15\ \mu\text{m}$, while static freezing, where the temperature is kept constant at 177 K , results in channels of increasing size away from the initial ice crystal nucleation site. The effect of gelation before freeze-casting is also investigated. Gelation inhibits ice crystal growth, which significantly changes the morphology by making channel cross sections less elongated, while additionally introducing more dendrites and ceramic bridges in the structure. The latter significantly dominates the flow path through the gelled structures, affecting the calculated tortuosity, which increases to $\tau \approx 4$ when compared to non-gelated samples where calculated tortuosities are in the range of ~ 1.3 to ~ 3 . Finally, we present a systematic and automatic approach for evaluating channel and wall sizes and calculating tortuosities. This is based on analysis of images obtained by scanning electron microscopy using a continuous particle size distribution method and the TauFactor application in MATLAB[®].

KEYWORDS

directional porosity, dynamic freezing, freeze-casting, gelation, gelation-freeze-casting, ice-templating, magnetocaloric, static freezing

1 | INTRODUCTION

Engineering of porous ceramics by freeze-casting has gained increased interest during the past 20 years,^{1,2} as it is an easy processing route to fabricate anisotropic, high porosity ceramics, polymers, and metals.

Freeze-casting, or ice-templating, is a novel templating technique based on the anisotropic growth of ice crystals in, typically, aqueous suspensions upon directional freezing. Directional freezing is achieved by bringing one side of the suspension into contact with a cooling source, later on

referred to as the cold side, creating a thermal gradient across the suspension. When ice crystals grow in a ceramic suspension with an appropriate thermal gradient they cause a segregation of ceramic particles resulting in a two-phase system of ice and ceramic. Removing the ice by sublimation followed by (partial) sintering results in a ceramic structure with anisotropic porosity in the form of directional macropores where the ice used to be. The dimensions of the macropores thus depend on the size of the ice crystals and are typically of the order $\sim 1\ \mu\text{m}$ to $\sim 100\ \mu\text{m}$.^{3–5} While water is the most common solvent, alternatives such as camphene⁶ or *tert*-butyl

alcohol⁷ have been used successfully, however, with different solidification temperatures and altered morphologies. With no temperature control other than that of a specific coolant, the macropore dimensions are typically graded throughout the structures being smaller at the bottom than at the top. In addition, the porosity of freeze-cast structures is hierarchical having maintained microporosity within the walls.^{1,8} These physical properties make freeze-cast structures advantageous for, for example, biomedical applications^{9,10} or applications of limited thickness such as filters and ceramic support structure for, for example, membranes or fuel cells.^{5,11,12} However, for applications where the ceramic is a medium for oscillating flows of fluids or gasses in larger bodies, homogeneous channel sizes and consistent morphology are preferred.^{13,14}

In freeze-casting, the morphology of the pores very strongly depends on the freezing conditions; most notably is the conclusion that the faster the freezing front moves, the narrower will the resulting channels be.^{3–5} Thus, controlling the freezing front velocity is equivalent to controlling the structural dimensions. Another possible way of controlling the morphology of the pores of a freeze-cast structure is to alter the chemical composition of the solvent and thus the physical properties of the solvent during freezing. One way of doing so is by gelation of samples prior to freezing, achieved by introducing a gelling agent, such as gelatin, into the suspension.

Previously, gelation has been used in gelcasting¹⁵ as a near-net-shaping technique for ceramic processing. Combining gelation and freeze-casting using gelatin was introduced by Fukushima et al,^{16,17} who showed that initial gelation of samples completely alters the morphology of the pores while achieving complex shapes throughout the entire ceramic body. The gelled freeze-cast structures have, however, primarily been used for processing of insulating materials,¹⁶ membranes,¹⁸ and biomedical purposes,¹⁹ where the latter utilizes the hierarchical nature of freeze-cast structures, as previously mentioned. However, until now gelled freeze-cast structures have been processed using primarily static freezing profiles.^{16–19} For a static freezing profile the cold side is kept at a constant temperature below the freezing temperature of the solvent throughout the freeze-casting process. Static freezing profiles lead to a changing freezing front velocity during casting, resulting in structures with varying macropore sizes.^{3–5}

In this paper, we investigate the effect of implementing dynamic freezing profiles, more specifically conditions where the temperature of the cold side is decreased linearly in time throughout the freeze-casting process. Dynamic freezing profiles lead to a more steady freezing front velocity.^{3–5} Here, we investigate the implementation of dynamic freezing profiles together with gelation, and the combined influence of these freezing conditions on the resulting porosity, and morphology of pores of the freeze-cast structures are reported. For the

microstructural analysis a systematic and automated image quantification technique has been developed and used.

The approach of implementing static and dynamic freezing profiles and gelation prior to freeze-casting is carried out on $\text{La}_{0.66}\text{Ca}_{0.33-x}\text{Sr}_x\text{Mn}_{1.05}\text{O}_3$ (LCSM) ceramic powders. Ceramic processing—and thus freeze-casting—of LCSM powders is similar to that of LSM powders used by Lichtner et al,^{5,20} and has previously been reported by the authors of this paper.²¹ In addition, LCSM is magnetocaloric, meaning that the temperature of the material will change if a magnetic field is applied.²² The Curie temperature, which is the transition temperature between the ferromagnetic and paramagnetic states, of LCSM can be conveniently tuned around room temperature by varying the amount of dopants²³—that is, the ratio between calcium, Ca, and strontium, Sr—making it applicable as regenerator material in magnetic refrigeration.²⁴ In this context, freeze-casting offers the possibility of engineering monolithic LCSM structures with aligned, directional porosity in the form of macropores—also referred to as microchannels—a geometry which is advantageous for heat transfer.²⁵

2 | MATERIALS AND METHODS

2.1 | Powder properties and preparation of ceramic suspensions

Ceramic suspensions for freeze-casting were prepared from 20 vol% powders of $\text{La}_{0.66}\text{Ca}_{0.26}\text{Sr}_{0.07}\text{Mn}_{1.05}\text{O}_3$ (LCSM, CerPoTech, Norway) in distilled water, with the addition of 2.5 wt%, relative to the ceramic powder, of DURAMAX™ D-3005 (Rohm and Haas, Dow Chemical, USA) as dispersing agent.

The specific surface area and density of the powder were determined by the BET method using a Nova 4000e (Quantachrome Instruments, USA), and by gas pycnometry using an AccuPyc II 1340 (Micromeritics, USA), respectively. The particle size distributions of both raw powder and milled suspensions were determined using an LS 13 320 Laser Diffraction Particle Size Analyser (Beckman Coulter). Additionally, the surface charge as a function of pH was measured using a Zeta potentiometer coupled with a pH probe, Zeta Potential Analyzer (Colloidal Dynamics, USA), and determined by titration of an aqueous suspension of 0.9 wt% powder with 0.1 mol/L NaOH and 0.1 M HCl. Powder properties are summarized in Table 1.

Measurements of the surface charge show that the zeta potential reaches a plateau at the lower pH range, indicating that a stable slurry is achieved at $\text{pH} < 7$. All slurries were thus adjusted from a $\text{pH} \sim 8.5$ to $\text{pH} \sim 6$ by dropwise addition of nitric acid. In order to achieve a sufficient dispersion of powders, slurries were mixed by sonication using a homogenizer (S-450A, Branson Ultrasonics, USA)

TABLE 1 Summarization of powder properties of $\text{La}_{0.66}\text{Ca}_{0.26}\text{Sr}_{0.07}\text{Mn}_{1.05}\text{O}_3$

Density (g/cm^3)	Specific surface area (m^2/g)	d_{50} (μm)	Isoelectric point
6.04	17.92	0.34	8.8

for 2×30 seconds and subsequently homogenized using a low energy ball mill with zirconia balls with $\phi = 10$ mm for 24 hours. Thereafter, 1.5 wt%, relative to the ceramic powder, of DURAMAX™ B-1022 (Rohm and Haas, Dow Chemical) was added as binder and mixed for an additional 30 minutes using a low energy ball mill. Suspensions were de-aired under low vacuum for a few minutes immediately before casting.

In order to investigate the effect of gelation of samples, an additional gelation step was implemented for some samples prior to freeze-casting. Gelation was achieved by preparing a solution of gelatin (granular, type A from porcine, lab grade, Ward's Science, USA), corresponding to 0.3 wt% relative to the ceramic powder, by dissolving granular gelatin in distilled water and stirring at 323 K using a magnetic stirrer. The suspension of powder and dispersant, prepared as described above without the addition of binder, was also heated to 323 K and the gelatin solution was mixed with the suspension by continuous stirring while maintaining the temperature in order to avoid premature hardening of the gelatin. The suspension was then transferred to a mold closed at the bottom using a thin sheet of aluminum foil attached by vacuum grease, and left to harden overnight at 278 K. The samples were subsequently left at ambient conditions to reach an equilibrium temperature with the surroundings before freeze-casting.

The relative amount of gelatin powder was chosen such that the suspension just loses fluidity at ambient conditions after hardening overnight at 278 K. The formed gel network thus offers an increased viscosity or gel strength²⁶ for stabilizing the suspension and provides an additional step of net-shaping if desired.¹⁶ However, in the current work, the gel network was applied to inhibit the ice crystal growth and thereby modify the pore morphology.

2.2 | Freeze-casting procedure

Samples were frozen directionally at static and dynamic temperature profiles using a freeze-casting setup previously described by Lichtner et al.^{20,27} The setup consisted of a large copper rod with $\phi = 76$ mm immersed in a bath of liquid nitrogen. A large interface between copper and liquid nitrogen achieved by fins cut into the copper rod provided increased temperature control, a faster freezing of samples and allowed for manual control of the freezing rate, by controlling the amount of liquid nitrogen in the bath. The temperature of the copper rod was monitored by the application of a K-type thermocouple. Cylindrical acrylic molds of inner and outer diameter of 18 mm and 45 mm, respectively,

were directly mounted on the top of the copper rod using vacuum grease while the top of the molds were left open to ambient conditions. The large thermal mass of the copper rod and the thick walls of the acrylic mold with high thermal resistance ensured continuous freezing conditions and minimal heat exchange with the surroundings. Samples were frozen either dynamically or statically.

Dynamic freeze-casting of samples was achieved by manually adjusting the level of liquid nitrogen resulting in a freezing rate of -10 K/min. The de-aired suspension was poured into the mold and the temperature was decreased continuously from ambient. The freezing rate was kept constant during the entire freezing procedure.

Static freeze-casting of samples was achieved by placing the copper rod in a cooling bath of liquid nitrogen and acetone. The acrylic mold was closed at the bottom using a thin sheet of aluminum foil attached by vacuum grease. The mold containing a de-aired suspension was then transferred to the copper rod when this had reached a steady temperature of 177 K. Due to the large thermal mass of the copper rod, the temperature of the rod did not change significantly during freezing of samples and was thus assumed to be constant resulting in a static freezing.

After freeze-casting, ice was removed from the samples by sublimation in a freeze drier while the samples were still in their molds (0.200 mBar, 223 K, FreeZone 2.5, Labconco) for at least 24 hours. Dried samples were subsequently sintered in air at 1423 K for 3 hours (heating rate of 2 K/min) with an initial burnout of organic additives at 723 K for 4 hours.

2.3 | Structure characterization and quantification

Ceramic samples were prepared for mechanical handling and structural analysis by infiltration with epoxy (EpoFix, resin and hardener, Struers ApS, Ballerup, Denmark). Epoxy infiltrated samples were cut in half parallel to the freezing direction and one half was then sliced perpendicular to the freezing direction in thicknesses of 2 mm. These were then polished and coated with a ~ 12 nm thick carbon layer. Images of the perpendicular and parallel cross sections of the samples were obtained using a scanning electron microscope (SEM, TM3000, Hitachi High-Technologies). The microstructure of samples was investigated as a function of sample height, that is, the vertical distance—parallel to the freezing direction—from the bottom of the sample and to the specific point of interest. Three images were obtained at each cross section of interest, both for the parallel cut samples and for

the perpendicular cut samples, in order to realize a statistically significant data set.

The macropores of the samples will in the following be referred to as microchannels, as a fluid can be envisioned to flow through these. The microchannels in the ceramic samples were characterized by analyzing SEM images using an image analysis software developed in MATLAB® (The MathWorks, Inc.). First the SEM images were binarized using a threshold value, as shown in Figure 1A. The analysis then depends on whether parallel or perpendicular cross sections, with respect to the freezing direction, are investigated:

For SEM images of cross sections perpendicular to the freezing direction, the size of the channels or walls are estimated by a continuous particle size distribution method. This is done by fitting circles of increasing size in every point in all channels (or walls) in a binarized image, determining the largest circle that can be fitted within all points in the channels (or walls), yielding a direct measure of the size of the channel (or wall).²⁸ The radius of these fitted circles are shown for the channels and the walls in Figure 1B,C, respectively. As can be seen from the images, the above procedure results in a distribution of fitted circles throughout the SEM image. The average channel or wall dimension can then be calculated from this distribution. Additionally, macroporosities, or channel-porosities, were estimated from the binarized images. SEM images used for estimating the channel and wall sizes were obtained at magnifications of $\times 100$ to $\times 500$. We found that the analysis of channel and wall sizes were independent of magnification in this range.

For some samples aspect ratios of the cross section of the channels were also determined. This was done by manually fitting ellipses to channels in ImageJ and then calculating the ratio between the minor and major axis. For the relevant samples approximately 100 channels at a sample height of 6 mm was fitted with ellipses to determine the average aspect ratio.

For SEM images of cross sections parallel to the freezing direction, the quality of the structure in terms of allowing a fluid to pass through can be estimated. This is done

by calculating the tortuosity, τ , of the channels. Tortuosity is a measure of the curviness of channels, in this case, evaluating the ratio between the direct distance across a cross section and the distance across the same cross section through a channel. A factor of $\tau = 1$ corresponds to a direct flow path, while the greater the tortuosity the greater the curviness or skewness of the channels. Tortuosity was calculated using the TauFactor application²⁹ in MATLAB® (The MathWorks, Inc.). The software calculates the tortuosity in 2D from SEM cross-sectional images instead of the more intricate and time consuming procedure of doing a 3D X-ray tomography analysis of entire samples.^{28,30,31} However, calculating tortuosity from 2D cross sections requires considerations about the magnification of analyzed SEM images. A too large magnification results in very few channels per image, while a too small magnification results in closed pores. The lamellar channels of freeze-cast structures have previously been shown to be arranged in domains of varying orientations and angles relative to the freezing direction,^{20,32} as is also evident from the perpendicular cross sections in Figure 2, resulting in what appears to be closed pores in the parallel cross-sectional images.

We found that images obtained at different sample heights at a magnification of $\times 500$ met the aforementioned criteria while still representing and maintaining general channel structure characteristics in form of wall morphology, skewness of channels and width of channels and walls. Thus, tortuosity was calculated parallel to the freezing direction across cross-sectional areas of $331 \times 248 \mu\text{m}$.

3 | RESULTS AND DISCUSSION

Dynamic and static freezing conditions both result in anisotropic macroporosity in the form of microchannels running along the freezing direction. The cross section of each channel is ellipsoidal, giving an overall lamellar morphology, and

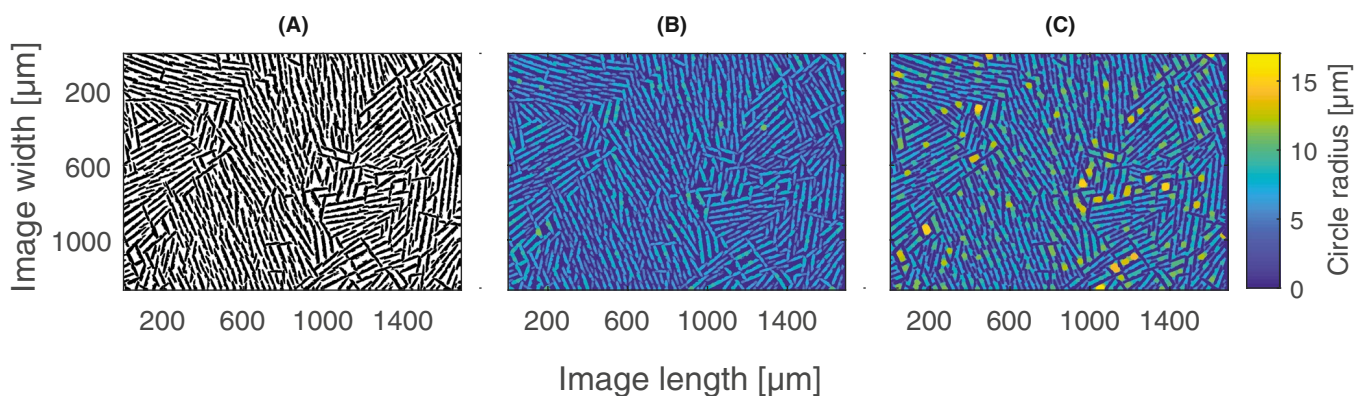


FIGURE 1 Processing of SEM images obtained from cross sections perpendicular to the freezing direction in order to estimate channel and wall sizes. (A) Binarized SEM image, where white indicates ceramic walls and black is voids or channels. Circles are fitted to either the channels (B) or walls (C), with the fitted circle radius indicated by the color bar

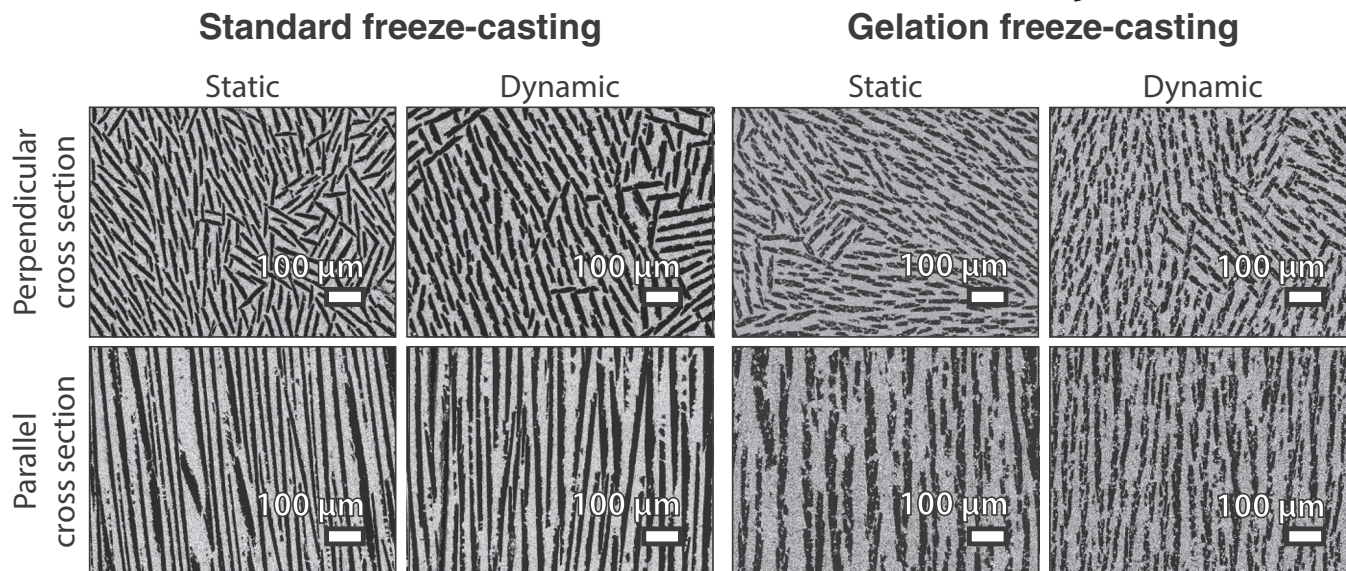


FIGURE 2 SEM micrographs of cross sections perpendicular and parallel to the freezing direction at sample heights of 6 mm and 6 ± 2 mm, respectively. White areas are ceramic walls while black areas are porosity in the form of lamellar, ellipsoidal channels

the channels are ordered in domains of various orientations, as is evident on Figure 2. The porosity is hierarchical with macroporosity in the form of channels and microporosity in the ceramic walls, where the total porosity of non-gelated freeze-cast samples are $\sim 65\%$ while the gelated samples have a total porosity of $\sim 70\%$.

Introducing an initial gelation of the solvent by adding gelatin and leaving it to harden causes the medium in which the ice grows to change, thereby changing the final morphology of the ice crystals and thus the resulting pores.^{16,18,19,33} While the macroporosity of the gelated structures are still lamellar and the perpendicular pore shape is overall ellipsoidal, as is evident from Figure 2, the general morphology is significantly different.

3.1 | Characterizing and quantifying morphology

Various approaches have been taken to characterize and quantify morphology of freeze-cast microstructures during the past 20 years of increased interest in these porous materials. Generally, pore and wall sizes are measured in optical images or SEM micrographs of perpendicular cross sections. Additionally, for lamellar morphologies the periodicity can be quantified by the structure wavelength, which is determined as the sum of the width of a channel and the width of the adjacent wall in a perpendicular cross section.³ Anisotropy of pores is usually evaluated by simple visual comparison between perpendicular and parallel cross sections. Low tortuosity of macropores is often claimed as a characteristic for freeze-cast structures,^{11,12,29,34,35} but is rarely calculated and evaluated with respect to freezing

conditions. Miller et al.⁶ calculated tortuosities, however, only for static freezing conditions and only at one sample height.

Here we evaluate the tortuosity dependence on static and dynamic freezing conditions, and show that tortuosity calculations in 2D, in combination with automatic detection and evaluation of channel and wall sizes, can be used to quantify and evaluate the microstructure and homogeneity of channels in a freeze-cast material. To maintain an automatic, fast and reproducible workflow for analysis of a large quantity of SEM micrographs for morphological characterization of freeze-cast structures, MATLAB[®] has been used.

3.2 | Size distributions of microchannels

Analyzing the SEM micrographs of cross sections perpendicular to the freezing direction of freeze-cast structures as described in Section 2.3 yields a distribution of fitted circle sizes as shown in Figure 3. Only results from analysis of pores at the top (sample height of 8 mm) and bottom (sample height of 2 mm) of samples are shown in order not to clutter the plot.

As is clear from Figure 3, the pore size distributions, for all structures except the dynamically frozen structure without gelatin, are shifted toward larger channel sizes from bottom to top indicating a conical shape of channels, the width of channels being smaller at the bottom than at the top. Average channel and wall sizes are estimated by averaging the distributions of fitted circles weighed by area at each perpendicular cross section. This is done for a range of sample heights, that is, not just those shown in Figure 3. The average channel

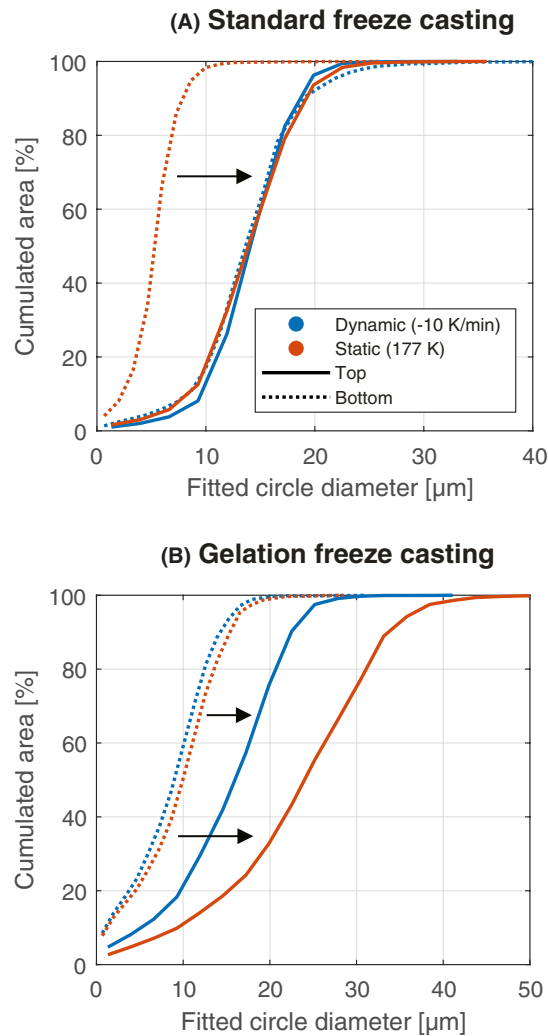


FIGURE 3 Size distribution of circles fitted to pores of cross-sectional SEM images. Only distributions at cross sections at the top (sample height of 8 mm) and bottom (sample height of 2 mm) of freeze-cast structures without (A) and with (B) gelatin are shown here. The arrows indicate the change going from the bottom to the top of the sample

and wall size, as a function of distance from the cold finger, for both statically and dynamically frozen samples, as well as for non-gelated and gelated samples, are shown in Figure 4. As can be seen from Figure 4A, freeze-cast structures frozen using a static freezing profile of 177 K have inhomogeneous microstructure, where both channel size and wall size increase along the sample height. When the temperature of the cold finger is static the suspension will initially freeze very fast. As the freezing front moves further away from the cold finger, due to low thermal resistance of the frozen ceramic, the temperature gradient at the freezing front decreases which reduces the freezing kinetics, that is, the freezing front velocity, giving the ice crystals more time to grow perpendicular to the freezing direction. Larger ice crystals result in larger channel and wall sizes. These results are in accordance with previous studies correlating the channel size to the velocity

of the freezing front, where the channel size increase with a decrease in freezing front velocity.^{3–5}

However, while the channel sizes of the statically frozen structures increases by a factor of 5 from bottom to the top, the dynamically frozen structures maintain a channel size of $\sim 15 \mu\text{m}$ all the way through for the non-gelated samples. By implementing a dynamic temperature profile of -10 K/min the decreasing temperature gradient across the freezing front is compensated and presumably maintained during the complete freezing, resulting in steady freezing kinetics, that is, a constant freezing front velocity, and thus in homogeneous channel and wall sizes all the way through the freeze-cast structures.

The above reasoning moreover explains the intersection of channel sizes in Figure 4A at a sample height of 8 mm, after which channels in statically frozen structures are larger than those in dynamically frozen structures. Eventually, the freezing kinetics of the statically frozen samples will be slower than at the equivalent height of dynamically frozen samples resulting in increasing ice crystal growth and thus larger channels in the final ceramic.

The estimated wall sizes follow the same trend as the channel sizes, although slightly larger. Regarding gelated samples, however, here the dynamic freezing profiles do not result in a homogeneous structure. Moreover, the variation in the channel size for dynamically frozen structures is less than that for static frozen structures. The reason for this is discussed subsequently in Section 3.4.

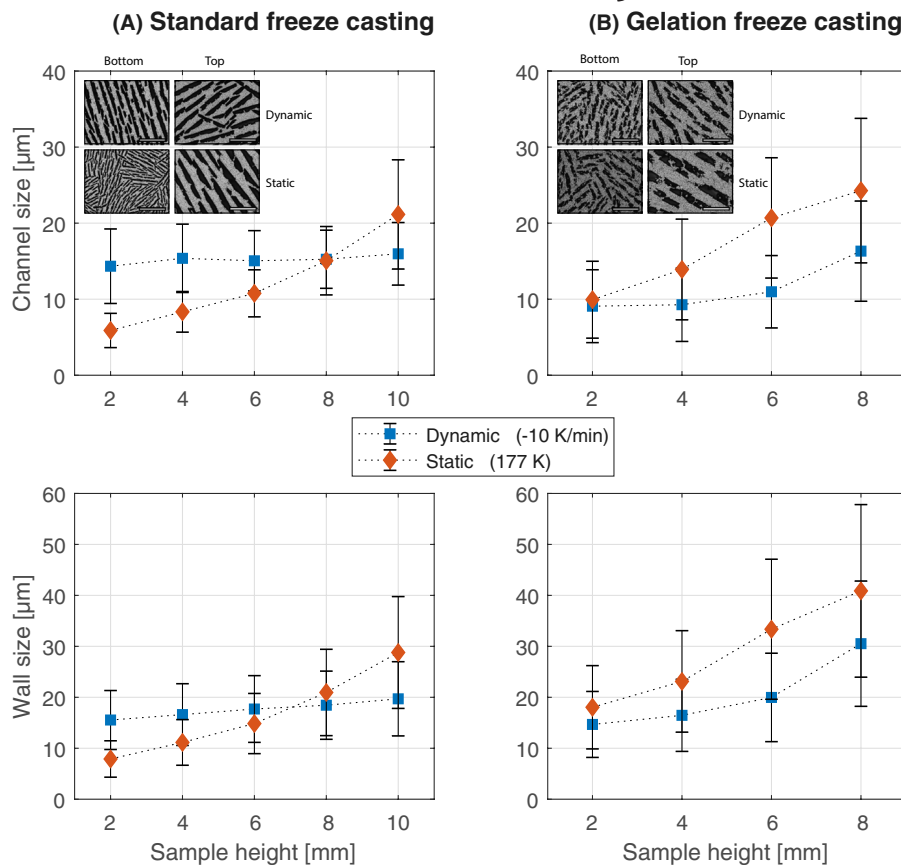
3.3 | Tortuosity of microchannels

A similar conclusion, as for the size distribution, can be reached when evaluating the tortuosity of the structures frozen without initial gelation.

Tortuosity can be directly correlated to the nature of ice crystal growth under the conditions described in Section 2.2. The growth of ice crystals in ceramic suspensions during freeze-casting has previously been observed by in situ X-ray radiography.^{36,37} Upon freezing, rapid nucleation takes place at the bottom copper surface forming ice crystals that grow in random directions. This is the isotropic region with no resulting directional porosity. Eventually, ice crystals growing along the direction of the temperature gradient are favored, resulting in a region of aligned crystals. This region is referred to as the steady state region or the anisotropic region. In this region, aligned, lamellar ice crystals are arranged in domains of various orientations, resulting in the equivalent inverse, aligned, lamellar channels evident on the perpendicular cross sections in Figure 2. The larger and more aligned the ice crystals are, the larger and straighter will the resulting channels be, leading to calculated tortuosities that are smaller.

The calculated tortuosities of microchannels in freeze-cast structures frozen statically are shown in Figure 5. As

FIGURE 4 Channel and wall size as a function of distance from the cold finger (sample height) of freeze-cast structures frozen under static (\diamond) and dynamic freezing (\square) profiles without (A) and with (B) gelatin. SEM insets are of cross sections perpendicular to the freezing direction at a sample height of 2 mm (bottom) and 8 mm (top), where the scale bar indicates 100 μm



can be seen from the figure, samples frozen without an initial gelation step, Figure 5A, have a decreasing tortuosity along the sample height, while it is almost constant for the dynamically frozen structures. Based on tortuosity and channel sizes determined from SEM micrographs, implementing dynamic freezing profiles thus increases the morphological homogeneity of non-gelated freeze-cast structures, making them almost completely homogeneous with respect to channel size and tortuosity.

While calculated tortuosities of non-gelated samples thus reflect freezing conditions, tortuosity for the gelated structures, however, is seen to have significantly larger error bars and also no clear trend is seen in the results. The reason for this will be discussed in the following section.

3.4 | Morphology of gelated structures

As is evident from Figure 2, the channels of gelated freeze-cast structures—similar to those without gelation—are lamellar and the cross sections are ellipsoidal, however, the aspect ratio decreases when comparing the nongelated samples, to the gelated samples in Table 2. The channels of the gelated samples thus become less ellipsoidal, converging toward a more cylindrical shape, as previously described by Fukushima et al.²⁶ The change in morphology of the channels is likely due to the increased resistance the growing ice

crystals meet due to the gel network making it harder for the crystals to push aside suspended particles.

Another plausible consequence of the resistance from the gel network can be seen in the higher magnification micrographs in Figure 6A, where the walls seem slightly less dense in the gelated freeze-cast structure. During freeze-casting the formation of ice crystals pushes the suspended particles together causing these to segregate into what will become the walls of the structures upon drying and sintering. It is possible that the gel network inhibits this segregation to some extent during the casting process, resulting in a less dense packing of particles in the walls of the gelated structures when comparing to the non-gelated structure in Figure 6B. In addition, the estimated channel-porosities, or macroporosity, of gelated freeze-cast structures are lower than those of non-gelated samples as seen in Table 2 even though the total porosity of gelated samples is larger than non-gelated samples. Moreover, the macroporosity was found to not vary significantly throughout the length of the samples.

While the implementation of a dynamic freezing profile—compared to static freezing—significantly changes the dimensions of the channels along the sample height for non-gelated structures, resulting in more homogeneous channel sizes and tortuosities, as evident from Figures 3–5, this is not the case for gelated structures. Both statically and dynamically frozen gelated structures are inhomogeneous

in channel size as can be seen in Figure 4B, where an increasing channel and wall size along the sample height is seen. It is especially remarkable that the channel sizes for the gelated samples are not homogeneous throughout the sample, as is clear from Figure 4B, even though the dynamic freezing profile is used. This could be due to the altered

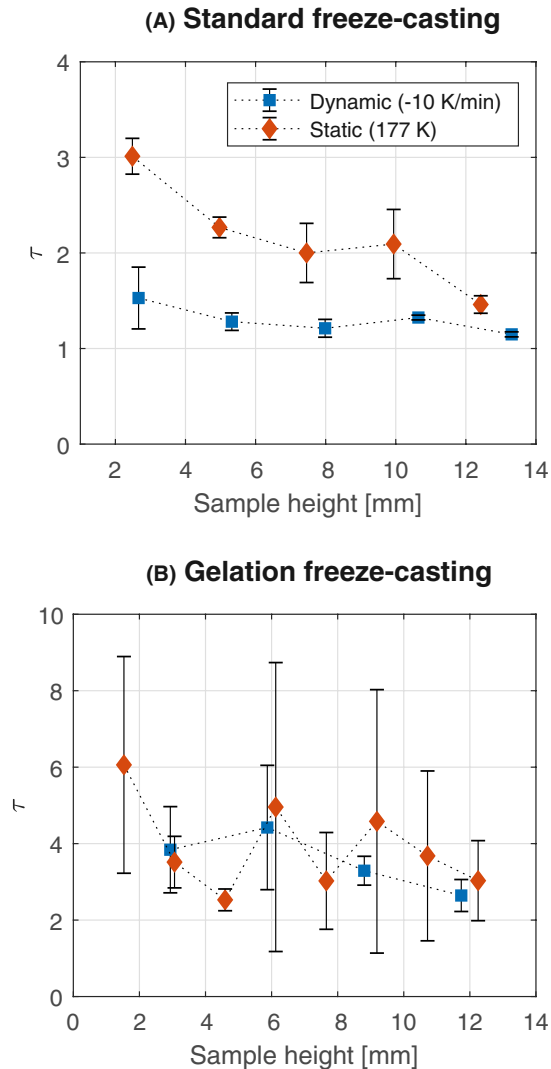


FIGURE 5 Calculated tortuosities, τ , as a function of distance from the cold finger (sample height) of freeze-cast structures frozen statically and dynamically. Tortuosity is calculated from cross sections of $331 \mu\text{m} \times 248 \mu\text{m}$ parallel to the freezing direction. Three cross sections have been evaluated at each sample height. Results of both non-gelated (A) and gelated samples (B) are shown

structure of the gelated freeze-cast sample, which is more unstructured than the corresponding standard freeze-cast sample. The significant difference in internal structure, or morphology, is clearly seen in Figure 5 showing the tortuosity of the respective samples. The larger tortuosity of the gelated samples reveal a somewhat more chaotic morphology which is thought to slightly decrease the thermal conductivity of the sample. Hence, throughout the length of the sample the freezing conditions change due to an increasing thermal resistance resulting in larger channels at the top of the sample. However, the effect is small as the channels are seen only to increase in size in the latter part of the sample. A direct measurement of the freezing front velocity during casting of both standard and gelated samples could clarify this assumption, however, with the present freeze-casting setup where only visible tracking of the freezing front is possible (see Lichtner et al.,⁵ Figure 1) this was impossible due to the color (or lack thereof) of LCSM powders. Additionally, clarifying the altered freezing kinetics of gelated samples could then lead to a further tuning of dynamic freezing conditions—for example, implementation of exponential or stepwise dynamic temperature profiles—which might prove as a way of engineering homogeneous, gelated freeze-cast structures.

The resulting pores in the freeze-cast gelated structures are, despite the change in morphology and homogeneity, in the same size range as the standard freeze-cast ones. Meanwhile, the calculated tortuosities of structures frozen with an initial gelation step, Figure 5B, are generally larger than non-gelated structures and not directly correlated with sample height or channel size, but rather, scattered around $\tau \approx 4$ inconsistently.

The variability in the channel size and calculated tortuosity is partly due to the presence of dendrites and ceramic bridges across channels. As can be seen on the horizontal cross sections in Figure 6A, ceramic bridges connect channel walls across the pores, while dendrites results in an obviously higher surface roughness than non-gelated structures when comparing parallel cross sections in Figure 6A,B. Bridges and dendrites increase the overall curviness of channels. For gelated freeze-cast samples, the finer scale contributions of dendrites and bridges to the calculated tortuosity overshadow that of the size and skewness of the channels.

Gelation thus provides an obstacle in fine-tuning and specific engineering of structures if one has a specific channel

	Freezing conditions	Aspect ratio	Channel-porosity (%)
Standard	Dynamic (-10 K/min)	7.3 ± 3.6	49 ± 1
	Static (177 K)	6.6 ± 2.8	47 ± 2
Gelation	Dynamic (-10 K/min)	3.9 ± 1.4	41 ± 1
	Static (177 K)	3.3 ± 1.5	43 ± 2

TABLE 2 Aspect ratios and channel-porosity of dynamically and statically frozen freeze-cast structures

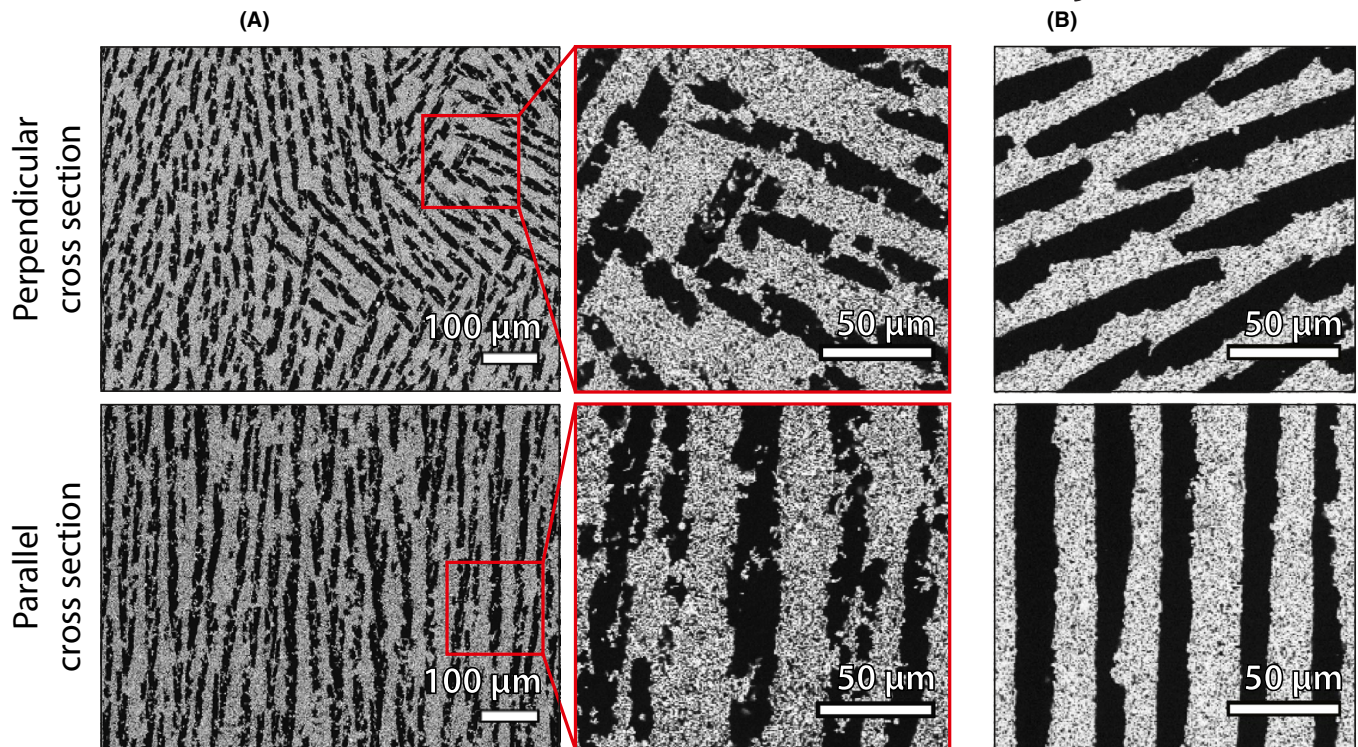


FIGURE 6 SEM images of cross sections perpendicular and parallel to the freezing directions of a gelated (A) and a non-gelated (B) sample, both frozen dynamically at -10 K/min. Perpendicular and parallel cross sections are at sample heights of 6 mm and 6 ± 2 mm, respectively. Higher magnification micrographs show the rougher nature of the wall surface of gelated structures in the form of dendrites and ceramic bridges connecting the walls of the channels. In addition, the walls of the gelated sample appear less dense than those of the non-gelated sample

size in mind and a need for homogeneous, low tortuosity channels. It does, however, provide a way of altering the morphology of channels in freeze-cast structures, making the channels less ellipsoidal, more tortuous, and more connected. These types of microstructures could have other advantages and applications. Specifically, it has been shown that the bridges between pore channels have a significant effect on the mechanical properties of freeze-cast materials.^{20,38}

4 | CONCLUSION

Freeze-casting of ceramic suspensions, with and without gelation prior to freezing, of powders of the magnetocaloric LCSM ceramic results in rigid ceramic structures with anisotropic macroporosity in the form of microchannels running along the freezing direction. The perpendicular cross section of channels is ellipsoidal giving an overall lamellar geometry. Channel and wall sizes were quantified using an automated approach for analysis of 2D SEM micrographs obtained on cross sections perpendicular and parallel to the unidirectional freezing direction. The microstructure was examined as a function of distance from the cold finger for both static and dynamic freezing conditions for samples with and without partial gelation. For non-gelated samples, static freezing at

177 K led to structures with channels of increasing size along the sample height, being $5 \mu\text{m}$ at the bottom and $20 \mu\text{m}$ wide at the top. However, dynamic freezing conditions, where the cold finger was cooled at -10 K/min, resulted in channels of homogeneous size throughout the sample with a channel size of $\sim 15 \mu\text{m}$.

Implementing an initial gelation step prior to freezing inhibits ice crystal growth during the casting process, significantly changing the morphology, making the cross section less ellipsoidal and introducing more dendrites and ceramic bridges. Both statically and dynamically frozen structures had channels of increasing size along the sample height, ranging from $10 \mu\text{m}$ to $25 \mu\text{m}$ for static structures and from $10 \mu\text{m}$ to $15 \mu\text{m}$ for dynamic structures.

The calculated tortuosity of non-gelated structures followed the trend of the channel sizes. For statically frozen samples, tortuosity decreased from $\tau = 3$ at the end close to the cold finger to $\tau = 1.5$ at the other end. For dynamically frozen samples, the tortuosity was constant at $\tau \approx 1.3$ throughout the sample. For gelated samples the calculated tortuosities at various sample heights showed significant variation around $\tau \approx 4$. This is attributed to the increased presence of dendrites and ceramic bridges infiltrating the pore space and dominating the flow path through the structures.

Freeze-casting using dynamic freezing profiles hold the promise of a processing route with the ability to control and optimize channel size and tortuosity of homogeneous structures, yielding high tunability of ceramics for applications where the ceramic is a medium for, for example, fluid flow and heat transfer. Partial gelation of the slurry prior to freeze-casting provides another process variable to control and optimize the porous structure. However, further optimization of the slurry and the dynamic freezing conditions is needed to obtain homogenous microstructures using this approach. In some applications, the bridges spanning the pore space may be desirable for, for example, optimized mechanical strength or increased tortuous flow.

4.1 | Supporting data

SEM micrographs are provided as supporting data, <https://doi.org/10.11583/DTU.7813523>

ACKNOWLEDGMENTS

This work is funded by the Independent Research Fund Denmark—Technologies and Productions Sciences, project no. 6111-00073B. The authors wish to extend their gratitude to Peter Stanley Jørgensen, associate professor, Technical University of Denmark, for software and expertise in regards to analysis of SEM images. C. D. Christiansen moreover wishes to acknowledge the Otto Mønsted Foundation for financial support and thanks Prof. Rajendra Bordia's research group—specifically doctoral alumni Dr. Aaron Lichtner, Mr. Milad Azami, and Ms. Michelle Greenough—for constructive discussions and guidance and for providing equipment and workspace for parts of this work.

ORCID

Cathrine D. Christiansen  <https://orcid.org/0000-0003-3738-8267>

Kaspar K. Nielsen  <https://orcid.org/0000-0001-7938-4577>

Rajendra K. Bordia  <https://orcid.org/0000-0001-9256-0301>

Rasmus Bjørk  <https://orcid.org/0000-0002-3728-2326>

REFERENCES

- Fukasawa T, Ando M, Ohji T, Kanzaki S. Synthesis of porous ceramics with complex pore structure by freeze-dry processing. *J Am Ceram Soc.* 2001;84(1):230–2. <https://doi.org/10.1111/j.1151-2916.2001.tb00638.x>
- Deville S. The lure of ice-templating: recent trends and opportunities for porous materials. *Scripta Mater.* 2018;147:119–24. <https://doi.org/10.1016/j.scriptamat.2017.06.020>
- Deville S, Saiz E, Tomsia AP. Ice-templated porous alumina structures. *Acta Mater.* 2007;55(6):1965–74. <https://doi.org/10.1016/j.actamat.2006.11.003>
- Waschkies T, Oberacker R, Hoffmann MJ. Control of lamellae spacing during freeze casting of ceramics using double-side cooling as a novel processing route. *J Am Ceram Soc.* 2009;92(suppl 1):79–84. <https://doi.org/10.1111/j.1551-2916.2008.02673.x>
- Lichtner AZ, Jauffrès D, Martin CL, Bordia RK. Processing of hierarchical and anisotropic porosity LSM-YSZ composites. *J Am Ceram Soc.* 2013;96(9):2745–53. <https://doi.org/10.1111/jace.12478>
- Miller SM, Xiao X, Faber KT. Freeze-cast alumina pore networks: effects of freezing conditions and dispersion medium. *J Eur Ceram Soc.* 2015;35(13):3595–605. <https://doi.org/10.1016/j.jeurceramsoc.2015.05.012>
- Tang Y, Qiu S, Wu C, Miao Q, Zhao K. Freeze cast fabrication of porous ceramics using tert-butyl alcohol/water crystals as template. *J Eur Ceram Soc.* 2016;36(6):1513–8. <https://doi.org/10.1016/j.jeurceramsoc.2015.12.047>
- Lichtner AZ, Jauffrès D, Roussel D, Charlot F, Martin CL, Bordia RK. Dispersion, connectivity and tortuosity of hierarchical porosity composite SOFC cathodes prepared by freeze-casting. *J Eur Ceram Soc.* 2015;35(2):585–95. <https://doi.org/10.1016/j.jeurceramsoc.2014.09.030>
- Deville S, Saiz E, Nalla RK, Tomsia AP. Freezing as a path to build complex composites. *Science (New York, N.Y.)*. 2006;311(5760):515–8. <https://doi.org/10.1126/science.1120937>
- Porter MM, Imperio R, Wen M, Meyers MA, McKittrick J. Bioinspired scaffolds with varying pore architectures and mechanical properties. *Adv Funct Mater.* 2014;24(14):1978–87. <https://doi.org/10.1002/adfm.201302958>
- Bouville F, Maire E, Deville S. Lightweight and stiff cellular ceramic structures by ice templating. *J Mater Res.* 2014;29(02):175–81. <https://doi.org/10.1557/jmr.2013.385>
- Gurauskis J, Graves CR, Moreno R, Nieto MI. Self-supported ceramic substrates with directional porosity by mold freeze casting. *J Eur Ceram Soc.* 2017;37(2):697–703. <https://doi.org/10.1016/j.jeurceramsoc.2016.08.031>
- Nielsen KK, Engelbrecht K, Christensen DV, Jensen JB, Smith A, Bahl CRH. Degradation of the performance of microchannel heat exchangers due to flow maldistribution. *Appl Therm Eng.* 2012;40:236–47. <https://doi.org/10.1016/j.applthermaleng.2012.02.019>
- Lei T, Engelbrecht K, Nielsen KK, Veje CT. Study of geometries of active magnetic regenerators for room temperature magnetocaloric refrigeration. *Appl Therm Eng.* 2017;111:1232–43. <https://doi.org/10.1016/j.applthermaleng.2015.11.113>
- Gilissen RU, Erauw JP, Smolders A, Vanswijgenhoven E, Luyten J. Gelcasting, a near net shape technique. *Mater Des.* 2000;21:251–7.
- Fukushima M, Nakata M, Zhou Y, Ohji T, Yoshizawa YI. Fabrication and properties of ultra highly porous silicon carbide by the gelation freezing method. *J Eur Ceram Soc.* 2010;30(14):2889–96. <https://doi.org/10.1016/j.jeurceramsoc.2010.03.018>
- Fukushima M, Tsuda S, Yu IY. Fabrication of highly porous alumina prepared by gelation freezing route with antifreeze protein. *J Am Ceram Soc.* 2013;96(4):1029–31. <https://doi.org/10.1111/jace.12229>
- Fukushima M, Yoshizawa YI. Fabrication and morphology control of highly porous mullite thermal insulators prepared by gelation freezing route. *J Eur Ceram Soc.* 2016;36(12):2947–53. <https://doi.org/10.1016/j.jeurceramsoc.2015.09.041>

19. Zhang L, Le Coz-Botrel R, Beddoes C, Sjöström T, Su B. Gelatin freeze casting of biomimetic titanium alloy with anisotropic and gradient pore structure. *Biomed Mater.* 2017;12(1):015014. <https://doi.org/10.1088/1748-605X/aa50a1>
20. Lichtner A, Roussel D, Jauffrés D, Martin CL, Bordia RK. Effect of macropore anisotropy on the mechanical response of hierarchically porous ceramics. *J Am Ceram Soc.* 2016;99(3):979–87. <https://doi.org/10.1111/jace.14004>
21. Christiansen CD, Nielsen KK, Bjørk R. Freeze-casting to create directional micro-channels in regenerators for magnetic refrigeration. In *Proceedings of TherMag VIII, 8th IIF-IIR International Conference on Caloric Cooling*, 2018; pages 96–101, Darmstadt, Germany. <https://doi.org/10.18462/iir.11072>
22. Smith A. Who discovered the magnetocaloric effect? Warburg, Weiss, and the connection between magnetism and heat. *European Physical Journal H.* 2013;38(4):507–17. <https://doi.org/10.1140/epjh/e2013-40001-9>
23. Dinesen A, Linderoth S, Mørup S. Direct and indirect measurement of the magnetocaloric effect in $\text{La}_{0.67}\text{Ca}_{0.33}\text{Sr}_x\text{MnO}_{3-\delta}$. *J Phys: Condens Matter.* 2005;17(39):6257–69. <https://doi.org/10.1088/0953-8984/17/39/011>
24. Bahl CRH, Velázquez D, Nielsen KK, Engelbrecht K, Andersen KB, Bulatova R, et al. High performance magnetocaloric perovskites for magnetic refrigeration. *Appl Phys Lett.* 2012;100(12). <https://doi.org/10.1063/1.3695338>
25. Lei T, Engelbrecht K, Nielsen KK, Neves Bez H, Bahl CRH. Study of multi-layer active magnetic regenerators using magnetocaloric materials with first and second order phase transition. *J Phys D Appl Phys.* 2016;49(34):345001. <https://doi.org/10.1088/0022-3727/49/34/345001>
26. Fukushima M, Ohji T, Hyuga H, Matsunaga C, Yoshizawa YI. Effect of gelatin gel strength on microstructures and mechanical properties of cellular ceramics created by gelation freezing route. *J Mater Res.* 2017;32(17):3286–93. <https://doi.org/10.1557/jmr.2017.94>
27. Lichtner AZ. Anisotropic and hierarchical porosity in multifunctional ceramics. Phd dissertation, University of Washington, 2015.
28. Jørgensen PS, Ebbenhøj SL, Hauch A. Triple phase boundary specific pathway analysis for quantitative characterization of solid oxide cell electrode microstructure. *J Power Sources.* 2015;279:686–93. <https://doi.org/10.1016/j.jpowsour.2015.01.054>
29. Cooper SJ, Bertei A, Shearing PR, Kilner JA, Brandon NP. TauFactor: An open-source application for calculating tortuosity factors from tomographic data. *SoftwareX.* 2016;5:203–10. <https://doi.org/10.1016/j.softx.2016.09.002>
30. De Angelis S, Jørgensen PS, Esposito V, Tsai EHR, Holler M, Kreka K, et al. Ex-situ tracking solid oxide cell electrode microstructural evolution in a redox cycle by high resolution ptychographic nanotomography. *J Power Sources.* 2017;360:520–7. <https://doi.org/10.1016/j.jpowsour.2017.06.035>
31. De Angelis S, Jørgensen PS, Tsai EHR, Holler M, Kreka K, Bowen JR. Three dimensional characterization of nickel coarsening in solid oxide cells via ex-situ ptychographic nano-tomography. *J Power Sources.* 2018;383:72–9. <https://doi.org/10.1016/j.jpowsour.2018.02.031>
32. Deville S, Munch E, Saiz E, Tomsia AP. Architectural control of freeze-cast ceramics through additives and templating. *J Am Ceram Soc.* 2009;92(7):1534–9. <https://doi.org/10.1111/j.1551-2916.2009.03087.x>
33. Fukushima M, Yoshizawa YI, Ohji T. Macroporous ceramics by gelation-freezing route using gelatin. *Adv Eng Mater.* 2014;16(6):607–20. <https://doi.org/10.1002/adem.201400067>
34. Deville S. Freeze-casting of porous ceramics: A review of current achievements and issues. *Adv Eng Mater.* 2008;10(3):155–69. <https://doi.org/10.1002/adem.200700270>
35. Seuba J, Deville S, Guizard C, Stevenson AJ. The effect of wall thickness distribution on mechanical reliability and strength in unidirectional porous ceramics. *Sci Technol Adv Mater.* 2016;17(1):128–35. <https://doi.org/10.1080/14686996.2016.1140309>
36. Deville S, Maire E, Lasalle A, Bogner A, Gauthier C, Leloup J, et al. In situ X-ray radiography and tomography observations of the solidification of aqueous alumina particle suspensions—Part I: Initial instants. *J Am Ceram Soc.* 2009;92(11):2489–96. <https://doi.org/10.1111/j.1551-2916.2009.03163.x>
37. Bareggi A, Maire E, Lasalle A, Deville S. Dynamics of the freezing front during the solidification of a colloidal alumina aqueous suspension: In situ x-ray radiography, tomography, and modeling. *J Am Ceram Soc.* 2011;94(10):3570–8. <https://doi.org/10.1111/j.1551-2916.2011.04572.x>
38. Roussel D, Lichtner A, Jauffrés D, Villanova J, Bordia RK, Martin CL. Strength of hierarchically porous ceramics: discrete simulations on X-ray nanotomography images. *Scripta Mater.* 2016;113:250–3. <https://doi.org/10.1016/j.scriptamat.2015.11.015>

How to cite this article: Christiansen CD, Nielsen KK, Bordia RK, Bjørk R. The effect of gelation on statically and dynamically freeze-cast structures. *J Am Ceram Soc.* 2019;00:1–11. <https://doi.org/10.1111/jace.16500>

Heat transfer and flow resistance analysis of a novel freeze-cast regenerator

Jierong Liang, Cathrine D. Christiansen, Kurt Engelbrecht, Kaspar K. Nielsen, Rasmus Bjørk, Christian R.H. Bahl

Submitted for peer-review in: *International Journal of Heat and Mass Transfer*

Processing and characterization of freeze-cast structures was carried out by me, while passive testing, model fit and data analysis was carried out by the first-author Jierong Liang. The work was carried out at Department of Energy Conversion and Storage, Technical University of Denmark during the Ph.D. period. I am co-author of the paper.

Heat Transfer and Flow Resistance Analysis of a Novel Freeze-Cast Regenerator

Jierong Liang, Cathrine D. Christiansen, Kurt Engelbrecht, Kaspar K. Nielsen, Rasmus Bjørk, Christian R.H. Bahl*

Department of Energy Conversion and Storage, Technical University of Denmark, 4000 Roskilde, Denmark

*E-mail address: chrb@dtu.dk

Abstract: The heat transfer and flow resistance of a novel freeze-cast porous regenerator of the magnetocaloric ceramic $\text{La}_{0.66}\text{Ca}_{0.27}\text{Sr}_{0.06}\text{Mn}_{1.05}\text{O}_3$ was experimentally characterized. Such a porous architecture may be useful as a regenerator geometry in magnetic refrigeration applications due to the sub-millimeter hydraulic diameters that can be achieved. Here the heat transfer effectiveness and friction losses are characterized using experiments and processed with a 1D numerical model. Empirical correlations of the friction factor and Nusselt number are reviewed and chosen for modelling the specific geometry. The experimental results show that the freeze-cast regenerator has increased heat transfer effectiveness and pressure drop compared to reference packed bed regenerators made from epoxy bonded spherical and irregular particles, as well as packed, unbonded spheres. Fixing the pressure drop and regenerator size, the freeze-cast regenerator achieves 10-15% higher heat transfer performance compared to packed bed regenerators.

Keywords: Magnetic regeneration; Thermal regenerator; Freeze-casting; Lamellar microchannel; Thermal evaluation

Highlights:

- (1) First application of freeze-casting techniques in magnetic refrigeration.
- (2) Heat transfer and flow resistance in a lamellar micro channel structure are characterized.
- (3) Thermal evaluations on freeze-cast regenerators are performed via passive testing and numerical model.
- (4) High heat transfer performance is obtained in a freeze-cast regenerator.

1. Introduction

1.1. Introduction to magnetic refrigeration

As one of the promising alternative refrigeration technologies, research in room temperature magnetic refrigeration mainly focusses on: magnetocaloric materials [1], magnet arrangements [2], and regenerator designs [3,4]. The last issue is to pursue the best practical performance of regenerators fabricated using industrially relevant magnetocaloric materials (MCMs) and processing paths. MCMs can convert energy from magnetic work (field change) to thermal energy (temperature change), based on the magnetocaloric effect [5,6]. Rare earths (gadolinium and its alloys) [7], intermetallics (La-Fe-Si based) [8] and ceramics (i.e. $\text{La}_{0.66}\text{Ca}_{0.33-x}\text{Sr}_x\text{Mn}_{1.05}\text{O}_3$) [9] are commonly used MCMs for the applications of room temperature magnetic refrigeration. Due to the intrinsic material characteristics, the magnetocaloric effect is small

[10,11]. It is characterized by the isothermal entropy difference (ΔS_{iso}) and adiabatic temperature change (ΔT_{ad}). For the benchmark MCM gadolinium (Gd), the value of ΔT_{ad} in a 1 T magnetic field is about 3.0 K - 3.5 K, experimentally, depending on the purity of the Gd [12,13]. Refrigeration cycles such as the Carnot cycles and the Ericsson cycles are restricted by the small ΔT_{ad} . The active magnetic regenerative cycle is generally adopted in magnetic refrigeration prototypes [14], which are based on progressively creating and maintaining an axial temperature gradient along the MCM regenerator [15]. In the active magnetic regenerator (AMRs) cycle, four steps are conducted: 1) magnetization; 2) flow from cold to hot reservoir through the regenerator; 3) demagnetization; and 4) flow from cold to hot reservoir. Each infinitesimally small part of the regenerator bed undergoes a unique refrigeration cycle and interacts with the adjacent material via the heat transfer fluid.

Potential regenerator geometries can be tested with an applied magnetic field as an active regenerator or with no applied magnetic field as a passive regenerator and various test devices of each type have been presented in the literature [16]. The AMR characterization involves both the magnetocaloric and heat transfer properties of the regenerator, which are generally characterized based by the temperature span, cooling capacity and efficiency of the AMR system [17]. Other AMR studies have focused on flow profiles [18] and working conditions [19,20]. A passive testing device is essentially a synchronized AMR device with zero applied magnetic field. Passive testing focusses on the heat transfer performance and pressure drop characteristics of the geometry and can be performed on materials with or without a magnetocaloric effect. The effectiveness (η) and friction factor (f) are the most important performance metrics that reflect the behavior of heat transfer and viscous friction. Lei et al. [21] compared η and f between two epoxy bonded regenerators with spherical and irregular particles on a passive test rig. Trevizoli et al. [22] performed a parametric η - NTU analysis and viscous friction factor characterization of packed bed regenerators to be used in AMR cycles with different diameters of stainless steel spheres using a passive apparatus. Šarlah et al. [23] carried out passive experiments to characterize the Colburn j -factor and the friction factor among six different geometries. Passive characterization is an efficient way to focus on the behavior of heat and mass transfer, especially for a new regenerator morphology while ignoring the magnetocaloric effect.

In passive mode, the regenerator serves as a thermal storage heat exchanger with oscillating fluid flow. Intermittent alternating heat transfer takes place between the solid matrix and the fluid in two periods: 1) hot blow: fluid from the high-temperature reservoir warms up the solid matrix; 2) cold blow: reversing the fluid flow and the matrix releases the stored heat. From this point of view, an efficient regenerator requires [24]: 1) a large value of the overall heat transfer coefficient times surface area; 2) a large thermal inertia to decrease temperature oscillations; and 3) a low friction factor to minimize pumping power consumption and viscous losses. Over the last decades, various geometries have been developed and tested for AMR applications, such as: 1) packed particle bed [25], 2) parallel plate [26], 3) micro-channel [27], and 4) packed screen bed [28]. These geometries have their own advantages and weaknesses. Concerning the heat transfer performance and friction dissipation, the parallel plates and micro-channel matrices normally exhibit small values [29,30]; while packed particle beds exhibit both high values of η and f . Thus, any new geometry of regenerator might exhibit different heat transfer performance and parasitic losses, and needs to be passively characterized prior to being used in an AMR device. A new applicable geometry could be that of a freeze-cast ceramic.

1.2. Shaping by freeze-casting

Freeze-casting, or ice-templating, is a processing technique used to shape, typically, ceramics into monolithic, anisotropic structures with an aligned channel-geometry of highly tunable dimensions and porosity. The channels are typically on the order of ~ 1 to ~ 100 μm wide [31–33]. Freeze-cast structures

have great mechanical durability and have been used in a broad range of applications, primarily within biomaterials for tissue engineering or membranes for catalysis, electrodes, filters etc. [34].

In freeze-casting, a suspension of ceramic particles in water is frozen directionally by bringing only one side of the suspension into contact with a cooling source. This initiates directional growth of ice crystals along the temperature gradient, causing a segregation of particles resulting in a two-phase structure of ceramic and ice. The latter is then removed by sublimation. Subsequent sintering results in a rigid ceramic structure with directional porosity in the form of parallel, well-defined channels as seen in Fig. 1a. The morphology and dimensions of these channels strongly depend on freezing conditions [32,35,36], while the porosity depends on the ceramic load of the slurry. The structural and dimensional characteristics, and thus flow properties of the freeze-cast structure, can thus be adjusted and optimized by changing processing parameters.

Utilizing this processing route for shaping of magnetocaloric ceramics such as $\text{La}_{0.66}\text{Ca}_{0.27}\text{Sr}_{0.06}\text{Mn}_{1.05}\text{O}_3$ (LCSM), thus results in an attractive regenerator geometry of lamellar micro-channels as shown in Fig. 1. The freeze-cast geometry can be summarized as follows:

- (1) Narrow, lamellar pores with an ellipsoid cross-section on the micrometer-scale. The lack of square corners for this pore shape, compared to other micro-channel geometries, could result in the increment in local heat transfer coefficient [37,38].
- (2) Non-ordered orientations of the major axes of the ellipsoidal channels in the plane perpendicular to the flow direction.
- (3) Low tortuosity, i.e. almost straight channels.
- (4) Tunable porosity and large specific surface area, providing a geometry that will presumably exhibit high convection coefficient with reasonable flow resistance.

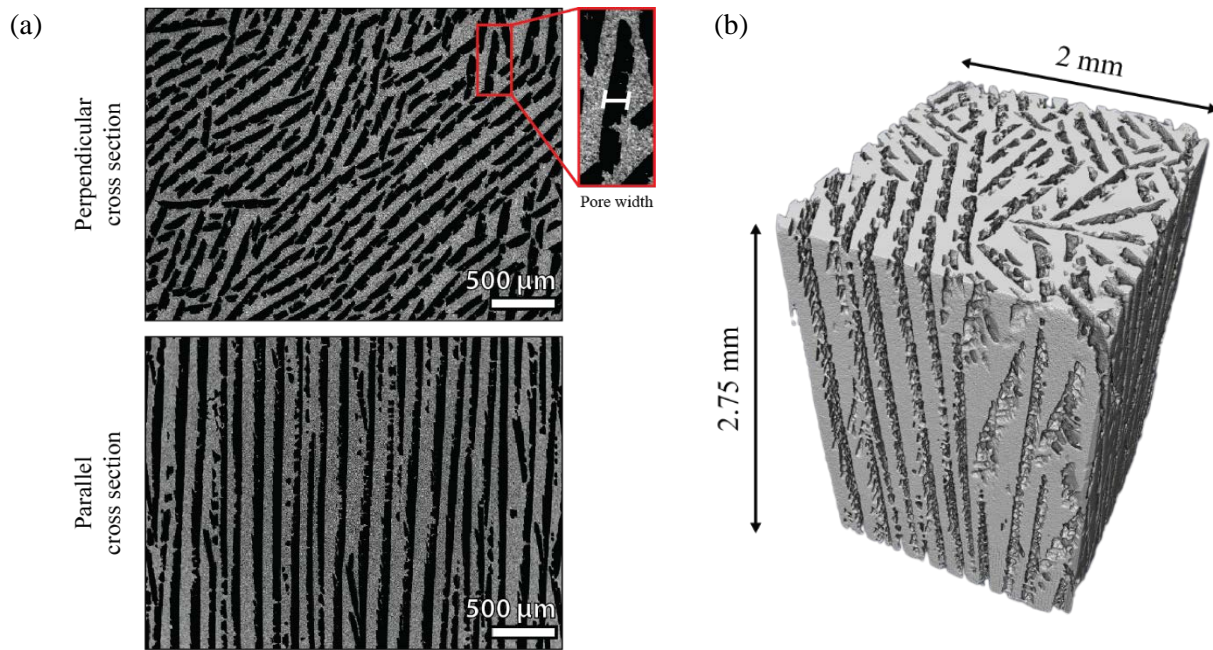


Fig. 1 Geometry of freeze-cast LCSM ceramics. (a) SEM micrographs of cross sections of a freeze-cast sample where grey areas are the ceramic walls and black areas are porosity in the form of aligned, lamellar channels. Micrographs are obtained at cross sections perpendicular and parallel to the freezing direction in the center of the structure. (b) 3D

reconstruction of freeze-cast LCSM ceramic based on interactive segmentation using Avizo software (Thermo Fischer Scientific) of tomography images obtained using an X-ray Microscope (ZEISS Xradia 520 Versa).

In this paper, we propose a novel freeze-cast matrix as a possible regenerator for an AMR and present measurements of regenerator effectiveness and pressure drop for a freeze-cast regenerator. These results are compared with a packed bed of spheres, which is considered a baseline AMR regenerator geometry. Furthermore, a 1D model framework [39] is used to derive the specific empirical correlations of Nusselt number and friction factor by fitting the model to the measured inlet and outlet temperatures and measured pressure drops. The numerical model is validated over a broad range of operating conditions. The model helps to better understand the internal phenomena of heat transfer and flow resistance, which is difficult to measure experimentally. The thermal evaluations can be used to assist in the new regenerator development of physics-based predictive capabilities, performance metrics, and design guidelines.

2. Sample fabrication and characterization

2.1. Freeze-casting procedure

The fabrication and characterization of freeze-cast ceramics follows the process described by Christiansen *et al.* [36,40], with slight alterations regarding suspension composition and freezing conditions.

Freeze-cast ceramics were prepared from suspensions of 30 vol% of LCSM (CerPoTech, Norway) in MilliQ water with 2.5 wt%, solid to ceramic ratio, of dispersant (DURAMAX™ D-3005, Rohm and Haas, Dow Chemical, USA). Additionally, the pH of the suspension was adjusted from ~8 to ~6.5 with dropwise addition of 1M nitric acid to establish a sufficient dispersion of particles. The suspension was then mixed on a low energy ball mill with alumina balls (Ø10 mm) for at least 72 hours until a consistent particle size of $d_{50} = 1.2 \mu\text{m}$ was reached. 2 wt%, solid to ceramic ratio, of binder (DURAMAX™ B-1022, Rohm and Haas, Dow Chemical, USA) was added and the suspension was mixed for an additional 24 hours. Both binder and dispersing agent were chosen based on their low viscosity and thus suspensions were easily de-aired immediately before casting by brief sonication in order to avoid bubbles.

Cylindrical Teflon™ molds, with inner diameter of 30.5 mm and outer diameter of 50 mm, and a detachable copper bottom were pre-cooled in an ice-bath along with the ceramic suspension prior to casting. The suspension was poured into the mold, which was then attached to the cold finger of a novel freeze-casting device utilizing thermoelectric cooling for precise temperature control, making it possible to set a specific temperature profile of the cold finger during casting. By lowering the temperature of the cold finger while keeping the suspension and mold open to ambient conditions of 5 °C, the suspension is frozen directionally from the bottom and up. The temperature of the cold finger is kept at 2.5°C for 300 s prior to freezing to equilibrate the temperature of the mold and suspension, and is then decreased at -1 K/min until the entire suspension is frozen solid. A linearly decreasing temperature profile was chosen in order to achieve homogenous channel widths along the sample height in accordance with previous work [36].

Ice was subsequently removed from the frozen samples in a freeze-drier (Christ Alpha 1-2 LD plus, Buch & Holm) for 24 hours. Dry samples were fired in air, initially burning out the organic additives at 250 and 450 °C, with a holdtime of 2 hours at each temperature and a heating rate of 15 K/min, followed by sintering at 1100 °C for 12 hours with a heating rate of 30 K/min.

2.1.1. Structural characterization of freeze-cast ceramics

Freeze-cast samples for testing were cut into smaller pieces as described in section 2.1.2. Top and bottom parts were mounted in epoxy (Epofix, Struers, Denmark), and the cross section was then imaged using a scanning electron microscope (TM3000, Hitachi High-Technologies). The analysis of micrographs follows

that described by Christiansen *et al.* [36], where channel width (as defined in Fig. 1a), macro porosity and tortuosity are determined. Additionally, the perimeter of channels can be measured in binarized micrographs of cross sections perpendicular to the freezing direction yielding a measurement of the specific surface area. A total of 21 micrographs, each covering ~300 channels in the perpendicular cross section, obtained evenly distributed across the cross sections of the freeze-cast samples have been analyzed to calculate the average structural parameters. These parameters have been summarized in Table 1. As measurements of the tortuosity requires imaging of cross sections parallel to the channel direction, and thus requires additional destructive procedures, the calculation of tortuosity is based on a sample fabricated from the same suspension and frozen under the same conditions.

As is seen on Fig. 1, the overall geometry of the channels in freeze-cast structures are lamellar with channels running along the freezing direction. In the horizontal plane the shape of channels are ellipsoidal with a pore width as shown on Fig. 1. While the orientation of channels in the horizontal plane is ordered in smaller domains, channels are highly aligned in the plane parallel to the freezing direction. Tortuosity is a measure of this alignment and curviness of channels and is calculated as the ratio between the direct distance across a cross section parallel to the freezing direction and the average distance through a channel. Thus, a tortuosity of $\mathfrak{T} = 1$ describes a direct flow path through the structure, while an increase in tortuosity corresponds to an increasingly curved and obstructed flow path.

The total porosity, or sample porosity, ε , of ~70 % of the freeze-cast structure is directly related to the ceramic load of the suspension during processing, however, in the final structure only two thirds of this is accounted for by channels, i.e. the channel porosity or macro porosity, ε_p , as given in Table 1. The remaining porosity consists of micro porosity in the walls. As only the macro porosity is assumed to act as flow paths for fluid, ε_p is used for determining pore velocity while ε is adopted for solid mass calculations. Additionally, the hydraulic diameter is derived as follows:

$$D_h = 4\varepsilon_p/\alpha \quad (1)$$

where α is the specific surface area.

2.1.2. Preparation of freeze-cast regenerator

A single freeze-cast regenerator matrix is composed of two combined monolithic pieces of freeze-cast ceramic frozen at identical conditions and thus with homogenous structural characteristics. Two pieces are used to ensure a sufficient length and thermal mass of the regenerator for the AMR system used. Each piece of 15 mm is cut from a full freeze-cast sample with a length of approximately 29 mm. Due to the nature of freeze-cast ceramics, the bottom part of the sample does not contain aligned channels [41,42] and thus the bottom 8 mm and remaining top of the sample are discarded. The matrix, with a total of 30.0 g, is mounted in a transparent housing ($\varnothing 30 \text{ mm} \times 40 \text{ mm}$) using silicone glue, sealing possible gaps between the housing and the solid matrix and thus avoiding fluid flowing around the freeze-cast matrix. The transparent housing helps to observe the conditions of bypass flow and residual bubbles.

2.2. Reference regenerators

Three benchmark regenerators were used for comparison. One is a Gd packed sphere bed regenerator which is used as baseline, as this is the most commonly used type of regenerator for passive and active characterizations in magnetic refrigeration. Furthermore, epoxy bonded regenerators made from irregular or spherical particles of $\text{La}(\text{Fe},\text{Mn},\text{Si})_{13}\text{H}_y$ referred to as VAC-A and VAC-B, respectively, are used as a mean of testing state of the art magnetocaloric regenerators.

The diameter of particles in the Gd bed is ~ 0.3 mm, and it uses the same housing as the freeze-cast regenerator. A mesh screen is used to keep the particles in the housing. Although this housing geometry is not optimal for the Gd regenerator, it is important to ensure that the tested regenerators have the same system effects beyond the regenerator, such as dead volume loss and heat leaks.

The epoxy bonded regenerators were not tested in this work. Instead their experimental data are taken from the references [21,39] directly. The geometry parameters of the reference regenerators in this paper are included in Table 1.

Table 1: Geometry parameters of tested regenerators. Structural characteristics of freeze-cast ceramics are from image analysis of obtained micrographs. The corresponding measurements are based on the analysis of 15 images evenly distributed along the height parallel to the freezing direction of a freeze-cast sample and are given as an average. Data of other reference regenerators are also introduced from the publish works. The size of housing is specified as diameter and length.

Parameters	Freeze-cast	Gd packed bed [39]	VAC-A [21]	VAC-B [21]
Housing (mm×mm)	Ø30×40	Ø30×40	Ø20×70	Ø20×70
Pore width (μm)	72.0 ± 6.4	/	/	/
Avg. particle diameter (mm)	/	0.3	0.56	0.58
Sample porosity	0.72	0.45	0.46	0.48
Macro porosity	0.42	0.45	0.46	0.48
Hydraulic diameter (mm)	0.102	0.160	0.410	0.380
Specific surface area (m^{-1})	1.64×10^4	1.10×10^4	4.49×10^3	5.05×10^3
Tortuosity	1.6 ± 0.3	/	/	/

3. Passive characterization of heat transfer and pressure drop

3.1. Experimental setup description

The infrastructure of the passive regenerator test apparatus was published previously [21]. The instrumentation and connections are shown in Fig. 2, including the regenerator assembly, cold and hot reservoirs, piston and motor assembly and check valves.

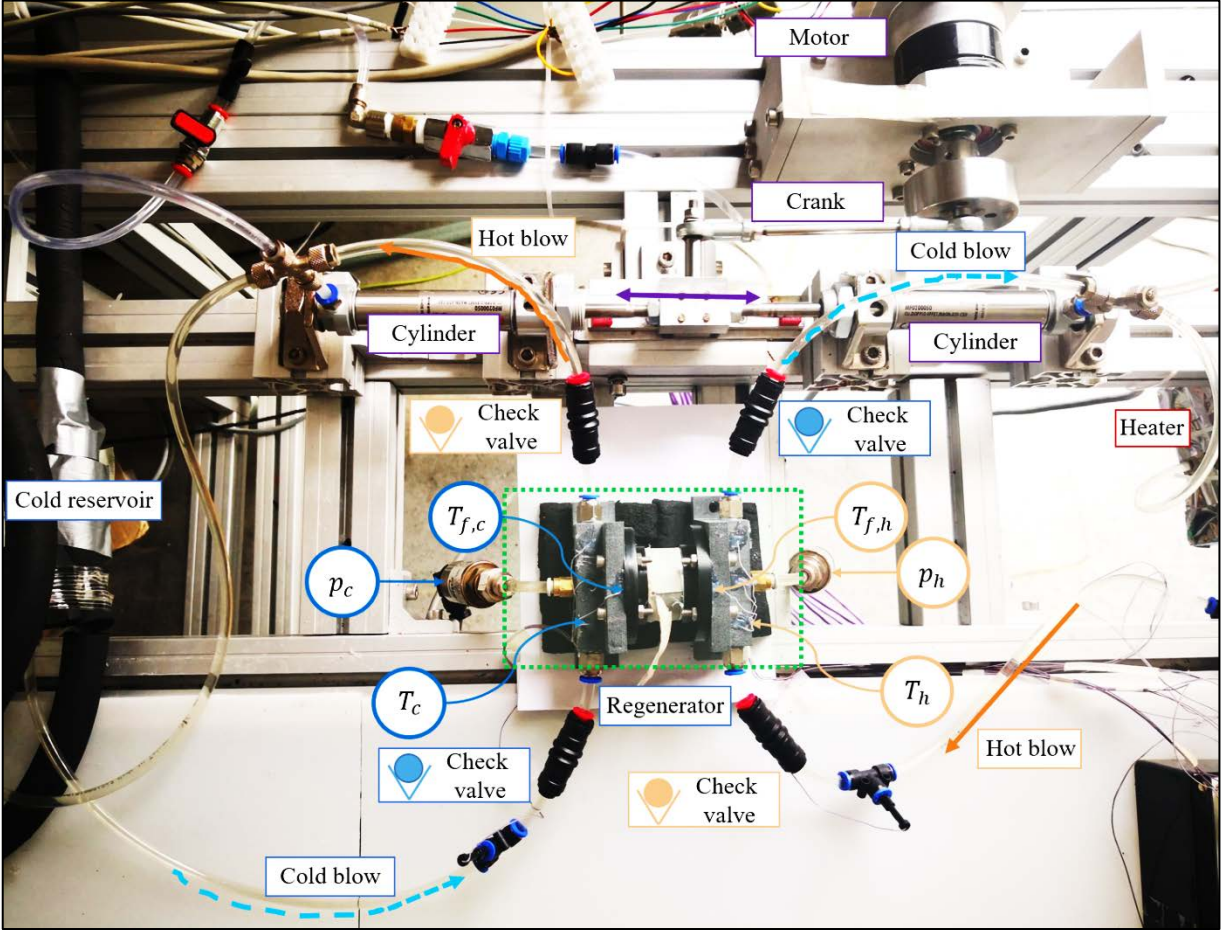


Fig. 2 Passive test rig with hot blow and cold blow flow directions illustrated. The regenerator is connected to manifolds at both ends. Each manifold integrates the functions of flow separation, thermocouple and pressure transducer installations. The outflow from the manifold will go through the outlet check valve, piston, cold reservoir or heater, inlet check valve, and then back to the inlet of the manifold.

The regenerator assembly consists of regenerative material, 3D-printed resin housing and manifolds with thermocouples (Omega, type E) and pressure transducers (Gems, 2.5 bar). Within the green dashed box shown in Fig.2, four check valves direct the fluid flow. The end temperature probes are set in $T_{f,h}$ and $T_{f,c}$, which are positioned to almost touch the screens at each end of the regenerator. Another two thermocouples that represent inflow and outflow temperatures, are positioned in T_h and T_c outside the dashed box. Two pressure transducers are set at the ends of the regenerators measuring the pressure drop. Data acquisition is performed with a National Instruments (NI) cDAQ9174 system connected to an NI 9213 thermocouple module and an NI 9203 current module (for the pressure transducers). The tests are performed using tap water as the heat transfer fluid.

The piston and motor assembly is a motor-crank system connected to two cylinders, one for each direction of flow. The motor rotary frequency control and displacement record are implemented by a linear encoder. The oscillating flow is generated by the reciprocating movement of the two cylinders. In Fig.2, the solid arrows represent the hot blow, while the dashed arrows indicate the cold blow.

All tests performed in this work are carried out for balanced flow conditions in both the freeze-cast regenerator and the Gd packed sphere bed regenerator. The temperature span between the hot and cold end

is set as a constant for comparison. With a small temperature span it is not easy to capture the temperature breakthroughs in $T_{f,h}$ and $T_{f,c}$ during the blow, and therefore a 10 K span is used here, as this is suitable based on the existing heater capacity. To reveal the heat capacity sensitivity on local temperature and bound the Curie temperature of LCSM ($\sim 19^\circ\text{C}$), the variation of cold reservoir temperature T_c tested is from 15°C to 30°C , with an increment of 5°C . The testing temperature intervals represent the peak bounded, decreasing region, buffer region and flat region, respectively, as indicated in Fig.3. During each measurement with fixed reservoir temperatures, the piston stroke was adjusted to control the specific heat of the fluid, in order to keep the utilization constant. The frequency was varied from 0.50 to 2 Hz in steps of 0.25 Hz. The uncertainty analysis is described in Appendix. A.

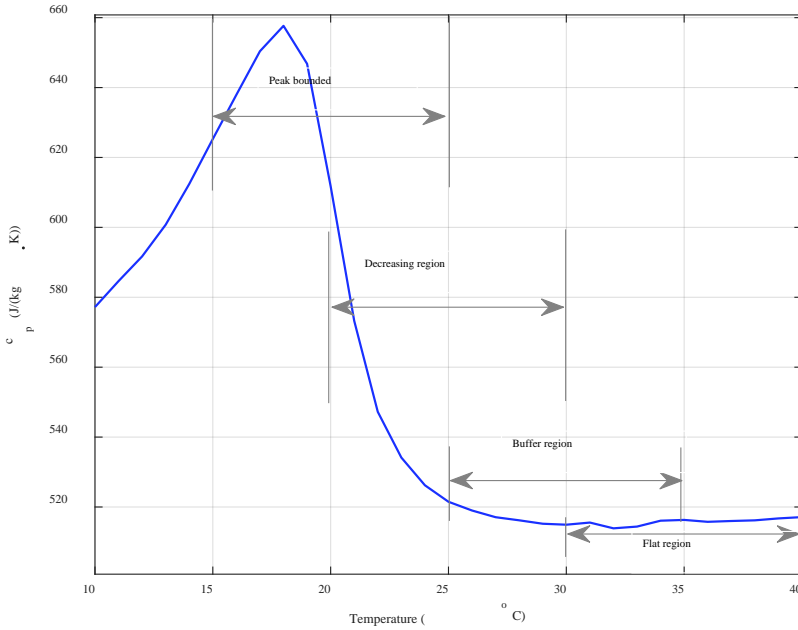


Fig. 3 Temperature dependency of specific heat capacity of LCSM in zero field.

3.1.1. Performance metrics

To introduce the effectiveness- NTU method for passive characterization, the relationship of effectiveness, utilization (U) and number of transfer unit (NTU) will be investigated experimentally and numerically in the following section. The utilization is a preliminary design parameter to characterize the system configuration [16]. Due to small-scale channels, in the expression for the U we assume that the solid thermal mass accounts for the total thermal mass, the fluid specific heat capacity is temperature independent and the flows are balanced.

$$U = \frac{\int_0^{\tau/2} \dot{m}_f c_f dt}{m_s c_s} \quad (2)$$

Here the subscripts f and s denote solid and fluid respectively. Note that the background value of solid specific heat capacity c_s is used rather than the peak value. As a measure of the intensity of heat transfer, the NTU is defined as:

$$NTU = \frac{h\alpha V_r}{2/\tau \int_{\tau/2}^{\tau} \dot{m}_{f,c} c_{f,c} dt} \quad (3)$$

Where h , α and V_r are heat transfer coefficient, specific surface area and regenerator volume, respectively. $\dot{m}_{f,c}c_{f,c}$ indicates that the thermal mass rate is taken from the cold blow. Accordingly, the Nu is defined as:

$$Nu = \frac{hD_h}{k_f} \quad (4)$$

Where D_h and k_f are hydraulic diameter and thermal conductivity of the fluid. As a metric of heat transfer performance, the effectiveness in each blow period (subscripts h and c are for hot and cold blow, respectively) are given by:

$$\eta_h = \frac{T_h - 2/\tau \int_{\tau/2}^{\tau} T_{f,c} dt}{T_h - T_c} \quad (5)$$

$$\eta_c = \frac{2/\tau \int_0^{\tau/2} T_{f,h} dt - T_c}{T_h - T_c} \quad (6)$$

Flow resistance is characterized by the relationship between the friction factor (f) and Reynolds number (Re). In oscillatory flow situations, pressure drop amplitude and cycle average pressure drop are adopted to define the oscillatory friction factor (f_{osc}) [43] and cycle average friction factor (f_{avg}) [44] respectively. f_{osc} is suitable for correlation fitting, flow pattern and system operating range determinations [45,46], while f_{avg} is directly linked to pumping work and comparison with steady flow [47]. To be consistent with the existing framework of f correlations in Table B1 which will be discussed below, f_{osc} is selected to define the friction factor.

$$f = \frac{\Delta p_{max}}{L_r} \frac{D_h}{2\rho_f(v_{f,max})^2} \quad (7)$$

Regarding the definition of Re , the velocity term can be superficial velocity, pore velocity or angular velocity. Here the Reynolds number based on the pore velocity is chosen also to be consistent with the correlations in Table B1:

$$Re_p = \frac{\rho_f(v_f/\varepsilon_m)D_h}{\mu_f} \quad (8)$$

Where v_f and μ_f are fluid superficial velocity and dynamic viscosity, respectively.

3.2. Data analysis tools

As a novel micro-channel matrix, there has been little research effort to model the solid-fluid heat transfer and flow resistance in freeze-cast sample like architectures. Developing the specific correlations for heat transfer and friction dissipation to be used in porous media models, is therefore necessary to derive the internal parameters i.e. Nu and NTU . It is also an effective tool for model predictions in the future.

3.2.1. Numerical model

Since a freeze-cast regenerator as a random geometry cannot be fully addressed in a two-dimensional space, a 1D model is suitable here. The energy and mass governing equations are taken from Lei 2016 [39] to characterize the interior transient temperature distribution, as well as the pressure drop. The two equations are coupled by means of the heat convection term.

The energy balance on the fluid:

$$\begin{aligned}
& \underbrace{\frac{\partial}{\partial x} \left(k_{disp} A_c \frac{\partial T_f}{\partial x} \right)}_{\text{Heat conduction}} - \underbrace{\dot{m}_f \frac{\partial h_f}{\partial x}}_{\text{Enthalpy flow}} - \underbrace{\frac{Nu k_{disp}}{d_h} a_s A_c (T_f - T_s)}_{\text{Heat convection with solid}} - \underbrace{h_{wf} a_{wf} A_c (T_f - T_w)}_{\text{Heat convection with housing}} + \\
& \underbrace{\left[\frac{\partial p}{\partial x} \frac{\dot{m}_f}{\rho_f} \right]}_{\text{Viscous dissipation}} = \underbrace{A_c \varepsilon \rho_f c_f \frac{\partial T_f}{\partial t}}_{\text{Energy storage}} \quad (9)
\end{aligned}$$

The solid energy equation:

$$\frac{\partial}{\partial x} \left(k_{stat} A_c \frac{\partial T_s}{\partial x} \right) + \underbrace{\frac{Nu k_{disp}}{d_h} a_s A_c (T_f - T_s)}_{\text{Heat convection}} = \underbrace{A_c (1 - \varepsilon) \rho_s c_s \frac{\partial T_s}{\partial t}}_{\text{Energy storage}} \quad (10)$$

Where T , p , A_c , \dot{m} , h , ρ , c , ε , a and d_h are temperature, pressure, cross sectional area, mass flowrate, specific enthalpy, density, specific heat, sample porosity, specific area and hydraulic diameter, respectively. Subscripts f, s and w refer to fluid, solid and housing wall, respectively. The static conductivity (k_{stat}) and fluid dispersion (k_{disp}) conductivity, which are considering the 3-D conduction and axial dispersion effect in porous AMR beds, respectively, are illustrated in Eq. (11-12) [48].

$$k_{stat} = (1 - \varepsilon)k_s + \varepsilon k_f \quad (11)$$

$$k_{disp} = k_f \frac{Pe^2}{210} \quad (12)$$

Where Pe is the Péclet number. This 1D model integrates all the major terms of (1) temperature dependence of fluid properties (dynamic link to CoolProp [49]), interpolation from experimental data in magnetocaloric effect and demagnetization factor [50], (3) temperature dependent heat capacity of MCM, (4) axial thermal conduction, (5) pressure drop and (6) thermal dispersion.

3.2.2. Form of Nusselt number and friction factor correlations

The specific correlations can be derived from the existing correlations of laminar flow with micro-channels in Appendix B. These correlations typically show a difference between the flow conditions of steady state or oscillatory flow, the region of developing or developed flow, and different channel shapes. The following correlation forms are chosen considering the flow characteristics of developing and oscillatory within the narrow shape micro-channels and use the same form as [51] for the friction factor and Nu :

$$f = c_1 Re_p^{-1} + c_2 \quad (13)$$

$$Nu = c_3 [L_r / (D_h Re_p Pr)]^{c_4} \quad (14)$$

Where $c_1 \sim c_4$ are fitting parameters that are assumed to only depend on matrix morphology. Note that the correlations are valid for liquid laminar flow.

$$[c_1, c_2, c_3, c_4] = f(D_h, \mathfrak{T}) \quad (15)$$

\mathfrak{T} is the channel tortuosity:

$$\mathfrak{T} = L_{pore} / L_r \quad (16)$$

Where L_{pore} is the average pore length, L_r is the length of the regenerator sample. When one specific matrix is designated, the parameters of $c_1 \sim c_4$ can be treated as constants and fitted from experimental results.

Experimental data for a range of frequencies and utilizations are used to fit the parameters in Eq. (13-14). In the friction factor fit, the oscillatory friction factor defined in Eq. (7) can be treated as temporal independent and can be fitted all through the experimental operating conditions. The Nu is sensitive to the fluid flowrate and therefore the time. Multi objective fitting as shown in Eq. (17) is implemented by using the numerical model to find the set of parameters that best matches the experimental temperature outlet curves to those predicted by the model:

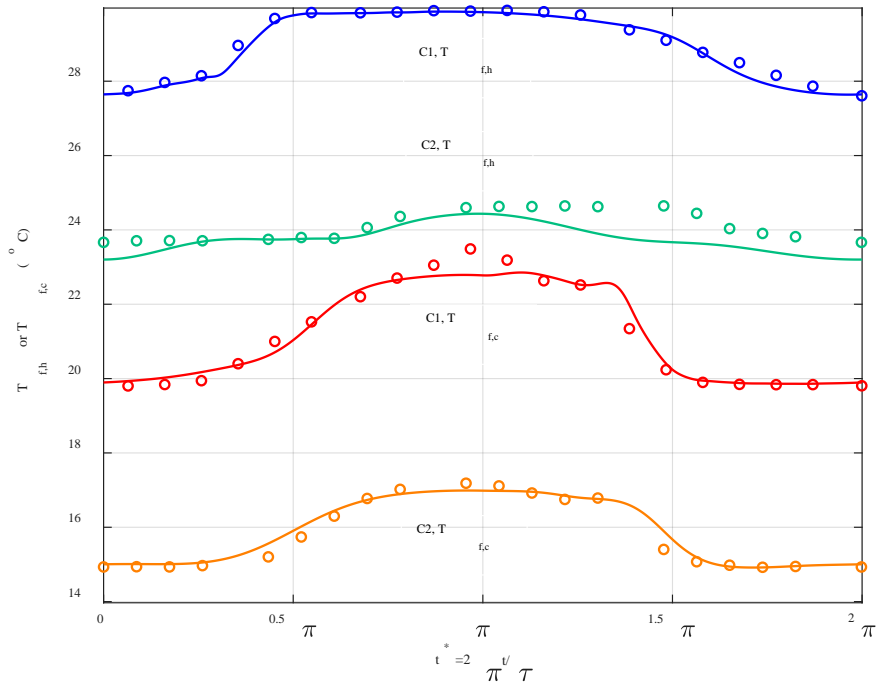
$$\min_{c_3 > 0, c_4 \in R} \mathbf{r}(\mathbf{r}), \quad \mathbf{r} = \begin{bmatrix} r_1(c_3, c_4) \\ r_2(c_3, c_4) \\ r_3(c_3, c_4) \\ r_4(c_3, c_4) \end{bmatrix}, \quad \begin{matrix} r_1 \sim (freq_{min}, U_{min}) \\ r_2 \sim (freq_{max}, U_{min}) \\ r_3 \sim (freq_{min}, U_{max}) \\ r_4 \sim (freq_{max}, U_{max}) \end{matrix} \quad (17)$$

Where \mathbf{r} is the residual tensor for Nu fitting. In detail, the residual r_1 is derived from the case when the frequency and utilization are set at the minimum values within the operating range; while $r_2 \sim r_4$ correspond to other extreme cases with the variables of frequency ($freq$) and utilization (U).

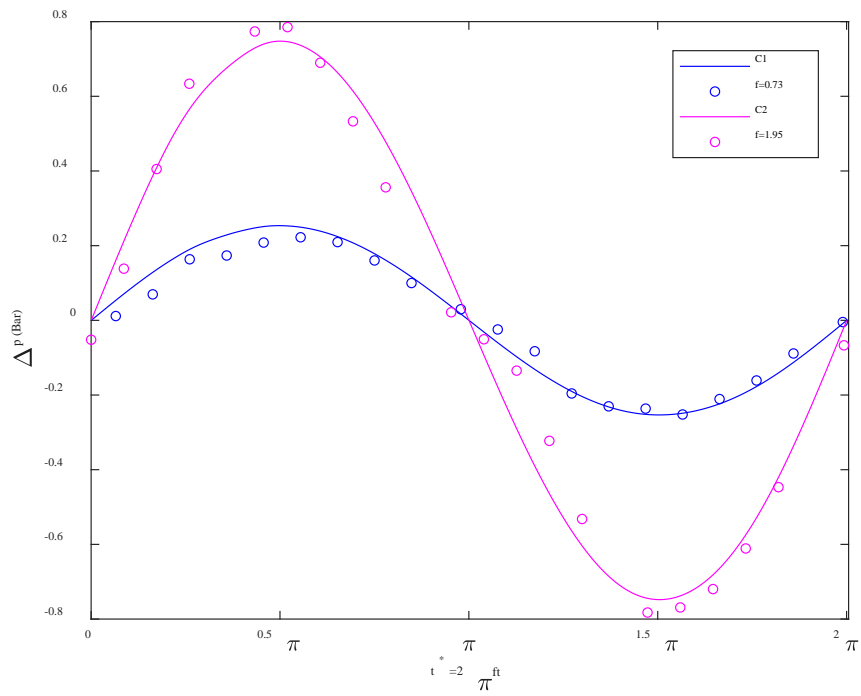
3.2.3. Model validation

Since new correlations are implemented, the parameters can be fitted with experiments. Neglecting the effect of fluid viscosity due to the temperature, c_1 and c_2 in Eq.(13) are fitted by pressure drop measurements. Based on the correctness of material properties, end temperature readings reflect the internal heat transfer conditions. Therefore $T_{f,h}(t)$ and $T_{f,c}(t)$ are only responsible for adjusting c_3 and c_4 in Eq.14. The modelling validation results with 20 experimental points in each curve are shown in Fig.4 (a) and (b) for temperature and pressure drop respectively, for a number of different operating conditions. The model fits the overall behavior of the experiments without significant trend differences. In addition, the root mean square error (RMSE) in 84 operating conditions is summarized in Fig.4(c). Comparing the fit and experimental data, the deviation is < 0.5 °C at temperature and < 0.02 bar at pressure drop, which indicates that the simulation results are in good agreement with the experimental readings, and thus that the model can be used to reveal the internal characteristics of a freeze-cast regenerator.

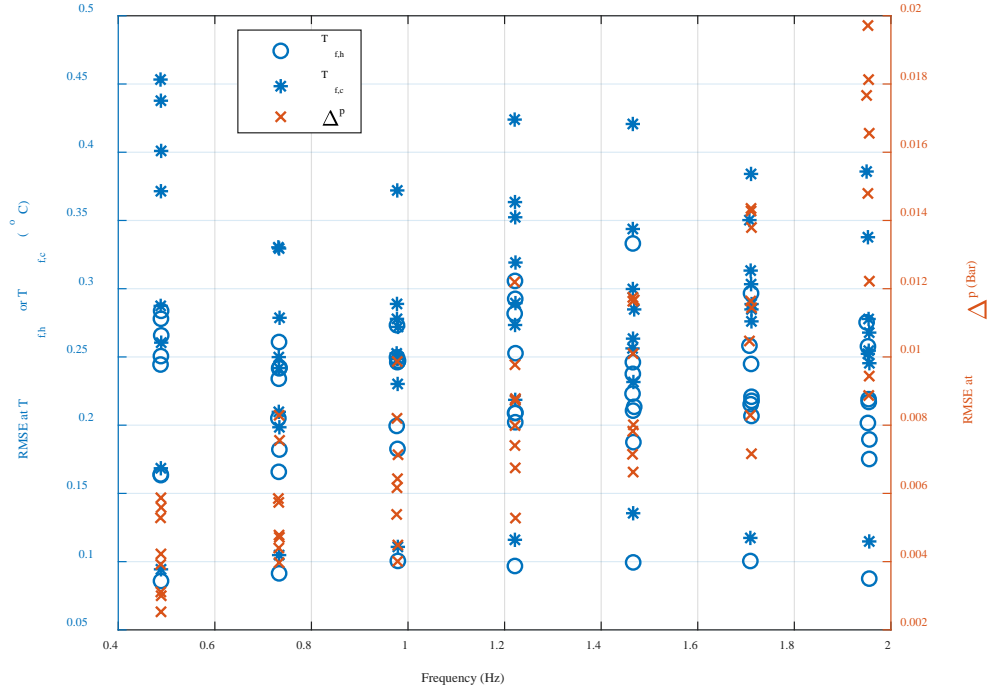
In order to reveal the sensitivity in terms of the heat transfer coefficient, Fig.4 (d) presents the temperature responses of $T_{f,c}$ with the artificial perturbation of the heat transfer coefficient in the hot blow. Since the errors of most correlations in the area of heat transfer are normally within 50%, perturbations of $\pm 50\%$ are adopted here to observe the system response. A perturbation in the decreasing direction is sensitive to temperature response, especially if its factor value is less than 0.8. On the other hand, the perturbation in the increasing direction (>1) is insensitive to temperature response, due to the small interface temperature differences. In this state, heat transfer performance is sufficient enough that over-scaling in heat transfer coefficient does not result in better performance significantly.



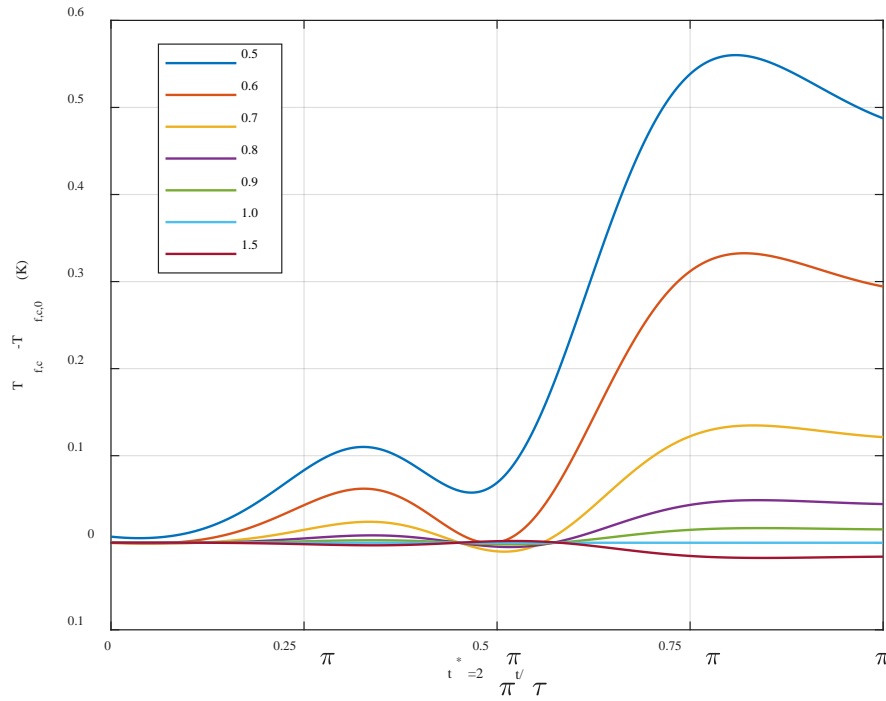
(a)



(b)



(c)



(d)

Fig. 4 Validations of (a) temperature and (b) pressure drop temporal evolution, C1 and C2 are different operating conditions corresponding to $T_{c1} = 20$ °C, $f_1 = 0.75$ Hz and $T_{c2} = 15$ °C, $f_2 = 2$ Hz respectively. Figure (c) is RMSE between the fit and experimental data under different frequencies. Figure (d) is the impact of heat transfer coefficient

perturbation on the temperature profiles of cold end in the hot blow; y-axis is the temperature perturbation response of $T_{f,c}$ based on factor = 1.0, the legend is showing the perturbation factors.

4. Results and discussions

The regenerator has been tested for nearly 700 hours in the passive experiment setup. It is noted that in the first sets of experiments, fine powder was observed coming out of the regenerator and was intercepted in the meshes. With the operation time increasing, the amount of powder coming out of the regenerator became less and less, until finally no powder could be seen with the naked eye. This illustrates both the somewhat brittle nature of LCSM materials but also the fact that residual “loose” material might be present within the freeze-cast structures after sintering.

4.1. Nusselt-Reynolds correlations

The overall spatial and temporal average Nusselt number (\overline{Nu}) is plotted as a function of cycle average \overline{Re}_p in Fig.5. In general, the trend of $Nu \sim Re$ is a sublinear relationship, which is similar to the cases of packed sphere beds [48], but different from the constant relationship in macro parallel plates [52]. For comparison, the fitted correlation for local Nu from Eq. (14) with $c_3 = 0.34$ and $c_4 = -0.32$ is plotted in the same figure. The correlation for local Nu also fits the \overline{Nu} well, which is convenient for overall evaluations of the freeze-cast regenerator. In comparison with the cases of the packed bed and rectangular micro-channel, also shown in Fig.6, the absolute values of \overline{Nu} are relatively low for the freeze-cast regenerator. The main reasons for this are:

(1) Small hydraulic diameter: referring to the definition of Nu (Eq. (4)), a small hydraulic diameter results in a relatively small Nu value based on the same heat transfer coefficient. Recalling Table.1, the hydraulic diameter of the packed bed regenerator is significantly larger than that of the freeze-cast regenerator. In Fig.5, the Nu in the packed bed regenerator outperforms that of the freeze-cast regenerator. Note that high Nu does not absolutely result in high heat transfer performance, because heat transfer area is another key factor.

(2) Limitation in oscillating blow evaluation: like single blow characterizations [53], temperature breakthroughs are insignificant when the interstitial temperature difference is tiny. In these situations, heat transfer enhancements only cause a slight change in temperature difference of solid-liquid, and therefore only small variations in temperature breakthroughs at the two ends of the regenerator. As illustrated in Fig.4 (d), heat transfer coefficient is probably under-estimated due to this insensitivity.

(3) Different characterization methodologies: The Nu in the packed bed is from an ideal situation of steady state, no dead volume or maldistribution of the flow. In the case of rectangular micro channels in Fig.5, the fit is from the steady state counterblow experiments without the effect of dead volume. For the characterization of a freeze-cast regenerator, factors of dead volume and uneven flow are unavoidably brought into the testing due to the nature of the passive rig. In principal, curves for Fig.5 are not exactly in the same level of characterization. The values in the Nu fit on freeze-cast regenerator are further under-estimated due to these external influences.

According to the fit of Eq.(14), when Re_p approaches 0 in the limit, the Nu is unphysically approaching 0. However, in no-flow periods of (de)magnetization ($Re_p = 0$) in AMR characterization, Nu should rather attain a positive value [54] considering the interstitial heat transfer via conduction. Thus, the fit extrapolated to near $Re_p = 0$ may not be valid. The experimental Re_p in this study ranged from 1 to 15. Thus, the Nu fit in this paper is reasonably confined in the passive characterization within the operating range.

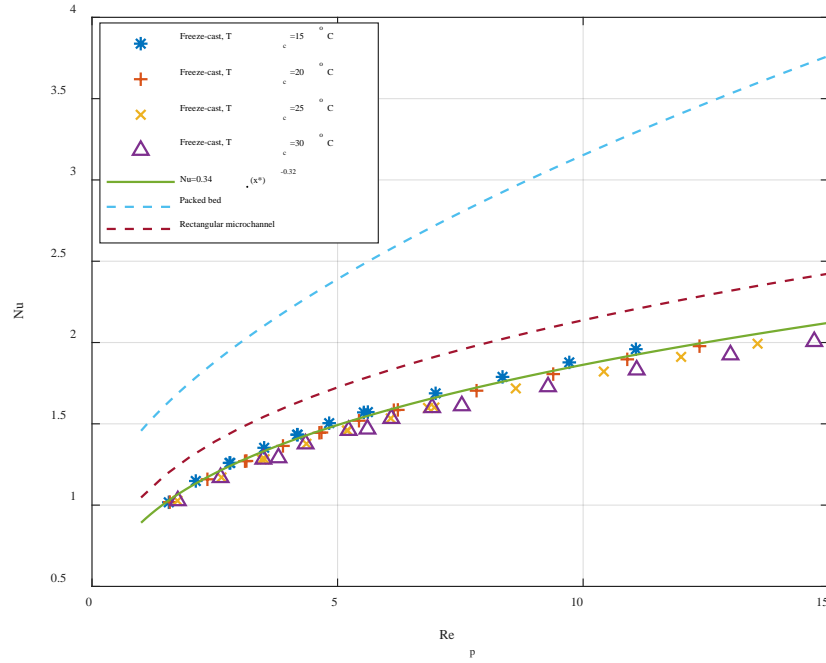


Fig.5 Nusselt number as a function of Reynolds number. The markers are $(\overline{Re}_p, \overline{Nu})$ from the numerical model with fitted correlations under different operations. The plotting of packed bed is taken from the correlations of Ref. [48] with the same parameters as the reference Gd regenerator. The fit of rectangular micro channel heat exchanger is taken from Ref. [51] based on the counterblow experiment of steady state. The width and depth of the rectangular micro channels are 0.2 mm and 0.6 mm, respectively.

4.2. Friction factor correlations

The behavior of $f \sim Re$ is depicted in Fig.6 at different operating conditions. The absolute values of f are relatively high due to the small hydraulic diameter. The general trend of the $f \sim Re$ relationship collapses into one single curve. These relations are picked up by model fitting from Eq. (13) ($c_1 = 359$ and $c_2 = -0.395$) and also fit the form of the Ergun equation ([55], rewritten in Eq.(18)). The model profiles are in qualitative agreement with the experimental behavior. The physical relations of $f \sim Re$ from packed beds are still suitable for freeze-cast regenerators with different regression parameters.

$$f = \underbrace{\beta_1 \frac{(1-\varepsilon)^2}{\varepsilon^4} \cdot \left(\frac{6D_h}{D_{sp}}\right)^2}_{c_1 \text{ regression}} \cdot Re_p^{-1} + \underbrace{\beta_2 \frac{1-\varepsilon}{16\varepsilon^3} \cdot \left(\frac{6D_h}{D_{sp}}\right)}_{c_2 \text{ regression}} \quad (18)$$

Where D_{sp} is the particle diameter and $\beta_1 \approx 2.5$ and $\beta_1 = 2.4$ in Ref.[55].

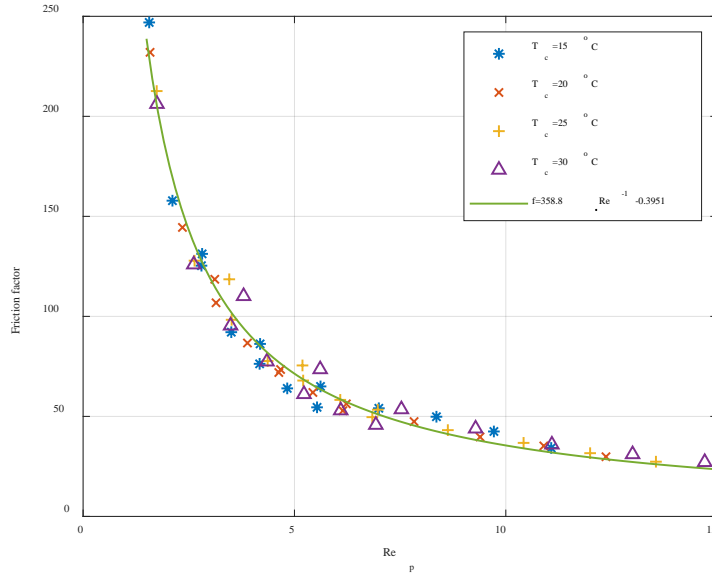


Fig.6 Experimental friction factor as a function of Reynolds number under different conditions for the freeze-cast regenerator.

4.3. Heat transfer versus flow resistance

To evaluate the whole regenerator, the curves of $\eta \sim (U, NTU)$ are presented in Fig.7 for both the freeze-cast regenerator and the baseline Gd packed sphere regenerator. Theoretically, the regenerator can only reach the ideal 100% effectiveness when the utilization is lower than or equal to unity. Therefore, the utilization of the Gd regenerator is set at ~ 0.59 , compared to the value of 0.67 in the freeze-cast regenerator. These discrete numbers of utilization are due to the limited setting in piston stroke and its cross sectional area in the passive rig.

Based on the fixed utilization and housing size but different T_c in the freeze-cast regenerator, the experiments lead to different $\eta \sim NTU$ curves. The reasons are attributed to the loss differences between the different regenerators, as well as the impact of temperature dependent properties of the regenerator material (Fig.3). In general, the effectiveness is observed to increase with NTU . Note that within the operating conditions' range, increasing the operating frequency decreases the NTU . The reason can be identified from the definition in Eq.(3), the fluid thermal mass increments are more significant than the heat transfer coefficient enhancement. In some utilization regions, the effectiveness is decreasing with increasing NTU . From our extra testing in this passive rig, and combined with previous work [56], we summarize the reasons of this decreasing trend as: (1) Trade-off between heat transfer improving rate and heat transfer cycle time; (2) Axial heat conduction when operating at low utilization; (3) Dead void effect, especially in high NTU (low frequency); and (4) Equipment problems, such as the piston working at high frequency (low NTU) and long stroke (high utilization) would breathe in some air, reducing the local utilization or causing some miscalculation due to the out-of-phase of $T_{f,h}$ and $T_{f,c}$. The values of effectiveness of the Gd and freeze-cast regenerators are compared at $T_c = 30^\circ\text{C}$ to ensure the temperature is far away from the peak value of the specific heat in both LCSM and Gd. Although the Gd regenerator has the advantage of $\sim 10\%$ lower value of utilization than the freeze-cast regenerator, the absolute values of effectiveness in the freeze-cast regenerator are still slightly higher than the Gd one on average (0.942 compared to 0.935). NTU in the freeze-cast regenerator is also higher than for the Gd regenerator. That means that the freeze-cast regenerator shows excellent heat transfer performance.

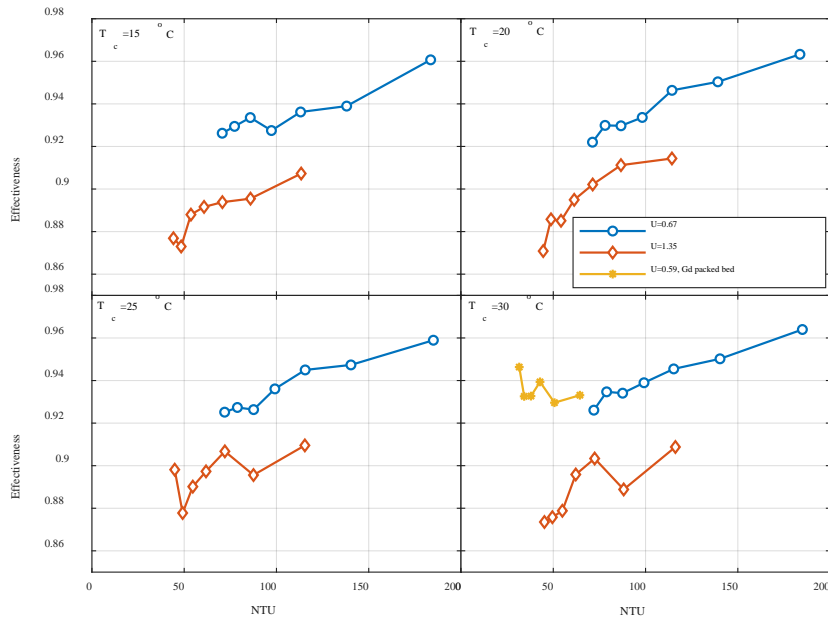


Fig.7 Effectiveness curves for freeze-cast regenerator and baseline regenerator.

Regarding the utilization impact, most regenerators follow the conventional behaviors that effectiveness increases when the utilization decreases. High effectiveness requires a small difference of regenerator temperature profile between hot blow and cold blow, which indicates a small utilization with lower penetration of inflow fluid into the material matrix. In Fig.8, we compare the effectiveness versus the utilization among different regenerators. In this dimension, the freeze-cast regenerator also has the best value of effectiveness among other regenerators.

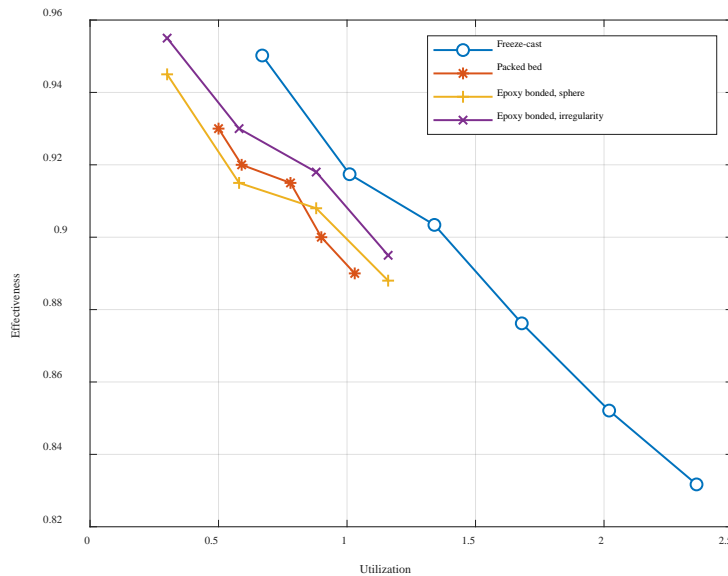


Fig.8 Effectiveness comparison for the freeze-cast regenerator, Gd packed bed regenerator and epoxy bonded regenerators with spherical and irregular particles.

From Fig.A1, the pressure drop signal is approximately a sinusoidal waveform. The minor deviations are probably caused by the check valves' response, inertial velocity and sensor fluctuations. More important concerns are the relation of maximum pressure drop and pore velocity under different conditions. We compare the viscous dissipation effect of the freeze-cast regenerator and other regenerators by using the curve of pressure drop versus pore velocity in Fig.9. From the curve the trend of the freeze-cast regenerator is captured as a nearly linear behavior, which is similar to the parallel plate regenerators [56]. In this case, most of the working conditions are in the Darcy regime. The variations are mainly caused by the temperature dependence of the fluid viscosity. Higher temperature values result in a relatively lower pressure drop. On the other hand, the absolute values of pressure drop in the freeze-cast regenerator are larger than in the Gd packed bed and epoxy bonded regenerators with spherical particles, because of the small scale of the channels. In the case of the epoxy bonded regenerator with irregular particles, its curve is close to that of the freeze-cast regenerator. However, the housings in the epoxy bonded regenerators are thinner and longer than in the freeze-cast and Gd packed bed regenerators, which is shown in Table 1. Consequently, the measured pressure drop in the freeze-cast regenerator is larger than in epoxy bonded and Gd packed bed regenerators based on the similar housing.

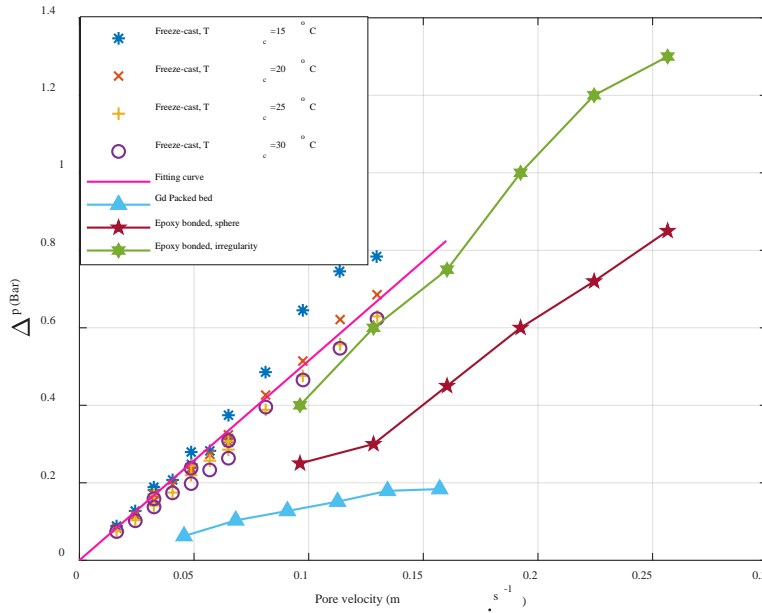


Fig.9 Comparison of pressure drop versus pore velocity among freeze-cast regenerator, Gd packed bed regenerator and epoxy bonded regenerators with irregular and spherical particles.

In order to connect heat transfer and flow resistance and highlight the characteristics of the target regenerator, the data of UA (heat transfer coefficient times heat transfer area) versus pressure drop between the freeze-cast regenerator and the baseline Gd packed bed regenerator are plotted in Fig. 10. It should be noted that adopting UA as a representative of heat transfer performance is due to its small error as well as including not only values of Nu but also the surface area of the regenerator. From the general heat transfer rate equation of $\dot{Q} = UA \Delta T$, the total heat transfer area A is obtained from the image analysis mentioned previously with unquantified error. However, the terms of \dot{Q} and ΔT are derived indirectly from temperature data through the numerical modelling. Since the errors of modelling and temperature measurements are validated to be small, the errors of \dot{Q} , ΔT and therefore the UA , can be treated as being small. In general, UA increases with the pressure drop. Some variations are captured based on the same Δp ,

because different working temperatures result in a variation of viscosity values and therefore different values of Re_p . The freeze-cast regenerator exhibits higher values of heat transfer performance for a given pressure drop compared to the packed Gd sphere regenerator. The main contributions are large specific area and small hydraulic diameter. When fixing the pressure drop, the value of UA in the freeze-cast regenerator is approximate 10-15% higher than that in Gd regenerator. Based on existing features, this regenerator is more suitable for running in the situations of low flowrate and high performance requirements. On the other hand, it is necessary to develop variable freeze-cast regenerators that fit in different flow conditions. For instance, freeze-cast regenerators with large pore size and porosity may exhibit relatively low flow resistance.

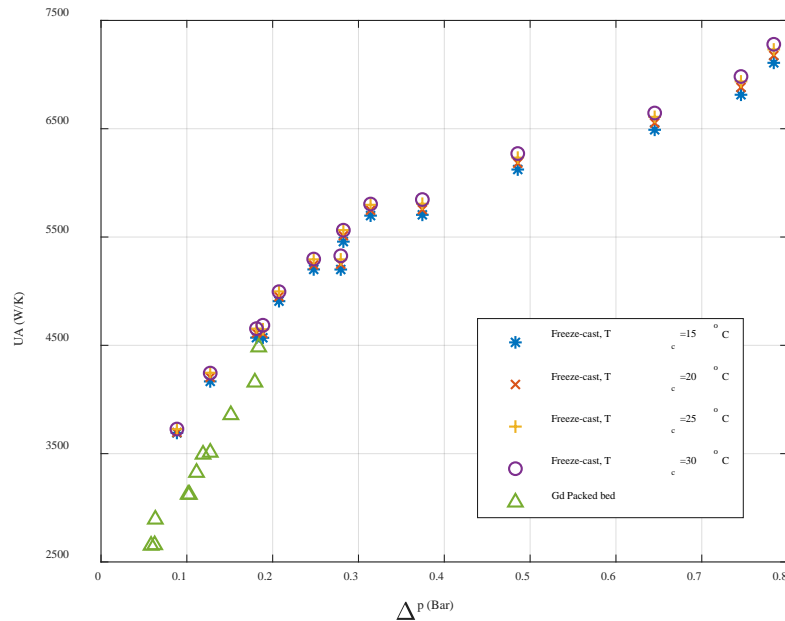


Fig.10 UA and pressure drop between freeze-cast and Gd packed bed regenerators.

5. Conclusion

In this study, a novel type of regenerator fabricated by the technique of freeze-casting was thermally and hydraulically characterized. A passive test rig was used to obtain the effectiveness and friction factor, as well as the modelling correlation validations of heat and mass transfer. Numerical analysis was performed to reveal the in-depth thermodynamic parameters of NTU and heat transfer coefficients. The following features are obtained due to the thermal evaluations:

- (1) The overall Nusselt number matches the local fitted Nusselt number correlation well, and the increasing trend with Reynolds number is sublinear. The absolute value of the Nusselt number is relatively low due to the small hydraulic diameter, limitation of oscillating blow evaluation and external thermal loss interference.
- (2) The relationship of friction factor and Reynolds number fit in the Ergun equation form, but with different regression parameter values.
- (3) The freeze-cast regenerator has both higher effectiveness and pressure drop than in the packed gadolinium sphere bed and epoxy bonded regenerators.

- (4) The pressure drop shows a nearly linear behavior due to the low Reynolds numbers. The curve trend is fitting in the situation of Darcy regime.
- (5) The combined characteristics of heat transfer performance and flow resistance of the freeze-cast regenerator are high. When the pressure drop is held constant, the UA values for the freeze-cast regenerators are 10-15% higher than the values in the packed bed regenerator. Further, the pore size and porosity could be tunable within certain range for different potential applications.

The characterization and modelling correlations are only based on the current pore size and tortuosity of the sample. Sensitivity studies on the parameters of hydraulic diameter, porosity and channel tortuosity, as well as the parametric passive and active characterizations, will be covered in future work.

Acknowledgments

J. Liang is grateful for financial support of the CSC (China Scholarship Council) scholarship. C. D. Christiansen, R. Bjørk and K. K. Nielsen wish to acknowledge the financial support of the Independent Research Fund Denmark—Technologies and Productions Sciences, project no. 6111 - 00073B.

Appendix A: Uncertainty analysis

To carry out uncertainty analysis, temperature and pressure measurements are regarded as observations here and designated as X . Extensive repeatability cycles are performed to validate the experimental procedure. To correct the reading oscillations, average treatments between cycles are taken into the data reduction for deriving the mean values:

$$\bar{X}(t) = \frac{1}{n} \sum_{i=0}^n X(t + i \cdot \tau), \quad X = T_h, T_c, T_{f,h}, T_{f,c}, p_1, p_2 \quad (\text{A.1})$$

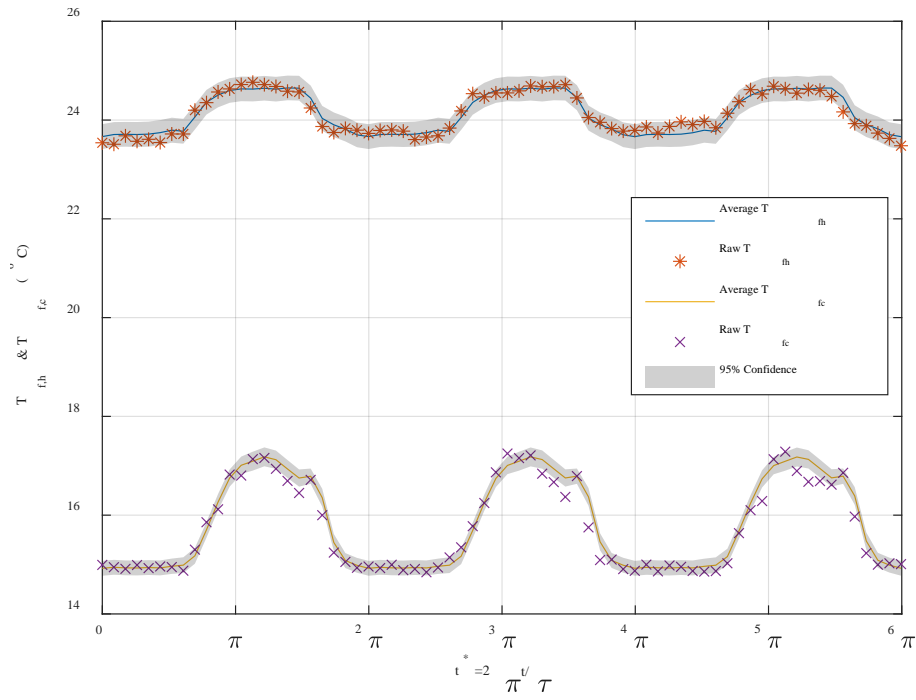
Where repeatability number $n = 20$; t and τ represent the time readings and cycle period, respectively. For small sets of data, the standard deviation of repeatability is defined by averaging the cycle deviations [57]:

$$\sigma_1(t) = \sqrt{\sum_{i=1}^n (X(t + i \cdot \tau) - \bar{X}(t))^2 / (n - 1)} \quad (\text{A.2})$$

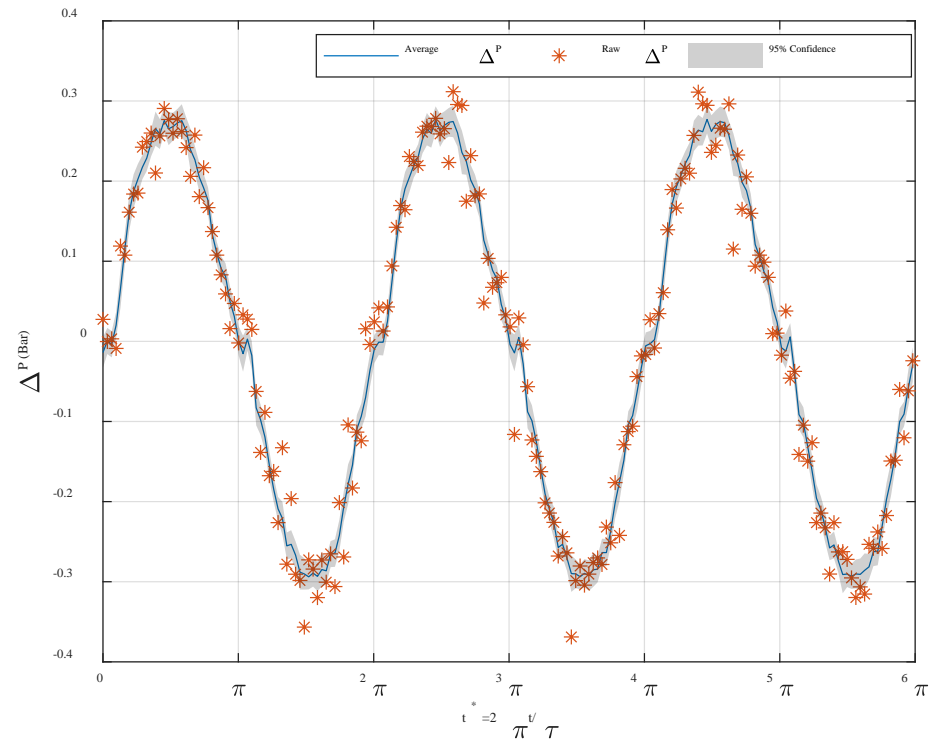
Assuming the measurement uncertainties are only due to issues with the repeatability, the overall standard deviation is written from the error propagation principle:

$$\sigma(t) = \sqrt{\sigma_1^2(t) + \sigma_2^2(t)} \quad (\text{A.3})$$

Where $\sigma_2(t)$ is the instrument deviation based on current local temperature of 0.5% and pressure of 0.25%. We extract four cycles of temperature and pressure measurements with 95% confidence level region $X \pm 2\sigma$ in Fig.A1. Less than 3% uncertainties are obtained from both temperature and pressure measurements.



(a)



(b)

Fig.A1 Temperature (a) and pressure drop (b) measurements of a single operating condition compared with the average data over 20 cycles

Appendix B: Relevant Nusselt number and friction factor correlations

Table B1: Correlations for the average Nusselt number and friction factor in micro-channels matrix.

References	Boundary condition	Correlations	Fitting form
Shih [58]	Developed laminar flow, rectangular	$f = 24(1 - 1.3553 \alpha + 1.9467 \alpha^2 - 1.7012 \alpha^3 + 0.9564 \alpha^4 - 0.2537 \alpha^5)/Re$	$f = P(\alpha)/Re$
Jiang et al. [51]	Developed laminar flow, rectangular	$f = 68.53/Re$, smooth $f = 1639/Re^{1.48}$, $Re < 600$, roughness $f = 36.4/Re + 0.45$, porous	$f = aRe^b + c$
Hornbeck [59]	Developing laminar flow, circular	$f_{app} = \frac{D_h}{4L}(13.74(x^+)^{1/2} + (1.25 + 64x^+ - 13.74(x^+)^{1/2})/(1 + 0.0021(x^+)^{-2}))$	As left
Steink and Kandlikar [60]	Developing laminar flow, rectangular	$K(\infty) = 0.6796 + 1.2197 \alpha + 3.3089 \alpha^2 - 9.5921 \alpha^3 + 8.9089 \alpha^4 - 2.9959 \alpha^5$	$f_{app} = f + \frac{D_h}{4x}P(\alpha)$
Lorenzini and Morini [61]	Developed laminar flow, trapezoidal and rectangular with rounded corners	For each fixed α $f = 14.226Re^{-1} \sum_{i=0}^5 A_i \left(\frac{R_c}{H_{r1}}\right)^i$ $Nu = 3.608 \sum_{i=0}^5 A_i \left(\frac{R_c}{H_{r1}}\right)^i$ R_c is the curvature of the channel corner	$f = P\left(\frac{R_c}{H_{r1}}\right) Re^b$ $Nu = P\left(\frac{R_c}{H_{r1}}\right)$
Liou et al. [62]	Laminar, parallelogram serpentine	$f = Re^{-0.8} \sum_{j=0}^5 \sum_{i=0}^5 A_{i,j} \alpha^i \theta^j$ $Nu = Re^{0.5} \sum_{j=0}^5 \sum_{i=0}^5 B_{i,j} \alpha^i \theta^j$ θ is included angle	$f = P(\alpha, \theta) Re^a$ $Re = P(\alpha, \theta) Re^b$
Choi et al. [63]	Laminar, circular	$Nu = 0.000972Re^{1.17} Pr^{1/3}$ $Re < 2000$	$Nu = aRe^b Pr^c$
Hausen et al. [64]	Laminar, circular	$Nu = \frac{3.657 + 0.19(x^*)^{-0.8}}{1 + 0.117(x^*)^{-4.67}}$	$Nu = \frac{a + b(x^*)^d}{1 + c(x^*)^e}$
Jiang et al. [51]	Laminar, rectangular	$Nu = 0.52(x^*)^{-0.62}$ $x^* < 0.05$ $Nu = 2.02(x^*)^{-0.31}$ $x^* > 0.05$	$Nu = a(x^*)^b$
Kandlikar et al. [38]	Developed laminar flow, rectangular	$Nu = 8.235(1 - 10.6044 \alpha + 61.1755 \alpha^2 - 155.1803 \alpha^3 + 176.9203 \alpha^4 - 72.9236 \alpha^5)$	$Nu = P(\alpha)$
Sadeghi et al. [65]	Developed laminar flow, arbitrary cross section	Characteristic length: \sqrt{A} instead of D_h $Nu_{\sqrt{A}} = C_1 \left(\frac{I_p}{A^2}\right)^{C_2} \left(\frac{\sqrt{A}}{P}\right)^{C_3}$ I_p is polar moment of inertia P is perimeter, A is cross sectional area	$Nu_{\sqrt{A}} = C_1 \left(\frac{I_p}{A^2}\right)^{C_2} \left(\frac{\sqrt{A}}{P}\right)^{C_3}$
Shah and London [66]	Developing laminar flow, rectangular	$Nu = 4.363 + 8.68(10^3 x^*)^{-0.506} e^{-41x^*}$	$Nu = a + b(10^3 x^*)^c e^{dx^*}$
Lee and Garimella [67]	Developing laminar flow, rectangular	$Nu = \frac{1}{C_1(x^*)^{C_2+C_3}} + C_4$ For $1 \leq \alpha \leq 10, x < L_t$ $C_1 = P_3(\alpha)$, $C_2 = const$ $C_3 = P_2(\alpha)$, $C_4 = P_3(\alpha)$	$Nu = \frac{1}{C_1(x^*)^{C_2+C_3}} + C_4$ For $1 \leq \alpha \leq 10, x < L_t$ $C_{1,3,4} = P(\alpha)$ $C_2 = const$

Note that in Table B1, the Reynolds number is based on the pore velocity. Heat transfer fluid is assumed to be incompressible. The non-dimensionalized length (x^+) and dimensionless length (x^*) are defined as:

$$x^+ = L_r / (D_h Re_p) \quad (\text{B.1})$$

$$x^* = L_r / (D_h Re_p Pr) \quad (\text{B.2})$$

where Pr is the Prandtl number.

References

- [1] V. Franco, J.S. Blázquez, J.J. Ipus, J.Y. Law, L.M. Moreno-Ramírez, A. Conde, Magnetocaloric effect: From materials research to refrigeration devices, *Prog. Mater. Sci.* 93 (2018) 112–232. doi:10.1016/j.pmatsci.2017.10.005.
- [2] R. Bjørk, A.R. Insinga, A topology optimized switchable permanent magnet system, *J. Magn. Magn. Mater.* 465 (2018) 106–113. doi:10.1016/j.jmmm.2018.05.076.
- [3] T. Lei, K. Engelbrecht, K.K. Nielsen, C.T. Veje, Study of geometries of active magnetic regenerators for room temperature magnetocaloric refrigeration, *Appl. Therm. Eng.* 111 (2017) 1232–1243. doi:10.1016/j.applthermaleng.2015.11.113.
- [4] A. Czernuszewicz, J. Kaleta, D. Kołosowski, D. Lewandowski, Experimental study of the effect of regenerator bed length on the performance of a magnetic cooling system, *Int. J. Refrig.* 97 (2019) 49–55. doi:10.1016/j.ijrefrig.2018.09.023.
- [5] A. Smith, Who discovered the magnetocaloric effect? Warburg, Weiss, and the connection between magnetism and heat, *Eur. Phys. J. H.* (2013). doi:10.1140/epjh/e2013-40001-9.
- [6] V.K. Pecharsky, K.A. Gschneidner, Giant magnetocaloric effect in Gd₅(Si₂Ge₂), *Phys. Rev. Lett.* (1997). doi:10.1103/PhysRevLett.78.4494.
- [7] V.K. Pecharsky, K.A. Gschneidner, Magnetocaloric effect and magnetic refrigeration, *J. Magn. Magn. Mater.* (1999). doi:10.1016/S0304-8853(99)00397-2.
- [8] V. Basso, M. Küpferling, C. Curcio, C. Bennati, A. Barzca, M. Katter, M. Bratko, E. Lovell, J. Turcaud, L.F. Cohen, Specific heat and entropy change at the first order phase transition of La(Fe-Mn-Si)₁₃H compounds, *J. Appl. Phys.* 118 (2015). doi:10.1063/1.4928086.
- [9] A.R. Dinesen, S. Linderoth, S. Mørup, Direct and indirect measurement of the magnetocaloric effect in La_{0.67}Ca_{0.33-x}Sr_xMnO₃ ± δ(x ∈ [0;0.33]), *J. Phys. Condens. Matter.* 17 (2005) 6257–6269. doi:10.1088/0953-8984/17/39/011.
- [10] A. Gschneidner, V.K. Pecharsky, A.O. Tsokol, Recent developments in magnetocaloric materials, *Reports Prog. Phys.* 68 (2005) 1479–1539. doi:10.1088/0034-4885/68/6/R04.
- [11] E. Brück, O. Tegus, D.T.C. Thanh, K.H.J. Buschow, Magnetocaloric refrigeration near room temperature (invited), *J. Magn. Magn. Mater.* (2007). doi:10.1016/j.jmmm.2006.10.1146.
- [12] S.Y. Dan'kov, A. Tishin, V. Pecharsky, K. Gschneidner, Magnetic phase transitions and the magnetothermal properties of gadolinium, *Phys. Rev. B - Condens. Matter Mater. Phys.* (1998). doi:10.1103/PhysRevB.57.3478.
- [13] R. Bjørk, C.R.H. Bahl, M. Katter, Magnetocaloric properties of LaFe_{13-x}Co_xSi_y and commercial grade Gd, *J. Magn. Magn. Mater.* (2010). doi:10.1016/j.jmmm.2010.08.013.
- [14] B. Yu, M. Liu, P.W. Egolf, A. Kitanovski, A review of magnetic refrigerator and heat pump prototypes built before the year 2010, *Int. J. Refrig.* 33 (2010) 1029–1060. doi:10.1016/j.ijrefrig.2010.04.002.
- [15] J. Romero Gómez, R. Ferreira Garcia, A. De Miguel Catoira, M. Romero Gómez, Magnetocaloric effect: A review of the thermodynamic cycles in magnetic refrigeration, *Renew. Sustain. Energy Rev.* 17 (2013) 74–82. doi:10.1016/j.rser.2012.09.027.
- [16] A. Kitanovski, J. Tušek, U. Tomc, U. Plaznik, M. Ožbolt, A. Poredoš, Magnetocaloric Energy Conversion: From Theory to Applications, 2015. doi:10.1007/978-3-319-08741-2.
- [17] Z. Li, J. Shen, K. Li, X. Gao, X. Guo, W. Dai, Assessment of three different gadolinium-based regenerators in a rotary-

- type magnetic refrigerator, *Appl. Therm. Eng.* 153 (2019) 159–167. doi:10.1016/j.applthermaleng.2019.02.100.
- [18] F.P. Fortkamp, D. Eriksen, K. Engelbrecht, C.R.H. Bahl, J.A. Lozano, J.R. Barbosa, Experimental investigation of different fluid flow profiles in a rotary multi-bed active magnetic regenerator device, *Int. J. Refrig.* 91 (2018) 46–54. doi:10.1016/j.ijrefrig.2018.04.019.
- [19] K. Navickaitė, H.N. Bez, T. Lei, A. Barcza, H. Vieyra, C.R.H. Bahl, K. Engelbrecht, Experimental and numerical comparison of multi-layered La(Fe,Si,Mn)₁₃Hy active magnetic regenerators, *Int. J. Refrig.* 86 (2018) 322–330. doi:10.1016/j.ijrefrig.2017.10.032.
- [20] P. V. Trevizoli, A.T. Nakashima, G.F. Peixer, J.R. Barbosa, Performance evaluation of an active magnetic regenerator for cooling applications – part I: Experimental analysis and thermodynamic performance, *Int. J. Refrig.* 72 (2016) 192–205. doi:10.1016/j.ijrefrig.2016.07.009.
- [21] T. Lei, K. Navickaitė, K. Engelbrecht, A. Barcza, H. Vieyra, K.K. Nielsen, C.R.H. Bahl, Passive characterization and active testing of epoxy bonded regenerators for room temperature magnetic refrigeration, *Appl. Therm. Eng.* 128 (2018) 10–19. doi:10.1016/j.applthermaleng.2017.08.152.
- [22] P. V. Trevizoli, G.F. Peixer, J.R. Barbosa, Thermal-hydraulic evaluation of oscillating-flow regenerators using water: Experimental analysis of packed beds of spheres, *Int. J. Heat Mass Transf.* 99 (2016) 918–930. doi:10.1016/j.ijheatmasstransfer.2016.03.014.
- [23] A. Šarlah, J. Tušek, A. Poredoš, Comparison of thermo-hydraulic properties of heat regenerators applicable to active magnetic refrigerators, *Stroj. Vestnik/Journal Mech. Eng.* 58 (2012) 16–22. doi:10.5545/sv-jme.2010.250.
- [24] A.A. Boroujerdi, M. Esmaili, Characterization of the frictional losses and heat transfer of oscillatory viscous flow through wire-mesh regenerators, *Alexandria Eng. J.* 54 (2015) 787–794. doi:10.1016/j.aej.2015.06.001.
- [25] P. Li, M. Gong, J. Wu, Geometric optimization of an active magnetic regenerative refrigerator via second-law analysis, *J. Appl. Phys.* 104 (2008). doi:10.1063/1.3032195.
- [26] K.K. Nielsen, K. Engelbrecht, C.R.H. Bahl, The influence of flow maldistribution on the performance of inhomogeneous parallel plate heat exchangers, *Int. J. Heat Mass Transf.* 60 (2013) 432–439. doi:10.1016/j.ijheatmasstransfer.2013.01.018.
- [27] J.D. Moore, D. Klemm, D. Lindackers, S. Grasemann, R. Träger, J. Eckert, L. Löber, S. Scudino, M. Katter, A. Barcza, K.P. Skokov, O. Gutfleisch, Selective laser melting of La(Fe,Co,Si)₁₃geometries for magnetic refrigeration, *J. Appl. Phys.* 114 (2013). doi:10.1063/1.4816465.
- [28] T. Lei, K. Engelbrecht, K.K. Nielsen, C.T. Veje, J. Tušek, C.R.H. Bahl, Modelling and comparison studies of packed screen regenerators for active magnetocaloric refrigeration, in: *Proceedings of the 6th IIF-IIR international Conference on Magnetic Refrigeration*, 2014.
- [29] R. Radebaugh, B. Louie, Simple, First Step To the Optimization of Regenerator Geometry., in: *Natl. Bur. Stand. Spec. Publ.*, 1985.
- [30] J. Li, T. Numazawa, K. Matsumoto, Y. Yanagisawa, H. Nakagome, A modeling study on the geometry of active magnetic regenerator, in: *AIP Conf. Proc.*, 2012: pp. 327–334. doi:10.1063/1.4706936.
- [31] S. Deville, E. Saiz, A.P. Tomsia, Ice-templated porous alumina structures, *Acta Mater.* (2007). doi:10.1016/j.actamat.2006.11.003.
- [32] T. Waschkes, R. Oberacker, M.J. Hoffmann, Control of lamellae spacing during freeze casting of ceramics using double-side cooling as a novel processing route, in: *J. Am. Ceram. Soc.*, 2009. doi:10.1111/j.1551-2916.2008.02673.x.
- [33] A.Z. Lichtner, D. Jauffrès, C.L. Martin, R.K. Bordia, Processing of hierarchical and anisotropic porosity LSM-YSZ composites, *J. Am. Ceram. Soc.* (2013). doi:10.1111/jace.12478.
- [34] S. Deville, The lure of ice-templating: Recent trends and opportunities for porous materials, *Scr. Mater.* (2018). doi:10.1016/j.scriptamat.2017.06.020.
- [35] B.S. Deville, Freeze-Casting of Porous Ceramics : A Review of Current Achievements, (2008) 155–169. doi:10.1002/adem.200700270.
- [36] C.D. Christiansen, K.K. Nielsen, R.K. Bordia, R. Bjørk, The effect of gelation on statically and dynamically freeze-cast structures, *J. Am. Ceram. Soc.* (2019). doi:10.1111/jace.16500.

- [37] W.M. Kays, M.E. Crawford, *Convective Heat and Mass Transfer*, McGraw-Hill, Inc., 1993.
- [38] S.G. Kandlikar, S. Garimella, D. Li, S. Colin, M. King, *Heat Transfer and Fluid Flow in Minichannels and Microchannels*, 2013. doi:10.1016/C2011-0-07521-X.
- [39] T. Lei, *Modeling of active magnetic regenerators and experimental investigation of passive regenerators with oscillating flow*, Technical University of Denmark, 2016.
- [40] C.D. Christiansen, K.K. Nielsen, R. Bjørk, Freeze-casting to create directional micro-channels in regenerators for magnetic refrigeration, *Proc. TherMag VIII, 8th IIF-IIR Int. Conf. Caloric Cool.* (2018) 96–101. doi:10.18462/iir.11072.
- [41] A. Bareggi, E. Maire, A. Lasalle, S. Deville, Dynamics of the freezing front during the solidification of a colloidal alumina aqueous suspension: In situ x-ray radiography, tomography, and modeling, *J. Am. Ceram. Soc.* (2011). doi:10.1111/j.1551-2916.2011.04572.x.
- [42] S. Deville, E. Maire, A. Lasalle, A. Bogner, C. Gauthier, J. Leloup, C. Guizard, In situ X-ray radiography and tomography observations of the solidification of aqueous alumina particle suspensions - Part I: Initial instants, *J. Am. Ceram. Soc.* (2009). doi:10.1111/j.1551-2916.2009.03163.x.
- [43] S. Choi, K. Nam, S. Jeong, Investigation on the pressure drop characteristics of cryocooler regenerators under oscillating flow and pulsating pressure conditions, *Cryogenics (Guildf)*. 44 (2004) 203–210. doi:10.1016/j.cryogenics.2003.11.006.
- [44] T.S. Zhao, P. Cheng, Oscillatory pressure drops through a woven-screen packed column subjected to a cyclic flow, *Cryogenics (Guildf)*. 36 (1996) 333–341. doi:10.1016/0011-2275(96)81103-9.
- [45] K. Nam, S. Jeong, Novel flow analysis of regenerator under oscillating flow with pulsating pressure, *Cryogenics (Guildf)*. 45 (2005) 368–379. doi:10.1016/j.cryogenics.2005.01.001.
- [46] F. Mohd Saat, A. Jaworski, Friction Factor Correlation for Regenerator Working in a Travelling-Wave Thermoacoustic System, *Appl. Sci.* 7 (2017) 253. doi:10.3390/app7030253.
- [47] Y. Ju, Y. Jiang, Y. Zhou, Experimental study of the oscillating flow characteristics for a regenerator in a pulse tube cryocooler, *Cryogenics (Guildf)*. 38 (1998) 649–656. doi:10.1016/S0011-2275(98)00037-X.
- [48] K. Engelbrecht, *A Numerical Model of an Active Magnetic Regenerator Refrigerator with Experimental Validation*, University of Wisconsin-Madison, 2008.
- [49] I.H. Bell, J. Wronski, S. Quoilin, V. Lemort, Pure and pseudo-pure fluid thermophysical property evaluation and the open-source thermophysical property library coolprop, *Ind. Eng. Chem. Res.* (2014). doi:10.1021/ie4033999.
- [50] K.K. Nielsen, A. Smith, C.R.H. Bahl, U.L. Olsen, The influence of demagnetizing effects on the performance of active magnetic regenerators, *J. Appl. Phys.* 112 (2012). doi:10.1063/1.4764039.
- [51] P. Jiang, M. Fan, G. Si, Z. Ren, Thermal-hydraulic performance of small scale micro-channel and porous-media heat exchangers, *Int. J. Heat Mass Transf.* 44 (2001).
- [52] M. Nickolay, H. Martin, Improved approximation for the Nusselt number for hydrodynamically developed laminar flow between parallel plates, *Int. J. Heat Mass Transf.* 45 (2002) 3263–3266. doi:10.1016/S0017-9310(02)00028-5.
- [53] P.J. Heggs, D. Burns, Single-blow experimental prediction of heat transfer coefficients. A comparison of four commonly used techniques, *Exp. Therm. Fluid Sci.* (1988). doi:10.1016/0894-1777(88)90003-9.
- [54] K.K. Nielsen, G.F. Nellis, S.A. Klein, Numerical modeling of the impact of regenerator housing on the determination of Nusselt numbers, *Int. J. Heat Mass Transf.* 65 (2013) 552–560. doi:10.1016/j.ijheatmasstransfer.2013.06.032.
- [55] S. Ergun, A.A. Orning, Fluid Flow through Randomly Packed Columns and Fluidized Beds, *Ind. Eng. Chem.* 41 (1949) 1179–1184. doi:10.1021/ie50474a011.
- [56] Paulo Vinicius Trevizoli, *Development of thermal regenerators for magnetic cooling applications*, Federal University of Santa Catarina, 2015.
- [57] J.P. Holman, *Experimental Methods for Engineers*, Eighth Edi, The McGraw-Hill companies, 2011.
- [58] F.S. Shih, Laminar flow in axisymmetric conduits by a rational approach, *Can. J. Chem. Eng.* 45 (1967) 285–294. doi:10.1002/cjce.5450450507.
- [59] R.W. Hornbeck, Laminar flow in the entrance region of a pipe, *Appl. Sci. Res.* (1964). doi:10.1007/BF00382049.

- [60] M.E. Steinke, Single-Phase Liquid Heat Transfer in Microchannels, *Int. Conf. Microchannels Minichannels*. (2005) 1–12. doi:10.1115/ICNMM2006-96227.
- [61] M. Lorenzini, G. Morini, Poiseuille and Nusselt numbers for laminar flow in microchannels with rounded corners, in: *2nd Micro Nano Flows Conf.*, West London, 2009. <http://dspace.brunel.ac.uk/handle/2438/6936>.
- [62] T.M. Liou, C.S. Wang, H. Wang, Nusselt number and friction factor correlations for laminar flow in parallelogram serpentine micro heat exchangers, *Appl. Therm. Eng.* 143 (2018) 871–882. doi:10.1016/j.applthermaleng.2018.08.021.
- [63] S.B. Choi, R.F. Barron, R.O. Warrington, Fluid flow and heat transfer in microtubes, *Am. Soc. Mech. Eng. Dyn. Syst. Control Div. DSC*. 32 (1991) 123–134.
- [64] Helmuth Hausen, *Heat Transfer in Counterflow Parallel Flow And Cross Flow*, 1983.
- [65] E. Sadeghi, M. Bahrami, N. Djilali, Estimation of nusselt number in microchannels of arbitrary cross section with constant axial heat flux, *Heat Transf. Eng.* 31 (2010) 666–674. doi:10.1080/01457630903466647.
- [66] R.K. Shah, A.L. London, *Laminar Flow Forced Convection in Ducts*, 1978. doi:10.1016/B978-0-12-020051-1.50022-X.
- [67] P.S. Lee, S. V. Garimella, Thermally developing flow and heat transfer in rectangular microchannels of different aspect ratios, *Int. J. Heat Mass Transf.* 49 (2006) 3060–3067. doi:10.1016/j.ijheatmasstransfer.2006.02.011.

Novel freeze-casting device with high precision thermoelectric temperature control for dynamic freezing conditions

Cathrine D. Christiansen, Kaspar K. Nielsen, Rasmus Bjørk

Submitted for peer-review in: *Review of Scientific Instruments*

Experimental work, post processing and data analysis carried out at Department of Energy Conversion and Storage, Technical University of Denmark during the Ph.D. period. I am the first-author of the paper.

Novel freeze-casting device with high precision thermoelectric temperature control for dynamic freezing conditions

Cathrine D. Christiansen,^{1, a)} Kaspar K. Nielsen,¹ and Rasmus Bjørk¹

Department of Energy Conversion and Storage, Technical University of Denmark, Frederiksborgvej 399, DK-4000 Roskilde, Denmark

(Submitted for peer-review in: *Review of Scientific Instruments*, October 2019)

A novel freeze-casting device utilizing a thermoelectric element for high precision temperature control allowing for dynamic freezing conditions of freeze-cast materials is presented.

Freeze-casting is a processing route for producing materials of anisotropic porosity in the form of aligned and well-defined microchannels. In freeze-casting, particulates of a material are suspended in a solvent and a thermal gradient is applied across for directional freezing. Controlling the thermal gradient across the suspension amounts to controlling the kinetics and freezing direction in the suspension and thus the resulting structural features and dimensions of the microchannels.

The performance of the device presented here was evaluated by directional freezing of both water and aqueous ceramic suspension samples using both linear and exponential freezing profiles. The freezing front was successfully tracked by continuously measuring the temperature gradient along the sample using thermocouples directly mounted in the freeze-casting mould. The current minimum operational temperature of the freeze-caster is ~ 220 K, with freezing front velocities in the range of ~ 5 $\mu\text{m/s}$ to 30 $\mu\text{m/s}$ for sample lengths of 5 mm to 25 mm.

Keywords: Freeze-casting; ice-templating; thermoelectric cooling; temperature control; dynamic freezing

I. INTRODUCTION

Freeze-casting presents a processing route for engineering of microchannels in various materials. Freeze-cast materials contain anisotropic porosity in the form of aligned and well-defined macropores, i.e. microchannels. The alignment of porosity ensures porous materials of e.g. enhanced mechanical strength and flow properties in the direction of the microchannels, making these materials advantageous for e.g. biomedical applications¹, filters² and catalytic support structures^{3,4}. For a broader scope of the recent applications and materials used in freeze-casting, the reader is referred to Deville⁵.

Freeze-casting, or ice-templating, is a novel templating technique based on the anisotropic growth of ice crystals in aqueous suspensions of a particulate material upon directional freezing. This is achieved by bringing one side of the suspension into contact with a cooling source thus creating a thermal gradient across the suspension. When ice crystals grow in a suspension with an appropriate thermal gradient they cause a segregation of material particles resulting in a two-phase body of ice and material. Removing the ice by sublimation results in a structure

with anisotropic porosity in the form of directional macropores where the ice used to be. The dimensions of the macropores thus depend on the size of the ice crystals and are typically of the order ~ 1 μm to ~ 100 μm ^{3,6-8}. Moreover, the morphology of the pores strongly depends on the freezing conditions; most notably is the conclusion that the faster the freezing front moves, the narrower the resulting channels will be^{3,6-8}.

We adopt here the following definition of the freezing front: at any time during the freezing a cross section of the suspension will undergo the transformation from the liquid to the solid state and the speed of this front is the freezing front velocity. The cross section need not be flat and will in general be convex due to the mould boundary condition, as shown by *in situ* X-ray radiography^{9,10}.

Controlling the thermal gradient across the suspension amounts to controlling the kinetics, i.e. the freezing front velocity, and freezing direction in the suspension and thus the resulting structural features and dimensions. The thermal gradient depends on the temperature of the cooling source, and high precision temperature control of the cooling source coupled with high spatial resolution temperature monitoring is therefore crucial in the engineering of materials by freeze-casting.

For constant temperature of the cooling source, the growing solid part of the suspension will act as an increasing thermal resistance, slowing down the freezing front velocity. Constant temperature of the cooling source therefore leads to graded structures of varying pore sizes^{8,11}. The pore size has been shown to depend directly on the freezing front

^{a)}Electronic mail: cadech@dtu.dk

velocity with approximately constant freezing front velocities yielding nearly homogeneous channel sizes throughout the freeze-cast structures^{7,12}. However, to achieve a constant freezing front velocity, dynamic freezing conditions must be implemented to counteract the increasing thermal resistance from the frozen body. Various dynamic temperature profiles of the cooling source during freeze-casting have been tested, where both linear^{3,6-8}, exponential¹³⁻¹⁵ and parabolic¹⁰ freezing functions significantly increased the homogeneity of structural features and dimensions of microchannels throughout the sample length.

However, implementation of temperature profiles for freezing control as well as measures for monitoring of freezing conditions poses specific requirements for the design of a freeze-casting device.

A. Designing a freeze-casting device

In all its simplicity, all that is required for a functioning freeze-caster is a cooling source, i.e. a thermal reservoir with a temperature below that of the suspension solidification temperature. A container that keeps the suspension such that only one side is brought into thermal contact with the cooling source is then mounted on the reservoir. In this way, a thermal gradient is created throughout the suspension, which is also isolated from the ambient.

The **cooling source** most often consist of a liquid refrigerant brought into thermal contact with a coldfinger or a plate of a material with large thermal conductivity^{1,3,4,13,15,16}. In the most common freeze-casting set-up, a copper rod is immersed directly into a container of liquid nitrogen. **Temperature control** of the non-immersed end of the rod is then achieved by either the level of nitrogen in the container³ or by a heating sleeve installed at the top of the rod typically equipped with a thermocouple and PID control^{1,3,4,13,15,16}. In such a set-up, one side of a suspension contained in a mould can be brought into contact with the copper rod. This type of set-up is thus referred to as a **one-sided set-up**.

With the implementation of an additional cooling source at the opposite side of the freezing suspension, in a so-called **double-sided set-up**^{6,7,12}, full thermal control across the sample and thus of the thermal gradient is achieved, however, with difficulties arising from the expansion of the freezing suspension. Additionally, a multi-sided set-up can be achieved for mould designs with one or more sides of a thermally conducting material introducing a cold side perpendicular to the cooling source resulting in **bidirectional freezing**^{16,17}. Bidirectional freezing imposes a second thermal gradient on the

freezing suspension and thus additional ordering of the channel orientations in the plane perpendicular to the freezing direction. Furthermore, the ordering of the structural and material gradients in the final freeze-cast can be altered with rotational freezing for fabrication of tubes¹⁸, freezing in magnetic^{1,19} and electrostatic¹⁹ fields and tape-freeze casting²⁰.

Designing a freeze-casting device is all about controlling the freezing conditions, common for all freeze-casting set-ups is therefore the need for a cooling source with temperature control. While the liquid refrigerant for the aforementioned set-ups is typically in the form of volatile liquid nitrogen or ethanol, a thermoelectric element where the applied voltage determine the temperature represents an alternative cooling source^{21,22}. Furthermore, a possibility of tracking the freezing front is desired. Tracking of the freezing front can be done visually by using a see-through mould made from e.g. acrylic glass and equipped with a scalebar^{3,7}. However, this requires a clear visual distinction between the solid phase and the liquid phase, which is not always the case²³. Temperature measurements of the freezing suspension, either by attaching thermocouples¹⁵ or by use of thermal infrared imaging²⁴, poses an alternative tracking method granted that the exact solidification temperature of the suspension is known. The solidification temperature of the suspension moreover defines the desired working range of the freeze-casting set-up. In this work, the freeze-casting device is optimized for aqueous suspensions as water is easily accessible and exerts a low vapour pressure at STP, thus, no precautions against solvent evaporation is necessary in the experimental set-up. With a solidification temperature of 273.15 K for pure water, the desired operational temperature span of the freeze-caster must therefore be in a range around this temperature.

Here, we present a custom-built freeze-casting device with thermoelectric temperature control for implementation of dynamic freezing conditions in combination with a novel interchangeable mould design using temperature measurements for tracking of the freezing front.

II. FREEZE-CASTING DEVICE

The freeze-casting device is shown in FIG. 1. The central part of the freeze-caster is contained within the vacuum chamber (A) where the thermoelectric unit (Peltier element) for temperature control is found as elaborated on in the close-up of FIG. 2. The thermoelectric unit is powered by a power supply (Aim-TTi CPX 400SP)(D). A Pfeiffer turbo pump (Hicube 80 ECO)(F) is running during opera-

tion, keeping the pressure inside the vacuum chamber at 10^{-4} mbar to avoid condensation and to ensure proper performance, while a Julabo temperature bath (CF 40)(G) is connected to a heat sink on which the Peltier element is mounted. A PC (C) is connected, running control software and logging temperature measurements from the Keithley (2700 DMM, with scanner card 7700)(E).



FIG. 1: Full freeze-casting set-up. A: Vacuum chamber. B: Teflon mould mounted on cold finger. C: PC running control and data logging software. D: Power supply. E: Keithley. F: Turbo pump. G: Julabo CF40 chiller.

In FIG. 2 the details of the device are provided. Inside the vacuum chamber (A) is a Cu cold-finger (E) mounted on a Peltier element (QuickCool QC-127-2.0-15.0 accepting up to 15.5 V and 15 A)(D). The gap between cold finger and vacuum chamber is sealed using a Teflon flange (F) and heat is transported away from the Peltier element by the heatsink (Custom Thermoelectrics WBA-3.0-0.85-CU-01)(C) connected to the Julabo. Tubes for cooling fluids and electronics are attached through port holes (B). The term *electronics* cover power supply for the Peltier element and Pt-100 elements (G) attached at both the top of the Peltier element and the top of the cold finger, just inside the vacuum chamber, for precise monitoring and control of temperature.

A. Vacuum sealing & thermal management

The sealing of the vacuum chamber is carried out with conventional O-ring seals. The critical point of the chamber is the top sealed with a custom Teflon vacuum flange; see FIG. 2a)(F). Here, a radial seal is implemented with tolerances that allow for the Cu and Teflon parts to shrink as the temperature is decreased. As seen in TABLE I, the Teflon flange has a much larger coefficient of thermal expansion than Cu, however, as both the O-ring and the Teflon flange are made of materials with very low thermal conductivity, the resulting contraction of the Teflon flange is comparable to or smaller than that of the Cu rod. As a result, the vacuum holds sufficiently throughout the entire specified temperature range of the device.

The heat exchanger at the bottom of the Peltier element is positioned on a steel-plate (for modest thermal conductivity) that in turn is positioned on four legs made of plastic screws ensuring a large thermal resistance from the heat exchanger to the frame of the vacuum chamber. On top of the Peltier element a thin Al-disk is installed with the Cu-finger mounted on top. The Al-disk is clamped with plastic screws to the bottom steel plate. Choosing aluminum for the plate on top of the Peltier element is a balance between having a large thermal conductivity and a minimal thermal mass. Furthermore, Al is easier to machine than Cu. The cold-finger is made of Cu as the largest possible thermal conductivity is desired. The cooling power of the device is spent both on increasing the temperature gradient across these internal parts and to absorb the latent heat of fusion from the freezing front. Hence, the finger has been made as thin and short as possible given various room requirements in order to ensure as small a thermal mass as possible. This ensures i) a quick response of the system when the temperature is set to be changed and ii) the ability to reach the lower temperature limit set by the combined Peltier-element and chiller in combination at the top of the Cu-finger as the combined thermal mass of the Al- and Cu-components is low relative to the latent heat of fusion at the freezing front.

B. Moulds & temperature tracking

The mould design for the freeze-caster is interchangeable for high flexibility and various freezing conditions. For the purpose of verifying the set-up a simple, cylindrical design was chosen. The mould walls are made of Teflon with a detachable copper bottom for optimal thermal conductivity between sample and coldfinger. Teflon mould and Cu bot-

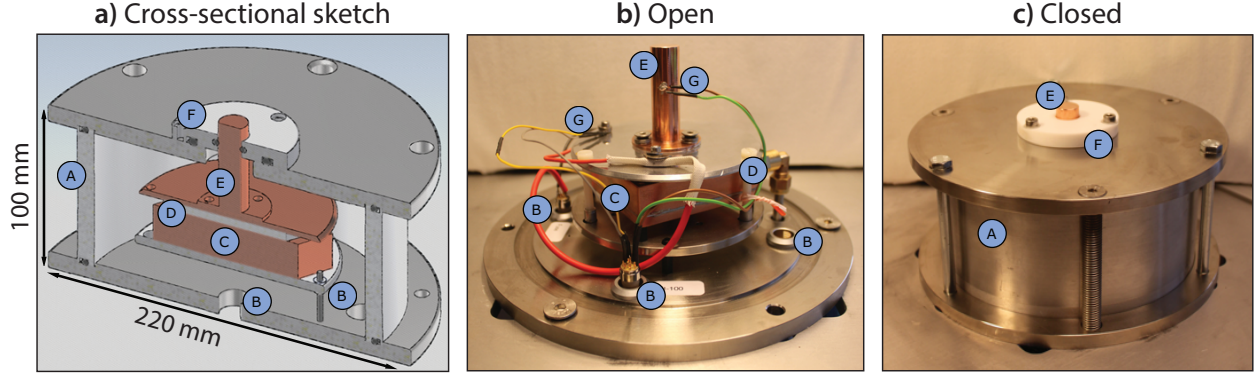


FIG. 2: Close-up of freeze-caster. A: Vacuum chamber, B: Port holes for tubing and electronics, C: Heat exchanger, D: Peltier element, E: Cold finger, F: Teflon vacuum flange, G: Pt-100 elements

tom are assembled using vacuum grease for easy and quick disassembly. The mould is shown in FIG. 3.

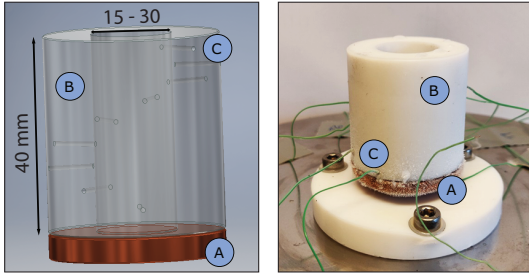


FIG. 3: Cylindrical mould design for freeze-caster. A: Detachable Cu bottom. B: Cylindrical Teflon mould. C: Thermocouple inserts in helical pattern.

Teflon has a very low coefficient of friction easing the demoulding of samples. Moreover, the thermal conductivity of Teflon is also very low, see TABLE I, thermally isolating the freezing sample from the surroundings while not cooling down faster than the sample. This prevents bidirectional freezing, i.e. where the mould walls act as a cooling source as well as the mould bottom.

The thermal contraction of Teflon is larger than that of Cu, which causes an issue with a composite mould of both materials. However, assembling the mould parts using vacuum grease allows the two materials to contract independently without tension. Moreover, the mould is kept open at the top in order to allow room for the water expanding as it transitions into ice.

The mould is equipped with a detachable copper bottom with the primary function of ensuring high thermal conductivity between the freezing sample and the coldfinger of the freeze-casting device. A thermocouple insert ($\text{\O}1$ mm x 4.5 mm depth) for temperature monitoring and a circular 3.5 mm indentation matching the diameter of the coldfinger

TABLE I: Thermal properties of Teflon, copper and ice: coefficient of linear thermal expansion, thermal conductivity and thermal diffusivity, respectively.

	α 10^{-6}K^{-1}	k $\text{Wm}^{-1}\text{K}^{-1}$	λ $10^{-6}\text{m}^2\text{s}^{-1}$
Teflon	112 - 125	0.250	0.124
Copper	17	401	111
Ice	51	2.2	1.13

are drilled into the bottom of the Cu mould-part for easy mounting and demounting of the mould.

As previously mentioned, the freezing rate, or freezing front velocity is paramount for the resulting internal dimensions of the freeze-cast structure and temperature control and monitoring is thus vital in order to evaluate the processing of a freeze-cast structure. Thermocouple inserts ($\text{\O}1$ mm) are drilled into the Teflon mould along its height. Inserts are 9.25 mm deep leaving 0.75 mm of Teflon wall between the freezing suspension and the thermocouple, inevitably resulting in a thermal lag with regards to tracking the freezing front position. However, as the lag is assumed to be consistent for all thermocouple positions, this will in principle not affect the evaluation of the freezing front velocity, but only provide an offset to the freezing front position with respect to time. The thermocouple inserts are placed in a helical pattern along the length of the mould, as shown on FIG. 3(C), with a 4 mm spatial resolution along the freezing direction. This pattern ensures that the thermal loss due to changes in mould wall thickness is distributed radially across the sample to avoid a significant distortion of the freezing front surface. Thermocouples type K are mounted in the inserts with thermal paste to ensure

proper thermal conduction.

C. Implementation of temperature control

The control software is custom made in C# and facilitates a PID (proportional-integral-derivative) controller with a feedback loop for controlling the temperature of the coldfinger. The coldfinger is equipped with a Pt-100 element just inside the vacuum chamber as close to the freezing sample as possible; see FIG. 2b)(G). The temperature at this position is continuously fed to the software and adjusted according to the PID settings to fit a given set-temperature. The set-temperature can be constant or defined to be a function of time, e.g. a linear function or an exponential function, as has been suggested for obtaining a constant freezing front velocity¹⁵.

III. EXPERIMENTAL METHODS

In order to evaluate the performance and demonstrate the capabilities and limitations of the freeze-caster, samples of water and samples of ceramic suspensions were frozen using various dynamic temperature profiles.

A. Implementation of temperature profiles

An exponential freezing function was chosen based on work by Stolze et al.^{14,15} and Flauder et al.¹³, as described below, while constant freezing rates were chosen in the range of -0.5 to -20 K/min, resulting in linear temperature profiles. Under equivalent conditions, these freezing rates should yield freeze-cast ceramics with approximate constant channel dimensions in the order of $1 - 100 \mu\text{m}$ ^{3,6,8}.

Stolze et al.^{14,15} derives and verifies an exponential cooling function, Equation (1), for maintaining a constant freezing front velocity, during directional solidification of a ceramic suspension

$$f(t) = T_0 + \frac{H_f}{c_s} \left(1 - \exp\left(\frac{v_f^2}{\lambda_s} t\right) \right). \quad (1)$$

Here subscript s and f denote the solid and fluid, respectively. T_0 is the solidification temperature of the suspension, H_f is the heat of fusion, c_s is the specific heat capacity and λ_s is the thermal diffusivity, where the latter is related to the thermal conductivity, k_s , as follows: $\lambda_s = k_s/\rho_s c_s$.

For exponential freezing of water samples, coefficients for the exponential freezing function $f(t) =$

$A + Be^{Ct}$ were chosen such that it fulfills Equation (1) with the physical properties of water at 273 K listed in TABLE II and $v_f = 5, 10, 15, 20 \mu\text{m/s}$, assuming that Equation (1) also holds true for water alone.

B. Freeze-casting

Samples of ceramic suspensions were frozen using linear temperature profiles, while water samples were frozen using both exponential and linear freezing profiles. In order to avoid significant supercooling of water, tap water containing natural minerals was used.

The preparation of ceramic suspensions for freeze-casting, post-processing of freeze-cast specimens and structural analysis follows that previously described by Christiansen et al.^{8,25}. A ceramic suspension was prepared from 25 vol% powders of $\text{La}_{0.67}\text{Ca}_{0.27}\text{Sr}_{0.06}\text{Mn}_{1.05}\text{O}_3$ (LCSM, CerPoTech) in MiliQ water, with the addition of 2.5 wt%, relative to the ceramic powder, of DURAMAX™ D-3005 (Rohm and Haas, Dow Chemical) as dispersing agent and 2.0 wt%, relative to the ceramic powder, of DURAMAX™ B-1022 (Rohm and Haas, Dow Chemical) as binder. The suspension were mixed using a low energy ball mill for at least 48 hours or until all agglomerates had been eliminated and a consistent particle size distribution was established as analyzed using a Laser Diffraction Particle Size Analyser (LS 13 320, Beckman Coulter), reaching a median particle size of $\sim 1.8 \mu\text{m}$.

The water or ceramic suspension and mould was pre-cooled in an ice-bath. The mould was then mounted directly onto the coldfinger. The mould was equipped with thermocouples while ensuring sufficient thermal contact by applying thermal paste at the contact interface between the copper bottom and coldfinger as well as in the thermocouple inserts.

Meanwhile, bubbles were removed from the ceramic suspension using sonication and the de-aired ceramic suspension or water was transferred to the mould. Mould and sample was encapsulated in insulating foam and a styrofoam box which kept the ambient temperature below 280 K at all times. The temperature was kept constant at 275 K for 5–10 minutes before applying an either linear or exponential freezing profile. Temperature measurements were obtained until the sample was frozen solid.

Temperature measurements were obtained until the sample was frozen solid. Three samples were frozen for each applied temperature profile in order to realize a statistically significant data set.

The frozen ceramic freeze-cast samples were subsequently freeze-dried for at least 24 hours and sin-

TABLE II: Physical properties of water at 273 K; heat of fusion, specific heat capacity, density and thermal conductivity, respectively.

H_f	c	ρ	k
333.55 kJ kg ⁻¹	2.108 kJ (kg K) ⁻¹	920 kg m ⁻³	2.2 · 10 ⁻³ kW (m K) ⁻¹

tered at 1100 °C in air for 3 hours (heating rate of 30 K/hour), with initial burnout of organics at 250 °C and 450 °C (heating rate of 15 K/hour). Samples were then infiltrated with epoxy and cut into smaller specimens revealing cross sections for imaging using a scanning-electron microscope (SEM, TM3000, Hitachi High-Technologies). Internal, structural dimensions of freeze-cast samples were estimated by image analysis using a continuous particle size distribution method²⁶ as described by Christiansen et al.⁸.

IV. RESULTS & DISCUSSION

A. Evaluation of freezing conditions and performance

All temperature curves for samples frozen at various freezing rates showed a few reoccurring characteristics. The measured temperature profiles for all thermocouple positions for a sample of water frozen at -2 K/min are shown in FIG. 4a). Small fluctuations are filtered away by a median filter in MATLAB® and temperature measurements of the thermocouple furthest away from the coldfinger is evaluated as in FIG. 4b).

For all samples of water a super cooling followed by rapid nucleation resulted in a sudden release of latent heat, observed as a spike in temperature measurements with a temporal delay up along the sample. The spike is indicated by the arrow in FIG. 4a). This phenomenon was also observed for suspensions of ceramic powders, however, to a much smaller degree, as the powder particulates introduced an extensive number of nucleation sites compared to the water and super cooling was thus significantly less dominating.

For pure water at 1 atm the freezing point is 273.15 K, however, for tap water and especially for water-based ceramic suspensions with both particulates and organic additives, freezing point depression will result in a lower freezing temperature. Thus, 273.15 K cannot be used as a temperature indicator for the position of the freezing front as the actual freezing point will be lower. However, when looking at the temperature profiles at various thermocouple position during freezing in FIG. 4, a significant bump in the temperature curve for the thermocouple at 25.5 mm is evident at $T_{\text{trans}} = 271.45$ K with

the equivalent time $t_{\text{trans}} = 2074.4$ s indicating an increase in the cooling rate. As the thermal conductivity of ice is four times greater than that of water, an increase in cooling rate at a given position is exactly what is expected to occur as the liquid water transitions into ice, and this bump thus indicates the transition temperature, i.e. the freezing temperature for either the water or the ceramic suspension. Therefore, the time at which the freezing front reaches a given thermocouple position can be estimated and thereby the average freezing front velocity between two thermocouple positions can be calculated. Generally, the bump related to the transition temperature can be identified for all thermocouple positions. For practical reasons, the transition temperature is found from the temperature curve for the thermocouple furthest away from the coldfinger when freezing kinetics are evaluated for frozen samples in Section IV A 1.

In FIG. 4b), the second bump at time t_{solid} , evident at all thermocouple positions at the same time, indicates an increase in the cooling rate of the sample when it has completely transitioned into ice and no more latent heat is released in the system. t_{solid} is thus the total freezing time.

In the case of samples frozen at -2 K/min, the time, t_{trans} , at which the thermocouple at the top of the mould reaches T_{trans} coincides with the coldfinger reaching the minimum temperature of the freeze-caster. 25.5 mm sample height is thus close to the capacity of the freeze-caster for samples of water frozen at this temperature profile, as the temperature of the coldfinger beyond t_{trans} no longer follows the pre-set temperature profile. This is illustrated in FIG. 5, where the absolute value of the offset temperature is seen to significantly increase beyond 2000 s. The current minimum temperature of ~ 220 K of the current freeze-casting device can be decreased by replacing the Julabo chiller with a chiller of lower minimum temperature thereby increasing the achievable sample height for aqueous samples.

Furthermore, the current maximum temperature of the freeze-casting device is defined by the maximum operational temperature of the Peltier element of 440 K, making it also suitable for freeze-casting of suspensions with alternative solvents such as camphene²¹ or *tert*-butyl alcohol¹⁹, with solidification temperatures of 325 K and 298 K, respectively. Both are well within the operational tem-

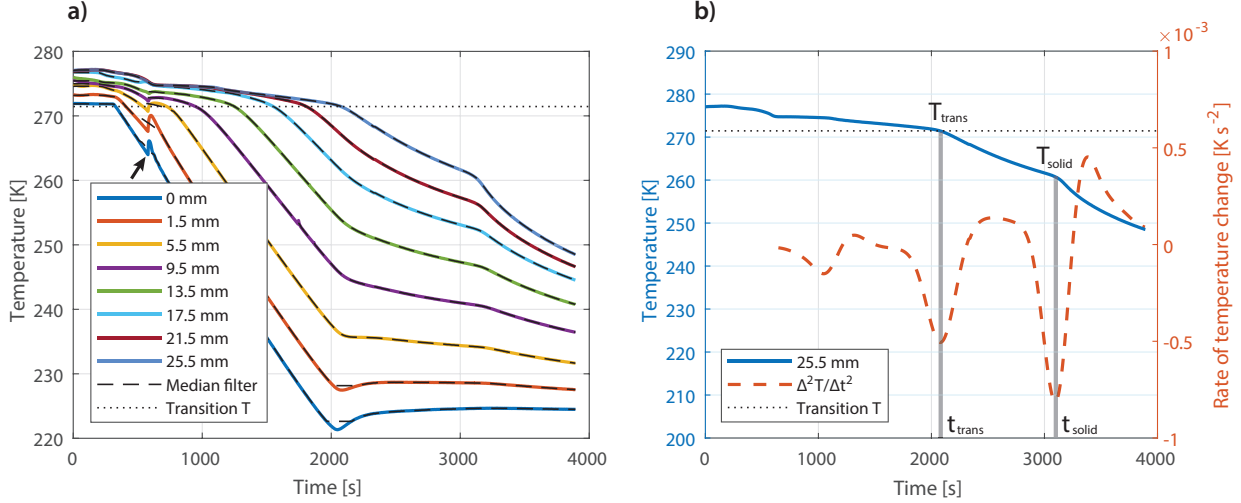


FIG. 4: Temperature measurements at all thermocouple positions as a function of time obtained for a water sample frozen at -2 K/min. (a) All temperature measurement are filtered using a median filter in MATLAB[®]. The black arrow indicates the onset of freezing with a spike in temperature due to release of latent heat upon sudden nucleation in a super cooled sample. (b) The orange curve shows $\frac{\Delta^2 T}{\Delta t^2}$ for the thermocouple positioned at 25.5 mm. From peak analysis the change in cooling rate for estimating the freezing temperature, T_{trans} , and thus the freezing front position at t_{trans} as well as the total freezing time, t_{solid} , of the sample is evaluated.

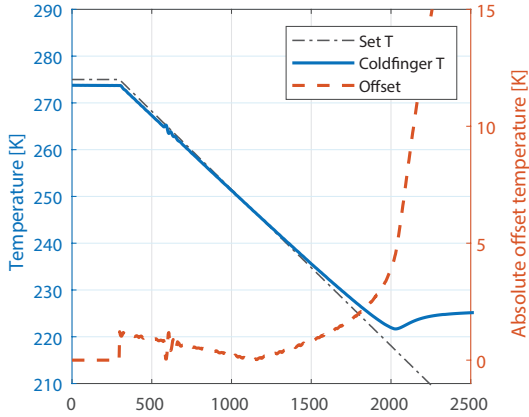


FIG. 5: Coldfinger and preset temperature as a function of time for water sample frozen at a constant freezing rate of -2 K/min. Eventually, the coldfinger reaches the minimum temperature of the freeze-caster in its current configuration, and the absolute offset temperature, i.e. the temperature difference between the two, significantly increases.

perature span of the freeze-casting set-up presented here.

1. Linear and exponential freezing profiles

By evaluating measured temperature curves as described in the previous section, the capacity of the freeze-caster can be evaluated for various dynamic freezing profiles. Estimated freezing front velocities and maximum heights for water samples are given in FIG. 6 for both linear freezing profiles (a–b) and exponential freezing profiles (c–d).

As the bottom part of the suspensions typically underwent super cooling followed by sudden nucleation, as previously discussed and indicated by the arrow on 4a), large deviations of freezing front velocities were found for velocities estimated close to the copper bottom. Only freezing front velocities from a distance of 7.5 mm from the copper bottom are thus plotted on FIG. 6a,c).

As previously discussed, t_{solid} indicates the time at which the sample is completely frozen. For higher freezing rates this occurs after the coldfinger has reached the minimum temperature of the set-up. The maximum height in FIG. 6b,d) is thus estimated as the height of the frozen part of a freezing sample at the time where the offset between the temperature of the coldfinger and the preset temperature profile exceeds 3 K, and is thus the maximum sample length that can be achieved at a given temperature profile.

For the purpose of freeze-casting where a constant freezing front velocity throughout a specific sample length is desired, only linear freezing profiles with

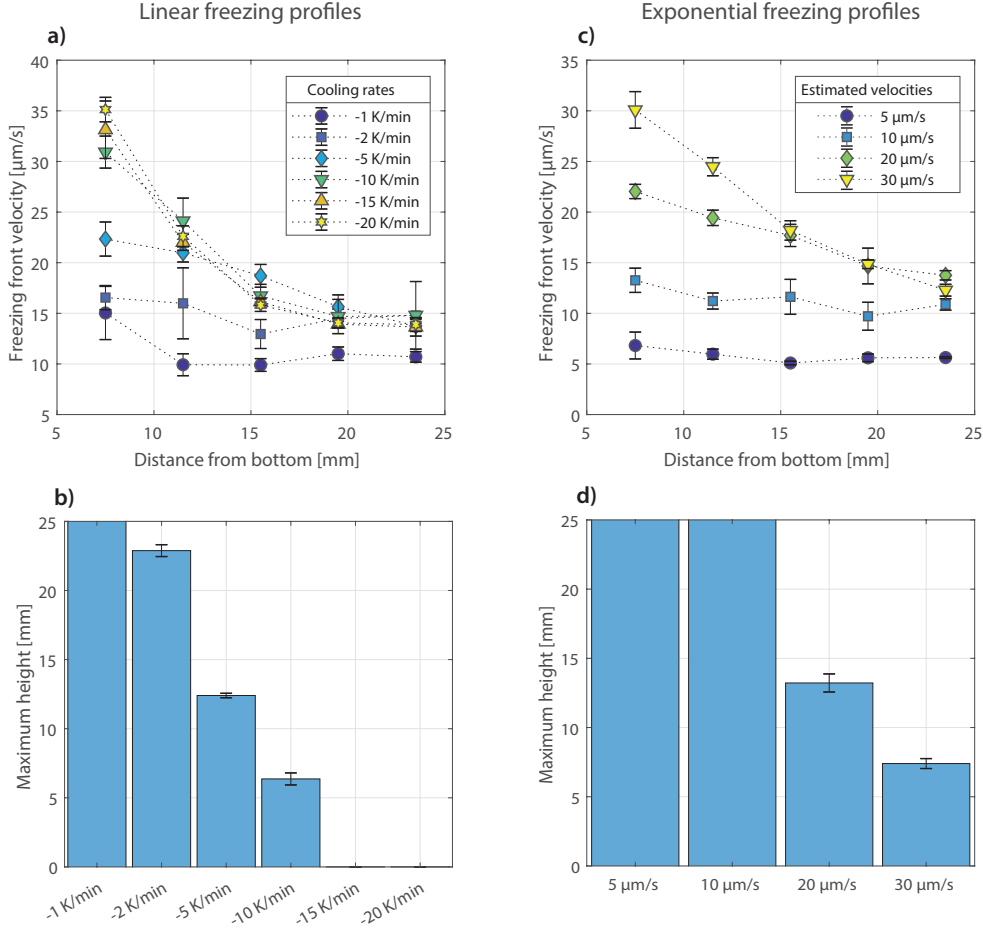


FIG. 6: Evaluated freezing front velocities and estimated maximum height based on $|T_{offset}| < 3$ K for samples frozen using linear (a–b) or exponential (c–d) temperature profiles. Note that an indicated maximum sample height of 25 mm in (b,d) is merely the maximum measurable height. Actual maximum sample heights are assumed greater.

cooling rates of -1 K/min and -2 K/min or exponential freezing profiles with estimated velocities of $5 \mu\text{m/s}$ and $10 \mu\text{m/s}$ met these criteria. Regarding the latter, samples of *estimated* freezing front velocities of 5 and $10 \mu\text{m/s}$ almost matched the measured *actual* freezing front velocities, validating Equation 1. Additionally, applying exponential temperature profiles versus linear temperature profiles appear to have slight influence on the consistency of the freezing front velocity throughout the samples, however, a larger sample batch is required to fully confirm this assumption.

From FIG. 6 it appears that the maximum freezing front velocity maintainable over the length of a 25 mm sample is $\sim 15 \mu\text{m/s}$ for the current freeze-caster configuration. As less latent heat will have to be removed during freezing from a ceramic suspension as a given volume fraction is substituted with ceramic powder, it is expected that the maximum freezing front velocity would be slightly greater for

a ceramic suspension.

The capacity of the current freeze-caster set-up could be improved by replacing the chiller, allowing for greater freezing front velocities and larger samples. The set-up presented here is prepared for liquid nitrogen as a cooling fluid if larger cooling rates capacities are needed in the future.

2. Implementation of feedback mechanism

The current freeze-caster configuration allows for implementation of various dynamic temperature functions for the temperature of the coldfinger during freeze-casting. These can be derived from modeling, experimental data or empirical knowledge. A possible future upgrade of the freeze-casting device presented is to implement a direct feedback loop while freezing. Monitoring the freezing front with an appropriate temporal and spatial resolution while

continuously adjusting the set temperature could enhance the accuracy of reaching the desired temperature profile.

B. Freeze-cast ceramics

Freeze-casting of LCSM suspensions results in ceramic structures of directional porosity in the form of well defined macropores – or microchannels – running parallel to the freezing direction, as illustrated in FIG. 7.

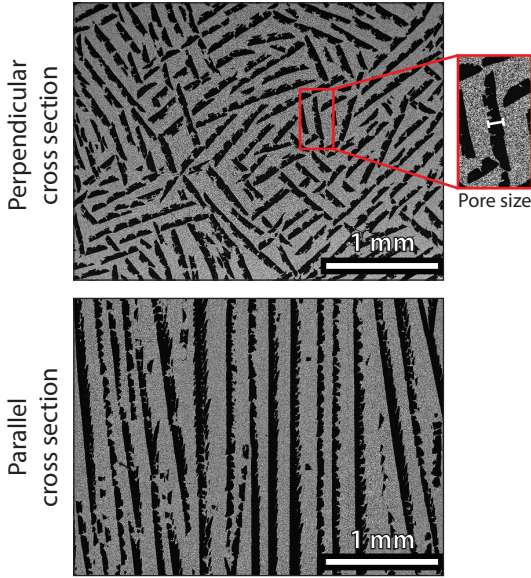


FIG. 7: SEM micrographs of a freeze-cast LCSM ceramic, where grey areas are ceramic walls, while black voids are micro-channels. Images are obtained on cross sections perpendicular or parallel to the freezing direction at a sample height of 12 ± 1 mm. The sample was frozen dynamically at a freezing rate of -1.5 K/min. Close-up indicates 'pore size' as plotted in FIG. 8.

The channels are lamellar in shape with an ellipsoidal cross section. Channels are ordered in domains of different orientations in the perpendicular cross section. A simple re-design of the mould allowing for bidirectional freezing according to Bai et al.¹⁶ and Hu et al.¹⁷ could ensure an alignment of domains in the perpendicular cross section. The width of the channels, or pore size, as defined on FIG. 7 in the close-up, can be determined by image analysis. Mean pore sizes are estimated from 12 SEM micrographs obtained on cross sections parallel to the channel orientation at four sample heights evenly distributed throughout the samples, as described previously^{8,25}. Mean pore sizes as a function of freezing front velocity for samples frozen us-

ing various linear freezing profiles are given in FIG. 8 with corresponding cooling rates in the legend. Both pore size and freezing front velocity are averaged over a sample height of 7.5 mm – 20 mm.

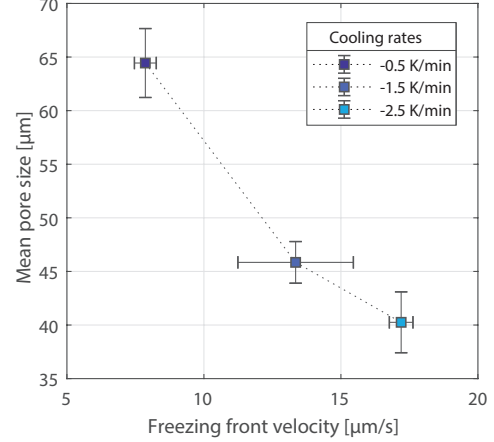


FIG. 8: Mean pore size as a function of freezing front velocity. The freezing front velocity depends on the freezing rate indicated in the legend. The faster the freezing front velocity the smaller the resulting pore size.

As is evident from FIG. 8, the mean pore size strongly depends on the freezing front velocity, decreasing in size with an increase in freezing rate, achieving channel widths in the range $\sim 40 - 65$ μm .

V. CONCLUSION

A freeze-casting device utilizing a thermoelectric element for high precision temperature control for implementation of dynamic freezing conditions was presented.

The performance of the device was evaluated by directional freezing of water and aqueous ceramic suspension samples using both linear and exponential freezing profiles. The freezing front was successfully tracked by measuring the temperature gradient along the sample using thermocouples directly mounted in the freeze-casting mould. The maximum freezing front velocity maintainable over the length of a 25 mm sample was ~ 15 $\mu\text{m/s}$ for the current freeze-caster configuration.

Implementing linear freezing profiles with cooling rates of -0.5 K/min to -2 K/min resulted in LCSM ceramic with lamellar microchannels with pore widths of ~ 40 to ~ 75 μm .

The current operational temperature range of the freeze-caster is $\sim 220 - 440$ K. The performance and capacity of the freeze-casting device can be enhanced

by implementation of i) a direct feedback loop for immediate adjustment of the freezing profile, and ii) liquid nitrogen as cooling fluid.

- ²⁵Cathrine D. Christiansen, Kaspar K. Nielsen, and Rasmus Bjørk. Functionally graded multi-material freeze-cast structures with continuous microchannels. (*submitted*), 2020.
- ²⁶P. S. Jørgensen, S. L. Ebbenhøj, and A. Hauch. doi: 10.1016/j.jpowsour.2015.01.054.

ACKNOWLEDGEMENTS

This work is funded by the Independent Research Fund Denmark – Technologies and Productions Sciences, project no. 6111-00073B.

- ¹Michael M. Porter, Pooya Niksiar, and Joanna McKittrick. doi:10.1111/jace.14183.
- ²Jordi Seuba, Sylvain Deville, Christian Guizard, and Adam J. Stevenson. . doi:10.1080/14686996.2016.1197757.
- ³Aaron Z. Lichtner, David Jauffrès, Christophe L. Martin, and Rajendra K. Bordia. doi:10.1111/jace.12478.
- ⁴J. Gurauskis, C. R. Graves, R. Moreno, and M. I. Nieto. doi:10.1016/j.jeurceramsoc.2016.08.031.
- ⁵Sylvain Deville. doi:10.1016/j.scriptamat.2017.06.020.
- ⁶Sylvain Deville, Eduardo Saiz, and Antoni P. Tomsia. . doi:10.1016/j.actamat.2006.11.003.
- ⁷Thomas Waschkies, Rainer Oberacker, and Michael J. Hoffmann. . doi:10.1111/j.1551-2916.2008.02673.x.
- ⁸Cathrine D. Christiansen, Kaspar K. Nielsen, Rajendra K. Bordia, and Rasmus Bjørk. doi:10.1111/jace.16500.
- ⁹Sylvain Deville, Eric Maire, Audrey Lasalle, Agnès Bogner, Catherine Gauthier, Jérôme Leloup, and Christian Guizard. . doi:10.1111/j.1551-2916.2009.03163.x.
- ¹⁰Andrea Bareggi, Eric Maire, Audrey Lasalle, and Sylvain Deville. doi:10.1111/j.1551-2916.2011.04572.x.
- ¹¹Kristen L. Scotti and David C. Dunand. doi: 10.1016/j.pmat.2018.01.001.
- ¹²T Waschkies, R Oberacker, and M J Hoffmann. . doi: 10.1016/j.actamat.2011.04.046.
- ¹³Stefan Flauder, Uwe Gbureck, and Frank A. Müller. doi: 10.1016/j.actbio.2014.08.020.
- ¹⁴Christian Stolze, Tobias Janoschka, Stefan Flauder, Frank A. Müller, Martin D. Hager, and Ulrich S. Schubert. . doi:10.1021/acsami.6b05018.
- ¹⁵Christian Stolze, Tobias Janoschka, Ulrich S. Schubert, Frank A. Müller, and Stefan Flauder. . doi: 10.1002/adem.201500235.
- ¹⁶Hao Bai, Yuan Chen, Benjamin Delattre, Antoni P. Tomsia, and Robert O. Ritchie. doi:10.1126/sciadv.1500849.
- ¹⁷Zhi-jie Hu, Xiang-tian Shen, Shu-li Geng, Ping Shen, and Qi-chuan Jiang. doi:10.1016/j.ceramint.2017.12.130.
- ¹⁸Jordi Seuba, Jerome Leloup, Stephane Richaud, Sylvain Deville, Christian Guizard, and Adam J. Stevenson. . doi: 10.1016/j.jeurceramsoc.2017.01.014.
- ¹⁹Yufei Tang, Sha Qiu, Qian Miao, and Cong Wu. doi: 10.1016/j.jeurceramsoc.2015.12.012.
- ²⁰Stephen W. Sofie. doi:10.1111/j.1551-2916.2007.01720.x.
- ²¹S. M. Miller, X. Xiao, and K. T. Faber. doi: 10.1016/j.jeurceramsoc.2015.05.012.
- ²²Noriaki Arai and Katherine T. Faber. doi: 10.1016/j.scriptamat.2018.10.037.
- ²³Cathrine D. Christiansen, Kaspar K. Nielsen, and Rasmus Bjørk. Freeze-casting to create directional microchannels in regenerators for magnetic refrigeration. In *Proceedings of TherMag VIII, 8th IIF-IIR International Conference on Caloric Cooling*, pages 96–101, Darmstadt, Germany, 2018. doi:10.18462/iir.11072.
- ²⁴A. Z. Lichtner. *Anisotropic and Hierarchical Porosity in Multifunctional Ceramics*. Phd dissertation, University of Washington, 2015.

Paper IV

Functionally graded multi-material freeze-cast structures with continuous microchannels

Cathrine D. Christiansen, Kaspar K. Nielsen, Rasmus Bjørk

In print: *Journal of the European Ceramic Society*

Related publication(s): Supporting information & data – Functionally graded multi-material freeze-cast structures with continuous microchannels. DOI: 10.11583/DTU.9878894

Experimental work, post processing and data analysis carried out at Department of Energy Conversion and Storage, Technical University of Denmark during the Ph.D. period. I am the first-author of the paper.



Contents lists available at ScienceDirect

Journal of the European Ceramic Society

journal homepage: www.elsevier.com/locate/jeurceramsoc

Original Article

Functionally graded multi-material freeze-cast structures with continuous microchannels

Cathrine D. Christiansen*, Kaspar K. Nielsen, Rasmus Bjørk

Department of Energy Conversion and Storage, Technical University of Denmark, Frederiksborgvej 399, DK-4000 Roskilde, Denmark

ARTICLE INFO

Keywords:

Freeze-casting
Functionally graded materials
Layered structure
Porous ceramics
Magnetocaloric

ABSTRACT

We present the processing of functionally graded multi-material freeze-cast structures, i.e. structures with varying material properties but continuous and homogeneous microchannels. We demonstrate this for stepwise, continuous, highly viscous and gelation freezing to achieve freeze-cast structures of graded $\text{La}_{0.66}\text{Ca}_{0.24}\text{Sr}_{0.09}\text{Mn}_{1.05}\text{O}_3$ (LCSM9) and $\text{La}_{0.67}\text{Ca}_{0.27}\text{Sr}_{0.06}\text{Mn}_{1.05}\text{O}_3$ (LCSM6) ceramics.

The two phases are successfully distinguished from one another by the addition of 10 wt% $\text{Ce}_{0.9}\text{Gd}_{0.1}\text{O}_2$ (CGO) to the LCSM6 phase. The relative Ce-content facilitates tracking of the LCSM6 phase using energy-dispersive X-ray (EDS) elemental analysis. Coupled with scanning electron microscopy, we show well-defined interfaces with continuous microchannels between the two LCSM phases in both green and sintered samples.

By implementing constant freezing rates of -1.5 K/min a consistent freezing front velocity of $\sim 13\ \mu\text{m/s}$ is maintained, and we found that a structural continuity can be maintained across the LCSM9–LCSM6/CGO interface, however, with varying pore morphology depending on the various freezing procedures.

1. Introduction

Through the past 20 years freeze-casting has become a versatile templating technique with a broad range of applications [1] within engineering of microchannels in polymer, metal and ceramic structures. However, thus far, ceramic freeze-casts consist of a single material or a composite of homogeneously distributed phases of materials. Freeze-casting of a functionally graded or layered structures with two or more phases of material separated by a distinct interface perpendicular to the channel orientation and continuous microchannels between the two phases has not yet been achieved. It would, however, be extremely useful in applications such as e.g. membrane- and filter-applications, flow catalysis or magnetic refrigeration, as the material properties can thus be varied along the microchannels throughout the freeze-cast structure.

During ceramic freeze-casting, an aqueous suspension of ceramic particles is frozen directionally driven by an imposed thermal gradient. The growing ice crystals causes segregation of the particles, which results in a two-phase structure of ceramic and ice. Subsequently, the latter is removed by sublimation. Sintering of the freeze-cast green body results in a rigid, monolithic ceramic with directional porosity in the form of parallel, well-defined channels. The morphology and dimensions of these channels strongly depend on freezing conditions, while

the porosity mainly depends on the ceramic load of the suspension [2–6]. The porosity is typically hierarchical with macroporosity in the form of larger, ice-templated pores – i.e. the channels – and inter-particle microporosity in the walls in the form of micropores.

The channels are directly shaped from the ice crystals and are in the ceramic green body the direct imprint of these. The continuity and low tortuosity of channels are due to the intrinsic properties of water during ice crystal formation under an applied thermal gradient. Layering of two separately frozen freeze-casts would therefore lead to a discontinuity in the channels across the interface between the two materials causing undesirable distortion of the otherwise homogeneous channels.

In order to achieve a structural continuity across the interface between two materials in freeze-casting, the freezing step should also be continuous across the interface ensuring continuous ice crystals. In order to do so, the materials must be layered in the wet stage, i.e. as liquid suspensions prior to freezing. However, upon being poured on top of each other with no further measures, the two suspensions will inevitably mix due to advection, convection and diffusion. An approach to inhibit this mixing and achieve a proper layering of liquid suspensions could be to alter the flow properties of the suspensions. In this work we investigate two approaches for doing so:

* Corresponding author.

E-mail addresses: cdech@dtu.dk (C.D. Christiansen), rabj@dtu.dk (R. Bjørk).<https://doi.org/10.1016/j.jeurceramsoc.2019.12.018>

Received 24 October 2019; Received in revised form 29 November 2019; Accepted 6 December 2019

0955-2219/ © 2019 Elsevier Ltd. All rights reserved.

- 1 Inhibiting flow/miscibility by increasing viscosity using polymeric/steric additives
- 2 Elimination of flow/miscibility by gelation

Polyvinylpyrrolidone (PVP) has previously been studied for its effects on rheological properties of ceramic suspensions, where viscoelasticity and viscosity were found to depend on the average molecular weight and suspension concentration of PVP [7,8]. Various PVP concentrations are thus added to ceramic suspensions for freeze-casting in this work to increase viscosity and thus inhibit flow and miscibility of suspensions in order to achieve a wet layering of these.

Gelation freeze-casting has successfully resulted in freeze-cast ceramics of well-defined parallel channels, however, with a slightly altered morphology [9,10,6]. Gelation freeze-casting provide an additional processing step in the gelation of suspensions, where near net-shaping of the gelated suspension is possible if desired. If gelation is carried out such that the suspension loses fluidity, gelated suspensions can in principle be processed and stacked perpendicular to the freezing direction, resulting in a composite gelated sample of layered suspensions of different materials.

As a ceramic we use the perovskite $\text{La}_{0.66}\text{Ca}_{0.33-x}\text{Sr}_x\text{Mn}_{1.05}\text{O}_3$ (LCSM), which is well known for its desirable magnetocaloric properties. The Curie temperature of LCSM can be controlled by varying the strontium doping with achievable Curie temperatures in the range of 267–375 K [11], making this material attractive for e.g. application as an active magnetic regenerator (AMR) material in magnetic refrigeration [12,13]. Magnetic refrigeration utilizes the AMR cycle and offers an alternative to conventional refrigeration [14]. AMR technology is based on a porous magnetic material through which an environmentally friendly fluid flows in order to transfer heat. The efficiency of the AMR cycle strongly depends on the geometry of the regenerator material. In order to improve the efficiency an optimal structure could consist of microchannels with a large porosity while maintaining a large specific surface area [12]. Freeze-casting offers a processing route for structures meeting these specific criteria [15]. However, in order to achieve an optimal operational temperature span of such a regenerator, a chemically graded, or layered, structure is desired [13]. The magnetocaloric effect, i.e. the change in temperature of a ferromagnetic material upon varying an externally applied magnetic field, peaks around the Curie temperature of the sample. The Curie temperature, T_C , defines the transition temperature between the ferro- and paramagnetic states. Joining multiple similar materials with slightly varying chemical properties and thus varying T_C , enhances the temperature range over which the AMR device operates [13,16]. Magnetic refrigeration is thus one possible application that would benefit greatly by graded freeze-cast structures.

In this work, graded freeze-cast structures of $\text{La}_{0.66}\text{Ca}_{0.24}\text{Sr}_{0.09}\text{Mn}_{1.05}\text{O}_3$ (LCSM9) and $\text{La}_{0.67}\text{Ca}_{0.27}\text{Sr}_{0.06}\text{Mn}_{1.05}\text{O}_3$ (LCSM6) are engineered by optimizing the suspension viscosities with the addition of PVP of various concentrations and average molecular weights and by gelation-freezing and net-shaping using gelatine. As LCSM6 and LCSM9 are very similar chemically, a $\text{Ce}_{0.9}\text{Gd}_{0.1}\text{O}_2$ (CGO) marker is added to the LCSM6 phase in order to distinguish the two phases chemically by energy-dispersive X-ray spectroscopy [17].

2. Materials and experimental procedures

Graded freeze-cast ceramics were prepared from layered aqueous suspensions of LCSM powders. Samples were prepared from the same stock suspensions with various concentrations of either commercially available amino-based dispersant and binder, polymers such as polyvinylpyrrolidone (PVP) or gelatin in order to change suspension properties and freezing conditions to achieve a distinct layering of the final freeze-cast structure.

Table 1

Summary of properties of LCSM6/CGO and LCSM9, where density was measured on powders that had been calcinated at 1000 °C for 2 h, the median particle size, d_{50} , is of suspensions after ball milling while onset temperature, T_{onset} and Curie temperature, T_C , is measured on green and sintered pellets, respectively.

	Density [g/cm ³]	d_{50} [μm]	T_{onset} [°C]	T_C [K]
LCSM6/CGO	6.10/6.92	0.41	1015	288/–
LCSM9	6.08	0.49	930	300

2.1. Material properties and suspension preparation

Two stock ceramic suspensions were prepared from 20 vol% powders in MilliQ water: one suspension was prepared solely from $\text{La}_{0.66}\text{Ca}_{0.24}\text{Sr}_{0.09}\text{Mn}_{1.05}\text{O}_3$ (LCSM9, CerPoTech), while the other was prepared from $\text{La}_{0.67}\text{Ca}_{0.27}\text{Sr}_{0.06}\text{Mn}_{1.05}\text{O}_3$ (LCSM6, CerPoTech) and $\text{Ce}_{0.9}\text{Gd}_{0.1}\text{O}_2$ (CGO, CerPoTech) in weight ratio 9:1, in the following referred to as suspensions/samples LCSM9 and LCSM6/CGO, respectively. LCSM powders were calcined at 1000 °C for 2 h prior to use. Material and suspension properties are summarized in Table 1.

To establish a sufficient dispersion of particles, 2.5 wt%, solid to ceramic ratio, of dispersant (DURAMAX™D-3005, Rohm and Haas, Dow Chemical) and dropwise addition of nitric acid to adjust the pH of suspensions from ~8 to ~6.5 was added. Suspensions were homogenized by ball milling in PE flasks using zirconia balls (Ø3–4 mm) as grinding media. To ensure even freezing kinetics and ice crystal growth through both layers of a sample, and thus homogeneous channel sizes, suspensions were ball milled until homogeneous and comparable in particle size distributions as shown in Fig. 1. Thus, LCSM6/CGO was ball milled at 25 rpm for ~72 h while LCSM9 was ball milled at 45 rpm for ~72 h. Particle size distributions of milled suspensions were monitored using a Laser Diffraction Particle Size Analyser (LS 13 320, Beckman Coulter), while the density of calcined powders were measured by gas pycnometry (AccuPyc II 1340, Micromeritics).

From these stock suspensions, suspensions of increased viscosity, Section 2.1.1, suspensions for gelation, Section 2.1.2, and samples for measurements of material characteristics were prepared.

Pellets for dilatometry and magnetization measurements were prepared by slip-casting given that the microporosity of slip-cast pellets to a larger degree resembles that of freeze-casts compared to e.g. pressed pellets. For slip-casting, cylindrical polytetrafluoroethylene (PTFE) moulds with inner diameter of 6 mm were placed on an alabaster

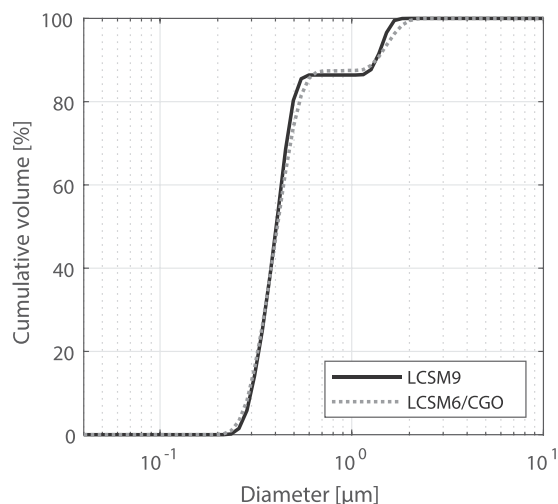


Fig. 1. Particle size distribution of suspensions after ball milling reaching median particle sizes of $d_{50} = 0.49 \mu\text{m}$ and $d_{50} = 0.41 \mu\text{m}$ for LCSM9 and LCSM6/CGO suspensions, respectively.

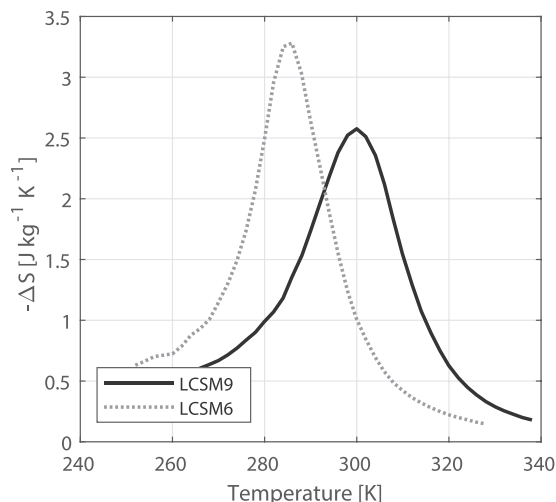


Fig. 2. Isothermal entropy change for slip-cast, sintered pellets of LCSM6 and LCSM9 at an applied field of 1.5 T, where the peak temperature can be estimated as the Curie temperature.

plaster medium. Stock suspensions for freeze-casting, with the addition of 2 wt% binder (DURAMAX™B-1022, Rohm and Haas, Dow Chemical) was poured into the moulds and left to dry for at least 48 h. Pellets for dilatometry were used in the green state while pellets for magnetization measurements were sintered using the same heating program as used for the freeze-cast samples (see Section 2.2).

Dilatometry measurements were performed using a single push-rod dilatometer (DIL 402, NETZSCH) with a 2 h hold at 550 °C (heating rate of 0.25 K/min) for burnout of additives and a 3 h hold at 1100 °C (heating rate of 0.5 K/min) for densification under normal atmosphere (flow rate of 20 mL/min). Shrinkage curves were analyzed using *Proteus Thermal Analysis* software (NETZSCH) for evaluation of onset temperatures (see Supporting information, Figure S1) and summarized in Table 1.

Magnetization measurements for evaluation of the Curie temperature were obtained using a vibrating sample magnetometer (VSM, 7407, Lake Shore Cryotronics). The isothermal magnetization was measured up to a maximum field of $\mu_0 H_{ext} = 1.5$ T from 250 K to 340 K with temperature steps of 2 K for determination of the Curie temperature and indirect measurements of the isothermal entropy change as shown in Fig. 2.

2.1.1. Viscosity

Viscous suspensions were prepared from stock suspensions of LCSM6/CGO and LCSM9, respectively, by adding 5 or 10 wt%, solid to ceramic ratio, polyvinylpyrrolidone K30 (PVP K30, $M_w \sim 40,000$, Sigma-Aldrich) or 5 wt%, solid to ceramic ratio, polyvinylpyrrolidone K90 (PVP K90, Fluka Chemika). For comparison, suspensions with the addition of 2 wt%, solid to ceramic ratio, of a low viscosity commercial binder (DURAMAX™B-1022, Rohm and Haas, Dow Chemical) were likewise prepared from both stock suspensions of LCSM6/CGO and LCSM9.

Suspensions were mixed on a low-energy ball mill at 10 rpm for ~ 24 h, after which viscosity curves of the eight suspensions were obtained using a rheometer (HAAKE RheoStress 600, Thermo Electron Corporation) equipped with a plate spindle (Platte P60 Ti L, Thermo Electron Corporation) with pre-shearing and reversing increase in shear rate from 0.1 to 50 s^{-1} at 21 °C. The plate spindle was equipped with a solvent trap to minimize evaporation during measurements. Viscosity curves are shown in Fig. 3, where it is evident that an increase in PVP load increases the viscosity.

Concentrations of PVP were chosen such that a sufficient range of viscosities was achieved. Increasing the PVP wt% further was found to

increase the viscosity further. However, increased concentrations of PVP in the suspensions lead to sticky and unmanageable suspensions that proved difficult to de-air and pour into moulds due to too large viscosity. Sintered freeze-cast ceramics would also often show severe crack formation. Thus, a maximum of 10 wt% PVP is used in the present work.

Viscous and standard suspensions were de-aired in vacuum and pre-cooled along with the polytetrafluoroethylene (PTFE) moulds in an ice bath for at least 30 min prior to freeze-casting to a temperature of approximately 0 °C. This was done partly to ensure consistent freezing-conditions and partly to minimize the thermal energy in the system.

2.1.2. Gelation

Suspensions for gelation were prepared from stock suspensions of LCSM6/CGO and LCSM9, respectively, by adding 1.5 wt%, solid to ceramic ratio, of gelatin (porcine skin, ~ 175 g Bloom, type A, Sigma-Aldrich). Gelatin was dissolved in suspensions by stirring at 45 °C for 30 min with a mechanical stirrer equipped with a propeller. The solutions were poured into pre-heated PTFE moulds (Ø20 mm) equipped with copper bottoms and then immediately de-aired in a vacuum-chamber for 5 min. Samples were left to harden at 2 °C for 17 h.

Gelated suspensions were then carefully removed from the moulds and sliced into 1–2 cm cylindrical specimens. These were stacked such that each final sample were composed of a slice of LCSM6/CGO in the bottom and a slice of LCSM9 in the top. The composite samples were then carefully transferred back to a mould and left to settle at 2 °C for 1 h before being frozen as described in Section 2.2. The gelatin content was chosen such that the suspension just loses fluidity upon gelation and is manageable for cutting and stacking.

2.2. Freeze-casting

The freeze-casting set-up and general procedure is described in detail by Christiansen et al. [18]. A set-up with a thermoelectric element for precise temperature control of a copper coldfinger was used to directionally freeze samples. PTFE moulds (Ø16 or 20 mm) equipped with thermocouples (K-type, gauge 36, Omega) along the height for monitoring of the freezing progression and a detachable copper bottom were used.

Generally, suspensions were frozen directionally in a PTFE mould by bringing the copper bottom of the mould into thermal contact with the coldfinger of the freeze-caster. Suspensions were frozen using a linear temperature profile, i.e. a constant decrease of the coldfinger temperature, of -1.5 K/min from an equilibrated temperature of 275 K. A linear temperature profile was chosen to ensure homogeneous channel sizes throughout the samples [3–6]. However, in order to achieve a distinct material interface, preparation of samples and freeze-casting procedure were varied depending on altered suspension or freezing conditions as follows:

Stepwise freezing was achieved by the initial freezing of one suspension, followed by freezing of the other suspension. Pre-cooled LCSM6/CGO suspension with B-1022 binder was poured into a mould open to ambient conditions of ~ 5 °C. Sample and mould were equilibrated at a coldfinger temperature of 275 K for 300 s before being frozen using a constant temperature change of -1.5 K/min. The suspension was frozen solid and the mould and frozen suspension were subsequently equilibrated at 270 K by adjusting the coldfinger temperature. Pre-cooled LCSM9 suspension was poured on top of the frozen suspension and frozen by immediately decreasing the temperature of the coldfinger from 270 K by -1.5 K/min until the top suspension was also completely frozen.

Continuous freezing follows the initial procedure of *stepwise freezing*, however, instead of letting the bottom suspension freeze solid, the LCSM9 suspension was added to the mould just before the freezing front, i.e. the solid/liquid interface, reached the top of the suspension. The freezing front position was evaluated by measuring the

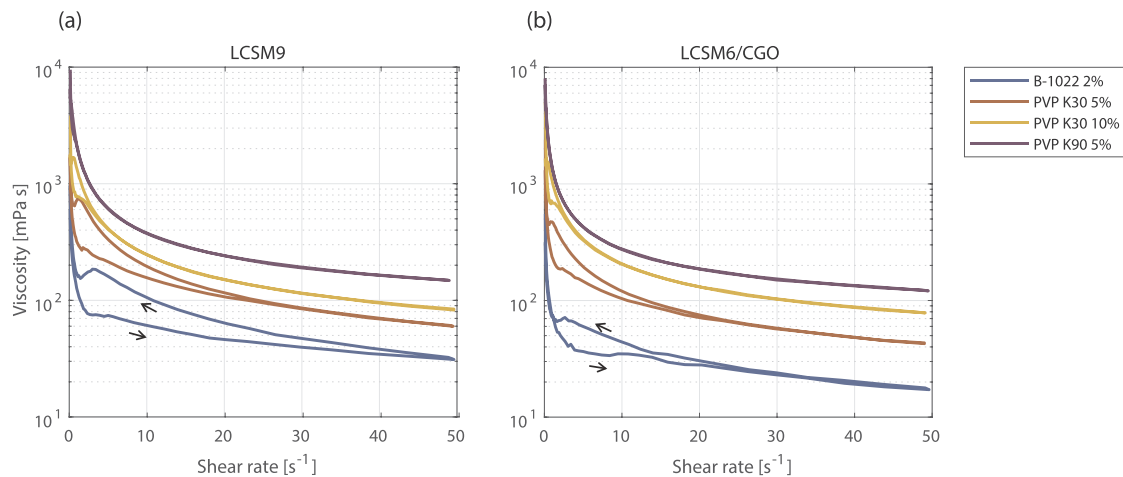


Fig. 3. Viscosity curves of (a) LCSM9 and (b) LCSM6/CGO suspensions with 2.5% DURAMAX™B-1022 binder, 5 or 10 wt% PVP K30 or 5 wt% PVP K90. The addition of the long polymers of PVP K30 and 90 significantly increases the viscosity of the suspensions. Arrows indicate the direction of measurements, and are only given for the bottom curve, but the trend is the same for all suspensions.

temperature along the height of the mould and the position of the freezing front was estimated at the position of 0 °C. A constant temperature change rate of -1.5 K/min of the coldfinger was maintained during the entire freezing process until the sample was frozen solid.

Increased viscosity allowed a direct layering of the liquid suspensions. Composite samples were prepared from suspensions of LCSM6/CGO and LCSM9 of the same binder content, respectively. 3 mL of LCSM6/CGO suspension was poured into a mould. Carefully, another 3 mL of LCSM9 suspension was layered on top using a syringe equipped with a 1.2×40 mm blunt filling needle. The tip of the needle was positioned such that it barely broke the surface of the first suspension at the approximate centre of the mould and the other suspension was very slowly transferred to the mould in order to maintain a layering of suspensions. Mould and layered suspension were left open to ambient conditions of ~ 5 °C and equilibrated at a coldfinger temperature of 275 K for 300 s before applying constant temperature change rate of -1.5 K/min until the sample was frozen solid.

Gelation freezing was achieved by freezing the already gelated and stacked samples. Pre-cooled gelated samples in PTFE moulds were mounted directly on the coldfinger of the freeze-caster, left open to ambient conditions of ~ 5 °C, equilibrated at a coldfinger temperature of 275 K for 600 s and frozen using a constant temperature change rate of -1.5 K/min until the sample was frozen solid.

Ice was removed from the frozen samples in a freeze-drier (Christ Alpha 1-2 LD plus, Buch & Holm) for 24 h. Green samples were then fired in air, initially burning out organic additives at 250 °C and 450 °C using a heating rate of 15 K/h, followed by sintering at 1100 °C for 3 h for samples with PVP and B-1022 with a heating rate of 30 K/h. Given the evaluated onset temperatures in Table 1, a more cautious sintering temperature of 1000 °C with a heating rate of 30 K/h was chosen for gelated samples, as these had a tendency to develop crack formations upon sintering at elevated temperatures.

2.2.1. Structural and chemical characterization

The structural analysis of freeze-cast samples is based on image analysis of SEM micrographs and follows the procedure described by Christiansen et al. [6]. Here, samples are mounted in epoxy (EpoFix, resin and hardener, Struers), cut into smaller specimens revealing cross sections perpendicular and parallel to the freezing direction, polished and coated with a ~ 12 nm thick carbon layer and imaged using a scanning electron microscope (SEM, TM3000, Hitachi High-Technologies). Mean pore size of the ice-templated pores, macroporosity, i.e. the channel porosity, and specific surface area were evaluated from binarized SEM images obtained perpendicular to the freezing direction.

Three images containing ~ 300 pores each were analyzed at each vertical sample position in order to obtain a statistically significant data set. SEM micrographs can be found as supporting data (see the “Supporting information and data” section). The quantification of pore size and specific surface area from image analysis was originally developed for analysis of 3D data [19,20]. Structural parameters of pore size, macroporosity and specific surface area – the latter in this case determined as area per volume – are all determined from binarized images, thus removing structural features smaller than a few microns and thereby disregarding e.g. inter-particle porosity and the pore size of micropores in the walls of the freeze-cast structures.

The LCSM9|LCSM6/CGO interface was evaluated at cross sections parallel to the freezing direction by SEM micrographs and energy-dispersive X-ray spectroscopy (EDS, Bruker). EDS spectra for elemental analysis were collected at interfaces over 512×384 pixels (pixel size of 3.2×3.2 μm , i.e. a total sample area of 1638×1229 μm), with a 128 μs dwell time per pixel and a total collection time of 600–1800 s. Accumulated EDS spectra either over a selection, as illustrated by yellow boxes in Fig. 4, or over all pixels in a sample area were analyzed using *Quantax Esprit 2.1* software (Bruker Microanalysis Software, Bruker), where deconvolution of peaks was achieved by series fit and quantified by standardless P/B-ZAF method.

The LCSM9|LCSM6/CGO interface was detected by evaluation of Ce-content at a given sample position. Cerium has a distinct L_{α} emission peak at 4.84 keV, as seen in the EDS spectra in Fig. 4, where accumulated EDS spectra of the selection above and below the interface is shown on the right. The Ce-peak is only clearly visible for the selection below the interface, i.e. the LCSM6/CGO phase. The element analysis was carried out for signals from lanthanum, calcium, strontium, manganese and cerium, thus, the overall analysis yielded the *relative Ce-content* of a given sample at a given position.

Accumulated, deconvoluted EDS spectra and identified background for all analysis points can be found as supporting data (see the “Supporting information and data” section).

3. Results and discussion

3.1. Interface characterization

Freeze-casting of LCSM suspensions with the implementation of stepwise, continuous, highly viscous and gelation freezing all resulted in a distinct layering of suspensions. This yielded a clearly visible and sharp interface between the two layers in both the green and sintered samples, as seen in Fig. 5 The figure shows a picture of a green body

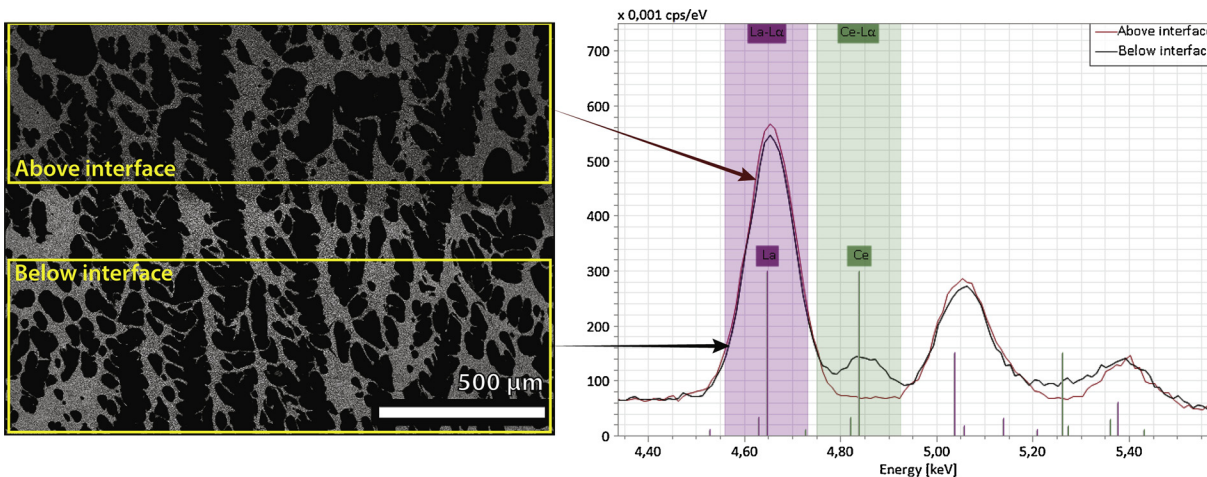


Fig. 4. Accumulated EDS spectra obtained above and below the LCSM9 and LCSM6/CGO interface, respectively, of a gelated freeze-cast sample. The analyzed region of the sample is indicated by the yellow boxes. The cerium L_{α} -peak at 4.84 keV is only clearly distinguishable in the accumulated spectra of the selection below the interface.

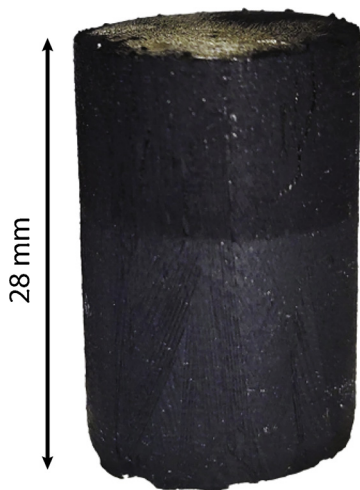


Fig. 5. Picture of freeze-cast green sample frozen from LCSM6/CGO (grey bottom layer) and LCSM9 (black top layer) suspensions with 5 wt% PVP K30.

freeze-cast sample, where the white CGO made the LCSM6/CGO phase grey and thereby visually identifiable.

Freeze-casting of a homogeneous suspension of particles generally results in structures with directional porosity in the form of micro-channels along the freezing direction, which was also the case for samples in this study, as evident from Fig. 6. However, what is remarkable, is that all procedures except for stepwise freezing, led to continuous channels across the interface. The interfaces in Fig. 6 are enhanced by adjusting the grayscale threshold of SEM images and correlating these with Ce-mapping in EDS analytical software. For ease of visualization in compressed and printed images a semi-transparent dashed line indicating the interface has been added as an eye-guide.

The relative Ce-content above and below the interfaces given in Fig. 6 are evaluated as described in Fig. 4. However, standardless EDS analysis is not sufficient for an exact quantification of the elemental composition. For comparison, EDS elemental analysis of a freeze-cast sample of only LCSM6 still yields a relative atomic Ce-content of 0.32%. Although, as the qualitative elemental composition of samples are known, the measured relative Ce-contents can still be evaluated between samples and are in this work thus used as a both visual and chemical marker of the LCSM6 phase.

A significant discontinuity in channels across the interface for the stepwise frozen sample is seen in Fig. 6(a), with evidently altered

channel geometry in the form of more narrow channels above the interface. The channel geometry in freeze-cast ceramics is directly shaped from the growing ice crystals during the freezing phase. The growth of ice crystals in ceramic suspensions during freeze-casting has previously been observed by *in situ* X-ray [21,22]. Upon freezing, rapid nucleation takes place at the cold side forming ice crystals that grow in random directions. This is the isotropic region with no resulting directional porosity. Eventually, ice crystals growing along the direction of the temperature gradient are favoured, resulting in a region of aligned crystals. This region is referred to as the steady state region or the anisotropic region. When freezing samples stepwise, the initial suspension frozen in the first step act as a cold side for the second suspension and a new nucleation zone occurs at the interface. This results in a second isotropic region and thus discontinuous channels as is evident from the significant size difference of channels above and below the dashed line in Fig. 6(a). To avoid a second nucleation zone, the second suspension was added before the freezing front had reached the top of the suspension, i.e. while the top of the first suspension was still liquid, and samples were then frozen continuously, eliminating the second isotropic region as seen in Fig. 6(b) and ensuring continuous channels.

Generally, freezing conditions have been chosen such that they could be kept consistent and reproducible, however, the continuous freezing conditions are much more difficult to reproduce as they rely on exact determination of the freezing front position. Given that the spatial resolution of thermocouples is 4 mm in our freeze-casting set-up [18], there will always be an uncertainty in immediate determination of freezing-front position and thus inconsistent freezing conditions. Additionally, the freezing front position is estimated at the thermocouple where the temperature is 0 °C, however, freezing point depression due to organic additives and ceramic particulates will lower the actual freezing point of the suspension and thereby increase the uncertainty of the freezing front position. By extension, it should be mentioned, that continuously frozen samples for which the position of the freezing front was underestimated during the continuous freezing resulted in discontinuous channels across the interface similar to those of stepwise freezing, as the conditions for these samples more closely resembled the latter procedure. However, as the interface does appear sharp and more or less planar with continuous channels across, continuous freezing of suspensions is a feasible processing route for achieving distinct layers in a freeze-cast structure for freeze-casting set-ups with precise and immediate monitoring of the freezing front. An obvious approach for immediate tracking of the freezing front is visually. As the freezing front has been found to be a well-defined, slightly concave planar

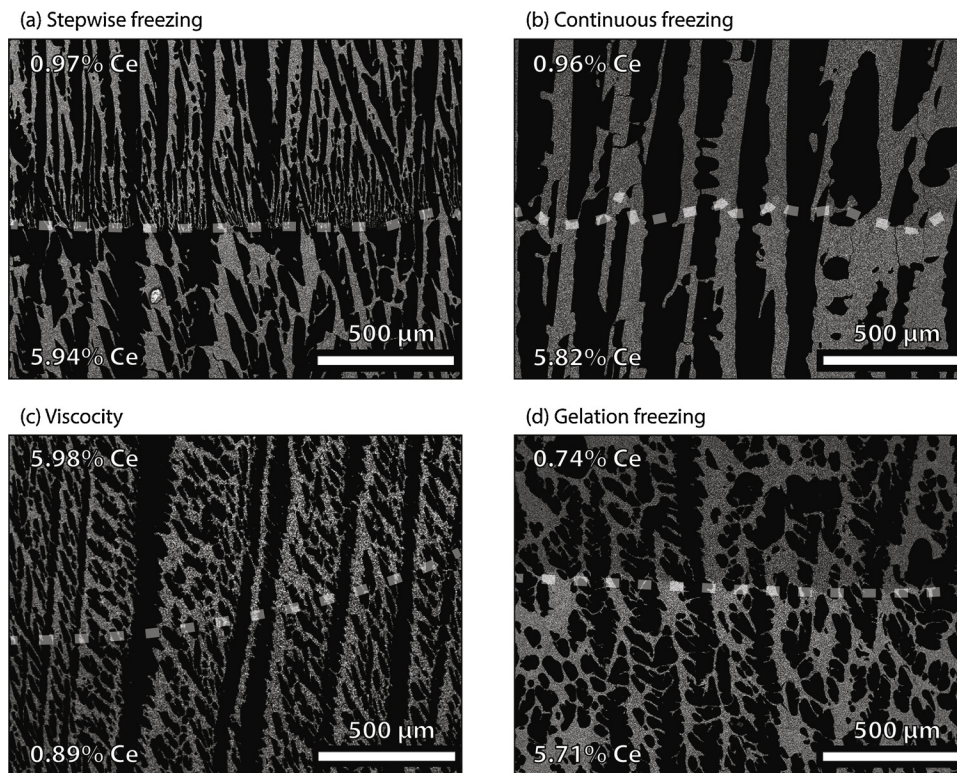


Fig. 6. SEM micrographs showing the interface between the LCSM9 and LCSM9/CGO layer of freeze-cast samples, where (a) is frozen stepwise, (b) is frozen continuously, (c) is frozen from a suspension with 10% PVP K30 for increased viscosity, and (e) is gelled prior to being frozen. The measured relative atomic content of Cerium for the two layers are indicated in the left corners and the dashed lines are eye-guides to emphasize the interface between the two layers. Images are obtained at cross sections parallel to the freezing direction at the approximate centre of the samples. Note that (a, b) and (d) are frozen with LCSM6/CGO layer at the bottom, while (c) is frozen with the LCSM6/CGO layer at the top.

interface perpendicular to the freezing direction [22], visual tracking has been successful in previous freeze-casting studies with the application of an acrylic glass mould equipped with a scale bar [5,4]. However, due to the colour of LCSM, the freezing front cannot be tracked visually [23].

3.2. Structural continuity across interfaces

As the freezing conditions for continuously frozen samples could not be kept consistent and stepwise frozen samples showed a clear discontinuity in channels across the LCSM9|LCSM6/CGO interface, a structural analysis was only carried out for freeze-cast samples frozen from viscous or gelled suspensions. Both of these displayed continuous channels across a distinct interface as is clear from Fig. 6(c, d).

Various viscosities of suspensions were tested in order to clarify the effect of viscosity on the sharpness and possibly the shape of the LCSM9|LCSM6/CGO interface. With the addition of long polymer chains in the form of PVP, the intermolecular forces and entanglement between polymer chains resist flow and thus miscibility of suspensions. The effect increases with increased concentration and length of polymers, e.g. the PVP K90 consists of on average longer chains than PVP K30 and thus results in greater viscosity at similar concentrations. In Fig. 6(c) the interface of a freeze-cast frozen from highly viscous suspensions with 10 wt% PVP K30 is shown. The interface is rather concave in shape. This shape is in accordance with the sample preparation procedure where the LCSM6/CGO suspension is added at the centre, pushing the other suspension radially aside, which will inevitably create a concave interface provided that the two suspensions do not mix.

The sharpness and position of LCSM9|LCSM6/CGO interfaces are evaluated by analyzing the relative Ce-content as a function of sample height in the centre of the samples as in Fig. 7, where the sample position is normalized at the interface. An increase in relative Ce-content thus indicates a transition from one layer to the other, where the steeper the curve the sharper the interface. The miscibility of viscous solutions appear to generally be very low and all interfaces are sharp

with a steep increase in relative Ce-content. All samples follow this trend, except for the sample frozen from suspensions with the commercial B-1022 binder and thus low viscosity. Here, a significant peak in relative Ce-content is found below the interface, followed by a drop in Ce-content immediately before a steep increase indicating the interface beyond which the relative Ce-content is more or less constant. This is due to the miscibility of the two suspensions, where, presumably, a drop of the LCSM6/CGO suspension has sunk into the LCSM9 phase and mixed. Additionally, the interface of the samples frozen from suspensions with only 5 wt% PVP K30 and thus the second lowest viscosity appears less sharp than for samples frozen from suspension of higher viscosity as the increase in relative Ce-content stretches over 4 mm, indicating a more blurred interface. Although a sharp interface is not achieved, these results hint that a graded interface could possibly be achieved by application of suspensions of fine-tuned viscosities somewhere between that of the B-1022 suspensions and that of the 5 wt% PVP K30 suspensions. Alternatively, a graded interface could be achieved by layering of three or more highly viscous suspensions with one or more mixed LCSM6/LCSM9 phase(s) between the two pure ones.

The freezing kinetics and thus resulting channel size and shape strongly depend on suspension properties such as particle size, viscosity and powder load [3,24]. Extra care was therefore taken to ensure equivalent particle loads, viscosities and particle sizes of both the LCSM9 and LCSM6/CGO suspension, as described in Section 2.1, which ensured structural continuity across the interface. Fig. 8(a–c) show structural properties of samples frozen from viscous and gelled suspensions. Pore size, porosity and specific surface area in Fig. 8 are those due to the ice-templated pores, as it is the structural homogeneity of these that are investigated. Continuity of all structural features is maintained across the interface, however, with a slightly increasing mean pore size for all samples in Fig. 8(a). Although, it is not unambiguous that the increase in mean pore size is due to changes in suspension properties. A direct indicator of the freezing kinetics is the estimated freezing front velocities as shown in Fig. 8(d), where a slight decrease in freezing front velocities moving from the bottom of samples

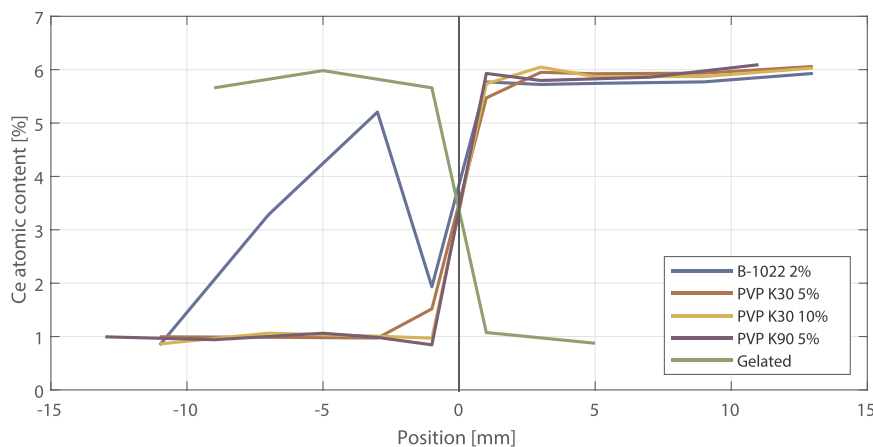


Fig. 7. Relative atomic Ce-content as a function of sample height for samples with varying viscosity or an initial gelation-step prior to freezing, evaluated using EDS elemental analysis. The greater the viscosity, the sharper the interface. Note that samples with B-1022 binder and PVP polymers are frozen with the LCSM6/CGO layer at the top, while the gelated sample is frozen with the LCSM6/CGO layer at the bottom.

across the interface to the top of samples is seen. As the pore size in freeze-cast ceramics is directly related to the freezing front velocity [3–5] the slight increase in pore sizes probably arises from the slight decrease in freezing front velocities, as the freezing front velocities were not controlled directly in this work. Only the freezing rate was controlled and kept constant, as all samples were frozen using a linear freezing profile where the temperature of the coldfinger was decreased at -1.5 K/min, resulting in a freezing front velocity of ~ 13 μ m/s.

The same trends are also observed for the gelated sample in Fig. 8(a–c); i.e. structural continuity is maintained across the LCSM6/CGO|LCSM9 interface. For gelated samples the interface between the two layers of LCSM9 and LCSM6/CGO directly reflects the shape of the cut-out specimens of gelated suspensions and thus gelation of suspensions prior to freezing ensures a sharp and planar interface, as seen in Fig. 6(d). With a homogeneous and proper gelation, the shape – or possible tilt, if so desired – of the interface can be fine-tuned along with the layer thickness and geometry. However, introducing a gelation-step also introduces additional possibilities of structural failure, as shown in Fig. 9. Fig. 9(a) illustrates delamination which can occur if the stacking of gelated suspensions are sloppy. Samples that were not stacked carefully prior to freezing would often delaminate and fracture along the interface.

Another critical failure in gelated freeze-cast structures is due to circular voids in the fired structure due to bubbles in the suspension, as can be seen in Fig. 9(b). As the suspension is heated and stirred using a propeller immediately before gelation, it is possible that air will be stirred into the solution forming bubbles. The freeze-cast in Fig. 9(b) was left to gelate without being de-aired in vacuum, and thus, circular cavities were found in the fired ceramic. De-airing the suspension immediately after it had been transferred to the mould proved highly efficient for eliminating bubbles and thus cavities.

3.3. Structural geometry and additives

Changing the suspension composition and properties significantly changes the resulting pore morphology as revealed in Fig. 8(a–c) where changes of the pore, or channel, morphology due to the addition of either PVP or gelation freezing is evident from the changing structural features.

While the measured macroporosity is more or less the same for all samples independent of additives, Fig. 8(b), this is not the case for pore sizes, Fig. 8(a). Pore sizes of freeze-casts prepared from highly viscous suspensions generally exhibit smaller pore sizes than samples frozen from low viscosity or gelated suspensions. During freezing, the long, entangled polymer chains presumably inhibit the fluidity of the highly viscous suspensions, thereby limiting the diffusion of water molecules to the growing ice crystals, resulting in smaller ice crystals and thereby smaller pores in the fired freeze-cast. Accordingly, the inverse

phenomena is seen for the specific surface area, Fig. 8(d), which is larger with increased viscosity and thus smaller pore sizes. The addition of PVP and pre-gelation does not seem to significantly affect the estimated freezing front velocities. Ice crystal growth in the z-direction, i.e. along the thermal gradient, during freeze-casting is thus not significantly affected by PVP or gelatin, meanwhile, the radial growth of ice crystals is suppressed due to limited diffusion of water.

A more thorough discussion of the effect on the pore morphology due to addition of polymers resulting in an increased viscosity [24] and pre-gelation using gelatin [9,10,6] has previously been studied and is thus beyond the scope of this work.

4. Conclusion

Functionally graded freeze-casts of LCSM6 and LCSM9 with continuous microchannels and structural integrity were achieved.

Freeze-casting of LCSM suspensions with the implementation of stepwise, continuous, highly viscous and gelation freezing all resulted in a distinct layering of suspensions. This yielded a clearly visible and sharp interface between the two layers in both the green and sintered samples. The latter three procedures resulted in continuous channels across the interface.

The two chemically very similar phases of LCSM6 and LCSM9 were successfully distinguished from one another by the addition of 10 wt% CGO to the LCSM6 phase, making it possible to track this phase using EDS analysis in order to evaluate the relative atomic Ce-content and using this as a marker.

Keeping the solid load and particle size distribution of all suspensions consistent, while ensuring an approximate constant freezing front velocity of ~ 13 μ m/s by implementing a constant temperature change rate of -1.5 K/min during freeze-casting, a structural continuity was maintained across the LCSM9|LCSM6/CGO interface. While the interface was concave in shape for frozen viscous suspensions, the interface of gelated samples directly reflected the shape of the cut-out specimens of gelated suspensions, thus ensuring a sharp and planar interface.

The overall pore morphology was found to reflect the changes in suspension properties. While the macroporosity of freeze-casts was found to be independent of changes in additives and gelation, the overall pore size of freeze-casts was found to decrease with an increase in PVP concentration and thus the viscosity. Both gelation and addition of PVP changes the pore morphology of freeze-cast specimens.

Supporting information and data

Supporting information and supporting data in the form of SEM micrographs and EDS spectra are available at: 10.11583/DTU.9878894

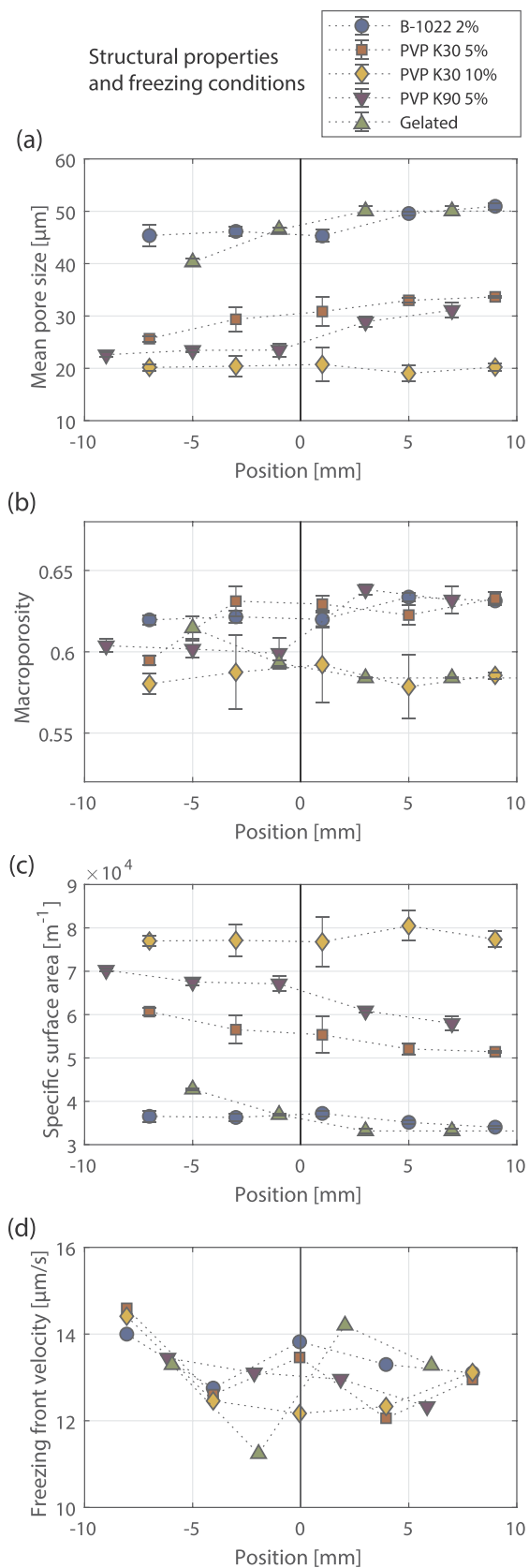


Fig. 8. Structural characterization of freeze-cast samples across the LSM6/CGO | LSM9 interface, where (a) mean pore size, (b) macroporosity and (c) specific surface area are all evaluated from image analysis of SEM micrographs. In (d) estimated freezing front velocities throughout the samples during freezing are given. All samples are frozen using the same constant freezing rate of the coldfinger of -1.5 K/min .

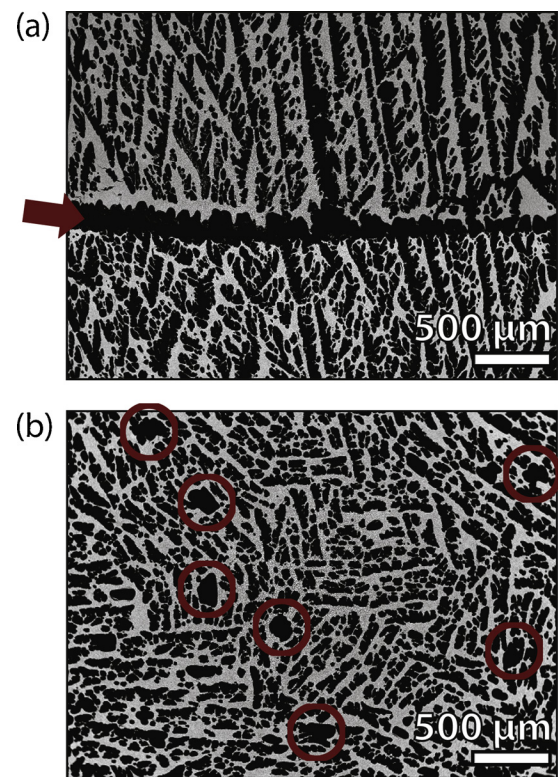


Fig. 9. Examples of failed gelated samples with (a) delamination along the interface due to faulty stacking of gelated specimens and (b) circular cavities in the structure due to bubbles in the suspension that was trapped during gelation.

Conflict of interest

The authors declare that there is no conflict of interest.

Acknowledgements

This work is funded by the Independent Research Fund Denmark | Technologies and Productions Sciences, project no. 6111-00073B. C. D. Christiansen moreover wishes to acknowledge the contributions of Karl T. S. Thydén, Jacob R. Bowen, Ebtisam Abdellahi, Lene Knudsen and Christian R. H. Bahl, Technical University of Denmark, in the form of valuable discussions and insights.

Appendix A. Supplementary data

Supplementary data associated with this article can be found, in the online version, at <https://doi.org/10.1016/j.jeurceramsoc.2019.12.018>.

References

- [1] K.L. Scotti, D.C. Dunand, Freeze casting – a review of processing, microstructure and properties via the open data repository, FreezeCasting.net, Prog. Mater. Sci. 94 (2018) 243–305, <https://doi.org/10.1016/j.pmatsci.2018.01.001>.
- [2] S. Deville, E. Saiz, R.K. Nalla, A.P. Tomsia, Freezing as a path to build complex composites, Science 311 (5760) (2006) 515–518, <https://doi.org/10.1126/science.1120937>.
- [3] S. Deville, E. Saiz, A.P. Tomsia, Ice-templated porous alumina structures, Acta Mater. 55 (6) (2007) 1965–1974, <https://doi.org/10.1016/j.actamat.2006.11.003>.
- [4] T. Waschki, R. Oberacker, M.J. Hoffmann, Control of lamellae spacing during freeze casting of ceramics using double-side cooling as a novel processing route, J. Am. Ceram. Soc. 92 (2009) 79–84, <https://doi.org/10.1111/j.1551-2916.2008.02673.x>.
- [5] A.Z. Lichtner, D. Jauffrès, C.L. Martin, R.K. Bordia, Processing of hierarchical and anisotropic porosity LSM-YSZ composites, J. Am. Ceram. Soc. 96 (9) (2013) 2745–2753, <https://doi.org/10.1111/jace.12478>.
- [6] C.D. Christiansen, K.K. Nielsen, R.K. Bordia, R. Bjørk, The effect of gelation on

- statically and dynamically freeze-cast structures, *J. Am. Ceram. Soc.* 102 (2019) 5796–5806, <https://doi.org/10.1111/jace.16500>.
- [7] M. Acosta, V.L. Wiesner, C.J. Martinez, R.W. Trice, J.P. Youngblood, Effect of polyvinylpyrrolidone additions on the rheology of aqueous, highly loaded alumina suspensions, *J. Am. Ceram. Soc.* 96 (5) (2013) 1372–1382, <https://doi.org/10.1111/jace.12277>.
- [8] D. Marani, B.R. Sudireddy, W.-R. Kiebach, L. Nielsen, S. Ndoni, Rheological properties of poly(vinylpyrrolidone) as a function of molecular weight, *Nordic Rheol. Soc. Annu. Trans.* 22 (2014).
- [9] M. Fukushima, Y.I. Yoshizawa, T. Ohji, Macroporous ceramics by gelation-freezing route using gelatin, *Adv. Eng. Mater.* 16 (6) (2014) 607–620, <https://doi.org/10.1002/adem.201400067>.
- [10] M. Fukushima, T. Ohji, H. Hyuga, C. Matsunaga, Y.I. Yoshizawa, Effect of gelatin gel strength on microstructures and mechanical properties of cellular ceramics created by gelation freezing route, *J. Mater. Res.* 32 (17) (2017) 3286–3293, <https://doi.org/10.1557/jmr.2017.94>.
- [11] A. Dinesen, S. Linderoth, S. Mørup, Direct and indirect measurement of the magnetocaloric effect in $\text{La}_{0.67}\text{Ca}_{x0.33}\text{-Sr}_x\text{MnO}_3$, *J. Phys.: Condens. Matter* 17 (39) (2005) 6257–6269, <https://doi.org/10.1088/0953-8984/17/39/011>.
- [12] T. Lei, K. Engelbrecht, K.K. Nielsen, C.T. Veje, Study of geometries of active magnetic regenerators for room temperature magnetocaloric refrigeration, *Appl. Therm. Eng.* 111 (2017) 1232–1243, <https://doi.org/10.1016/j.applthermaleng.2015.11.113>.
- [13] C.R.H. Bahl, D. Velázquez, K.K. Nielsen, K. Engelbrecht, K.B. Andersen, R. Bulatova, N. Pryds, High performance magnetocaloric perovskites for magnetic refrigeration, *Appl. Phys. Lett.* 100 (12) (2012), <https://doi.org/10.1063/1.3695338>.
- [14] A. Smith, C. Bahl, R. Bjørk, K. Engelbrecht, K.K. Nielsen, N. Pryds, Materials challenges for high performance magnetocaloric refrigeration devices, *Adv. Energy Mater.* 2 (11) (2012) 1288–1318, <https://doi.org/10.1002/aenm.201200167>.
- [15] J. Liang, C.D. Christiansen, K. Engelbrecht, K.K. Nielsen, R. Bjørk, C.R. Bahl, Heat transfer and flow resistance analysis of a novel freeze-cast regenerator, (2020) (submitted).
- [16] P. Govindappa, P.V. Trevizoli, O. Campbell, I. Niknia, T.V. Christiaanse, R. Teyber, S. Misra, M.A. Schwind, D. Van Asten, L. Zhang, A. Rowe, Experimental investigation of $\text{MnFeP}_{x1}\text{-As}_x$ multilayer active magnetic regenerators, *J. Phys. D: Appl. Phys.* 50 (31) (2017) 315001, <https://doi.org/10.1088/1361-6463/aa7a33>.
- [17] R. Bulatova, C. Bahl, K. Andersen, L.T. Kuhn, N. Pryds, Functionally graded ceramics fabricated with side-by-side tape casting for use in magnetic refrigeration, *Int. J. Appl. Ceram. Technol.* 12 (4) (2015) 891–898, <https://doi.org/10.1111/ijac.12298>.
- [18] C.D. Christiansen, K.K. Nielsen, R. Bjørk, Novel freeze-casting device with high precision thermoelectric temperature control for dynamic freezing rates, (2020) (submitted).
- [19] P. Jørgensen, S. Ebbenhøj, A. Hauch, Triple phase boundary specific pathway analysis for quantitative characterization of solid oxide cell electrode microstructure, *J. Power Sources* 279 (2015) 686–693, <https://doi.org/10.1016/j.jpowsour.2015.01.054>.
- [20] S. De Angelis, P. Jørgensen, E. Tsai, M. Holler, K. Kreka, J. Bowen, Three dimensional characterization of nickel coarsening in solid oxide cells via ex-situ ptychographic nano-tomography, *J. Power Sources* 383 (2018) 72–79, <https://doi.org/10.1016/j.jpowsour.2018.02.031>.
- [21] S. Deville, E. Maire, A. Lasalle, A. Bogner, C. Gauthier, J. Leloup, C. Guizard, In situ X-ray radiography and tomography observations of the solidification of aqueous alumina particles suspensions. Part II: Steady state, *J. Am. Ceram. Soc.* 92 (11) (2009) 2497–2503, <https://doi.org/10.1111/j.1551-2916.2009.03264.x>.
- [22] A. Bareggi, E. Maire, A. Lasalle, S. Deville, Dynamics of the freezing front during the solidification of a colloidal alumina aqueous suspension: in situ X-ray radiography, tomography, and modeling, *J. Am. Ceram. Soc.* 94 (10) (2011) 3570–3578, <https://doi.org/10.1111/j.1551-2916.2011.04572.x>.
- [23] C.D. Christiansen, K.K. Nielsen, R. Bjørk, Freeze-casting to create directional micro-channels in regenerators for magnetic refrigeration, in: Proceedings of TherMag VIII, 8th IIF-IIR International Conference on Caloric Cooling, Darmstadt, Germany, 2018, pp. 96–101, , <https://doi.org/10.18462/iir.11072>.
- [24] M.M. Porter, R. Imperio, M. Wen, M.A. Meyers, J. McKittrick, Bioinspired scaffolds with varying pore architectures and mechanical properties, *Adv. Funct. Mater.* 24 (14) (2014) 1978–1987, <https://doi.org/10.1002/adfm.201302958>.

Characterization of freeze-cast micro-channel monoliths as active and passive regenerators

Jierong Liang, Cathrine D. Christiansen, Kurt Engelbrecht, Kaspar K. Nielsen, Rasmus Bjørk, Christian R.H. Bahl

Submitted for peer-review in: *Frontiers in Energy Research*

Processing and characterization of freeze-cast structures was carried out by me, while passive and active testing, model fit and data analysis was carried out by the first-author Jierong Liang. The work was carried out at Department of Energy Conversion and Storage, Technical University of Denmark during the Ph.D. period. I am co-author of the paper.

Characterization of Freeze-cast Micro-channel Monoliths as Active and Passive Regenerators

Jierong Liang*, Cathrine D. Christiansen, Kurt Engelbrecht, Kaspar K. Nielsen, Rasmus Bjørk, Christian R.H. Bahl

Department of Energy Conversion and Storage, Technical University of Denmark, 4000 Roskilde, Denmark

*E-mail address: jilia@dtu.dk

Abstract: The efficiency of the magnetic refrigeration process strongly depends on the heat transfer performance of the regenerator. As a potential way to improve the heat transfer performance of a regenerator, the design of sub-millimeter hydraulic diameter porous structures is realized by freeze-cast structures. Four freeze-cast regenerators with different pore widths are characterized experimentally and numerically. Empirical parameters are determined for the correlations of heat transfer and flow resistance via a 1D model. Thermal effectiveness and pressure drop are measured for thermal-hydraulic evaluations. Temperature span and specific cooling capacity are obtained to compare the magnetocaloric potential based on the material $\text{La}_{0.66}\text{Ca}_{0.27}\text{Sr}_{0.06}\text{Mn}_{1.05}\text{O}_3$. The stability of freeze-cast regenerators is validated by comparing the performance during, before and after oscillatory flow and periodic magnetic field tests. Smaller pore design obtain the better heat transfer performance and required mechanical strength, while pore design with significant dendrites provides the worst tradeoff between heat transfer performance and flow resistance.

Keywords: Magnetic refrigeration; Thermal regenerator; Freeze-casting; Lamellar microchannel; Thermal evaluation

Highlights:

- (1) First application of freeze-casting refrigerators in magnetic refrigeration.
- (2) Thermal-magneto-hydraulic evaluations on freeze-cast regenerators are conducted.
- (3) Stability in lamellar micro-channel structures are compared.
- (4) Small pore design obtain excellent heat transfer performance.

1. Introduction

Magnetic refrigeration represents an environmentally friendly cooling technology with the potential for cost-saving operation, by using a solid refrigerant and using a thermodynamic cycle that can be more efficient than vapor compression cooling. The temperature change of a magnetocaloric material (MCM) in response to a changing magnetic field can be analogue to the heating and the cooling of a gaseous medium in response to an adiabatic compression and expansion. The magneto-thermodynamic cycle named the active magnetic regenerator (AMR) cycle is commonly applied for prototypes in magnetic refrigeration [1], due to the limited values of isothermal entropy difference (ΔS_{iso}) and adiabatic temperature change (ΔT_{ad}) in existing MCMs. As a core component in the AMR cycle, the regenerator undergoes: 1) adiabatic magnetization; 2) isothermal flow from the cold to hot reservoir; 3) adiabatic demagnetization; and 4) reversed flow from the hot reservoir to the cold reservoir. AMRs, which perform as combined heat storage,

heat exchanger and thermal energy generator, are moving closer to a possible commercialization, as they can lift the temperature span many times the adiabatic temperature change of the MCM [1,2].

The MCM geometry is one of the critical factors that affects the AMR performance. The main reason is that a suitable porous structure of the MCM can effectively transfer the magnetic work to thermal energy at thermal reservoirs operating over a useful temperature span. Previous has focused on how the geometric parameters affect AMR performance. Lei et al. [3] simulated and analyzed the regenerator performance with packed sphere beds, parallel plates, micro channels and packed wire screen geometries. This aimed at finding the optimal operating parameters. Li et al. [4] tested and compared the performance of AMRs with gadolinium plates, spheres and flakes using a rotary magnetic refrigerator with the result that better cooling performance was obtained in the AMRs filled with flakes/spheres. Trevizoli [5] presented a systematic experimental evaluation of three AMRs with geometries of parallel-plate, pin array and packed sphere beds, based on approximately the same porosity and specific surface area; the AMR with packed spheres obtained the highest cooling capacity.

Packed bed regenerators are the most widely used geometry in AMRs due to their high cooling performance and easy fabrication. The reasons that other geometries such as parallel plates or mini-channels cannot easily replace the packed beds are: 1) thin walls are needed to facilitate heat conduction from the interior to the surface of MCM due to finite heat transfer [6]; 2) thin walls are difficult to fabricate due to insufficient mechanical strength in MCMs [7–9]; 3) high thermal performance requires small flow channel thickness, which can be difficult to manufacture consistently [10]. The porosity of the MCM should not be too high in order to ensure the mechanical strength and energy generation density of the regenerator. Consequently, thin wall geometry results in a small hydraulic diameter and thus high flow resistance.

Freeze-casting is an environmentally friendly materials processing route [11], which freezes a suspension of material particles and solvent (normally water). During the solidification process, ice dendrites grow and particles concentrate within the space between the ice dendrites, forming channels of nearly pure ice surrounded by particles. After the ice is removed by freeze drying, micro-channels remain. The freeze-casting technique is intrinsically flexible to tune the pore characteristics within a certain range [12–14]. From our tuning abilities at the Technical University of Denmark (DTU), the pore size can be tuned by changing suspension characteristics and solidification conditions [15–17]. Generally, each regenerator is most efficient over a specific domain of operating conditions, which depends itself on geometrical parameters. To achieve a more in-depth investigation of freeze-cast regenerators, this study focuses on identifying the proper pore size and the corresponding operating conditions. A freeze-cast regenerator identified as having small hydraulic diameter and which may be manufactured with thin walls, was preliminarily studied previously [18], with focus on the heat transfer potential of freeze-casting ceramics applied in a passive regenerator. From zero applied field test of a single sample, the main advantage of the freeze-cast regenerator is the excellent heat transfer performance due to the small hydraulic diameter and large specific surface area. However, the flow resistance is larger than in packed bed regenerators. Thus, more samples with different morphologies are valuable to further assess the potential of freeze-cast regenerators.

No experimental or modeling data about freeze-casted structures as AMRs in a time-varying magnetic field has previously been published. Active characterization using a linear AMR test machine [19] is a small-scale and simplified way to study the performance of freeze-cast regenerators with different geometry parameters. Temperature span and cooling capacity are the most common performance indicators in active characterizations [20]. In the active mode, the performance is strongly related to the magnetocaloric effect (MCE) of the material, operating conditions (utilization and frequency), and intrinsic geometry parameters (porosity, specific surface area and pore size) [21]. The MCM in the freeze-cast regenerator studied in this

work is $\text{La}_{0.66}\text{Ca}_{0.27}\text{Sr}_{0.06}\text{Mn}_{1.05}\text{O}_3$ (LCSM06), which is identified as one of the magnetocaloric ceramics ($\text{La}_{0.66}\text{Ca}_{0.33-x}\text{Sr}_x\text{Mn}_{1.05}\text{O}_3$, LCSMx [22]) with a second order phase transition (SOPT). LCSMx ceramics are attractive alternatives to the benchmark material gadolinium (Gd) due to similar specific isothermal entropy difference (ΔS_{iso}) during (de)magnetization [23], adjustable transition temperature, corrosion resistant and less expensive compounds. Bahl et al. [24] experimentally extrapolated the maximum zero-span cooling capacity, which is significantly larger than the highest measured value for Gd plates in the similar tests. For the purposes of easy fabrication and mechanical stability, LCSMx is one of the best choices to freeze-cast the first generation regenerator. Comparing the AMR performance of different freeze-cast regenerators based on the same MCM, is valuable to study the geometry effect on the conversion ability from magnetic work to thermal energy.

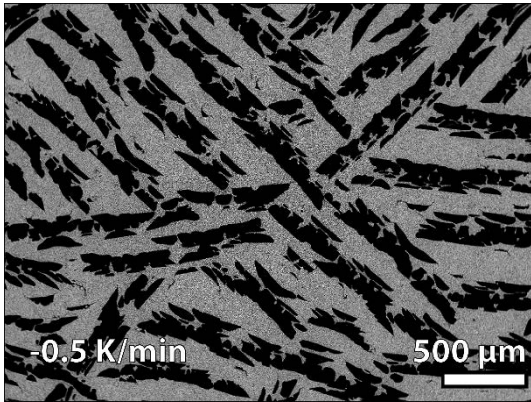
In this paper, four freeze-cast regenerators are tested passively without magnetic field to investigate the heat transfer and flow resistance characteristics. Combined with the modelling and fitting to the experimental data, correlations of Nusselt number and friction factor are determined. In the second step, active experiments of the same regenerators on a linear magnetocaloric test machine are carried out in order to evaluate the AMR performance. Finally, some of the passive and active experiments are repeated in order to validate the reproducibility and stability of the freeze-cast regenerators.

2. Regenerator preparation and geometric characterization

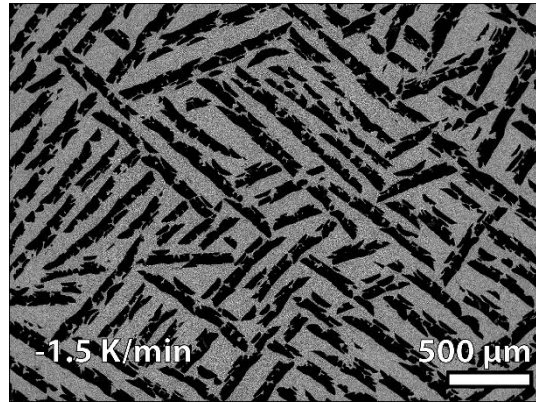
Three regenerators (#1, #2 and #3, Fig.1) were fabricated by freeze-casting under similar conditions to our previous study on freeze-cast regenerators (regenerator #4) [18]. A ceramic suspension for freeze-casting was prepared from 30 vol% of LCSM06 (CerPoTech, Norway) in MiliQ water with 2.5 wt%, solid to ceramic ratio, of dispersant (DURAMAX™ D-3005, Rohm and Haas, Dow Chemical, USA). PH was adjusted to ~7 by addition of 1M nitric acid in order to establish a sufficient dispersion of particles. The suspension was then homogenized for 72 hours on a low energy ball mill. 2 wt%, solid to ceramic ratio, of binder (DURAMAX™ B-1022, Rohm and Haas, Dow Chemical, USA), was added and the suspension was mixed for a few hours. The suspension was de-aired in vacuum immediately before casting. During freeze-casting, the suspension of LCSM06 particles in water was frozen directionally by bringing one side of the suspension into contact with a cooling source. Here, we utilized a custom-built freeze-casting set-up with thermoelectric temperature control of the cooling source [17]. The temperature of the cooling source is decreased by -0.5, -1.5 and -2.5 K/min (regenerators #1 to #3 respectively) and the arising thermal gradient causes ice crystals to grow along the gradient direction, pushing aside particles, causing these to segregate, which results in a two phase structure of ice crystals along the thermal gradient and segregated ceramic particles. The ice was removed by sublimation in a freeze-drier and the green bodies were sintered at 1100 °C for 12 hours, resulting in porous ceramic structures with well-defined microchannels where the ice used to be. The size of the ice crystals during freeze-casting, and thereby the size of the resulting micro-channels in the fired ceramic, depends on the freezing conditions; where faster cooling rates results in smaller channels [17]. Here, only the freezing rates were varied in order to achieve a range of pore widths enabling the study of the influence of pore width on AMR performance. The three new regenerators are compared with our previously published regenerator (#4), and all the geometrical parameters are summarized in Table.1. The structural features of the freeze-cast regenerators were characterized by image analysis of micrographs, as described in detail in previous studies [18]. Micrographs were obtained using a scanning electron microscope (TM3000, Hitachi High-Technologies). For each sample 12 micrographs, covering an area of 3310×2483 μm each, in the perpendicular cross section, obtained evenly distributed across the cross sections, were analyzed. Pore width, macro porosity, specific surface area and tortuosity were evaluated based on image analysis. The mean and standard deviation of all parameters are listed in Table.1. From the regenerators with small pore width to large pore width (Fig.1 (a) to (d)), the aspect ratio of cross sectional

pore shape increases. That means the freeze cast regenerators with the small pore width are prone to have narrow channels.

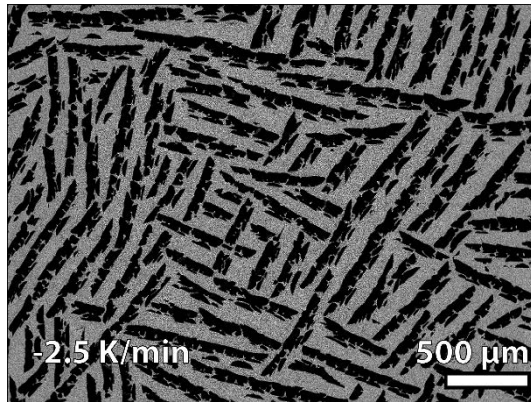
As freeze-casting is very sensitive to apparent conditions complicating the reproducibility of freeze-casts across different suspension batches, set-ups, furnace conditions etc. [25], regenerators #1-3 were fabricated from the same batch, frozen subsequently and dried and sintered together. Accordingly, regenerator #1-3 exhibits a larger degree of dendrites obstructing the channels than regenerator #4, which was fabricated from a different batch and with much smoother channel walls. Therefore, the measured mean pore width of regenerator #4 in Table.1 is greater than that of #3 in spite of the earlier argument stating that faster freezing results in smaller channels.



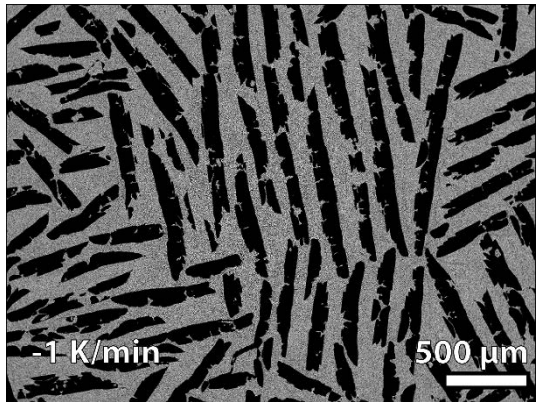
(a)



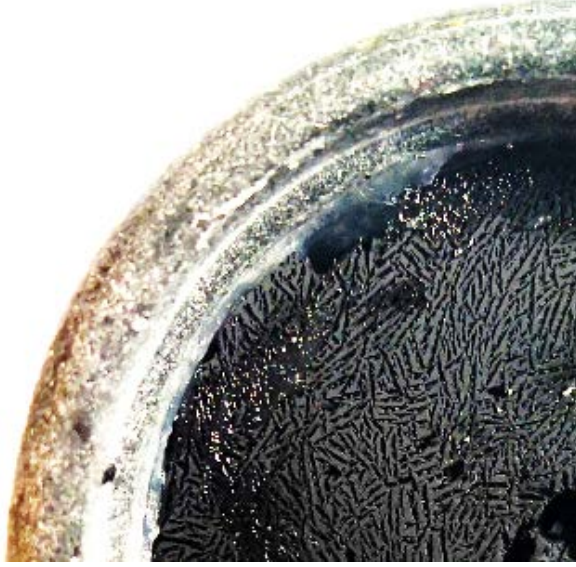
(b)



(c)



(d)



(e)



(f)

Fig.1 Geometry of freeze-cast regenerators. Scanning electron microscopy (SEM) micrographs of cross sections of the freeze-cast samples from regenerators #1 (a), #2 (b), #3 (c) and #4 (d), where grey areas are the ceramic walls and black areas voids in the form of aligned, lamellar channels. Micrographs were obtained at cross sections parallel to the freezing direction in the center of the structure. Photographs of regenerator #1 (e-f) after mounting the samples into the housing. A single freeze-cast regenerator matrix consists of two combined monolithic pieces of freeze-cast samples frozen at identical conditions and thus with homogenous structural characteristics.

Table 1: Geometrical parameters of the freeze-cast regenerators. Structural characteristics are from image analysis of scanning electron micrographs. The corresponding measurements for each regenerator are based on the analysis of 15 images evenly distributed along the axial direction and are given as an average. A single freeze-cast regenerator matrix is composed of two combined monolithic pieces of freeze-cast sample frozen at identical conditions and thus with homogenous structural characteristics.

Parameters	Regenerator #1	Regenerator #2	Regenerator #3	Regenerator #4
Shape ($\text{ØD} \times \text{L}$, mm \times mm)	$\text{Ø}30 \times 30$	$\text{Ø}30 \times 30$	$\text{Ø}30 \times 30$	$\text{Ø}30 \times 27$
Pore width (μm)	66.3 ± 4.6	49.6 ± 4.6	43.1 ± 5.1	71.6 ± 6.4
Total porosity	0.73	0.72	0.73	0.72
Macro porosity	0.415 ± 0.006	0.420 ± 0.006	0.441 ± 0.005	0.420 ± 0.008
Hydraulic diameter (μm)	94.9 ± 7.8	75.0 ± 6.9	66.3 ± 8.3	104 ± 7.6
Specific surface area (m^{-1})	$(1.75 \pm 0.11) \times 10^4$	$(2.24 \pm 0.16) \times 10^4$	$(2.66 \pm 0.27) \times 10^4$	$(1.61 \pm 0.08) \times 10^4$
Tortuosity	1.75 ± 0.14	1.75 ± 0.31	1.62 ± 0.40	1.61 ± 0.3
Mass (g)	29.85	29.33	30.04	27.23

In porous media, the pores can be interconnected, dead end or isolated [26]. The total void volume divided by the total volume occupied by the solid matrix and void volumes, is defined as the total porosity, or sample porosity (ϵ) in this study. However the fluid only flows through the interconnected pores. The volume fraction of the interconnected pores is defined as the effective porosity or macro porosity (ϵ_m), which is derived from image analysis. As seen from Table 1, the macro porosity is about 2/3 of the total porosity. Thus, the dead end pores are assumed negligible. The remaining porosity can be treated as micro porosity in the walls. In this study, ϵ_m is used for determining pore velocity while ϵ is adopted for solid mass calculations. Additionally, the hydraulic diameter (D_h) and tortuosity (\mathcal{L}) are derived as follows:

$$D_h = 4\epsilon_m/\alpha \quad (1)$$

$$\mathfrak{L} = L_{pore} / L_r \quad (2)$$

where α is the specific surface area derived from image analysis, L_{pore} is the average pore length, and L_r is the length of the regenerator sample.

3. Experiment and modelling

The experimental investigation was performed both on a passive rig [27] and active magnetocaloric test machine [28] at DTU. The device configurations are discussed elsewhere [29], but the overall experiment program and the simplified diagram of the test device with the key measurements are given in Fig.2. The hydraulic flow profile in the passive rig and the synchronization of flow profile and magnetic field in the active machine are shown in Fig. 3.

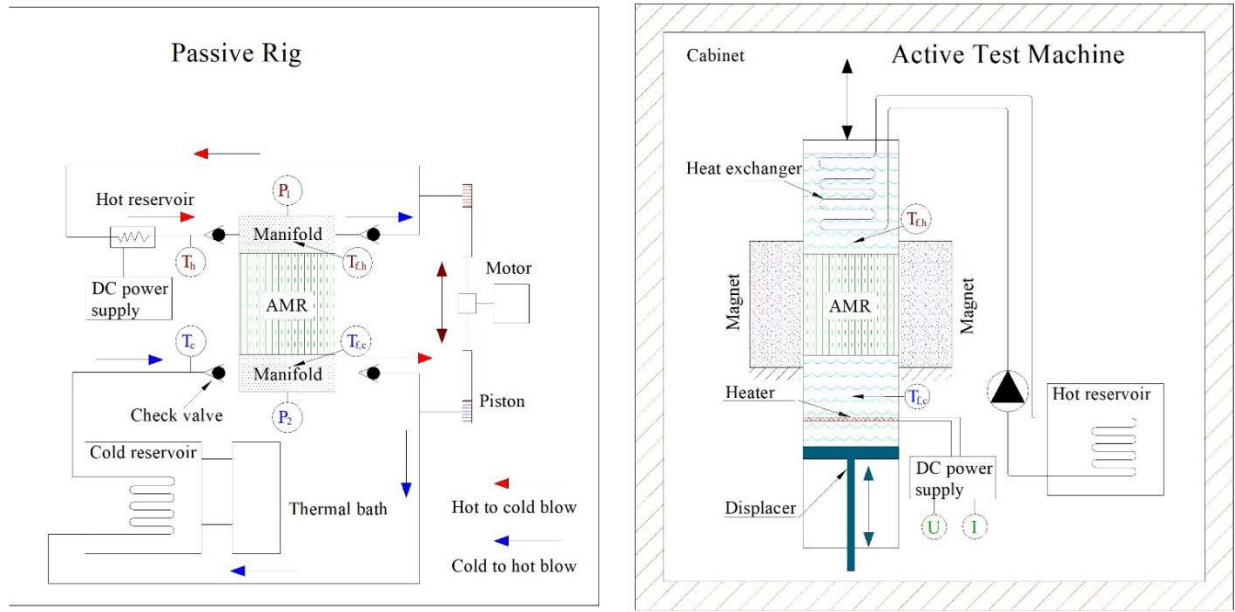
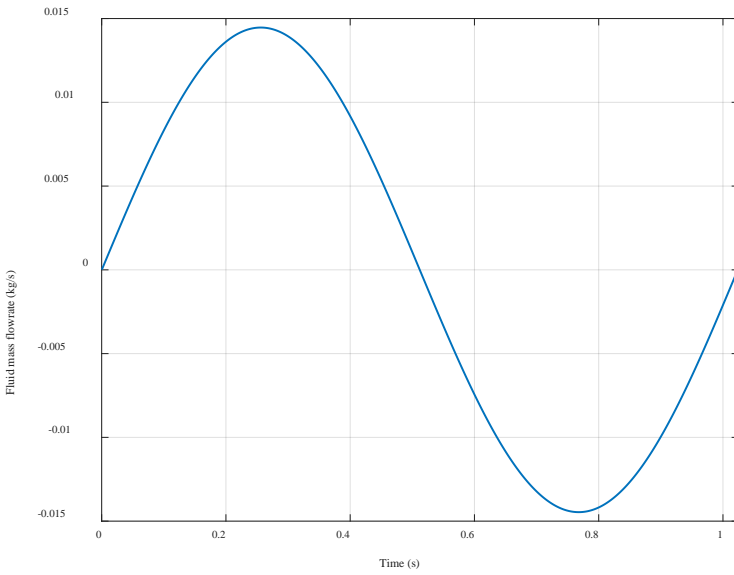
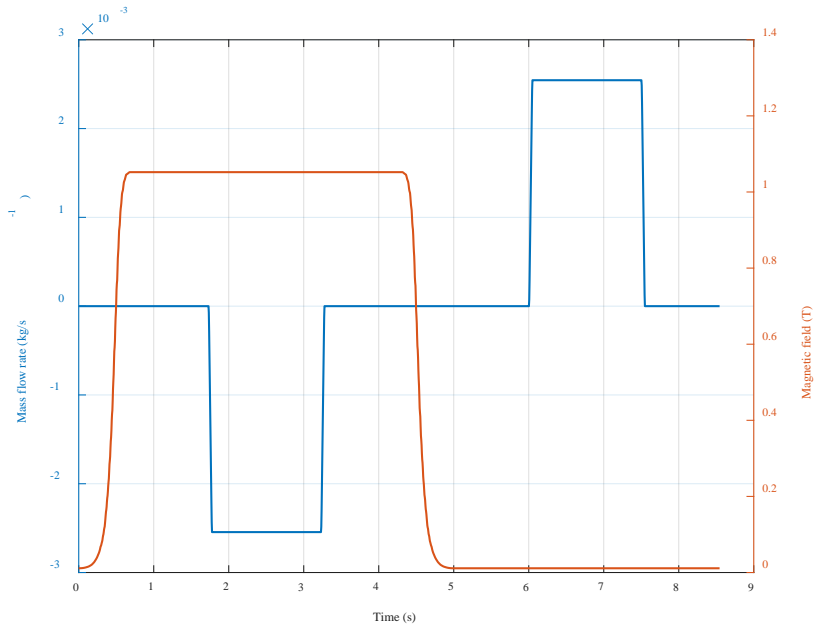


Fig.2 Schematic diagram of passive rig and AMR test machine. The passive rig consists of the regenerator, manifolds, cold and hot reservoirs, piston and motor assembly, and check valves. The manifolds are situated at the ends of the regenerator, which incorporates the type E thermocouples (Omega) and pressure transducers (Gems). The thermocouples for measuring $T_{f,h}(t)$ or $T_{f,c}(t)$ are positioned at the center of the cross section between the regenerator and manifold. The outflow from the manifold goes through the outlet check valve, piston, cold reservoir or heater, inlet check valve, and then back to the inlet of the manifold. The test machine, which is situated in a temperature-controlled cabinet, consists of a stationary Halbach array permanent magnet, a movable regenerator, a piston for displacing fluid, and hot and cold reservoirs. The temperature of the hot reservoir is regulated by a heat exchanger interacting with the ambient in a cabinet. The heat load in the cold reservoir is simulated by a resistance heater. The whole experiment procedure goes through: 1) passive test with different operating parameters; 2) passive test with different manifolds; 3) repetition of passive experiments; 4) active test; and 5) repetition of passive experiments.



(a)



(b)

Fig.3 Time evolution of (a) the fluid mass flow rate in passive rig and (b) the synchronized magnetic field and fluid mass flow rate in active test machine during the different steps of over one magnetic cycle. Since the passive rig and AMR test machine run at different frequencies, the amplitudes of fluid mass flow rate are significantly different between passive and active characterizations.

3.1. Passive characterization

Since the passive rig is essentially a synchronized AMR device with zero magnetic field, a comparative study of freeze-cast regenerators in terms of heat transfer performance and flow resistance can be addressed

here. In the passive rig, the regenerator is subjected to an oscillatory flow in steady state with constant reservoir temperatures. The regenerator is treated as a thermal storage heat exchanger subjected to intermittent alternating heat transfer facilitates between the solid matrix and the fluid in two periods: 1) hot blow: fluid from the high-temperature reservoir warms up the solid matrix; 2) cold blow: reversing the fluid flow and the matrix releases the stored heat. The information from temperature and pressure measurements is further processed to obtain the thermodynamic indicators. The predefined operating parameters consist of motor frequency (f), piston stroke (S_p) and piston cross sectional area ($A_{c,p}$). Thermo-hydraulic parameters such as utilization (U) and Reynolds number (Re_h) link to the operating conditions through:

$$U = \frac{\int_0^{\tau/2} \dot{m}_f c_f dt}{m_s c_s} = \frac{A_{c,p} S_p \rho_f c_f}{m_s c_s} \quad (3)$$

$$Re_h = \frac{\rho_f (v_f / \varepsilon_m) D_h}{\mu_f} \quad (4)$$

$$v_f = v_p (A_{c,p} / A_{c,r}) = \pi f S_p \sin(2\pi f t) (A_{c,p} / A_{c,r}) \quad (5)$$

Where ρ_f , c_f and μ_f are the density, specific heat capacity and dynamic viscosity of the fluid, respectively. The subscripts f and s denote solid and fluid phases respectively. Note that the solid specific heat capacity c_s is strongly temperature dependent with a peak near the transition temperature. Here we use the background value rather than the peak value. The Reynolds number based on the pore velocity and hydraulic diameter Re_h is selected to be consistent with the previous form of the correlations. $A_{c,p}$ and $A_{c,r}$ are the cross sectional areas of the piston and the regenerator respectively. v_f is the superficial velocity in the regenerator, which is a hypothetical flow velocity disregarding the skeleton of the porous medium. v_p is the moving velocity of the piston, its sinusoidal profile is determined by the crank motion in the passive rig.

The measurements for performance metrics are end pressure profiles ($p_1(t)$ and $p_2(t)$), end temperature profiles ($T_{f,h}(t)$ and $T_{f,c}(t)$) and reservoir temperatures (T_h and T_c). The heat transfer performance and flow resistance can be characterized by the Nusselt number (Nu), number of transfer unit (NTU), effectiveness (η_h and η_c) and friction factor [30] (f_{osc}).

$$Nu = \frac{h D_h}{k_f} \quad (6)$$

$$NTU = \frac{h \alpha V_r}{2/\tau \int_0^{\tau/2} \dot{m}_f c_f dt} \approx \frac{h \alpha V_r}{f A_{c,p} S_p \rho_f c_f} \quad (7)$$

$$\eta_h = \frac{\int_0^{\tau/2} \dot{m}_f c_f T_{f,h} dt - \int_0^{\tau/2} \dot{m}_f c_f T_{f,c} dt}{\int_0^{\tau/2} \dot{m}_f c_f (T_h - T_c) dt} \approx \frac{T_h - 2/\tau \int_0^{\tau/2} T_{f,c} dt}{T_h - T_c} \quad (8)$$

$$\eta_c = \frac{\int_{\tau/2}^{\tau} \dot{m}_f c_f T_{f,h} dt - \int_{\tau/2}^{\tau} \dot{m}_f c_f T_{f,c} dt}{\int_{\tau/2}^{\tau} \dot{m}_f c_f (T_h - T_c) dt} \approx \frac{2/\tau \int_{\tau/2}^{\tau} T_{f,h} dt - T_c}{T_h - T_c} \quad (9)$$

$$f_{osc} = \frac{\Delta p_{max}}{L_r} \frac{D_h}{2 \rho_f (v_{f,max})^2} = \frac{D_h \Delta p_{max}}{2 L_r \rho_f [\pi f S_p (A_{c,p} / A_{c,r})]^2} \quad (10)$$

Here h is the interstitial solid-fluid heat transfer, which is derived from modelling and fitting. The terms k_f , α , V_r and L_r are fluid thermal conductivity, specific surface area, volume and length of regenerator, respectively. In the NTU approximation (Eq. (7)), constant fluid properties are assumed due to the weak temperature dependence on density and specific heat capacity in pure water. η_h and η_c are effectivenesses

associated to hot blow and cold blow. The approximations in Eq. (8) and Eq. (9) eliminate the effect of possible mismatching phases of $T_{f,h}$, $T_{f,c}$ and \dot{m}_f during the measurements. The parameter f_{osc} is the oscillatory friction factor based on the maximum pressure drop consistent with the correlations.

Through the passive experiments, Nu and f_{osc} have been correlated through model fitting based on a single regenerator previously reported [18]. The parameters in the correlations are further validated by variable geometrical parameters, such as the pore size. The correlations in Nu and f_{osc} are taken from our previous study based on the regenerator #4.

$$f_{osc} = c_1 Re_h^{-1} + c_2 \quad (11)$$

$$Nu = c_3 [L_r / (D_h Re_h Pr)]^{c_4} \quad (12)$$

Where $c_1 \sim c_4$ are fitting parameters assumed to depend on matrix morphology only; Pr is the Prandtl number.

3.2. Active characterization

The AMR test machine is a small-scale reciprocating system (Fig.2), which consists of a fixed Halbach cylinder permanent magnet and a reciprocating regenerator. The apparatus performs a four-step AMR cycle; the applied magnetic field is changed periodically from approximately 0 to 1.1 T. Oscillatory fluid blows are generated by the piston synchronizing with the magnetic field changing. The period for each of the four steps cycle are controlled by the stepper motors, and marked ($\tau_1 \sim \tau_4$) in Fig.3 (a). Thus, the frequency in the AMR test machine is determined by:

$$f = 1/\tau = 1/(\tau_1 + \tau_2 + \tau_3 + \tau_4) \quad (13)$$

Where τ and $\tau_1 \sim \tau_4$ are the whole cycle period and the each step period, respectively. During the blow periods (τ_2 and τ_4), the flow profile is divided into parts taken up by flow pauses, flow ramps and full flow, all together add up to one for a complete cycle.

An electric heater works as a cooling load simulator at the cold end, of which power is determined by the product of voltage and current. The specific cooling capacity is defined as

$$\dot{q}_c = \frac{UI}{\dot{m}_s} \quad (14)$$

Where U and I are voltage and current respectively. As a compact design to reduce the dead volume effect [31], the thermocouples located at the hot end ($T_{f,h}(t)$) and cold end ($T_{f,c}(t)$), which are shown in Fig.2, are only used for reservoir temperature estimations.

$$T_h = \int_0^\tau T_{f,h}(t) dt \quad (15)$$

$$T_c = \int_0^\tau T_{f,c}(t) dt \quad (16)$$

$$\Delta T = T_h - T_c \quad (17)$$

Where ΔT is the temperature span. The whole apparatus is installed in a thermostatically controlled cabinet. The temperature T_h is controlled by adjusting the cabinet temperature due to heat interaction between the cabinet and heat exchanger. The temperature equilibrium between the hot reservoir and ambient is determined in part by heat leakage to the cabinet, which are minimized in the experimental setup. Although the system still must accept a small heat leak that deteriorates the performance, it is also a realistic operating condition for a real magnetic refrigeration application [32]. The temperature evolution speed is

observed to decrease with time as the system stabilizes. The cyclic steady state point is treated as a cutoff criterion for evaluating the performance [33], including Eq. (14-17). In the community of magnetic refrigeration, curves of cooling capacity (\dot{Q}_c) versus temperature span (ΔT) are usually defined as the cooling curves [34]. In general, the slope of the cooling curves is steeper in higher utilization conditions [4,35]. At the end-points of cooling curve are zero-span cooling capacity and no-load temperature span, which are essential metrics in AMR devices [36].

4. Results and discussions

Freeze-cast regenerators #1, #2 and #3 are compared experimentally in order to investigate the flow resistance, heat transfer performance, cooling capacity, regenerative temperature lift and mechanical stability. Relevant data regarding regenerator #4 may be found in our previous study [18].

4.1. Modelling correlations and validation

The fitting parameters in Eq. (11) and Eq. (12) determined for each regenerator are shown in Table. 2. The values of c_1 and c_2 are varied by different pore sizes, especially in regenerator #3 (the smallest pore size). The values of c_3 and c_4 are treated as constants because of negligible changes during the fitting program.

Table 2: The values of the correlation parameters by fitting program, c_3 and c_4 of regenerators #1 to #3 are treated as the same as the values in regenerator #4, because the deviations between the modelling and experiments are small.

Parameters	Regenerator#1	Regenerator #2	Regenerator #3	Regenerator #4
c_1	524.1	304.2	489.1	357.5
c_2	1×10^{-8}	1×10^{-6}	1×10^{-8}	1×10^{-8}
c_3	0.34	0.34	0.34	0.34
c_4	-0.32	-0.32	-0.32	-0.32

The deviations between experiment and the fit in $T_{f,h}(t)$, $T_{f,c}(t)$ and pressure drop are evaluated by the relative root mean square error (RRMSE) under all tested operating conditions and regenerators #1, and #2 and #3 in Fig.4. Comparing the fit and experimental data, the maximum temperature deviation is 1.18% and 3.6% for pressure drop, which indicates that the simulation results are in good agreement with the experimental readings and thus that the parameters in Table.2 can be used to model the internal characteristics of the freeze-cast regenerators.

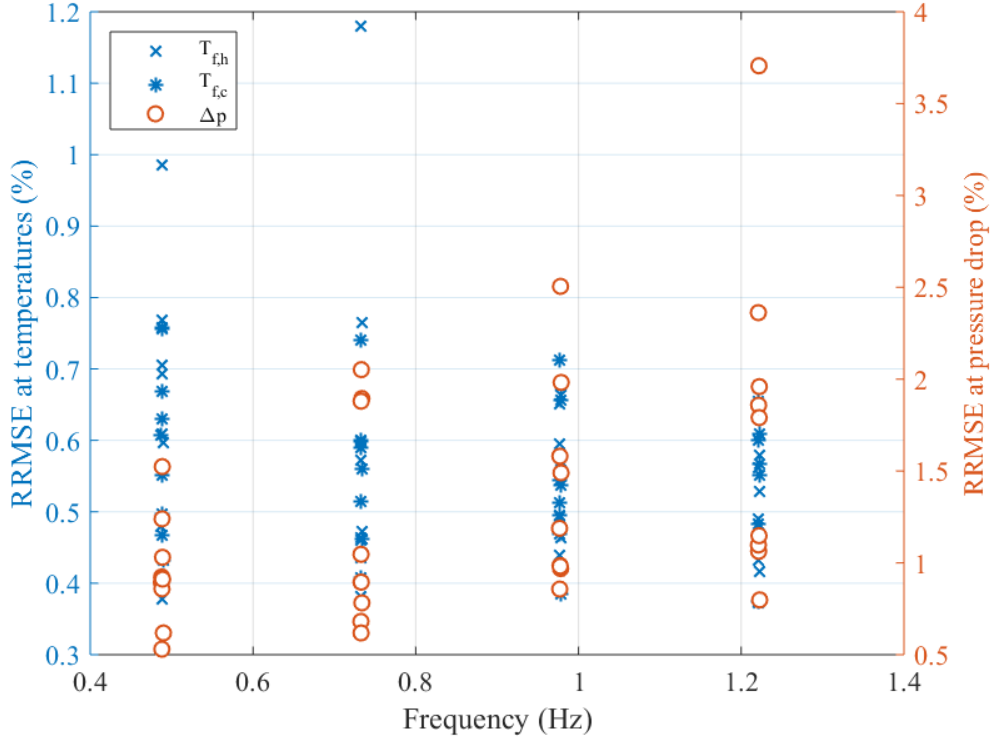


Fig. 4 Experimental and fit comparisons of relationships of RMSE distributions for regenerators #1, #2 and #3.

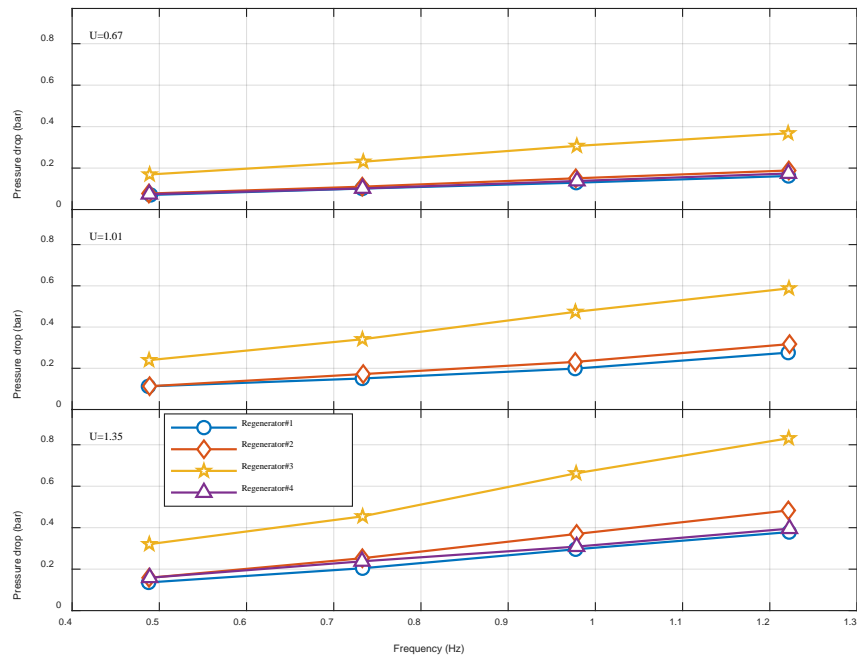
4.2. Passive performance analysis

Pressure drop is the major characteristic of the flow resistance in a regenerator. The pressure drop generally depends on pore velocity, regenerator length, hydraulic diameter, channel tortuosity and channel wall roughness. Since the tested regenerators are designed with the same length, tortuosity, macro porosity, total porosity and surface roughness, the curves of $\Delta p_{\max} \sim f$ in Fig.5 (a) are essentially the relations of the pressure drop and the pore velocity. As found in literature [27], the frequency and therefore the velocity responds quite linearly to the pressure gradient, which suggests that Darcy's law is valid for these regenerators. These phenomena are widely captured for small amplitude oscillating flows [37,38]. The oscillatory flow pressure loss increases both with increasing dimensionless oscillation amplitude ($\propto 1/D_h$) and kinetic Reynolds number [39]. Consequently, a smaller hydraulic diameter results in a higher pressure drop, based on the same flow conditions and other geometry parameters. The pressure drops in regenerators #1, #2 and #4 are similar. Around 100% higher pressure drop is observed in regenerator #3 than in other regenerators. This is probably attributed to high viscous resistance in low Re and some possibilities of blocked channels existing.

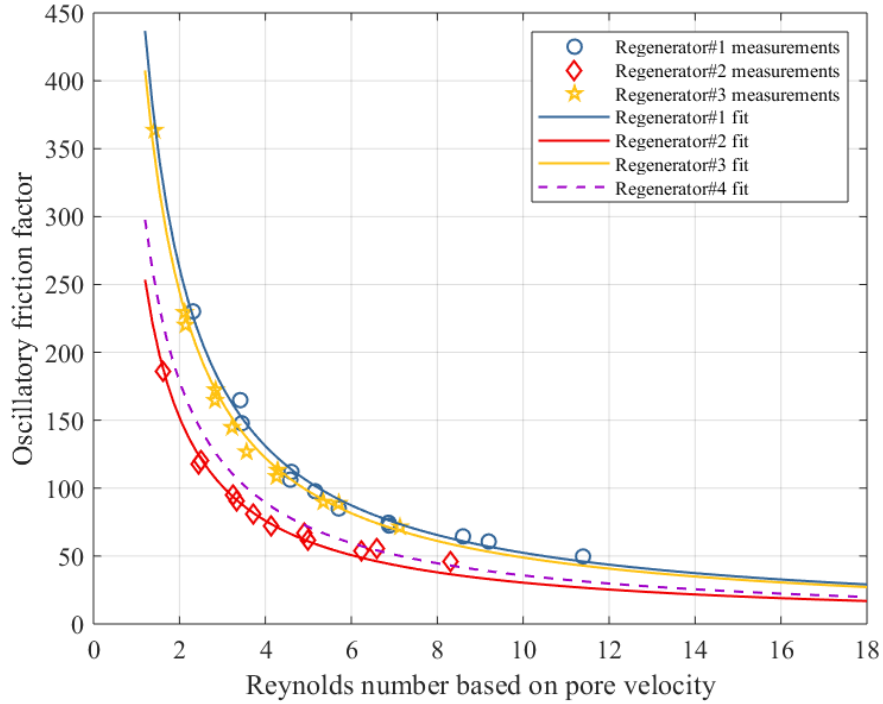
The dimensionless relationships of $f_{osc} \sim Re_h$ are shown in Fig. 5 (b). Because the variations in hydraulic diameter between the regenerators, the f_{osc} in regenerators #1 and #3 are close to each other, while the f_{osc} in regenerator #2 is lower. The friction factor in the pores for periodic steady flows can be generally defined as follows [39–41].

$$f_{osc} = \underbrace{\frac{2D_r^2}{c_1}}_{K} Re_h^{-1} + \underbrace{\frac{2D_r F}{\sqrt{K}}}_{c_2} \quad (18)$$

Where D_r is the inner diameter of the regenerator. K is the permeability of the porous media, which links to the pore structure as $K \propto (c, \varepsilon, \langle r \rangle)^2$ [42]. The geometric factor c is related to the shape, connectivity, aspect ratio and tortuosity of the pores. Average pore radius $\langle r \rangle$ indicates the pore width. F is the inertial coefficient, which is normally important when the flow velocity is high. Consequently, parameters c_1 and c_2 indicate the viscous and inertial forces, respectively. For low velocity the viscous term dominates, whereas for high velocity the inertia term does. Since the Re_h is quite low (<15), the corresponding low value of c_2 represents the weak inertial behavior in freeze-cast regenerators. Intrinsically the friction factor is mainly determined by the permeability. According to Fig.1, when the pore width decreases, the cross sectional shape of pores becomes narrow; the permeability might be reduced. However in regenerator #3 with large pore size, dendrites are obvious inside the pores; which also results in low permeability. Thus, the regenerator #2 might have the highest permeability among these three regenerators and therefore the lowest friction factor.



(a)



(b)

Fig. 5 (a) Pressure drop amplitude as a function of frequency and (b) oscillatory friction factor as a function of pore Reynolds number under different utilizations. All the regenerators are measured based on the same manifold and hydraulic system in the passive rig. All the regenerators have nearly the same sample porosity, macro porosity and shape. Note that there is ~10% reduction of the length of regenerator #4 due to practical reasons. The data for regenerator #4 are derived from Ref. [18].

Effectiveness is an index for heat storage evaluation. It depends on operating conditions (i.e. utilization and frequency), solid thermal conductivity and interstitial heat transfer performance. The $\eta_h \sim NTU$ curves based on each utilization in Fig. 6 reveal the comparison of interstitial heat transfer between different freeze-cast regenerators. In principal, the trends of $\eta_h \sim NTU$ for freeze-cast regenerators should be a positive correlation. As discussed previously [18], thermal losses and equipment problems may cause negative correlations at some points (see Fig. 6). Regenerator #3 exhibited the highest average effectiveness over NTU. This is probably attributed to the larger specific surface area shown in Table.1, and the higher interstitial heat transfer coefficient. Since the Nu correlations are the same among these freeze-cast regenerators (Table.2), smaller hydraulic diameter design results in higher heat transfer coefficient in Eq. (5). For each utilization in regenerators #1 to #3, the average η_h and the hydraulic diameter of regenerator are also in positive correlation. Smaller pore width or hydraulic diameter will cause higher heat transfer performance based on the same operating condition and geometry parameters. Regenerator #4 has estimated 10% MCM loss due to necessary modification to mount the regenerator in the housing. Thus, the effectiveness in regenerator #4 is the lowest as the local utilization is higher than for the others.

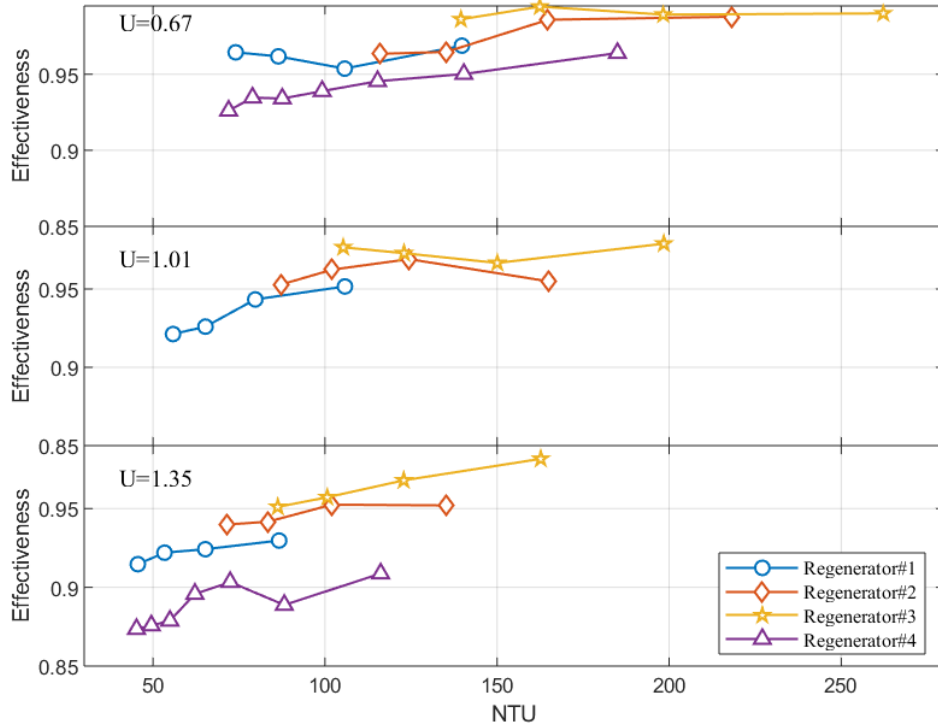


Fig. 6 Effectiveness as a function of NTU for different utilizations. The effectiveness is based on hot to cold blow. Since there is $\sim 10\%$ reduction in length in regenerator #4, the actual utilization in regenerator #4 is higher than others at the same subplot. The data at regenerator #4 are from our previous publication [18].

To couple the heat transfer and flow resistance characteristics, the UA (heat transfer coefficient times heat transfer surface area) versus pressure drop are plotted in Fig. 7. UA increases with the pressure drop with a sub-linear trend. The improvement of UA caused by increasing pressure drop decreases when the value of UA is sufficiently large. Regenerator #1 exhibits the lowest values of heat transfer performance for a given pressure drop compared to other freeze-cast regenerators. The main reasons are probably the details of the channel shape such as significant dendrites (Fig. 1 (a)) and larger friction factor (Fig. 4 (a)).

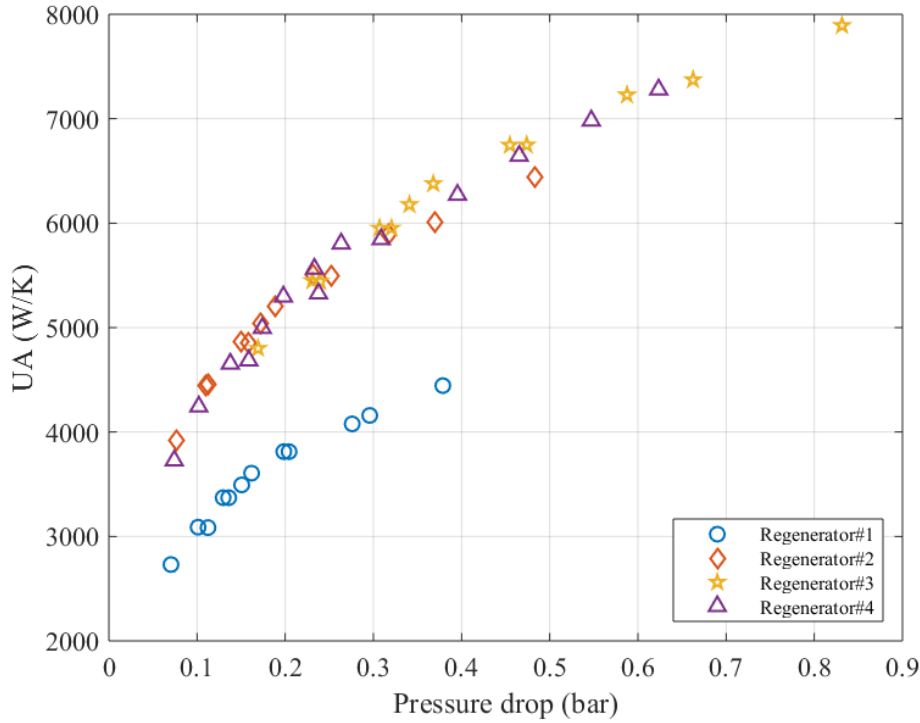


Fig.7 UA versus pressure drop among regenerators #1, #2, #3 and #4.

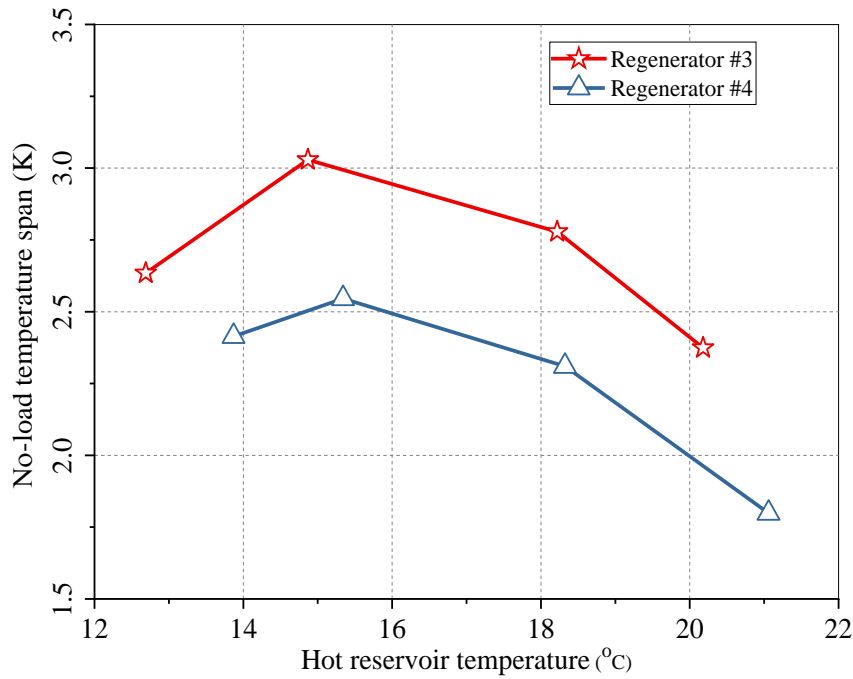
4.3. Active cooling performance comparison

Due to reasons described in Section 4.4, only regenerators #3 and #4 were tested successfully in the active test machine. Since the mass of each regenerator is small ($\sim 30\text{g}$), the absolute values of the temperature span are small in comparison to other results from the same AMR device [24,43]. However, the results shown in Fig. 8 are valid for comparable studies of the regenerators discussed here. Compared to relevant measures in Ref. [28,29,44] with first order phase transition (FOPT) materials, the no-load temperature span (ΔT_0) in Fig. 8 (a) is not so sensitive to the hot reservoir temperature due to the weaker temperature dependency of LCSM06 properties. MCMs always show the largest performance around their transition temperature. The maximum ΔT_0 for both regenerators #3 and #4 are located at $T_h = 15^\circ\text{C}$. This reveals that the actual transition temperatures of LCSM06 in the freeze-cast regenerators are around 15°C . As regards the absolute value of ΔT_{ad} , LCSMx cannot compete with Gd. Engelbrecht et al. [45] tested tape cast LCSMx plate regenerators, and obtained a maximum temperature span of 5.1°C , which was lower than the maximum temperature span in Gd. This was caused by higher specific heat capacity in LCSMx and therefore lower adiabatic temperature change (ΔT_{ad}).

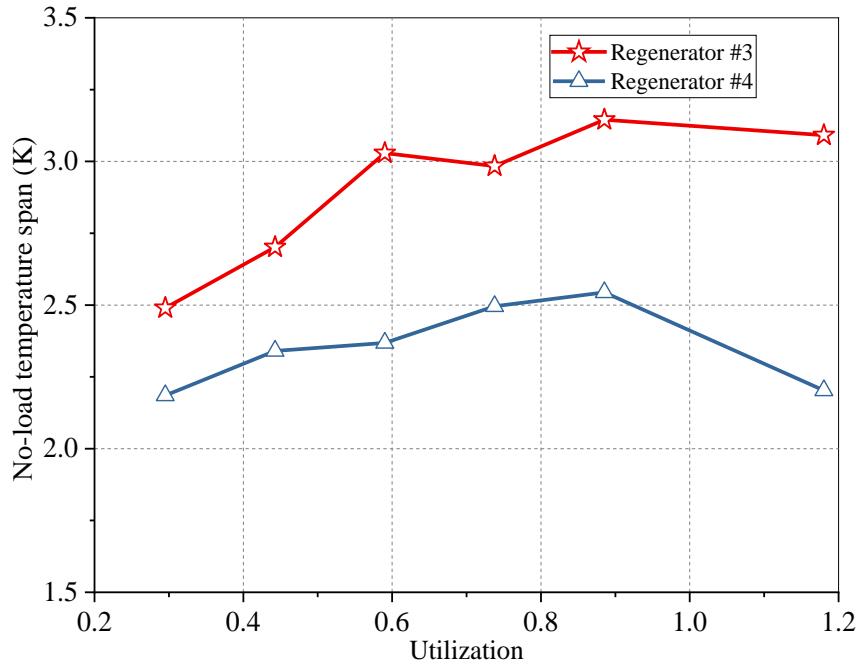
Curves of $\Delta T_0 \sim U$ presented in Fig. 8 (b) indicate the optimal utilizations are ~ 0.88 for both regenerators under no-load operations. In the active test machine, heat transfer to the ambient through the housing and piston are unavoidable. Since the amount of cooling capacity is small in freeze-cast regenerators, heat losses/gains are critical in the experiments. The optimum utilization is a balance between enough fluid being blown to maintain a high cooling capacity for covering the heat gain from the ambient, but at the same time little enough not to destroy the temperature span [46]. Since cooling capacity in freeze-cast regenerators is rather weak, the proportion of the ambient heat gain made by cooling capacity is large. Thus, the optimum utilization here is larger than common values reported in literature [20]. The temperature span

measured is between 2.5 and 3.2 K due to too small MCM mass compared to the inherent losses in the machine. Furthermore, the ΔT_0 is higher in regenerator # 3 than in regenerator #4, because of better heat transfer performance in regenerator #3.

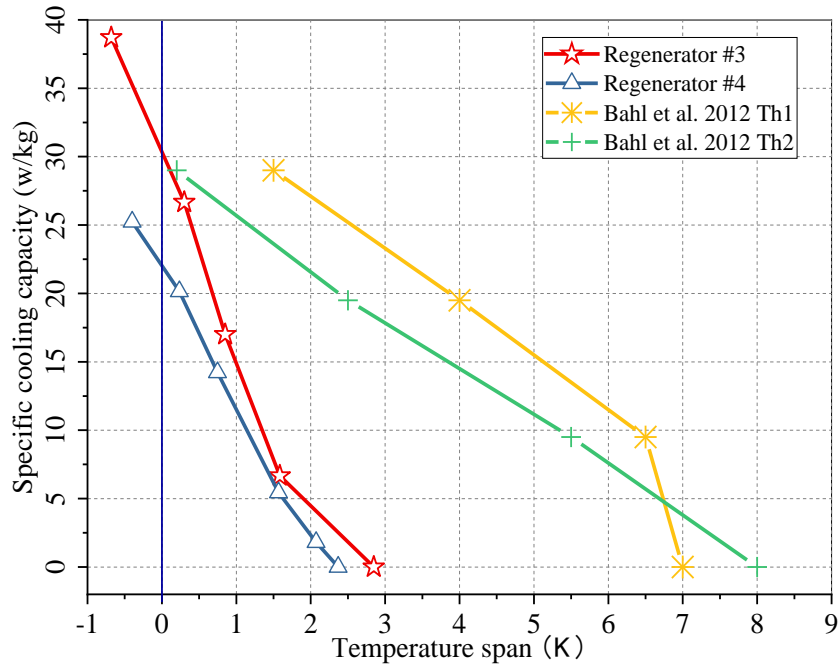
The cooling curves of specific cooling capacity (\dot{q}_c , Eq. (11)) versus ΔT are shown in Fig. 8 (c). The cooling curves are commonly reported as a linear approximation when spatial variations in the MCMs are negligible [35]. The cooling curves in regenerators #3 and #4 are inversely proportional. Since the performance metric \dot{q}_c considers the effect of MCM mass, the outperformance of cooling curves in regenerator #3 can be attributed to the excellent heat transfer performance contributions. Two cooling curves from Bahl et al. 2012 [24] are introduced in Fig. 8 (c), which are based on a graded two-layer regenerator, with two different LCSMx materials, in the form of stacked parallel plates. The MCM properties between the freeze-cast regenerators and the parallel plate regenerator are almost the same, except the different Curie temperatures. Since these regenerators are tested at the same machine but cannot maintain the same thermal isolations, the comparisons are only to validate the active experiments rather than performance analysis. The MCM mass of regenerators in Bahl et al. 2012 [24] is 51.1 g, comparing to 33.7g in regenerator #3. Due to the mass difference and two-layer MCM in parallel plate regenerator, the no-load temperature span in freeze-cast regenerators are smaller than in parallel plate regenerator. The specific zero-span cooling capacity ($\Delta T=0K$) in regenerator #3 is quite close to this parallel plate regenerator. Thus, the results from active experiments can reasonably reveal the performance difference between freeze-cast regenerators #3 and #4 due to different heat transfer performance.



(a)



(b)



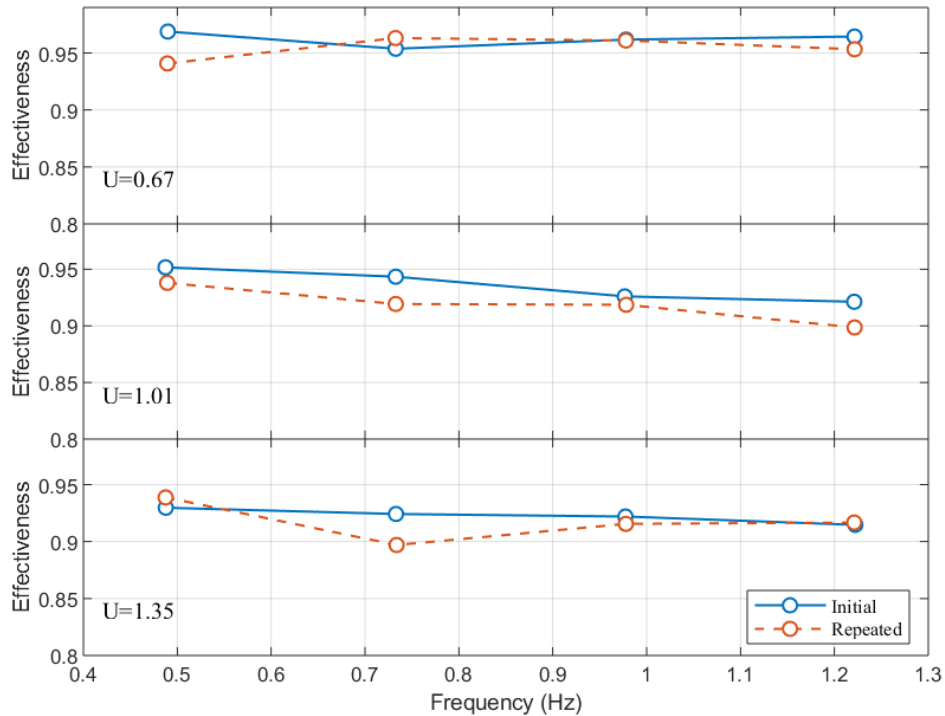
(c)

Fig. 8 (a) Temperature span as a function of hot reservoir temperature at a utilization of 0.59 between regenerators #3 and #4. (b) Temperature span as a function of utilization at hot reservoir temperature of $\sim 15^{\circ}\text{C}$ between regenerators #3 and #4. (c) Specific cooling capacity versus temperature span (cooling curves) at utilization of 0.59 and hot reservoir temperature of $\sim 15^{\circ}\text{C}$ between regenerator #3 and #4, and cooling curves from a parallel plate regenerator

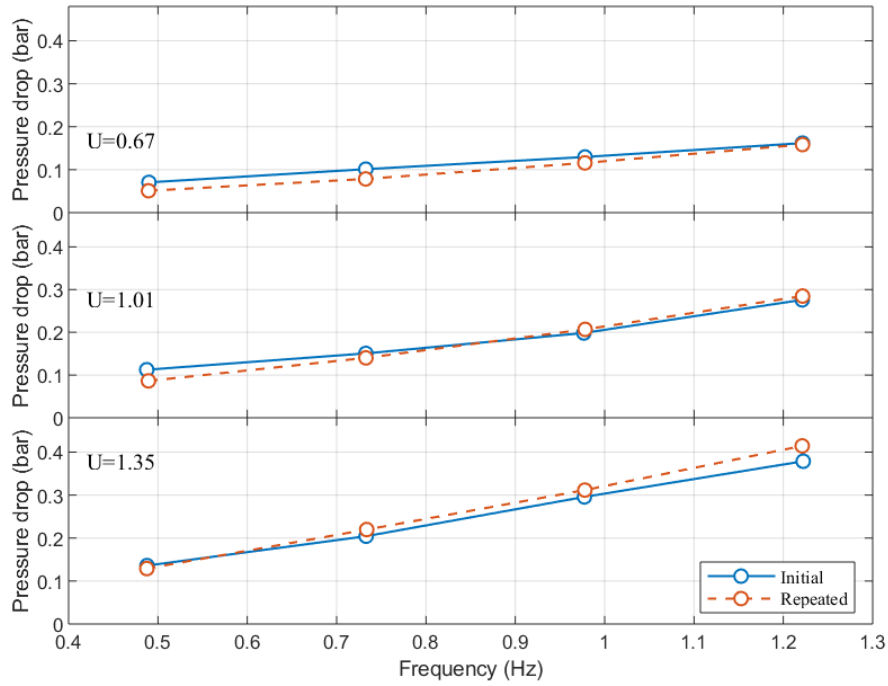
with similar MCM at utilization equals 0.5. T_{h1} and T_{h2} mean the hot reservoir temperatures are 8°C and 11°C respectively. The MCM in parallel plate regenerator is layered by two LCSMx with different Curie temperatures, which the MCM in freeze-cast regenerators is LCSM of single layer.

4.4. Regenerator stability

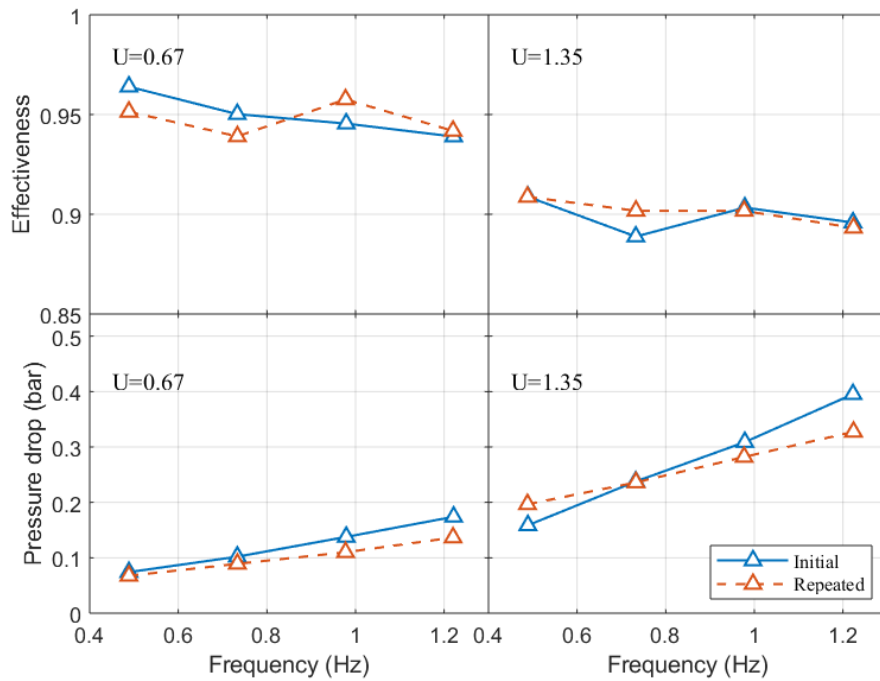
The material stability and integrity are critical factors for future commercialization. The stability mainly depends on geometrical parameters (i.e. porosity and pore size), and process routine (i.e. sintering temperature and period). All the regenerators were run at least 200 hours for the passive rig and 120 hours for the active test machine. All the regenerators survived the passive testing. In Fig.10 (a-b), regenerator #1 results repeated during a passive measurement before the active test. Comparing the effectiveness and pressure drop between the initial and a reproducing test, almost no variation is found in terms of heat transfer performance and flow resistance. It is thus to some extent shown that the regenerators can withstand the oscillatory flow impacts. However, regenerator #1 did not survive more than about 96-hours of active test; cracks were found at both ends. This means that the material cannot withstand the magnetic force during the reciprocating test for a long time. The reason is probably that a significant amount of MCM is in the form of dendrites inside the channels (Fig.1), thus reducing the effective form of the walls based on the fixed porosity. Due to an accidental issue, regenerator #2 was destroyed after passive testing and could not be run in the active test machine. Regenerators #3 and #4 successfully passed the passive and active tests without any visible wear. In Fig.10 (c), the passive test of regenerator #4 is repeated after all the passive and active tests finished. No significant changes in effectiveness are observed, which validates the material stability. The pressure drop decreases slightly probably because the fluid flow unclogged some channels. Similar results are also captured in regenerator #3, not presented here for brevity. Thus, all the freeze-cast regenerators can withstand oscillatory flow but the large pore design seems not to be suitable for periodic magnetic field conditions.



(a)



(b)



(c)

Fig. 10 Effectiveness (a) and pressure drop amplitude (b) comparisons between initial test and repeated test under utilizations of 0.67, 1.01 and 1.35 in regenerator #1. The curve marked 'repeated' stands for a repeated passive test after about 300 hours of passive testing. (c) Effectiveness and pressure drop amplitude comparisons between initial test and repeated tests under utilizations of 0.67 and 1.35 in regenerator #4. The reproducing experiment was done after nearly 700 hours of passive testing and 120 hours of active testing.

5. Conclusion

Four unconventional microchannel regenerators with different pore widths were fabricated by freeze-casting via different processing temperature profiles. All the regenerators were thermally and hydraulically characterized. The effectiveness and friction factor were derived from the passive experiments, while the cooling capacity and temperature lift were obtained from the active test machine experiments. The experimental data were fit to the correlations related to heat and mass transfer in a 1D model. The following performance features were obtained:

- (1) The correlations of Nusselt number among the four freeze-cast regenerators attained the same correlation parameters. The relationship of friction factor versus Reynolds number has the same equation form, but with different regression parameter values. Combined with the fitting parameters and the pore scanning image, regenerator #2 with the pore width of 49.6 μm obtained the highest flow permeability.
- (2) Freeze-cast regenerators based on the same other geometrical parameters (i.e. macro and total porosities, regenerator shape) and only the difference of pore width, show that larger pore size results in a decrease of both heat transfer effectiveness and pressure drop.
- (3) Combining the heat transfer performance (heat transfer coefficient times heat transfer area) and flow resistance (pressure drop), regenerator #1 with the pore width of 66.3 μm obtained the lowest performance than other freeze-cast regenerators.
- (4) Regenerators with a smaller pore width were found to have higher heat transfer effectiveness and higher cooling performance (specific cooling capacity and temperature span).

The stability of the freeze-cast regenerators was validated through comparing the initial and final performance parameters for passive operation. All the freeze-cast regenerators were run passively without significant performance reductions for hundreds of hours of operation. However, the regenerator with pore width 66.3 μm and significant dendrites developed crack formation when subjected to a periodic magnetic force.

Acknowledgments

J. Liang is grateful for financial support of the CSC (China Scholarship Council) scholarship. C. D. Christiansen, R. Bjørk and K. K. Nielsen wish to acknowledge the financial support of the Independent Research Fund Denmark—Technologies and Productions Sciences, project no. 6111 - 00073B. K.K. Nielsen also wishes to acknowledge the financial support of the Independent Research Fund Denmark – Technologies and Productions Sciences project no. 7017-00034B.

Reference

- [1] Kitanovski A, Tušek J, Tomc U, Plaznik U, Ožbolt M, Poredoš A. Magnetocaloric Energy Conversion: From Theory to Applications. 2015. doi:10.1007/978-3-319-08741-2.
- [2] Kitanovski A, Egolf PW. Thermodynamics of magnetic refrigeration. *Int J Refrig* 2006;29:3–21. doi:10.1016/j.ijrefrig.2005.04.007.
- [3] Lei T, Engelbrecht K, Nielsen KK, Veje CT. Study of geometries of active magnetic regenerators for room temperature magnetocaloric refrigeration. *Appl Therm Eng* 2017;111:1232–43. doi:10.1016/j.applthermaleng.2015.11.113.
- [4] Li Z, Shen J, Li K, Gao X, Guo X, Dai W. Assessment of three different gadolinium-based regenerators in a rotary-type magnetic refrigerator. *Appl Therm Eng* 2019;153:159–67. doi:10.1016/j.applthermaleng.2019.02.100.

- [5] Trevizoli P V., Nakashima AT, Peixer GF, Barbosa JR. Performance assessment of different porous matrix geometries for active magnetic regenerators. *Appl Energy* 2017;187:847–61. doi:10.1016/j.apenergy.2016.11.031.
- [6] Nielsen KK, Engelbrecht K. The influence of the solid thermal conductivity on active magnetic regenerators. *J Phys D Appl Phys* 2012;45. doi:10.1088/0022-3727/45/14/145001.
- [7] Monfared B, Palm B. Material requirements for magnetic refrigeration applications. *Int J Refrig* 2018;96:25–37. doi:10.1016/j.ijrefrig.2018.08.012.
- [8] Nielsen KK, Bahl CRH, Smith A, Engelbrecht K, Olsen UL, Pryds N. The influence of non-magnetocaloric properties on the performance in parallel-plate AMRs. *Int J Refrig* 2014;37:127–34. doi:10.1016/j.ijrefrig.2013.09.022.
- [9] Tušek J, Kitanovski A, Tomc U, Favero C, Poredoš A. Experimental comparison of multi-layered La-Fe-Co-Si and single-layered Gd active magnetic regenerators for use in a room-temperature magnetic refrigerator. *Int J Refrig* 2014;37:117–26. doi:10.1016/j.ijrefrig.2013.09.003.
- [10] Nielsen KK, Engelbrecht K, Bahl CRH. The influence of flow maldistribution on the performance of inhomogeneous parallel plate heat exchangers. *Int J Heat Mass Transf* 2013;60:432–9. doi:10.1016/j.ijheatmasstransfer.2013.01.018.
- [11] Deville BS. Freeze-Casting of Porous Ceramics: A Review of Current Achievements 2008:155–69. doi:10.1002/adem.200700270.
- [12] Scotti KL, Dunand DC. Freeze casting – A review of processing, microstructure and properties via the open data repository, FreezeCasting.net. *Prog Mater Sci* 2018;94:243–305. doi:10.1016/j.pmatsci.2018.01.001.
- [13] Naviroj M, Voorhees PW, Faber KT. Suspension- and solution-based freeze casting for porous ceramics. *J Mater Res* 2017. doi:10.1557/jmr.2017.133.
- [14] Fukasawa T, Ando M, Ohji T, Kanzaki S. Synthesis of Porous Ceramics with Complex Pore Structure by Freeze-Dry Processing. *J Am Ceram Soc* 2001. doi:10.1111/j.1151-2916.2001.tb00638.x.
- [15] Christiansen CD, Nielsen KK, Bjørk R. Freeze-casting to create directional micro-channels in regenerators for magnetic refrigeration. *Proc TherMag VIII, 8th IIF-IIR Int Conf Caloric Cool* 2018:96–101. doi:10.18462/iir.11072.
- [16] Christiansen CD, Nielsen KK, Bordia RK, Bjørk R. The effect of gelation on statically and dynamically freeze-cast structures. *J Am Ceram Soc* 2019. doi:10.1111/jace.16500.
- [17] Christiansen CD, Nielsen KK, Bjørk R. Novel freeze-casting device with high precision thermoelectric temperature control for dynamic freezing conditions. *Under Rev* n.d.
- [18] Liang J, Christiansen CD, Engelbrecht K, Nielsen KK, Bjørk R, Bahl CRH. Heat Transfer and Flow Resistance Analysis of a Novel Freeze-cast Regenerator. *Under Rev* n.d.
- [19] Bahl CRH, Petersen TF, Pryds N, Smith A. A versatile magnetic refrigeration test device. *Rev Sci Instrum* 2008;79. doi:10.1063/1.2981692.
- [20] Paulo Vinicius Trevizoli. Development of thermal regenerators for magnetic cooling applications. Federal University of Santa Catarina, 2015.
- [21] Tušek J, Kitanovski A, Zupan S, Prebil I, Poredoš A. A comprehensive experimental analysis of gadolinium active magnetic regenerators. *Appl Therm Eng* 2013;53:57–66. doi:10.1016/j.applthermaleng.2013.01.015.
- [22] Dinesen AR, Linderøth S, Mørup S. Direct and indirect measurement of the magnetocaloric effect in $\text{La}_{0.67}\text{Ca}_{0.33-x}\text{Sr}_x\text{MnO}_3 \pm \delta$ ($x \in [0;0.33]$). *J Phys Condens Matter* 2005;17:6257–69. doi:10.1088/0953-8984/17/39/011.
- [23] Dinesen AR. Magnetocaloric and magnetoresistive properties of $\text{La}_{0.67}\text{Ca}_{0.33-x}\text{Sr}_x\text{MnO}_3$. 2004.
- [24] Bahl CRH, Velázquez D, Nielsen KK, Engelbrecht K, Andersen KB, Bulatova R, et al. High performance magnetocaloric perovskites for magnetic refrigeration. *Appl Phys Lett* 2012;100. doi:10.1063/1.3695338.
- [25] Naleway SE, Fickas KC, Maker YN, Meyers MA, McKittrick J. Reproducibility of ZrO₂-based freeze casting for biomaterials. *Mater Sci Eng C* 2016. doi:10.1016/j.msec.2015.12.012.
- [26] Kaviany M. Principles of Heat Transfer in Porous Media. Springer; 1995. doi:10.1007/978-1-4612-4254-3.
- [27] Lei T. Modeling of active magnetic regenerators and experimental investigation of passive regenerators with oscillating flow. Technical University of Denmark, 2016.

- [28] Navickaitė K, Bez HN, Lei T, Barcza A, Vieyra H, Bahl CRH, et al. Experimental and numerical comparison of multi-layered La(Fe,Si,Mn)₁₃Hy active magnetic regenerators. *Int J Refrig* 2018;86:322–30. doi:10.1016/j.ijrefrig.2017.10.032.
- [29] Lei T, Navickaitė K, Engelbrecht K, Barcza A, Vieyra H, Nielsen KK, et al. Passive characterization and active testing of epoxy bonded regenerators for room temperature magnetic refrigeration. *Appl Therm Eng* 2018;128:10–9. doi:10.1016/j.applthermaleng.2017.08.152.
- [30] Choi S, Nam K, Jeong S. Investigation on the pressure drop characteristics of cryocooler regenerators under oscillating flow and pulsating pressure conditions. *Cryogenics (Guildf)* 2004;44:203–10. doi:10.1016/j.cryogenics.2003.11.006.
- [31] Trevizoli P V., Peixer GF, Nakashima AT, Capovilla MS, Lozano JA, Barbosa JR. Influence of inlet flow maldistribution and carryover losses on the performance of thermal regenerators. *Appl Therm Eng* 2018;133:472–82. doi:10.1016/j.applthermaleng.2018.01.055.
- [32] Arnold DS, Tura A, Ruebsaat-Trott A, Rowe A. Design improvements of a permanent magnet active magnetic refrigerator. *Int J Refrig* 2014;37:99–105. doi:10.1016/j.ijrefrig.2013.09.024.
- [33] Czernuszewicz A, Kaleta J, Kołosowski D, Lewandowski D. Experimental study of the effect of regenerator bed length on the performance of a magnetic cooling system. *Int J Refrig* 2019;97:49–55. doi:10.1016/j.ijrefrig.2018.09.023.
- [34] Rowe A. Configuration and performance analysis of magnetic refrigerators. *Int J Refrig* 2011;34:168–77. doi:10.1016/j.ijrefrig.2010.08.014.
- [35] Trevizoli P V., Nakashima AT, Peixer GF, Barbosa JR. Performance evaluation of an active magnetic regenerator for cooling applications – part I: Experimental analysis and thermodynamic performance. *Int J Refrig* 2016;72:192–205. doi:10.1016/j.ijrefrig.2016.07.009.
- [36] Teyber R. System Optimization and Performance Enhancement of Active Magnetic Regenerators. University of Victoria, 2018.
- [37] Hsu SH, Biwa T. Modeling of a stacked-screen regenerator in an oscillatory flow. *Jpn J Appl Phys* 2017;56:1–8. doi:10.7567/JJAP.56.017301.
- [38] Hsu CT, Fu H, Cheng P. On pressure-velocity correlation of steady and oscillating flows in regenerators made of wire screens. *J Fluids Eng Trans ASME* 1999. doi:10.1115/1.2822010.
- [39] Zhao TS, Cheng P. Oscillatory pressure drops through a woven-screen packed column subjected to a cyclic flow. *Cryogenics (Guildf)* 1996;36:333–41. doi:10.1016/0011-2275(96)81103-9.
- [40] Jin LW, Leong KC. Pressure drop and friction factor of steady and oscillating flows in open-cell porous media. *Transp Porous Media* 2008. doi:10.1007/s11242-007-9134-3.
- [41] Pamuk MT, Özdemir M. Friction factor, permeability and inertial coefficient of oscillating flow through porous media of packed balls. *Exp Therm Fluid Sci* 2012;38:134–9. doi:10.1016/j.expthermflusci.2011.12.002.
- [42] Nishiyama N, Yokoyama T. Permeability of porous media: Role of the critical pore size. *J Geophys Res Solid Earth* 2017;122:6955–71. doi:10.1002/2016JB013793.
- [43] Turcaud JA, Bez HN, Ruiz-Trejo E, Bahl CRH, Nielsen KK, Smith A, et al. Influence of manganite powder grain size and Ag-particle coating on the magnetocaloric effect and the active magnetic regenerator performance. *Acta Mater* 2015;97:413–8. doi:10.1016/j.actamat.2015.06.058.
- [44] Lei T, Nielsen KK, Engelbrecht K, Bahl CRH, Neves Bez H, Veje CT. Sensitivity study of multi-layer active magnetic regenerators using first order magnetocaloric material La(Fe,Mn,Si)₁₃Hy. *J Appl Phys* 2015;118. doi:10.1063/1.4923356.
- [45] Engelbrecht K, Bahl CRH, Nielsen KK. Experimental results for a magnetic refrigerator using three different types of magnetocaloric material regenerators. *Int J Refrig* 2011;34:1132–40. doi:10.1016/j.ijrefrig.2010.11.014.
- [46] Navickaitė K, Bez HN, Lei T, Barcza A, Vieyra H, Bahl CRH, et al. Experimental and numerical comparison of multi-layered La(Fe,Si,Mn)₁₃Hy active magnetic regenerators. *Int J Refrig* 2018;86:322–30. doi:10.1016/j.ijrefrig.2017.10.032.

Freeze-casting to create directional micro-channels in regenerators for magnetic refrigeration

Cathrine D. Christiansen, Kaspar K. Nielsen, Rasmus Bjørk

Published in: *Proceedings of TherMag VIII, 8th IIF-IIR International Conference on Caloric Cooling*, Darmstadt, Germany, 2018;96-101; DOI: 10.18462/iir.11072.

Experimental work, post processing and data analysis carried out at Department of Energy Conversion and Storage, Technical University of Denmark during the Ph.D. period. I am the first-author of the paper. The paper proceedings represent preliminary work in freeze-casting at DTU and was presented at an oral presentation at *TherMag VIII*.

PAPER ID: 0015

DOI: 10.18462/iir.thermag.2018.0015

Freeze-casting to create directional micro-channels in regenerators for magnetic refrigeration

Cathrine D. CHRISTIANSEN^(a), Kaspar K. NIELSEN, Rasmus BJØRK

Department of Energy Conversion and Storage, Technical University of Denmark

Frederiksborgvej 399, DK-4000, Roskilde, Denmark, ^(a)cadech@dtu.dk

ABSTRACT

We present the engineering of directional porosity in the form of lamellar micro-channels in the magnetocaloric ceramic of $\text{La}_{0.66}\text{Ca}_{0.27}\text{Sr}_{0.06}\text{Mn}_{1.05}\text{O}_3$ (LCSM) by freeze-casting. Freeze-casting is a templating technique based on the anisotropic growth of ice crystals in aqueous suspensions upon directional freezing, which, when applied to a suspension of LCSM results in hierarchical structures of aligned porosity in the form of micro-channels with widths of 5 μm to 20 μm . Channel sizes and tortuosity are measured and calculated from analysis of SEM images obtained at cross sections perpendicular and parallel to the freezing direction, respectively, while freezing conditions are monitored by temperature measurements. We propose that freeze-casting demonstrate apparent applicability within processing of ceramic materials for application as regenerator for magnetic refrigeration.

Keywords: Freeze-casting, ice templating, micro-channels, porous ceramics, magnetocaloric, magnetic refrigeration, active magnetic regenerator.

1. INTRODUCTION

Magnetic refrigeration utilizing the active magnetic regenerator (AMR) cycle offers an alternative to conventional refrigeration using cfc-gasses. The latter poses an environmental risk, while AMR technology is based on a porous magnetic material through which an environmentally friendly fluid flows transferring heat. The efficiency of the AMR cycle strongly depends on the geometry of the regenerator material. Common geometries are packed beds of epoxy-bonded spherical or irregular particles and parallel plates of varying thickness. While the packed beds offer a high heat transfer rate they are limited by their resistance to flow and fixed porosity. The plate geometry offers a low pressure drop but also a low surface area resulting in a reduced heat transfer rate. A geometry of micro-channels might pose an alternative, exhibiting a lower resistance to flow while maintaining a larger surface area and thus a high heat transfer rate (Lei et al., 2017). Although, such a geometry is hard to achieve by conventional processing routes.

Freeze-casting, or ice templating, however, introduces a potential processing route to fabricate micro-channels in ceramics. Freeze-casting is a templating technique where a ceramic aqueous suspension is directionally frozen resulting in the growth of anisotropic ice crystals, which redistributes the ceramic particles. Following this, water is sublimated from the frozen body by freeze-drying, leaving voids where the ice crystals were and thereby creating macro-pores or channels in the green body. Subsequent sintering results in a structure with parallel, well-defined channels with widths in the range $\sim 10 \mu\text{m}$ to $\sim 100 \mu\text{m}$, solid ceramic walls and tunable porosity (Deville et al., 2007; Lichtner et al., 2013). For a status on recent trends in freeze-casting, the reader is referred to (Deville, 2018).

The well-known $\text{La}_{0.66}\text{Ca}_{0.33-x}\text{Sr}_x\text{Mn}_{1.05}\text{O}_3$ magnetocaloric ceramic, for which the Curie Temperature can be conveniently controlled around room temperature by varying x (Dinesen et al., 2005), is highly relevant for application as regenerator-material in magnetic refrigeration (Bahl et al., 2012). In this context, we present engineered structures with aligned, directional porosity in $\text{La}_{0.66}\text{Ca}_{0.27}\text{Sr}_{0.06}\text{Mn}_{1.05}\text{O}_3$ ceramics by freeze-casting.

2. MATERIALS & METHODS

2.1. Powder properties and preparation of ceramic suspension

Ceramic suspensions were prepared from 14 vol% powders of $\text{La}_{0.66}\text{Ca}_{0.27}\text{Sr}_{0.06}\text{Mn}_{1.05}\text{O}_3$ (LCSM, CerPoTech, Norway) in distilled water, with the addition of 2.5 w.t. % (in relation to powder) of polyvinylpyrrolidone (PVP K15, $M_w \sim 10,000$ g/mol, Sigma-Aldrich, Germany) as dispersing agent.

The specific surface area and density of the powder were determined by the BET method using a Nova 4000e (Quantachrome Instruments, United States), and by gas pycnometry using an AccuPyc II 1340 (Micromeritics, United States), respectively. The particle size distribution (PSD) of both raw powders and milled suspensions was determined using a Laser Diffraction Particle Size Analyser (LS 13 320, Beckman Coulter). Powder properties are summarized in Table 1.

Table 1. Summarization of powder properties of $\text{La}_{0.66}\text{Ca}_{0.27}\text{Sr}_{0.06}\text{Mn}_{1.05}\text{O}_3$. The median of the particle size distribution is denoted d_{50} .

Density	Specific surface area	d_{50}
6.00 g/cm ³	10.12 m ² /g	2.6 μm

In order to achieve a sufficient dispersion of powders, slurries were upon mixing by stirring sonicated using a homogenizer (UP200St, Hielscher) for 60 seconds and subsequently homogenized using a low energy ball mill with zirconia balls ($\varnothing = 10$ mm) for 24 hours. 1.5 w.t. % (in relation to powder) of polyvinylpyrrolidone (PVP K30, $M_w \sim 30,000$ g/mol, Sigma-Aldrich, Germany) was added as binder and mixed for an additional 30 minutes before use. Suspensions were de-aired under low vacuum for a few minutes immediately before casting.

2.2. Freeze-casting procedure

Samples were frozen directionally with no other temperature control than that of liquid nitrogen. An acrylic cylindrical mould with an inner diameter of 16.5 mm, an outer diameter of 36 mm and with a detachable copper bottom containing approximately 5 mL of de-aired slurry was placed on top of a vertically positioned copper rod ($\varnothing = 20$ mm, $l = 315$ mm) directly immersed into a container of liquid nitrogen at 77 K. The mould was equipped with thermocouples (K-type, gauge 36, Omega) positioned at varying heights 6 mm apart by insets drilled radially inward in the mould leaving 750 μm mould wall between thermocouples and suspension. Thus, the temperature through the suspension could be monitored during freezing. The top of the mould was left open to ambient conditions and the suspension was frozen directionally due to the applied temperature gradient across the suspension in the vertical direction caused by the difference in temperature of the top of the copper rod and the ambient temperature.

Upon freeze-casting, samples were removed cautiously from their moulds and transferred to a freeze drier (Alpha 1-2 LD plus, Christ, Buch & Holm) where ice was removed from the samples by sublimation for at least 24 hours. Dry samples were subsequently sintered in air at 1150 °C for 3 hours (heating rate of 2 K/min) with an initial burnout of organic additives at 450 °C for 4 hours.

2.3. Structure characterization and quantification

Ceramic samples were prepared for mechanical handling and structural analysis by infiltration with epoxy (EpoFix, Struers Aps, Denmark). Samples were upon mounting cut in half parallel to the freezing direction and one-half of the sample was then cut in 4 mm slices perpendicular to the freezing direction. This procedure exposes parallel and perpendicular cross sections of the sample, which were then polished and coated with a ~12 nm thick carbon layer. Images of the cross sections were obtained using a scanning electron microscope (TM3000, Hitachi High-Technologies), and analysed using Matlab® (The MathWorks, Inc.). Three images at each sample height in the parallel cut samples and each slice cut in the perpendicular direction were obtained for statistical analysis. Channel widths were measured on perpendicular cross sections while tortuosity was calculated from parallel cross sections using a modified version of the TauFactor application (Cooper et al., 2016) in Matlab® (The MathWorks, Inc.). The software has been modified (De Angelis et al., 2018, 2017;

Jørgensen et al., 2015), for our purpose specifically for analysis in 2D, in order to calculate the tortuosity from SEM images. Tortuosity was calculated parallel to the freezing direction across cross sectional areas of 830 x 620 μm .

3. RESULTS & DISCUSSION

Freeze-casting a suspension of ceramic particles under the conditions described in the previous section results in hierarchical structures of aligned porosity in the form of micro-channels as shown in Figure 1. The channels are aligned and lamellar, but changes in morphology and size within one single sample are apparent.

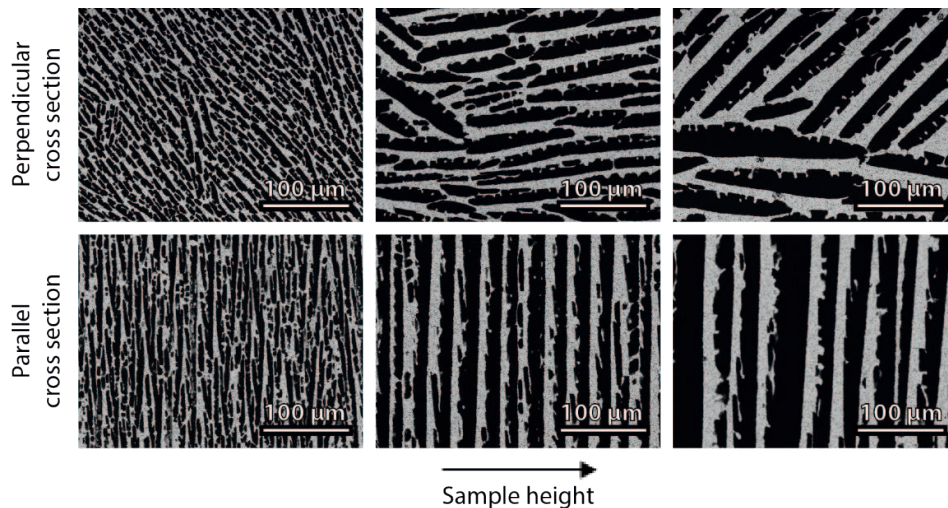


Figure 1: SEM images of cross sections perpendicular and parallel to the freezing direction, where the grey parts are ceramic walls while the black areas are voids or channels. Directional freezing thus results in a hierarchical, porous structure of lamellar micro-channels.

The structural properties of freeze-casted species can be quantified by the size, or width, of channels and tortuosity. From cross sections perpendicular and parallel to the freezing direction, it is evident that the channel size increases with increasing sample height. On the contrary, the tortuosity decreases with increasing sample height. Sample height is the vertical distance – parallel to the freezing direction – from the bottom of the sample and to the specific cross section of interest. The width of the lamellar channels at various heights in the sample are plotted in Figure 2a, while the calculated tortuosity at various heights in the sample are plotted in Figure 2b.

The calculated tortuosities of the channels drop drastically up through the sample. A tortuosity of $\tau = 1$ corresponds to a direct flow path, while the greater the tortuosity the greater the curviness of the channels. At the bottom of the sample, the calculated tortuosity was infinite, because no channels span across the entire analysed cross sections. The tortuosity can be directly correlated to the nature of ice crystal growth under the conditions described above. The growth of ice crystals in ceramic suspensions during freeze-casting has previously been observed by *in situ* x-ray (Bareggi et al., 2011; Deville et al., 2009). Upon freezing, rapid nucleation takes place at the bottom copper surface forming ice crystals growing in random directions. This is the isotropic region with no resulting directional porosity. Eventually, ice crystals growing along the direction of the temperature gradient are favoured, resulting in a region of aligned crystals. This region is referred to as the steady state region or the anisotropic region. In this region, aligned, lamellar ice crystals are arranged in domains of various orientations, as is also evident on the perpendicular cross sections in Figure 1 (top). The resulting channels are greater and more homogeneous in size, giving rise to a significant drop in calculated tortuosity.

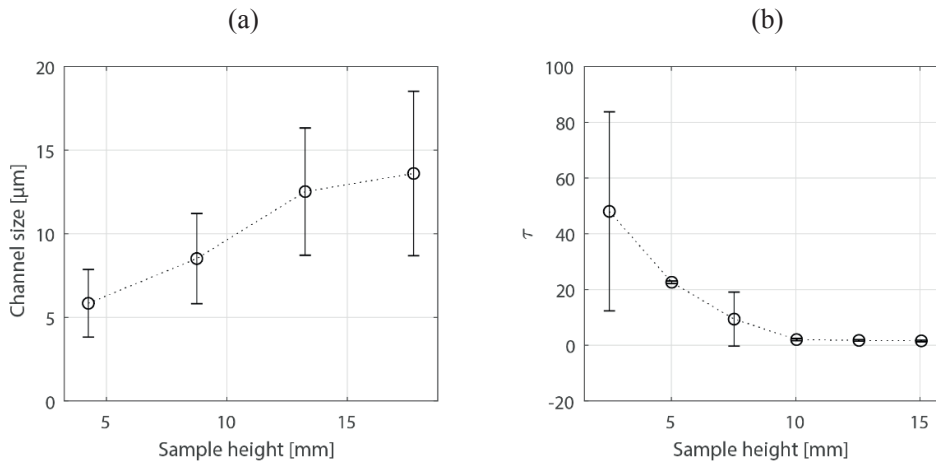


Figure 2: Structural properties of freeze-casted LCSM ceramics. (a) Channel size is measured as the width of lamellar pores on SEM images of perpendicular cross sections at various sample heights, while (b) tortuosity is calculated from SEM images obtained at various heights parallel to the freezing direction.

The channel size of freeze casted species has previously been correlated to the velocity of the freezing front, where the channel size increase with a decrease in freezing front velocity (Deville et al., 2007; Lichtner et al., 2013; Waschkies et al., 2009). The freezing front is the interface between the liquid ceramic suspension and the frozen sample of ice and ceramic phases. The freezing front in a ceramic suspension undergoing freeze-casting have previously been found, by *in situ* x-ray, to be a well-defined, slightly concave planar interface perpendicular to the freezing direction (Bareggi et al., 2011), and thus, it can often be tracked by visible inspection using a transparent mould.

However, due to the colour (or lack thereof) of LCSM, we found that it was not possible to visibly track the freezing front during casting for determination of the velocity of the freezing front. Instead, we installed thermocouples along the height of the casting mould in order to measure the temperature through the sample during freezing. This inevitably involves a thermal lag. The measured temperature of the copper mould bottom and at various positions in the mould during casting are shown in Figure 3a. These measurements allowed us to calculate the local freezing rate, i.e. the rate of temperature change. Assuming that the local freezing rate at the time of freezing ($T = 0 \text{ }^\circ\text{C}$) can be used as a measure to quantify the freezing conditions at the freezing front, a decrease of this quantity along the height of the sample is evident from Figure 3b.

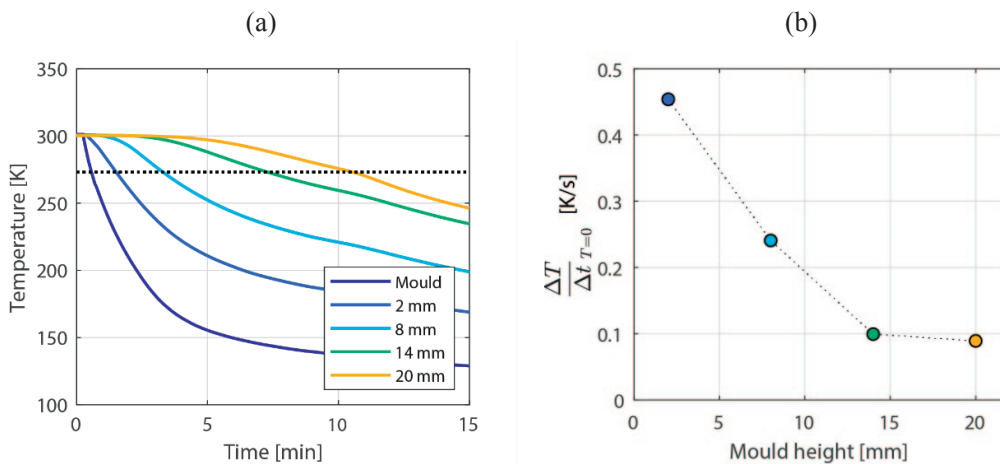


Figure 3: Freezing conditions for freeze-casted LCSM ceramics. (a) Temperature of mould bottom and at various positions along the height of the mould, the freezing point of water is indicated by the dashed line, and (b) the local freezing rates at the time of freezing.

The sample shrinkage in the direction of freezing upon sintering is approximately 25%, which means that Figure 2a-b and Figure 3b approximately span the same region of the sample. The structural properties of channel size and tortuosity is thus clearly correlated to the local freezing rate, where a decrease in local freezing rate increases the channel size and decreases tortuosity.

We found that these tendencies are true for various solid loads of 14-20 vol%, leading to ceramics of varying porosity, however, upon freeze-casting of an LCSM suspension of powders of larger particle size, we observed only vaguely defined channels:

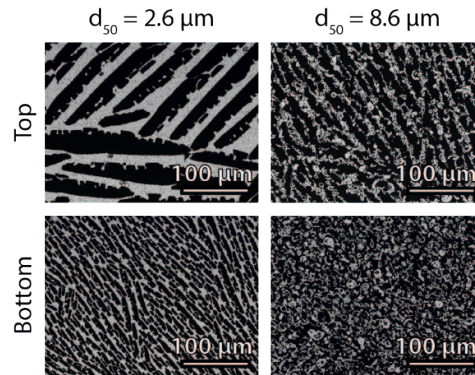


Figure 4: SEM images of cross sections perpendicular to the freezing front obtained at the top (sample height: 18 mm) and bottom (sample height: 4 mm) of samples prepared from ceramics of various particle size. d_{50} denote the median particle size of the particle size distribution of freeze-casted suspensions.

From Figure 4 it is evident that no channels have formed at the bottom of the sample freeze-casted from the suspension of larger particles. At the top of the sample, the wall thickness and particle sizes are in the same order of magnitude resulting in vaguely defined channels and walls, where the latter is varying in thickness and density. The lack of well-defined channels, specifically at the bottom, is presumably due to particle entrapment (Deville et al., 2007), the freezing rate simply resulted in a freezing front moving too fast thereby engulfing particles instead of ejecting them from the ice phase.

4. CONCLUSIONS

We show that freeze-casting a suspension of ceramic particles by directional freezing, applying no other temperature control than that of liquid nitrogen, results in hierarchical structures of anisotropic porosity in the form of micro-channels in the size range of 5 μm to 20 μm . The channels are aligned and lamellar. Structural properties such as channel size and tortuosity was determined from analysis of SEM images of cross sections obtained at various sample heights, revealing an increase in channel size and a decrease in tortuosity with increasing sample height. The micro-channels are shaped from the sublimated ice crystals and as such, the structural properties depend strongly on the morphology of the ice crystals, which is determined by the freezing conditions. We found that when freeze-casting ceramic suspensions using a set-up with no temperature control other than that of liquid nitrogen, the local freezing rate decreases as the freezing front moves further away from the copper rod, i.e. with increasing sample height.

Freeze-casting hold the promise of a processing route with the ability to tune and optimize channel size, tortuosity and also porosity, yielding high tunability of ceramics for energy application, specifically as regenerator-material for magnetic refrigeration. However, the applicability depend on implementation of enhanced control of freezing conditions in order to obtain more homogenous structures regarding channel size and tortuosity.

ACKNOWLEDGEMENTS

This work is funded by the Independent Research Fund Denmark | Technology and Production Sciences, project no. 6111-00073B, *Controlling ice growth to create micro-channel structures*. The authors wish to

extend their gratitude to Peter Stanley Jørgensen, associate professor, Technical University of Denmark, for software and expertise in regards to analysis of SEM images and to Dr. Rajendra Bordia, professor and chair, Clemson University, and his research group for exchange of technical knowledge.

REFERENCES

- Bahl, C.R.H., Velázquez, D., Nielsen, K.K., Engelbrecht, K., Andersen, K.B., Bulatova, R., Pryds, N., 2012. High performance magnetocaloric perovskites for magnetic refrigeration. *Appl. Phys. Lett.* 100. <https://doi.org/10.1063/1.3695338>
- Bareggi, A., Maire, E., Lasalle, A., Deville, S., 2011. Dynamics of the freezing front during the solidification of a colloidal alumina aqueous suspension: In situ x-ray radiography, tomography, and modeling. *J. Am. Ceram. Soc.* 94, 3570–3578. <https://doi.org/10.1111/j.1551-2916.2011.04572.x>
- Cooper, S.J., Bertei, A., Shearing, P.R., Kilner, J.A., Brandon, N.P., 2016. TauFactor: An open-source application for calculating tortuosity factors from tomographic data. *SoftwareX* 5, 203–210. <https://doi.org/10.1016/j.softx.2016.09.002>
- De Angelis, S., Jørgensen, P.S., Esposito, V., Tsai, E.H.R., Holler, M., Kreka, K., Abdellahi, E., Bowen, J.R., 2017. Ex-situ tracking solid oxide cell electrode microstructural evolution in a redox cycle by high resolution ptychographic nanotomography. *J. Power Sources* 360, 520–527. <https://doi.org/10.1016/j.jpowsour.2017.06.035>
- De Angelis, S., Jørgensen, P.S., Tsai, E.H.R., Holler, M., Kreka, K., Bowen, J.R., 2018. Three dimensional characterization of nickel coarsening in solid oxide cells via ex-situ ptychographic nano-tomography. *J. Power Sources* 383, 72–79. <https://doi.org/10.1016/j.jpowsour.2018.02.031>
- Deville, S., 2018. The lure of ice-templating: Recent trends and opportunities for porous materials. *Scr. Mater.* 147, 119–124. <https://doi.org/10.1016/j.scriptamat.2017.06.020>
- Deville, S., Maire, E., Lasalle, A., Bogner, A., Gauthier, C., Leloup, J., Guizard, C., 2009. In situ X-ray radiography and tomography observations of the solidification of aqueous alumina particle suspensions - Part I: Initial instants. *J. Am. Ceram. Soc.* 92, 2489–2496. <https://doi.org/10.1111/j.1551-2916.2009.03163.x>
- Deville, S., Saiz, E., Tomsia, A.P., 2007. Ice-templated porous alumina structures. *Acta Mater.* 55, 1965–1974. <https://doi.org/10.1016/j.actamat.2006.11.003>
- Dinesen, A., Linderoth, S., Mørup, S., 2005. Direct and indirect measurement of the magnetocaloric effect in $\text{La}_{0.67}\text{Ca}_{0.33-x}\text{Sr}_x\text{MnO}_3 \pm \delta$. *J. Phys. Condens. Matter* 17, 6257–6269. <https://doi.org/10.1088/0953-8984/17/39/011>
- Jørgensen, P.S., Ebbenhøj, S.L., Hauch, A., 2015. Triple phase boundary specific pathway analysis for quantitative characterization of solid oxide cell electrode microstructure. *J. Power Sources* 279, 686–693. <https://doi.org/10.1016/j.jpowsour.2015.01.054>
- Lei, T., Engelbrecht, K., Nielsen, K.K., Veje, C.T., 2017. Study of geometries of active magnetic regenerators for room temperature magnetocaloric refrigeration. *Appl. Therm. Eng.* 111, 1232–1243. <https://doi.org/10.1016/j.applthermaleng.2015.11.113>
- Lichtner, A.Z., Jauffrès, D., Martin, C.L., Bordia, R.K., 2013. Processing of hierarchical and anisotropic porosity LSM-YSZ composites. *J. Am. Ceram. Soc.* 96, 2745–2753. <https://doi.org/10.1111/jace.12478>
- Waschkies, T., Oberacker, R., Hoffmann, M.J., 2009. Control of lamellae spacing during freeze casting of ceramics using double-side cooling as a novel processing route. *J. Am. Ceram. Soc.* 92, 79–84. <https://doi.org/10.1111/j.1551-2916.2008.02673.x>

Bibliography

- [1] Sylvain Deville. Freezing Colloids: Observations, Principles, Control, and Use. doi: 10.1007/978-3-319-50515-2.
- [2] W A Maxwell, R S Gurnick, and A C Francisco. Preliminary investigation of the "freeze-casting" method for forming refractory powders. Technical report, National Advisory Committee for Aeronautics, Washington.
- [3] Ho Ming Tong, Isao Noda, and Carl C. Gryte. CPS 768 Formation of anisotropic ice-agar composites by directional freezing. *Colloid & Polymer Science*, 262(7):589–595, 1984. ISSN 0303402X. doi: 10.1007/BF01451524.
- [4] H. M. Tong and C. C. Gryte. Mechanism of lamellar spacing adjustment in directionally frozen agar gels. *Colloid & Polymer Science*, 263(2):147–155, 1985. ISSN 0303402X. doi: 10.1007/BF01412789.
- [5] Takayuki Fukasawa, Motohide Ando, Tatsuki Ohji, and Shuzo Kanzaki. Synthesis of Porous Ceramics with Complex Pore Structure by Freeze-Dry Processing. *Journal of the American Ceramic Society*, (1):230–232. ISSN 00027820. doi: 10.1111/j.1151-2916.2001.tb00638.x.
- [6] T. Fukasawa, Z. Y. Deng, M. Ando, T. Ohji, and Y. Goto. Pore structure of porous ceramics synthesized from water-based slurry by freeze-dry process. *Journal of Materials Science*, 36(10):2523–2527, 2001. ISSN 00222461. doi: 10.1023/A:1017946518955.
- [7] Sylvain Deville. Freeze-casting of porous ceramics: A review of current achievements and issues. *Advanced Engineering Materials*, 10(3):155–169, 2008. ISSN 14381656. doi: 10.1002/adem.200700270.
- [8] A. Z. Lichtner. *Anisotropic and Hierarchical Porosity in Multifunctional Ceramics*. Phd dissertation, University of Washington, 2015.
- [9] Sylvain Deville, Eduardo Saiz, and Antoni P. Tomsia. Ice-templated porous alumina structures. *Acta Materialia*, 55(6):1965–1974, 2007. ISSN 13596454. doi: 10.1016/j.actamat.2006.11.003.
- [10] Thomas Waschkes, Rainer Oberacker, and Michael J. Hoffmann. Control of Lamellae Spacing During Freeze Casting of Ceramics Using Double-Side Cooling as a Novel Processing Route. *Journal of the American Ceramic Society*, (SUPPL. 1):S79–S84, jan . ISSN 00027820. doi: 10.1111/j.1151-2916.2008.02673.x.

- [11] Aaron Z. Lichtner, David Jauffrès, Christophe L. Martin, and Rajendra K. Bordia. Processing of hierarchical and anisotropic porosity LSM-YSZ composites. *Journal of the American Ceramic Society*, 96(9):2745–2753, 2013. ISSN 00027820. doi: 10.1111/jace.12478.
- [12] Byung Ho Yoon, Young Hag Koh, Chee Sung Park, and Hyoun Ee Kim. Generation of large pore channels for bone tissue engineering using camphene-based freeze casting. *Journal of the American Ceramic Society*, 90(6):1744–1752, 2007. ISSN 00027820. doi: 10.1111/j.1551-2916.2007.01670.x.
- [13] S. M. Miller, X. Xiao, and K. T. Faber. Freeze-cast alumina pore networks: Effects of freezing conditions and dispersion medium. *Journal of the European Ceramic Society*, (13):3595–3605. ISSN 1873619X. doi: 10.1016/j.jeurceramsoc.2015.05.012.
- [14] Yufei Tang, Sha Qiu, Cong Wu, Qian Miao, and Kang Zhao. Freeze cast fabrication of porous ceramics using tert-butyl alcohol–water crystals as template. *Journal of the European Ceramic Society*, (6):1513–1518, . ISSN 0955-2219. doi: 10.1016/j.jeurceramsoc.2015.12.047.
- [15] Yasumasa Chino and David C. Dunand. Directionally freeze-cast titanium foam with aligned, elongated pores. *Acta Materialia*, 56(1):105–113, 2008. ISSN 13596454. doi: 10.1016/j.actamat.2007.09.002.
- [16] Aurelia I. Cuba Ramos and David C. Dunand. Preparation and Characterization of Directionally Freeze-cast Copper Foams. *Metals*, (4):265–273. ISSN 2075-4701. doi: 10.3390/met2030265.
- [17] Manabu Fukushima and Yu Ichi Yoshizawa. Fabrication of highly porous nickel with oriented micrometer-sized cylindrical pores by gelation freezing method. *Materials Letters*, pages 99–101, . ISSN 18734979. doi: 10.1016/j.matlet.2015.04.029.
- [18] Lei Zhang, Ronan Le Coz-Botrel, Charlotte Beddoes, Terje Sjöström, and Bo Su. Gelatin freeze casting of biomimetic titanium alloy with anisotropic and gradient pore structure. *Biomedical Materials*, (1):015014. ISSN 1748-605X. doi: 10.1088/1748-605X/aa50a1.
- [19] Haifei Zhang, Irshad Hussain, Mathias Brust, Michael F. Butler, Steven P. Rannard, and Andrew I. Cooper. Aligned two- and three-dimensional structures by directional freezing of polymers and nanoparticles. *Nature Materials*, 4(10):787–793, 2005. ISSN 14761122. doi: 10.1038/nmat1487.
- [20] Noriaki Arai and Katherine T. Faber. Hierarchical porous ceramics via two-stage freeze casting of preceramic polymers. *Scripta Materialia*, pages 72–76. ISSN 13596462. doi: 10.1016/j.scriptamat.2018.10.037.

- [21] Jemma L. Vickery, Avinash J. Patil, and Stephen Mann. Fabrication of graphene-polymer nanocomposites with higher-order three-dimensional architectures. *Advanced Materials*, 21(21):2180–2184, 2009. ISSN 09359648. doi: 10.1002/adma.200803606.
- [22] Philipp M. Hunger, Amalie E. Donius, and Ulrike G.K. Wegst. Structure-property-processing correlations in freeze-cast composite scaffolds. *Acta Biomaterialia*, (5):6338–6348. ISSN 17427061. doi: 10.1016/j.actbio.2013.01.012.
- [23] Phuong T.N. Nguyen and Joachim Ulrich. Fast Dispersible Cocoa Tablets: A Case Study of Freeze-Casting Applied to Foods. *Chemical Engineering and Technology*, 37(8):1376–1382, 2014. ISSN 15214125. doi: 10.1002/ceat.201400032.
- [24] Anikó Szepes, Joachim Ulrich, Zsuzsanna Farkas, József Kovács, and Piroska Szabó-Révész. Freeze-casting technique in the development of solid drug delivery systems. *Chemical Engineering and Processing: Process Intensification*, 46(3):230–238, 2007. ISSN 02552701. doi: 10.1016/j.cep.2006.06.004.
- [25] Sylvain Deville. Ice-templating, freeze casting: Beyond materials processing. 28(17): 2202–2219, 2013. ISSN 08842914. doi: 10.1557/jmr.2013.105.
- [26] Aaron Lichtner, Denis Roussel, David Jauffrés, Christophe L. Martin, and Rajendra K. Bordia. Effect of Macropore Anisotropy on the Mechanical Response of Hierarchically Porous Ceramics. *Journal of the American Ceramic Society*, 99(3):979–987, 2016. ISSN 15512916. doi: 10.1111/jace.14004.
- [27] Sylvain Deville, Eric Maire, Audrey Lasalle, Agnès Bogner, Catherine Gauthier, Jérôme Leloup, and Christian Guizard. In Situ x-ray radiography and tomography observations of the solidification of aqueous alumina particles suspensions. Part II: Steady state. *Journal of the American Ceramic Society*, 92(11):2497–2503, 2009. ISSN 00027820. doi: 10.1111/j.1551-2916.2009.03264.x.
- [28] Sylvain Deville, Eric Maire, Audrey Lasalle, Agnès Bogner, Catherine Gauthier, Jérôme Leloup, and Christian Guizard. In situ X-ray radiography and tomography observations of the solidification of aqueous alumina particle suspensions - Part I: Initial instants. *Journal of the American Ceramic Society*, 92(11):2489–2496, 2009. ISSN 00027820. doi: 10.1111/j.1551-2916.2009.03163.x.
- [29] Sylvain Deville, Etienne Munch, Eduardo Saiz, and Antoni P Tomsia. Architectural Control of Freeze-Cast Ceramics Through Additives and Templating. *J. Am. Ceram. Soc.*, 92(7):1534–1539, 2009. doi: 10.1111/j.1551-2916.2009.03087.x.
- [30] Hao Bai, Yuan Chen, Benjamin Delattre, Antoni P. Tomsia, and Robert O. Ritchie. Bioinspired large-scale aligned porous materials assembled with dual temperature gradients. *Science Advances*, 1(11):1–9, 2015. ISSN 23752548. doi: 10.1126/sciadv.1500849.

- [31] Zhi Jie Hu, Xiang Tian Shen, Shu Li Geng, Ping Shen, and Qi Chuan Jiang. 3D long-range ordered porous ceramics prepared by a novel bidirectional freeze-casting technique. *Ceramics International*, (5):5803–5806. ISSN 02728842. doi: 10.1016/j.ceramint.2017.12.130.
- [32] S. Deville, J. Adrien, E. Maire, M. Scheel, and M. Di Michiel. Time-lapse, three-dimensional in situ imaging of ice crystal growth in a colloidal silica suspension. *Acta Materialia*, (6):2077–2086, . ISSN 13596454. doi: 10.1016/j.actamat.2012.12.027.
- [33] Michael M. Porter, Russ Imperio, Matthew Wen, Marc A. Meyers, and Joanna McKittrick. Bioinspired scaffolds with varying pore architectures and mechanical properties. *Advanced Functional Materials*, 24(14):1978–1987, 2014. ISSN 16163028. doi: 10.1002/adfm.201302958.
- [34] Valentina Naglieri, Hrishikesh A. Bale, Bernd Gludovatz, Antoni P. Tomsia, and Robert O. Ritchie. On the development of ice-templated silicon carbide scaffolds for nature-inspired structural materials. *Acta Materialia*, (18):6948–6957. ISSN 13596454. doi: 10.1016/j.actamat.2013.08.006.
- [35] Denis Roussel, Aaron Lichtner, David Jauffrès, Julie Villanova, Rajendra K. Bordia, and Christophe L. Martin. Strength of hierarchically porous ceramics: Discrete simulations on X-ray nanotomography images. *Scripta Materialia*, pages 250–253. ISSN 13596462. doi: 10.1016/j.scriptamat.2015.11.015.
- [36] Steven E. Naleway, Christopher F. Yu, Michael M. Porter, Arijit Sengupta, Peter M. Iovine, Marc A. Meyers, and Joanna McKittrick. Bioinspired composites from freeze casting with clathrate hydrates. *Materials and Design*, pages 62–67, . ISSN 18734197. doi: 10.1016/j.matdes.2015.01.010.
- [37] Michael M. Porter, Pooya Niksiar, and Joanna McKittrick. Microstructural Control of Colloidal-Based Ceramics by Directional Solidification under Weak Magnetic Fields. *Journal of the American Ceramic Society*, 99(6):1917–1926, 2016. ISSN 15512916. doi: 10.1111/jace.14183.
- [38] Steven E. Naleway, Kate C. Fickas, Yajur N. Maker, Marc A. Meyers, and Joanna McKittrick. Reproducibility of ZrO₂-based freeze casting for biomaterials. *Materials Science and Engineering C*, pages 105–112, . ISSN 09284931. doi: 10.1016/j.msec.2015.12.012.
- [39] Jordi Seuba, Sylvain Deville, Christian Guizard, and Adam J. Stevenson. Gas permeability of ice-templated, unidirectional porous ceramics. *Science and Technology of Advanced Materials*, (1):313–323, . ISSN 18785514. doi: 10.1080/14686996.2016.1197757.
- [40] Jordi Seuba, Jerome Leloup, Stephane Richaud, Sylvain Deville, Christian Guizard, and Adam J. Stevenson. Fabrication of ice-templated tubes by rotational freezing: Microstruc-

- ture, strength, and permeability. *Journal of the European Ceramic Society*, (6):2423–2429, . ISSN 1873619X. doi: 10.1016/j.jeurceramsoc.2017.01.014.
- [41] J. Gurauskis, C. R. Graves, R. Moreno, and M. I. Nieto. Self-supported ceramic substrates with directional porosity by mold freeze casting. *Journal of the European Ceramic Society*, (2):697–703. ISSN 1873619X. doi: 10.1016/j.jeurceramsoc.2016.08.031.
- [42] Florian Bouville, Eric Maire, and Sylvain Deville. Lightweight and stiff cellular ceramic structures by ice templating. *Journal of Materials Research*, (02):175–181. ISSN 0884-2914. doi: 10.1557/jmr.2013.385.
- [43] S. J. Cooper, A. Bertei, P. R. Shearing, J. A. Kilner, and N. P. Brandon. TauFactor: An open-source application for calculating tortuosity factors from tomographic data. *SoftwareX*, pages 203–210. ISSN 23527110. doi: 10.1016/j.softx.2016.09.002.
- [44] Jordi Seuba, Sylvain Deville, Christian Guizard, and Adam J. Stevenson. The effect of wall thickness distribution on mechanical reliability and strength in unidirectional porous ceramics. *Science and Technology of Advanced Materials*, (1):128–135, . ISSN 1468-6996. doi: 10.1080/14686996.2016.1140309.
- [45] Cathrine D. Christiansen, Kaspar K. Nielsen, Rajendra K. Bordia, and Rasmus Bjørk. The effect of gelation on statically and dynamically freeze-cast structures. *Journal of the American Ceramic Society*, 102:5796–5806, 2019. ISSN 15512916. doi: 10.1111/jace.16500.
- [46] Sylvain Deville, Eduardo Saiz, Ravi K Nalla, and Antoni P Tomsia. Freezing as a path to build complex composites. *Science*, (5760):515–518, . ISSN 1095-9203. doi: 10.1126/science.1120937.
- [47] Qiang Fu, Mohamed N. Rahaman, Fatih Dogan, and B. Sonny Bal. Freeze-cast hydroxyapatite scaffolds for bone tissue engineering applications. *Biomedical Materials*, 3(2), 2008. ISSN 17486041. doi: 10.1088/1748-6041/3/2/025005.
- [48] Y-S Lin, M a Meyers, and E a Olevsky. Microchannelled hydroxyapatite components by sequential freeze drying and free pressureless spark plasma sintering. *Advances in Applied Ceramics*, (5&6):269–274. ISSN 1743-6753. doi: 10.1179/1743676111Y.0000000067.
- [49] Sylvain Deville, Sylvain Meille, and Jordi Seuba. A meta-analysis of the mechanical properties of ice-templated ceramics and metals. *Science and Technology of Advanced Materials*, (4):043501, . ISSN 1468-6996. doi: 10.1088/1468-6996/16/4/043501.
- [50] Jordi Seuba, Sylvain Deville, Christian Guizard, and Adam J. Stevenson. Mechanical properties and failure behavior of unidirectional porous ceramics. *Scientific Reports*, (April):1–11, . ISSN 20452322. doi: 10.1038/srep24326.

- [51] Ulrike G.K. Wegst, Matthew Schecter, Amalie E. Donius, and Philipp M. Hunger. Biomaterials by freeze casting. *Philosophical Transactions of the Royal Society A: Mathematical, Physical and Engineering Sciences*, 368(1917):2099–2121, 2010. ISSN 1364503X. doi: 10.1098/rsta.2010.0014.
- [52] Hyun Lee, Tae Sik Jang, Juha Song, Hyoun Ee Kim, and Hyun Do Jung. The production of porous hydroxyapatite scaffolds with graded porosity by sequential freeze-casting. *Materials*, 10(4):1–12, 2017. ISSN 19961944. doi: 10.3390/ma10040367.
- [53] T Waschies, R Oberacker, and M J Hoffmann. Investigation of structure formation during freeze-casting from very slow to very fast solidification velocities. *Acta Materialia*, (13):5135–5145, . ISSN 13596454. doi: 10.1016/j.actamat.2011.04.046.
- [54] Noah O. Shanti, Kiyoshi Araki, and John W. Halloran. Particle redistribution during dendritic solidification of particle suspensions. *Journal of the American Ceramic Society*, 89(8):2444–2447, 2006. ISSN 00027820. doi: 10.1111/j.1551-2916.2006.01094.x.
- [55] Andrea Bareggi, Eric Maire, Audrey Lasalle, and Sylvain Deville. Dynamics of the freezing front during the solidification of a colloidal alumina aqueous suspension: In situ x-ray radiography, tomography, and modeling. *Journal of the American Ceramic Society*, 94(10):3570–3578, 2011. ISSN 00027820. doi: 10.1111/j.1551-2916.2011.04572.x.
- [56] Kristen L. Scotti and David C. Dunand. Freeze casting – A review of processing, microstructure and properties via the open data repository, FreezeCasting.net. *Progress in Materials Science*, pages 243–305. ISSN 00796425. doi: 10.1016/j.pmatsci.2018.01.001.
- [57] Stefan Flauder, Uwe Gbureck, and Frank A. Müller. Structure and mechanical properties of β -TCP scaffolds prepared by ice-templating with preset ice front velocities. *Acta Biomaterialia*, (12):5148–5155. ISSN 18787568. doi: 10.1016/j.actbio.2014.08.020.
- [58] Christian Stolze, Tobias Janoschka, Stefan Flauder, Frank A. Müller, Martin D. Hager, and Ulrich S. Schubert. Investigation of Ice-Templated Porous Electrodes for Application in Organic Batteries. *ACS Applied Materials and Interfaces*, 8(36):23614–23623, 2016. ISSN 19448252. doi: 10.1021/acsami.6b05018.
- [59] Christian Stolze, Tobias Janoschka, Ulrich S. Schubert, Frank A. Müller, and Stefan Flauder. Directional Solidification with Constant Ice Front Velocity in the Ice-Templating Process. *Advanced Engineering Materials*, 18(1):111–120, 2016. ISSN 15272648. doi: 10.1002/adem.201500235.
- [60] Anders Smith, Christian R H Bahl, Rasmus Bjork, Kurt Engelbrecht, Kaspar K. Nielsen, and Nini Pryds. Materials challenges for high performance magnetocaloric refrigeration devices. *Advanced Energy Materials*, 2(11):1288–1318, 2012. ISSN 16146832. doi: 10.1002/aenm.201200167.

- [61] Anders Smith. Who discovered the magnetocaloric effect? Warburg, Weiss, and the connection between magnetism and heat. *European Physical Journal H*, 38(4):507–517, 2013. ISSN 21026459. doi: 10.1140/epjh/e2013-40001-9.
- [62] William Thomson. *Cyclopedia of the Physical Sciences*. Richard Green and Company, London and Glasgow, 2nd edition, 1860.
- [63] J. Romero Gómez, R. Ferreiro Garcia, A. De Miguel Catoira, and M. Romero Gómez. Magnetocaloric effect: A review of the thermodynamic cycles in magnetic refrigeration. *Renewable and Sustainable Energy Reviews*, 17:74–82, 2013. ISSN 13640321. doi: 10.1016/j.rser.2012.09.027.
- [64] Pierre Weiss and Auguste Piccard. Le phénomène magnétocalorique. *J. Phys. Theor. Appl.*, 7(1):103–109, 1917.
- [65] Thomas Frank Petersen, Nini Pryds, Anders Smith, Søren Linderøth, Stinus Jeppesen, and Hans-Jørgen Høgaard Knudsen. Magnetic Refrigeration and the Magnetocaloric Effect. In *Danske Køledage*, Jægerspris, 2006.
- [66] CR. Nave. Ferromagnetism, 2017. URL <http://hyperphysics.phy-astr.gsu.edu/hbase/Solids/ferro.html>.
- [67] Andrej Kitanovski, Jaka Tušek, Urban Tomc, Uroš Plaznik, Marko Ožbolt, and Alojz Poredoš. *Magnetocaloric Energy Conversion*. Springer. ISBN 978-3-319-08740-5. doi: 10.1007/978-3-319-08741-2.
- [68] Julia Lyubina. Magnetocaloric materials for energy efficient cooling. *Journal of Physics D: Applied Physics*, 50(5), 2017. ISSN 13616463. doi: 10.1088/1361-6463/50/5/053002.
- [69] Henrique Neves Bez. *Magnetocaloric materials and first order phase transitions*. Phd thesis, Technical University of Denmark, 2016.
- [70] R. Bjørk, C.R.H. Bahl, and M. Katter. Magnetocaloric properties of $\text{LaFe}_{13-x}\text{Co}_x\text{Si}_y$ and commercial grade Gd. *Journal of Magnetism and Magnetic Materials*, 322(24):3882–3888, 2010. ISSN 03048853. doi: 10.1016/j.jmmm.2010.08.013.
- [71] L. Von Moos, K. K. Nielsen, K. Engelbrecht, and C. R.H. Bahl. Experimental investigation of the effect of thermal hysteresis in first order material $\text{MnFe}(\text{P,As})$ applied in an AMR device. *International Journal of Refrigeration*, 37(1):303–306, 2014. ISSN 01407007. doi: 10.1016/j.ijrefrig.2013.05.005.
- [72] L. Von Moos, C. R.H. Bahl, K. K. Nielsen, and K. Engelbrecht. The influence of hysteresis on the determination of the magnetocaloric effect in $\text{Gd}_5\text{Si}_2\text{Ge}_2$. *Journal of Physics D: Applied Physics*, 48(2), 2015. ISSN 13616463. doi: 10.1088/0022-3727/48/2/025005.

- [73] G. Urbain, P. Weiss, and F. Trombe. Un nouveau métal ferromagnétique, le gadolinium. *Comptes Rendus*, (200):2132–2134, 1935.
- [74] A. Barcza, M. Katter, V. Zellmann, S. Russek, S. Jacobs, and C. Zimm. Stability and magnetocaloric properties of sintered La(Fe, Mn, Si) 13Hz alloys. *IEEE Transactions on Magnetics*, 47(10):3391–3394, 2011. ISSN 00189464. doi: 10.1109/TMAG.2011.2147774.
- [75] Tian Lei, Kaspar K. Nielsen, Kurt Engelbrecht, Christian R.H. Bahl, Henrique Neves Bez, and Christian T. Veje. Sensitivity study of multi-layer active magnetic regenerators using first order magnetocaloric material La(Fe,Mn,Si)13Hy. *Journal of Applied Physics*, (1), . ISSN 10897550. doi: 10.1063/1.4923356.
- [76] Henrique Neves Bez, Kristina Navickaitė, Tian Lei, Kurt Engelbrecht, Alexander Barcza, and Christian R.H. Bahl. Epoxy-bonded La(Fe,Mn,Si)13HZ as a multilayered active magnetic regenerator. In *7th IIF-IIR International Conference on Magnetic Refrigeration at Room Temperature*, Turin, Italy, 2016.
- [77] Kristina Navickaitė, Henrique Neves Bez, Tian Lei, Alexander Barcza, Hugo Vieyra, Christian R.H. Bahl, and Kurt Engelbrecht. Experimental and numerical comparison of multi-layered La(Fe,Si,Mn)13Hy active magnetic regenerators. *International Journal of Refrigeration*, 86:322–330, 2018. ISSN 01407007. doi: 10.1016/j.ijrefrig.2017.10.032.
- [78] K. Engelbrecht, K. K. Nielsen, C. R.H. Bahl, C. P. Carroll, and D. Van Asten. Material properties and modeling characteristics for MnFeP 1 - X As x materials for application in magnetic refrigeration. *Journal of Applied Physics*, 113(17), 2013. ISSN 00218979. doi: 10.1063/1.4803495.
- [79] J. D. Moore, D. Klemm, D. Lindackers, S. Grasmann, R. Träger, J. Eckert, L. Löber, S. Scudino, M. Katter, A. Barcza, K. P. Skokov, and O. Gutfleisch. Selective laser melting of La(Fe,Co,Si)13 geometries for magnetic refrigeration. *Journal of Applied Physics*, 114(4), 2013. ISSN 00218979. doi: 10.1063/1.4816465.
- [80] Alexander Funk, Jens Freudenberger, Anja Waske, and Maria Krautz. Getting magnetocaloric materials into good shape : Cold-working of La (Fe , Co , Si) 13 by powder-in-tube-processing. *Materials Today Energy*, pages 223–228. ISSN 2468-6069. doi: 10.1016/j.mtener.2018.05.009.
- [81] A Dinesen, S Linderoth, and S Mørup. Direct and indirect measurement of the magnetocaloric effect in La 0.67 Ca 0.33-x Sr x MnO 3. *Journal of Physics: Condensed Matter*, (39):6257–6269. ISSN 0953-8984. doi: 10.1088/0953-8984/17/39/011.
- [82] Christian R H Bahl, David Velázquez, Kaspar K. Nielsen, Kurt Engelbrecht, Kjeld B. Andersen, Regina Bulatova, and Nini Pryds. High performance magnetocaloric perovskites for magnetic refrigeration. *Applied Physics Letters*, 100(12), 2012. ISSN 00036951. doi: 10.1063/1.3695338.

- [83] David W. Richerson. *Modern Ceramic Engineering: Properties, Processing, and use in Design*. CRC Press, Taylor & Francis Group, 3rd edition, 2006.
- [84] R. Bjørk, C. R.H. Bahl, and K. K. Nielsen. The lifetime cost of a magnetic refrigerator. *International Journal of Refrigeration*, pages 48–62, . ISSN 01407007. doi: 10.1016/j.ijrefrig.2015.08.022.
- [85] R. Bjørk, K. K. Nielsen, C. R.H. Bahl, A. Smith, and A. C. Wulff. Comparing superconducting and permanent magnets for magnetic refrigeration. *AIP Advances*, (5), . ISSN 21583226. doi: 10.1063/1.4943305.
- [86] J.A. Barclay. The Theory of an Active Magnetic Regenerative Refrigerator. In *Goddard Space Flight Center Refrig. for Cryogenic Sensors*, pages 375–387. NASA, 1983. ISBN 6103544947.
- [87] Dan Eriksen, Kurt Engelbrecht, Christian Bahl, and Rasmus Bjørk. *Active magnetic regenerator refrigeration with rotary multi-bed technology*. PhD thesis, Technical University of Denmark, 2016.
- [88] A. Tura and A. Rowe. Permanent magnet magnetic refrigerator design and experimental characterization. *International Journal of Refrigeration*, (3):628–639. ISSN 01407007. doi: 10.1016/j.ijrefrig.2010.12.009.
- [89] Tian Lei, Kurt Engelbrecht, Kaspar K. Nielsen, and Christian T. Veje. Study of geometries of active magnetic regenerators for room temperature magnetocaloric refrigeration. *Applied Thermal Engineering*, pages 1232–1243, . ISSN 13594311. doi: 10.1016/j.applthermaleng.2015.11.113.
- [90] Tian Lei, Kurt Engelbrecht, Kaspar K. Nielsen, and Christian T. Veje. *Modeling of active magnetic regenerators and experimental investigation of passive regenerators with oscillating flow*. PhD thesis, Technical University of Denmark, 2016.
- [91] K. K. Nielsen, C. R.H. Bahl, A. Smith, N. Pryds, and J. Hattel. A comprehensive parameter study of an active magnetic regenerator using a 2D numerical model. *International Journal of Refrigeration*, (4):753–764, . ISSN 01407007. doi: 10.1016/j.ijrefrig.2009.12.024.
- [92] K. K. Nielsen, K. Engelbrecht, and C. R H Bahl. The influence of flow maldistribution on the performance of inhomogeneous parallel plate heat exchangers. *International Journal of Heat and Mass Transfer*, (1):432–439, . ISSN 00179310. doi: 10.1016/j.ijheatmasstransfer.2013.01.018.
- [93] K. K. Nielsen, C. R.H. Bahl, and K. Engelbrecht. The effect of flow maldistribution in heterogeneous parallel-plate active magnetic regenerators. *Journal of Physics D: Applied Physics*, 46(10), 2013. ISSN 00223727. doi: 10.1088/0022-3727/46/10/105002.

- [94] T. Lei, K. Engelbrecht, K. K. Nielsen, C. T. Veje, J. Tušek, and C. R.H. Bahl. Modelling and comparison studies of packed screen regenerators for active magnetocaloric refrigeration. *Refrigeration Science and Technology*, 2011-Janua:97–98, 2011. ISSN 01511637.
- [95] Tian Lei, Kristina Navickaitė, Kurt Engelbrecht, Alexander Barcza, Hugo Vieyra, Kaspar K. Nielsen, and Christian R.H. Bahl. Passive characterization and active testing of epoxy bonded regenerators for room temperature magnetic refrigeration. *Applied Thermal Engineering*, 128:10–19, 2018. ISSN 13594311. doi: 10.1016/j.applthermaleng.2017.08.152.
- [96] Nini Pryds, Frank Clemens, Mohan Menon, Pernille H. Nielsen, Karen Brodersen, Rasmus Bjørk, Christian R.H. Bahl, Kurt Engelbrecht, Kaspar K. Nielsen, and Anders Smith. A monolithic perovskite structure for use as a magnetic regenerator. *Journal of the American Ceramic Society*, 94(8):2549–2555, 2011. ISSN 00027820. doi: 10.1111/j.1551-2916.2011.04398.x.
- [97] Pei Xue Jiang, Ming Hong Fan, Guang Shu Si, and Ze Pei Ren. Thermal-hydraulic performance of small scale micro-channel and porous-media heat-exchangers. *International Journal of Heat and Mass Transfer*, 44(5):1039–1051, 2001. ISSN 00179310. doi: 10.1016/S0017-9310(00)00169-1.
- [98] Kaspar K. Nielsen, Kurt Engelbrecht, Dennis V. Christensen, Jesper B. Jensen, Anders Smith, and Christian R. H. Bahl. Degradation of the performance of microchannel heat exchangers due to flow maldistribution. *Applied Thermal Engineering*, 40:236–247, 2012. doi: 10.1016/j.applthermaleng.2012.02.019.
- [99] D. Eriksen, K. Engelbrecht, C. R.H. Bahl, R. Bjørk, K. K. Nielsen, A. R. Insinga, and N. Pryds. Design and experimental tests of a rotary active magnetic regenerator prototype. *International Journal of Refrigeration*, (1982):14–21. ISSN 01407007. doi: 10.1016/j.ijrefrig.2015.05.004.
- [100] Rasmus Bjørk. Controlling ice-growth to create micro-channel structures, 2016.
- [101] Regina Bulatova. *Experimental Tape Casting of Adjacently Graded Materials for Magnetic Refrigeration*. Phd dissertation, Technical University of Denmark, 2014.
- [102] Regina Bulatova, Christian Bahl, Kjeld Andersen, Luise Theil Kuhn, and Nini Pryds. Functionally Graded Ceramics Fabricated with Side-by-Side Tape Casting for Use in Magnetic Refrigeration. *International Journal of Applied Ceramic Technology*, 12(4): 891–898, 2015. ISSN 17447402. doi: 10.1111/ijac.12298.
- [103] R. Bulatova, M. Gudik-Sørensen, M. Della Negra, K. B. Andersen, A. Kaiser, and C. R.H. Bahl. The effect of tape casting operational parameters on the quality of adjacently graded ceramic film. *Ceramics International*, (4):4663–4671. ISSN 02728842. doi: 10.1016/j.ceramint.2015.11.042.

- [104] Anders Reves Dinesen. *Magnetocaloric and magnetoresistive*. Number August. 2004. ISBN 8755032230.
- [105] J. M.D. Coey, M. Viret, and S. Von Molnár. Mixed-valence manganites. *Advances in Physics*, 58(6):571–697, 2009. ISSN 14606976. doi: 10.1080/00018730903363184.
- [106] A. S. Bhalla, R. Guo, and R. Roy. The perovskite structure - a review of its role in ceramic science and technology. *Materials Research Innovations*, (1):3–26. ISSN 1432-8917. doi: 10.1007/s100190000062.
- [107] K. A. Gschneidner and V. K. Pecharsky. Magnetocaloric materials. *Annu. Rev. Mater. Sci.*, 30:387–429, 2000.
- [108] Christian R.H. Bahl. Unpublished data - magnetocaloric measurements of LCSM powders. 2018.
- [109] Rohm and Haas. Material Safety Data Sheet - DURAMAX D-3005 Dispersant. Technical report, 1997.
- [110] Rohm and Haas. Material Safety Data Sheet - DURAMAX B-1022. Technical report, 1999.
- [111] K. K. Nielsen, H. N. Bez, L. Von Moos, R. Bjørk, D. Eriksen, and C. R H Bahl. Direct measurements of the magnetic entropy change. *Review of Scientific Instruments*, 86(10), 2015. ISSN 10897623. doi: 10.1063/1.4932308.
- [112] J. García Ten, M. J. Orts, A. Saburit, and G. Silva. Thermal conductivity of traditional ceramics. Part I: Influence of bulk density and firing temperature. *Ceramics International*, 36(6):1951–1959, 2010. ISSN 02728842. doi: 10.1016/j.ceramint.2010.05.012.
- [113] Rajendra K. Bordia and Srinivasa Rao Boddapati. Aligned pore channels in 8mol% Yttria stabilized zirconia by freeze casting. pages 363–372, 2008.
- [114] R. M. Batista and E. N S Muccillo. Dilatometry analysis of the sintering process of nanostructured gadolinia-doped ceria. *Journal of Thermal Analysis and Calorimetry*, 126(3):1007–1013, 2016. ISSN 15882926. doi: 10.1007/s10973-016-5674-5.
- [115] P. S. Jørgensen, K. V. Hansen, R. Larsen, and J. R. Bowen. Geometrical characterization of interconnected phase networks in three dimensions. *Journal of Microscopy*, 244(1): 45–58, 2011. ISSN 00222720. doi: 10.1111/j.1365-2818.2011.03504.x.
- [116] P. S. Jørgensen, S. L. Ebbelhøj, and A. Hauch. Triple phase boundary specific pathway analysis for quantitative characterization of solid oxide cell electrode microstructure. *Journal of Power Sources*, pages 686–693. ISSN 03787753. doi: 10.1016/j.jpowsour.2015.01.054.

- [117] Salvatore De Angelis, Peter Stanley Jørgensen, Vincenzo Esposito, Esther Hsiao Rho Tsai, Mirko Holler, Kosova Kreka, Ebtisam Abdellahi, and Jacob R. Bowen. Ex-situ tracking solid oxide cell electrode microstructural evolution in a redox cycle by high resolution ptychographic nanotomography. *Journal of Power Sources*, pages 520–527, . ISSN 03787753. doi: 10.1016/j.jpowsour.2017.06.035.
- [118] Salvatore De Angelis, Peter Stanley Jørgensen, Esther Hsiao Rho Tsai, Mirko Holler, Kosova Kreka, and Jacob R. Bowen. Three dimensional characterization of nickel coarsening in solid oxide cells via ex-situ ptychographic nano-tomography. *Journal of Power Sources*, pages 72–79, . ISSN 03787753. doi: 10.1016/j.jpowsour.2018.02.031.
- [119] Mathworks. Image Processing Toolbox™ Reference R 2016a, 2016.
- [120] E. A. Olevsky, X. Wang, E. Bruce, M. B. Stern, S. Wildhack, and F. Aldinger. Synthesis of gold micro- and nano-wires by infiltration and thermolysis. *Scripta Materialia*, 56(10): 867–869, 2007. ISSN 13596462. doi: 10.1016/j.scriptamat.2007.01.037.
- [121] Yufei Tang, Sha Qiu, Qian Miao, and Cong Wu. Fabrication of lamellar porous alumina with axisymmetric structure by directional solidification with applied electric and magnetic fields. *Journal of the European Ceramic Society*, (5):1233–1240, . ISSN 1873619X. doi: 10.1016/j.jeurceramsoc.2015.12.012.
- [122] Michael B. Frank, Steven E. Naleway, Tsuk Haroush, Chin Hung Liu, Sze Hei Siu, Jerry Ng, Ivan Torres, Ali Ismail, Keyur Karandikar, Michael M. Porter, Olivia A. Graeve, and Joanna McKittrick. Stiff, porous scaffolds from magnetized alumina particles aligned by magnetic freeze casting. *Materials Science and Engineering C*, pages 484–492. ISSN 09284931. doi: 10.1016/j.msec.2017.03.246.
- [123] Stephen W. Sofie. Fabrication of functionally graded and aligned porosity in thin ceramic substrates with the novel freeze-tape-casting process. *Journal of the American Ceramic Society*, 90(7):2024–2031, 2007. ISSN 00027820. doi: 10.1111/j.1551-2916.2007.01720.x.
- [124] Cathrine D. Christiansen, Kaspar K. Nielsen, and Rasmus Bjørk. Freeze-casting to create directional micro-channels in regenerators for magnetic refrigeration. In *Proceedings of TherMag VIII, 8th IIF-IIR International Conference on Caloric Cooling*, pages 96–101, Darmstadt, Germany, 2018. doi: 10.18462/iir.11072.
- [125] Hans Dieter Baehr and Karl Stephan. *Heat and mass transfer*. Springer, 2nd edition, 2004. ISBN 9781420041583. doi: 10.4324/9780429035982-11.
- [126] J. A. Turcaud, H. N. Bez, E. Ruiz-Trejo, C. R.H. Bahl, K. K. Nielsen, A. Smith, and L. F. Cohen. Influence of manganite powder grain size and Ag-particle coating on the magnetocaloric effect and the active magnetic regenerator performance. *Acta Materialia*, pages 413–418. ISSN 13596454. doi: 10.1016/j.actamat.2015.06.058.

- [127] R. U. Gilissen, J. P. Erauw, A. Smolders, E. Vanswijghoven, and J. Luyten. Gelcasting, a near net shape technique. *Materials and Design*, 21:251–257, 2000.
- [128] Masayuki Nakata, Kimiaki Tanihata, Shunro Yamaguchi, and Katsuaki Suganuma. Fabrication of porous alumina sintered bodies by a gelate-freezing method. *Journal of the Ceramic Society of Japan*, 113(1323):712–715, 2005. ISSN 13486535. doi: 10.2109/jcersj.113.712.
- [129] Manabu Fukushima, Masayuki Nakata, You Zhou, Tatsuki Ohji, and Yu-ichi Yoshizawa. Fabrication and properties of ultra highly porous silicon carbide by the gelation – freezing method. *Journal of the European Ceramic Society*, (14):2889–2896, . ISSN 0955-2219. doi: 10.1016/j.jeurceramsoc.2010.03.018.
- [130] Manabu Fukushima, Sakae Tsuda, and Yu Ichi Yoshizawa. Fabrication of highly porous alumina prepared by gelation freezing route with antifreeze protein. *Journal of the American Ceramic Society*, 96(4):1029–1031, 2013. ISSN 00027820. doi: 10.1111/jace.12229.
- [131] Manabu Fukushima, Yu Ichi Yoshizawa, and Tatsuki Ohji. Macroporous ceramics by gelation-freezing route using gelatin. *Advanced Engineering Materials*, 16(6):607–620, 2014. ISSN 15272648. doi: 10.1002/adem.201400067.
- [132] Manabu Fukushima and Yu Ichi Yoshizawa. Fabrication and morphology control of highly porous mullite thermal insulators prepared by gelation freezing route. *Journal of the European Ceramic Society*, (12):2947–2953, . ISSN 1873619X. doi: 10.1016/j.jeurceramsoc.2015.09.041.
- [133] A. G. Ward. The chemical structure and physical properties of gelatin. *The Journal of Photographic Science*, 3:60–67, 1955.
- [134] K. B. Djagny, Z. Wang, and S. Xu. Gelatin: A valuable protein for food and pharmaceutical industries: Review. *Critical Reviews in Food Science and Nutrition*, 41(6):481–492, 2001. ISSN 10408398. doi: 10.1080/20014091091904.
- [135] Reinhard Schreiber and Herbert Gareis. *Gelatine Handbook: Theory and Industrial Practice*. Wiley-VCH, 2007. ISBN 9783527315482.
- [136] Madeleine Djabourov, Jacques Leblond, and Pierre Papon. Gelation of aqueous gelatin solutions. I. Structural investigation. *Journal de Physique*, 49(2):319–332, 1988. ISSN 0302-0738. doi: 10.1051/jphys:01988004902031900.
- [137] Sigma-Aldrich. Gelatin from porcine skin - product description, 2019. URL <https://www.sigmaaldrich.com/catalog/product/sigma/g2625?lang=en®ion=DK>.

- [138] Manabu Fukushima, Tatsuki Ohji, Hideki Hyuga, Chika Matsunaga, and Yu-ichi Yoshizawa. Effect of gelatin gel strength on microstructures and mechanical properties of cellular ceramics created by gelation freezing route. *Journal of Materials Research*, pages 1–8, . ISSN 0884-2914. doi: 10.1557/jmr.2017.94.
- [139] Kaspar K. Nielsen. *Numerical modeling and analysis of the active magnetic regenerator*. PhD thesis, Technical University of Denmark, Kgs. Lyngby, Denmark, 2010.
- [140] P Govindappa, P V Trevizoli, O Campbell, I Niknia, T V Christiaanse, R Teyber, S Misra, M A Schwind, D van Asten, L Zhang, and A Rowe. Experimental investigation of MnFeP 1-x As x multilayer active magnetic regenerators. *Journal of Physics D: Applied Physics*, 50:315001, 2017. doi: 10.1088/1361-6463/aa7a33.
- [141] Manuel Acosta, Valerie L. Wiesner, Carlos J. Martinez, Rodney W. Trice, and Jeffrey P. Youngblood. Effect of polyvinylpyrrolidone additions on the rheology of aqueous, highly loaded alumina suspensions. *Journal of the American Ceramic Society*, 96(5):1372–1382, 2013. ISSN 00027820. doi: 10.1111/jace.12277.
- [142] Debora Marani, Bhaskar Reddy Sudireddy, Wolff-Ragnar Kiebach, Lotte Nielsen, and Sokol Ndoni. Rheological properties of poly(vinylpyrrolidone) as a function of molecular weight. *Nordic Rheology Society. Annual Transactions*, 22, 2014. ISSN 16014057.
- [143] Jierong Liang, Cathrine D. Christiansen, Kurt Engelbrecht, Kaspar K. Nielsen, Rasmus Bjørk, and Christian R.H. Bahl. Heat Transfer and Flow Resistance Analysis of a Novel Freeze-Cast Regenerator. (*submitted*).
- [144] K. K. Nielsen, C. R.H. Bahl, A. Smith, R. Bjørk, N. Pryds, and J. Hattel. Detailed numerical modeling of a linear parallel-plate Active Magnetic Regenerator. *International Journal of Refrigeration*, 32(6):1478–1486, 2009. ISSN 01407007. doi: 10.1016/j.ijrefrig.2009.03.003.
- [145] C. R H Bahl, T. F. Petersen, N. Pryds, and A. Smith. A versatile magnetic refrigeration test device. *Review of Scientific Instruments*, 79(9), 2008. ISSN 00346748. doi: 10.1063/1.2981692.
- [146] Kurt Engelbrecht. *A Numerical Model of an Active Magnetic Regenerator Refrigerator with Experimental Validation*. PhD thesis, University of Wisconsin - Madison, 2008.
- [147] Frank P. Incropera and David P. DeWitt. *Fundamentals of heat and mass transfer*. Wiley, 4th edition. ISBN 0471304603.
- [148] Markus Nickolay and Holger Martin. Improved approximation for the Nusselt number for hydrodynamically developed laminar flow between parallel plates. *International Journal of Heat and Mass Transfer*, 45(15):3263–3266, 2002. ISSN 00179310. doi: 10.1016/S0017-9310(02)00028-5.